Magnetic and Magnetoelectric Properties of Some Collinear and Non-collinear Spin Ordered Magnetic Oxides

A Thesis

Submitted for the Degree of

Doctor of Philosophy

by

Somnath Ghara

Chemistry and Physics of Materials Unit

Jawaharlal Nehru Centre for Advanced Scientific Research

(A Deemed University)

Bangalore - 560064

May 2017

Dedicated to my parents

DECLARATION

I hereby declare that the matter embodied in the thesis entitled "**Magnetic and Magnetoelectric Properties of Some Collinear and Non-collinear Spin Ordered Magnetic Oxides**" is the result of investigations carried out by me at the Chemistry and Physics of Materials Unit, Jawaharlal Nehru Centre for Advanced Scientific Research, Bangalore, India under the supervision of Prof. A. Sundaresan and it has not been submitted elsewhere for the award of any degree or diploma.

In keeping with the general practice in reporting the scientific observations, due acknowledgements have been made whenever the work described is based on the findings of other investigators. Any omission that might have occurred due to oversight or error in judgement is regretted.

Bangalore

24/05/2017

Somnath Ghara

CERTIFICATE

I hereby certify that the matter embodied in this thesis entitled "**Magnetic and Magnetoelectric Properties of Some Collinear and Non-collinear Spin Ordered Magnetic Oxides**" has been carried out by Mr. Somnath Ghara at the Chemistry and Physics of Materials Unit, Jawaharlal Nehru Centre for Advanced Scientific Research, Bangalore, India under my supervision and it has not been submitted elsewhere for the award of any degree or diploma.

Prof. A. Sundaresan
(Research Supervisor)

ACKNOWLEDGEMENTS

Firstly, I would like to thank my research supervisor Prof. A. Sundaresan for introducing me to the field of multiferroics and providing me an opportunity to work under his guidance. I thank him for constant support and encouragement throughout my course of research investigations. I am really grateful for his patience and positive attitude toward me in various aspect of research work.

I would like thank Prof. C. N. R. Rao, FRS for providing me various experimental facilities and for being a constant source of inspiration.

I would like to thank Prof. S. Balasubramanian and Prof. C. Narayana, past and present chairmen, respectively, for allowing me to utilize the various facilities in the unit.

I acknowledge Sheikh Saqr Laboratory at JNCASR for providing various experimental facilities.

I specially thank Dr. E. Suard and Prof. J. Rodríguez-Carvajal from Institut Laue-Langevin for neutron diffraction study; Mr. B. G. Jeon, Mr. K. Yoo and Prof. K. H. Kim from Seoul National University for PUND measurements; Dr. N. V. Ter-Oganessian from Southern Federal University for theoretical studies; Dr. F. Francois from CELLS–ALBA synchrotron for synchrotron X-ray diffraction experiments; Mr. T. Thao Tran and Prof. P. S. Halasyamani from University of Houston for SHG measurements, Dr. A. Iyo from National Institute of Advanced Industrial Science and Technology for high pressure synthesis.

I would like to thank Prof. A. Sundaresan, Dr. R. Ganapathy, Prof. U. V. Waghmare, Prof. S. Narasimhan and Prof. T. N. Guru Row (IISc) for their informative course works.

I thank the technical staffs namely Mr. Srinath, Mr. Anil, Mr. Srinivasa, Mr. Vasu, Ms. Selvi, Mr. Mahesh for their helps in various experiments.

I would like to thank all of my past and present lab mates, Dr. Vengadesh, Dr. Pranab, Dr. Shipra, Mr. Madhu, Dr. Nitesh, Dr. Rana, Dr. Sundarayya, Dr. Rambabu, Mr. Bharath, Mr. Chandan, Mr. Abhijit, Mr. Premakumar, Mr. Amit, Mr. Ravi, Ms. Pavitra and Mr. Chandraiah for their various helps in the course of research and maintaining a friendly atmosphere in lab.

I thank Complab, Library, Hostel, Dhanvantari, Academics and Administration staffs for providing and maintaining various facilities.

I thank all my friends at JNCASR, specially Arpan, Abhijit, Avijit, Chandan, Jiarul, Nivedita, Saikat, Sanjay, Sisir and Subhajit for their company in various academic and nonacademic activities.

Finally, I would like to thank my parents and family members for being there always.

Preface

The aim of the thesis was to search for new magnetoelectric and multiferroic materials. Thus, the thesis presents a detailed study on magnetic, magnetoelectric and multiferroic properties of some collinear and non-collinear spin ordered magnetic oxides. The present investigations were undertaken on four different systems.

Chapter 1 gives an introduction to magnetoelectric and multiferroic materials. Since the symmetry is an important aspect of these properties, a detailed discussion on symmetry is given. Various mechanisms of inducing ferroelectricity by magnetic ordering are discussed.

Chapter 2 describes different experimental techniques used in the present work.

Chapter 3 discusses detailed magnetic and electrical properties of a complex oxide $BiMnFe_2O_6$, which crystallizes in a centrosymmetric orthorhombic structure (space group *Pbcm*). It exhibits a spiral antiferromagnetic ordering at 212 K with a peak in magnetization at $T_P \sim 35$ K. This compound has two potential mechanisms for inducing ferroelectricity. These are (i) the presence of lone pair active Bi^{3+} ions and (ii) spiral magnetic ordering of Fe^{3+}/Mn^{3+} spins. However, PUND measurements confirm that this material is non-polar. Further, it is shown that the peak in magnetization at low temperature (T_P) arises due to appearance of re-entrant spin glass state. Below T_P, both long-range spiral antiferromagnetic ordering and spin glass state coexist. Further, a magnetic anomaly is found around 170 K, where a dielectric anomaly with a significant intrinsic magnetodielectric effect is observed. Magnetic property changes drastically upon Sm^{3+} substitution at Bi^{3+} site in $Bi_{1-x}Sm_xMnFe_2O_6$ ($x = 0.1$ and 0.2). However, it does not induce spontaneous electric polarization. In $x = 0.2$ sample, a broad peak is found in magnetization, which is due to appearance of weak ferromagnetic state. Upon further cooling, an antiferromagnetic state is observed. For $x = 0.2$, magnetodielectric effect is observed at all temperatures below T_N. However, it has been shown that the magnetodielectric effect in the antiferromagnetic region has an intrinsic capacitive origin,

while it is governed by the extrinsic magnetoresistive effect in the weak ferromagnetic region.

Chapter 4 demonstrates the first experimental observation of linear magnetoelectric effect in *A*-site magnetic spinels, Co_3O_4 and $CoAl_2O_4$. Co_3O_4 exhibits a well-defined long range collinear antiferromagnetic ordering below T_N ~ 30 K. Magnetic field induced sharp dielectric anomaly is found around T_N, below which electric polarization is observed under applied magnetic fields and it varies linearly with applied magnetic fields. These results confirm the linear magnetoelectric effect in Co_3O_4. On the other hand, in case of $CoAl_2O_4$, there is no consensus on the magnetic ground state, whether it is spiral spin liquid or long-range collinear antiferromagnetic ordered state and there exist many contradicting experimental reports regarding its magnetic ground state. Different disordered samples of $Co_{1-x}Al_x[Al_{2-x}Co_x]O_4$ (x = 0.05, 0.07, 0.11 and 0.14) are prepared in the present study and it is found that the samples with $x \leq 0.11$ exhibit linear magnetoelectric effect, while the sample with x = 0.14 exhibits a spin glass state without magnetoelectric effect. The observation of magnetoelectric effect in low disordered $CoAl_2O_4$ suggests that the magnetic ground state is a long-range collinear antiferromagnetic ordered state. The experimental results are further supported by Monte Carlo calculations.

Chapter 5 is focused on the discovery of a new series of type-II multiferroics, RFeWO$_6$ (R = Dy, Eu, Tb and Y) which crystallize in an ordered aeschynite-type structure with polar $Pna2_1$ space group. Dielectric anomaly is found around the magnetic ordering temperature in all the samples, where electric polarization appears under zero magnetic fields. Further, magnetic field strongly influences both dielectric anomaly and electric polarization. These results indicate that the compounds RFeWO$_6$ are magnetoelectric multiferroics. Using neutron diffraction experiments, it is shown that an unusual noncollinear magnetic ordering of Fe^{3+} spins in DyFeWO$_6$ is responsible for inducing polarization.

Chapter 6 deals with the structural, magnetic and magnetodielectric properties of another aeschynite-type polar oxide, DyCrWO$_6$. A weak dielectric anomaly is found around T_N, which is suppressed by magnetic field. However, electric polarization is not observed. Some interesting results such as magnetization reversal and large magnetocaloric effect are observed at low temperature.

Chapter 7 presents the multiferroic and magnetic properties of another complex oxide $BaYFeO_4$, which crystallizes in a centrosymmetric orthorhombic structure (space group *Pnma*). It is reported that this oxide exhibits a cycloidal magnetic ordering below 35 K. An electric polarization is found below 35 K in zero magnetic field, which is associated with a dielectric anomaly. Dielectric anomaly and electric polarization are suppressed under high magnetic fields. Further, it is shown that a re-entrant spin glass state appears below 17 K.

Publications

1. "Reentrant spin-glass state and magnetodielectric effect in the spiral magnet $BiMnFe_2O_6$", **S. Ghara**, B.G. Jeon, K. Yoo, K. H. Kim and A. Sundaresan, *Phys. Rev. B*, **90**, 024413 (2014).
2. "Capacitive and magnetoresistive origin of magnetodielectric effects in Sm-substituted spiral antiferromagnet $BiMnFe_2O_6$", **S. Ghara**, K. Yoo, K. H. Kim and A. Sundaresan, *J. Appl. Phys.*, **118**, 164103 (2015).
3. "Magnetoelectric effect in simple collinear antiferromagnetic spinels", R. Saha, **S. Ghara**, E. Suard, D. H. Jang, K. H. Kim, N. V. Ter-Oganessian and A. Sundaresan, *Phys. Rev. B*, **94**, 14428 (2016).
4. "Linear magnetoelectric effect as a signature of long-range collinear anti-ferromagnetic ordering in the frustrated spinel $CoAl_2O_4$", **S. Ghara**, N. V. Ter-Oganessian and A. Sundaresan, *Phys. Rev. B*, **95**, 94404 (2017).
5. "Ordered aeschynite-type polar magnets RFeWO$_6$ (R = Dy, Eu, Tb and Y): A new family of type-II multiferroics", **S. Ghara**, E. Suard, F. Francois, T. T. Tran, P. S. Halasyamani, A. Iyo, J. Rodríguez-Carvajal, and A. Sundaresan, *Phys. Rev. B*, **95**, 224416 (2017).
6. "Structural, magnetic and dielectric properties of an aeschynite-type polar magnets $DyCrWO_6$", **S. Ghara**, E. Suard, F. Francois and A. Sundaresan (manuscript under preparation).
7. "Multiferroic properties and re-entrant spin glass behavior in $BaYFeO_4$", **S. Ghara** and A. Sundaresan (manuscript under preparation).

Miscellaneous Publications

1. "Temperature dependent magnetic, dielectric and Raman studies of partially disordered La_2NiMnO_6", P. Kumar, **S. Ghara**, B. Rajeswaran, D. V. S. Muthu, A. Sundaresan, AK Sood, *Solid State Commun.*, 184, 47 (2014).
2. "Effect of internal electric field on ferroelectric polarization in multiferroic $TbMnO_3$", C. De, **S. Ghara**, A. Sundaresan, *Solid State Commun.*, 205, 61 (2015).
3. "Stable p-type conductivity in B and N co-doped ZnO epitaxial thin film", R. Sahu, H. B. Gholap, G. Mounika, K. Dileep, B. Vishal, **S. Ghara**, R. Datta, *Phys. Status Solidi B,* 253, 504 (2015).
4. "Large linear magnetoresistance in topological crystalline insulator $Pb_{0.6}Sn_{0.4}Te$", S Roychowdhury, **S. Ghara**, S. N. Guin, A. Sundaresan, K. Biswas, *J. Solid State Chem.*, 233, 199 (2016).
5. "Is $CH_3NH_3PbI_3$ Polar?", P. Mahale, B. P. Kore, S. Mukherjee, M. S. Pavan, C. De, **S. Ghara**, A. Sundaresan, A. Pandey, T. N. Guru Row, D. D. Sarma, *J. Phys. Chem. Lett.*, 7, 2412 (2016).
6. "Structural and magnetic properties of a new and ordered quaternary alloy MnNiCuSb (SG: $F\bar{4}3m$)", Z. Haque, G. S. Thakur, **S. Ghara**, L. C. Gupta, A. Sundaresan, A. K. Ganguli, *J. Magn. Magn. Mater.*, 397, 315 (2016).
7. "Synthetically tuned structural variations in $CePd_xGe_{2-x}$(x = 0.21, 0.32, 0.69) towards diverse physical properties", S. Sarkar, S. Banerjee, P. Halappa, D. Kalsi, D. Mumbaraddi, **S. Ghara**, S. K. Pati, A. Sundaresan, I. D. Silva, S. Rayaprol, B. Joseph, S. C. Peter, *Inorg. Chem. Front.*, 4, 241 (2017).

Contents

Chapter 1

Introduction to magnetoelectrics and multiferroics

Summary

This chapter presents a brief introduction to the magnetoelectric and multiferroic materials and their possible applications. Starting from the definitions of magnetoelectric effect and multiferroicity, various ways by which ferroelectricity and magnetism can be combined in a single-phase material are discussed in details. Since the symmetry of the crystals is an important factor in these classes of materials, a brief discussion on the symmetry aspect is presented here. It is demonstrated that how symmetry itself can decide whether a material would be a magnetoelectric or multiferroic. Finally, the scope of the thesis is presented.

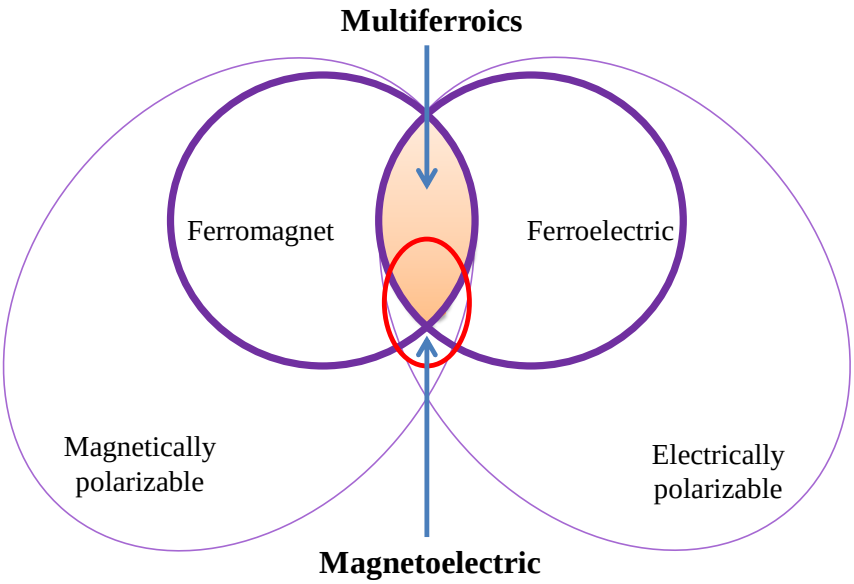

1.1 Magnetoelectrics

In general, the magnetization of a solid is governed by the spins of the electrons, while the charges of electrons or ions are responsible for electric polarization and thus they can be controlled by applying external magnetic and electric fields, respectively. Magnetoelectrics are one of the interesting classes of materials, where magnetization can be induced by applying electric field and electric polarization can be induced by applying magnetic field [1,2]. Therefore, these materials offer a great platform for electric field controlled magnetism and vice versa. The work on magnetoelectric effect started more than a century ago and it has progressed through the pioneering works of many great scientists (Figure 1.1) [1,3,4]. In 1894, Pierre Curie first proposed magnetoelectric effect on the basis of symmetry [5]. Later, Piccardo, Debye and Van Vleck suggested that magnetoelectric effect is impossible [6,7]. After two decades, Landau and Lifshitz showed that magnetoelectric effect may appear in the materials with certain types of magnetic and crystal symmetry [8]. Dzyaloshinskii in 1959 predicted that the antiferromagnetic structure of Cr_2O_3 should allow linear magnetoelectric effect [9]. This prediction was confirmed by experiments by two different groups. Astrov discovered electric field induced magnetization below magnetic ordering temperature in Cr_2O_3 [10,11]. Rado and Folen demonstrated the reverse effect i.e., the magnetic field induced electric polarization in Cr_2O_3 [12]. However, the magnetoelectric coefficient of Cr_2O_3 is small for application. Thus, many theoretical and experimental investigations were started in search for room temperature magnetoelectric materials with higher magnetoelectric coupling.

From theoretical point of view, the total energy of a material placed in a uniform magnetic field ($\vec{H}$) and electric field ($\vec{E}$) can be represented by [1],

$$F(E,H) = F_0 - P_i^s E_i - M_i^s H_i - \frac{1}{2}\epsilon_0 \epsilon_{ij} E_i E_j - \frac{1}{2}\mu_0 \mu_{ij} H_i H_j - \alpha_{ij} E_i H_j$$

$$- \tfrac{1}{2}\beta_{ijk} E_i H_j H_k - \tfrac{1}{2}\gamma_{ijk} H_i E_j E_k \qquad (1)$$

The electric polarization ($\vec{P}$) of the material can be obtained by,

$$P_i(E,H) = -\frac{\partial F}{\partial E_i} = P_i^s + \epsilon_0 \epsilon_{ij} E_j + \alpha_{ij} H_j + \beta_{ijk} H_j H_k \qquad (2)$$

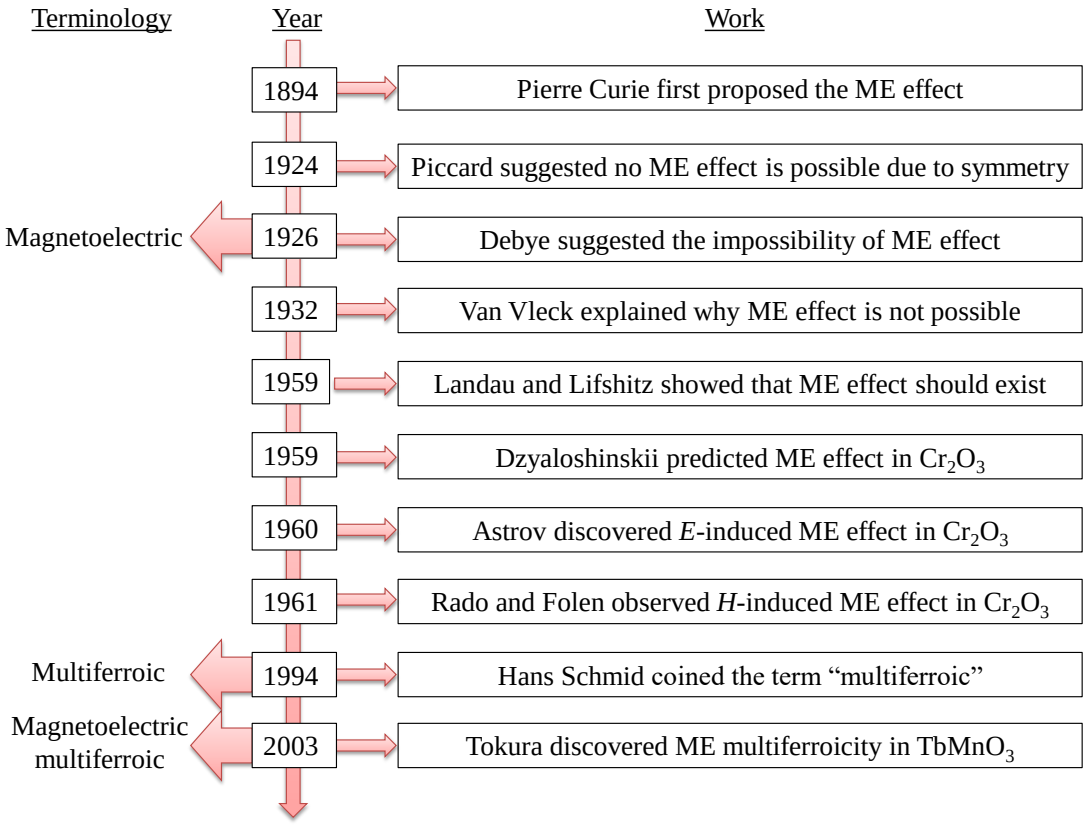

Figure 1.1 History and progress in the field of magnetoelectric and multiferroic materials.

The magnetization ($\vec{M}$) of the material can be obtained by,

$$M_i(E,H) = -\frac{\partial F}{\partial H_i} = M_i^s + \mu_0\mu_{ij}H_j + \alpha_{ji}E_j + \gamma_{ijk}E_jE_k \qquad (3)$$

Here, P_i^s and M_i^s denote the i^{th} component of the spontaneous electric polarization and spontaneous magnetization of the material. The second term in equation 2 (or 3) is associated with the polarization (magnetization) contributed by the electric field (magnetic field), where ε and μ are the electric and magnetic susceptibilities, respectively. The α_{ij}, known as linear magnetoelectric coefficient, is an axial tensor of rank 2, which couples electric and magnetic order parameters. This α_{ij} is responsible for controlling electric polarization by magnetic field and magnetization by electric field. The terms β_{ijk} and γ_{ijk} represent the higher order magnetoelectric coupling terms. Further, Equation 2 (or 3) indicates that if there is no spontaneous electric polarization (or magnetization), under E = 0 (or H = 0) condition, the electric polarization (or magnetization) is solely induced by magnetic field (or electric field).

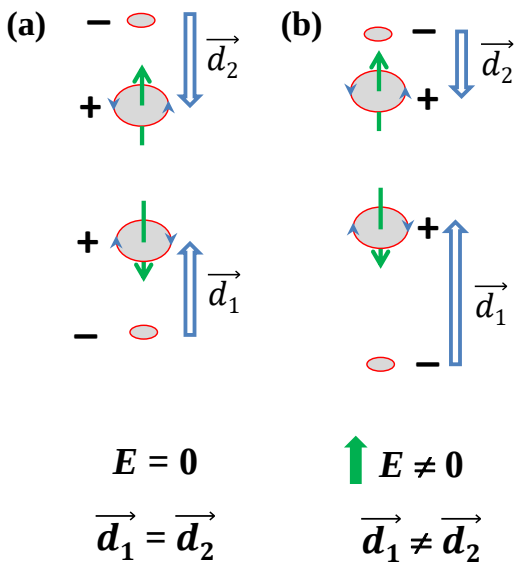

Figure 1.2 A simple model that explains the magnetoelectric effect.

In order to understand how magnetization is induced by electric field, a simple one dimensional model as shown in Figure 1.2 can be considered [13]. As shown in Figure 1.2(a), under zero electric field, there is no magnetization since the spins are opposite and no net electric polarization since $\vec{d}_1 = \vec{d}_2$. However, when electric field is applied along the chain direction, the cations and anions will be displaced in opposite directions as shown in Figure 1.2(b), resulting two nonequivalent electric dipoles ($\vec{d}_1 \neq \vec{d}_2$). This leads to a net electric polarization. Further, since the environment of the cations with opposite moments become different, a net magnetization will be induced. This phenomenon occurs in Cr_2O_3 under an external electric field [1]. However, the isostructural compound Fe_2O_3 is not magnetoelectric. This is because of the fact that the magnetoelectric effect is constrained by the symmetry of both crystal and magnetic structure. The detailed symmetry requirements of magnetoelectric effect are discussed later in this chapter.

1.2 Multiferroics

Ferroelectrics are those materials that exhibit spontaneous electric polarization below Curie temperature (T_C) and the direction of the electric polarization can be reversed by reversing external electric field. On the other hand, ferromagnets have spontaneous magnetization and it can be switched by reversing magnetic field. In multiferroics, both

of these two properties i.e., ferroelectricity and ferromagnetism, exist together [2,14,15]. In the current trend, the definition of multiferroics is expanded to include other long-range magnetic orders such as antiferromagnetism and ferrimagnetism. According to the classical concept, magnetic and ferroelectric order cannot coexist in a single phase material [3,14]. This is because of the fact that long-range magnetic order requires unpaired d^n electrons, while most of the ferroelectrics have d^0 electronic configuration. However, different routes have been adopted in order to combine these two mutually exclusive properties in a single phase material. Based on the mechanism of multiferroicity, these materials are classified in two main categories: type-I and type-II multiferroics [14,16,17].

1.2.1 Type-I multiferroics

In type-I multiferroics, ferroelectricity and magnetism occur independently by two different origins at different temperatures and thus the coupling between ferroelectricity and magnetism is very weak [14]. There are different ways by which one can combine these two properties independently in a single material. These are as follows.

1.2.1.1 Lone pair effect

In some bismuth or lead based perovskite oxides (ABO_3), the ferroelectricity appears due to the lone pair effect of $6s^2$ electrons of *A*-site cations (Bi^{3+} or Pb^{2+}) and magnetism appears from *B*-site cations [14,18]. Sometimes these $6s^2$ electrons do not participate in bonding; instead they form stereochemically active lone pair. The 6s orbitals of these ions are hybridized with their own *p* orbitals or with the *p* orbitals of oxygen ions and thus they are no longer spherical rather they become a lobe-type shape (Figure 1.3(a)) [16,18]. These lobes are free to rotate and can distort the crystal structure. When these lobes align in a uniform direction, they break inversion center and thus results a net electric polarization. The famous compound $BiFeO_3$ belongs to this class of multiferroics [18-20]. It crystallizes in a rhombohedral structure with polar space group *R*3*c* and thus it is ferroelectric at room temperature, where the ferroelectric transition occurs at T_C ~ 1100 K due to the breaking of inversion center by lone pair electrons of Bi^{3+} ions. Further, an antiferromagnetic ordering of Fe^{3+} spins occurs at T_N ~ 600 K and thus it becomes multiferroic below 600 K. Another compound, $BiMnO_3$ is also reported to be multiferroic where the ferroelectricity has the same origin i.e., the lone pair effect of

$6s^2$ electrons of Bi^{3+} ions [21,22]. $BiMnO_3$ is the only compound which has both the properties of ferroelectricity and ferromagnetism. However, it is a still a controversial issue whether it is ferroelectric or not [23].

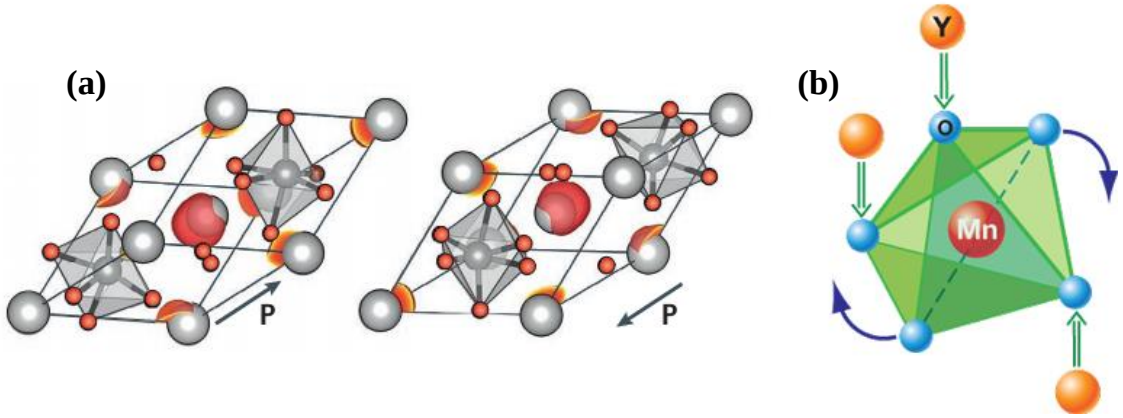

Figure 1.3 (a) Electric polarization due to the lone pair effect in $BiFeO_3$ (adapted with permission from Ref. [18], © (2016) by the Nature Publishing Group). (b) Distortion of MnO_5 polyhedra in $YMnO_3$ resulting a net polarization (adapted from Ref. [14]).

1.2.1.2 Geometric ferroelectric

In some materials, geometric frustration leads to a polar distortion in the lattice and results ferroelectricity. For example, the geometric frustration driven ferroelectricity is observed in $YMnO_3$ [24]. It crystallizes in a hexagonal structure with polar space group $P6_3cm$ under ambient pressure. The crystal structure of h-$YMnO_3$ consists of rigid MnO_5 polyhedra. Below ferroelectric transition temperature (T_C ~ 600 K), the MnO_5 polyhedra tilts in such a way that it results in two downward Y - O dipoles and one upward Y - O dipole (as shown in Figure 1.3(b)) and thus a resultant electric polarization appears [14,24]. Further, Mn^{3+} ions order antiferromagnetically below T_N ~ 80 K and as a result it becomes multiferroic below 80 K. The multiferroic fluorides BaMF_4 (M = Ni and Co) also belong to this class of multiferroics [25-27].

1.2.1.3 Charge ordering

In some oxides, sometimes charge ordering leads to ferroelectricity. Figure 1.4 can be considered to understand this mechanism [28]. In Figure 1.4(a), a neutral one-dimensional chain is shown where the charges at each site are equal. In Figure 1.4(b), the positive and negative charges are orderly arranged at these sites in the chain. In this case,

the sites become inequivalent and thus it can be called site centered charge ordering. Another type of charge ordering is also possible as shown in Figure 1.4(c), where the sites remain equivalent but bonds become different. This is called bond centered charge ordering. However, both these charge ordering cannot break the inversion center, since it results in equal and opposite dipoles which cancel each other. However, sometime both of the site centered and bond centered charge ordering can occur together and this breaks inversion center, and as a result a net polarization appears along the direction of the chain, as shown in Figure 1.4(d) [28]. As a typical example, the compound $LuFe_2O_4$ is reported to be ferroelectric due to charge ordering of Fe^{2+} and Fe^{3+} ions [29]. However, there is a lot of controversy regarding its ferroelectricity [30,31].

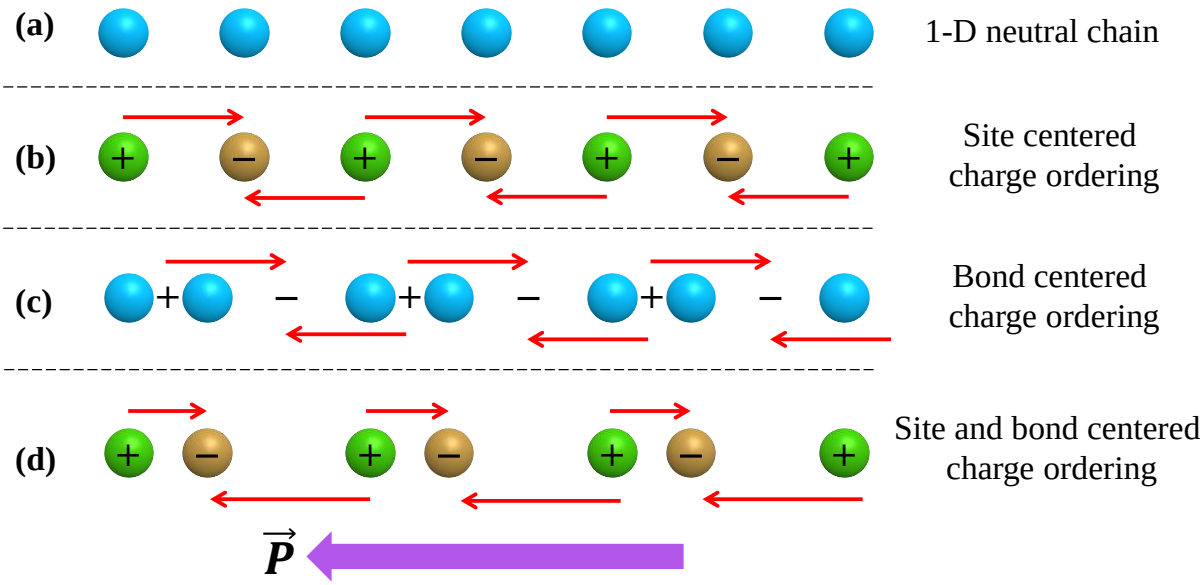

Figure 1.4 Schematic diagram to explain the electric polarization induced by charge ordering.

1.2.2 Type-II multiferroics

Type-II multiferroics are those where the ferroelectricity and magnetism appear due to a common origin [14]. The inversion symmetry in these multiferroics is broken by some particular type of magnetic ordering [14,17,18,32-34]. Since magnetism is

responsible for inducing electric polarization, the coupling between magnetism and ferroelectricity is very strong in type-II multiferroics. So far, there are mainly three microscopic mechanisms known to explain the magnetism induced ferroelectricity. These are exchange striction mechanism, spin current model or inverse DM interaction mechanism and *d* - *p* hybridization [33,34]. In describing these mechanisms, a cluster of two neighboring magnetic spins $\vec{S}_i$ and $\vec{S}_j$ and a ligand ion (oxygen) is considered. Electric polarization in this cluster induced by spin ordering can be written as [33],

$$\Delta P = P^{ms}(\vec{S}_i.\vec{S}_j)\vec{e}_{ij} + P^{sp}\vec{e}_{ij} \times (\vec{S}_i \times \vec{S}_j) + P^{orb}[(\vec{e}_{ij}.\vec{S}_i)\vec{S}_i - (\vec{e}_{ij}.\vec{S}_j)\vec{S}_j] \quad (4)$$

Here $\vec{e}_{ij}$ is a unit vector along the direction connecting the magnetic spins $\vec{S}_i$ and $\vec{S}_j$. Here, the first , second and third term represent electric polarization due to the exchange striction, inverse Dzyaloshinskii-Moriya interaction and *d-p* hybridization, respectively.

1.2.2.1 Exchange striction mechanism

In this mechanism, below magnetic ordering temperature, the crystal structure deforms due to the change in bond length caused by the magnetic ordering [33,34]. Certain types of magnetic structure favor this striction to be aligned uniformly throughout the lattice and thus the sum of the electric dipole moments associated with the bonds in the overall crystal structure does not cancel and results a macroscopic electric polarization [16,17]. The magnetic structure which induces macroscopic polarization due to exchange striction mechanism has to be commensurate [34].

As an example, the collinear up-up-down-down spin structure induces electric polarization due to exchange striction mechanism [16,17,32,34]. This typical up-up-down-down spin arrangement in a spin chain occurs due to the presence of competing nearest neighbor ferromagnetic (J_F) and next nearest neighbor antiferromagnetic (J_{AF}) interactions. Further, the ratio of these two interactions should be $|J_F/J_{AF}| > 1/2$. Note that if $|J_F/J_{AF}|$ is less than 1/2 but greater than 1/4, the spiral magnetic ground state will be preferred [32]. A simple schematic is shown in Figure 1.5 in order to understand how this mechanism induces electric polarization [16]. In the paramagnetic state, the lattice is composed of alternatingly arranged cations of different charges along a chain and thus it is centrosymmetric (Figure 1.5(a)). Here all the cation positions are inversion center. In the magnetically ordered state, if the spins are aligned in up-up-down-down fashion as

shown in Figure 1.5(b), this particular arrangement of spins itself breaks the inversion center. Because the cation positions are no longer inversion center, since spin direction remains invariant under inversion (shown by the schematic in Figure 1.12(b)). Further, as shown in Figure 1.5(c), due to the different strength of exchange interactions between two up-up (or down-down) ferromagnetic spins and up-down antiferromagnetic spins, the bond length connecting two up (or down) spins will differ from the bond length between two up-down spins and results a macroscopic polarization along the chain [16].

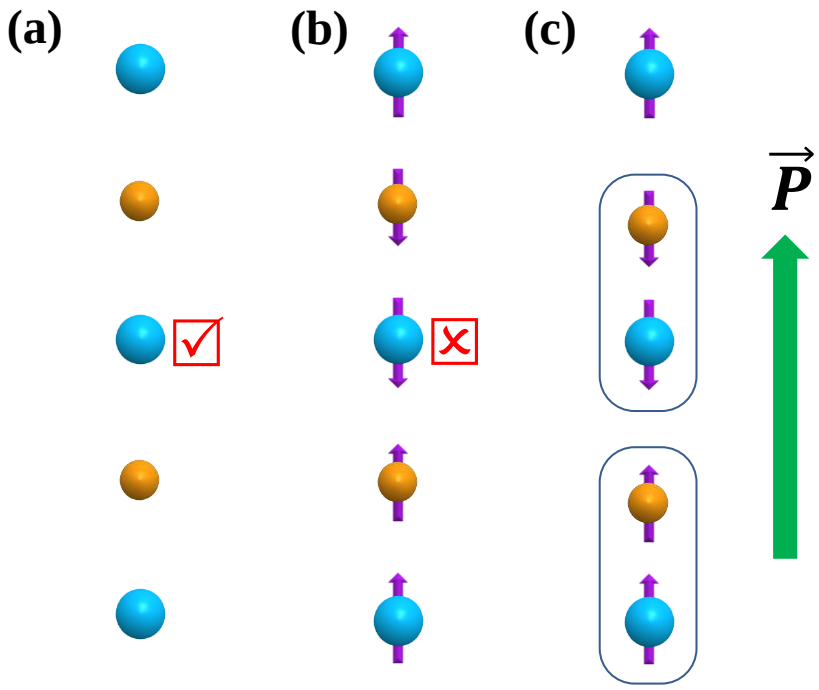

Figure 1.5 Schematic diagram to show up-up-down-down spin ordering induced electric polarization in one dimensional spin chain.

As for example, the up-up-down-down spin structure induced ferroelectricity is observed in Ca_3CoMnO_6 [35]. It crystallizes in a centrosymmetric structure with space group $R\bar{3}c$ with alternating order of Co^{2+} and Mn^{4+} ions occupying trigonal prismatic sites and octahedral sites, respectively. Below antiferromagnetic ordering temperature (T_N ~ 16.5 K), it possesses a commensurate up-up-down-down spin order as shown in Figure 1.6(a) [35]. Electric polarization emerges at antiferromagnetic ordering temperature along the spin chain due to exchange striction mechanism (Figure 1.6(b)) [35].

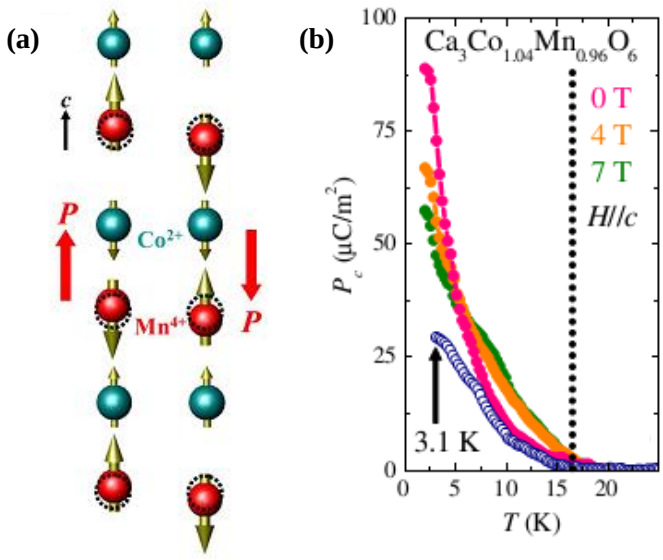

Figure 1.6 (a) Up-up-down-down magnetic structure of Ca_3CoMnO_6, (b) Electric polarization below up-up-down-down collinear magnetic ordering (adapted with permission from Ref. [35], © (2008) by the American Physical Society).

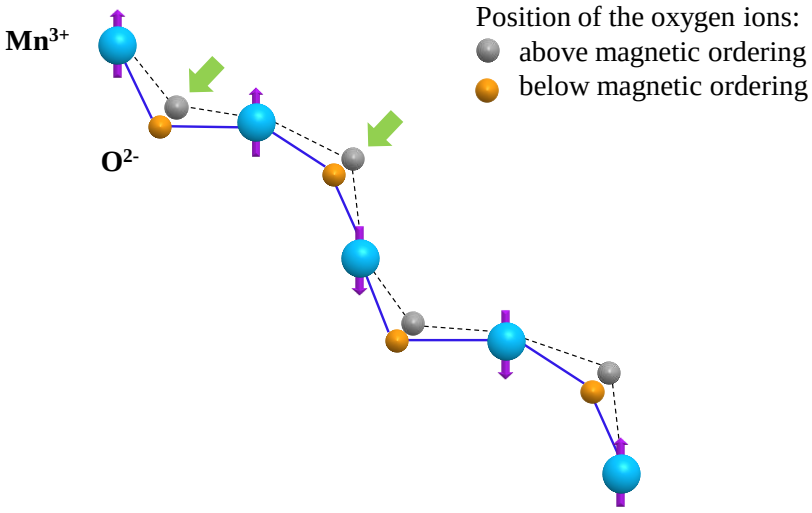

Figure 1.7 Up-up-down-down zigzag chain in orthorhombic RMnO$_3$ (R = Ho to Lu)

Another kind of up-up-down-down magnetic ordering is observed in some materials, where the up-up-down-down spin alignment is not linear, but they order in a zigzag fashion [34]. The orthorhombic manganites RMnO$_3$ (R = Ho to Lu), which can be stabilized only under high pressure, possess this type magnetic structure, which is known as *E*-type magnetic structure [36-38]. In this case, instead of two different magnetic ions

with different charges, only Mn^{3+} ions form this zigzag up-up-down-down structure. A typical zigzag up-up-down-down chain is shown in Figure 1.7. The important factor here in inducing electric polarization is not the Mn-Mn distances but the Mn-O-Mn bond angles [17]. According to the Goodenough–Kanamori rules, the Mn-Mn interaction will be ferromagnetic if the bond angle Mn-O-Mn is close to 90^0, while it will be antiferromagnetic if the bond angle is close to 180^0 [17,39-41]. Thus, in the present case, the oxygen atoms in Mn-O-Mn networks will shift in the same direction according to the ferromagnetic and antiferromagnetic exchange interaction between the up-up (or down-down) and up-down spins, respectively as indicated in Figure 1.7 and thus a resultant electric polarization will appear [17]. It is reported that the Mn^{3+} and Mn^{4+} spins in RMn_2O_5 are arranged in a similar zigzag chain and the electric polarization in these systems is also governed by the exchange striction mechanism [42,43]. However, the inverse DM interaction also contributes to the electric polarization due to the appearance of the incommensurate cycloidal magnetic phases at further lower temperature.

Exchange striction driven ferroelectricity is also observed in weak ferromagnetic systems such as $RFeO_3$ (R = Gd and Dy) [34,44,45]. In this case, the exchange striction between the R^{3+} and Fe^{3+} moments shifts the R^{3+} ions in such a way that it produces a uniform polar distortion which gives rise to a large macroscopic polarization.

1.2.2.2 Spin current model or inverse DM interaction

The electric polarization in noncollinear spiral magnetic structure is governed by the inverse Dzyaloshinskii-Moriya (DM) interaction, which is also known as spin current model [46]. The electric polarization induced by this mechanism is given by the second term in Equation (4). In general, the DM interaction is represented by [47,48],

$$I_{DM} = \vec{D}_{ij}.(\vec{S}_i \times \vec{S}_j) \qquad (5)$$

where $\vec{D}_{ij}$ is Dzyaloshinskii vector for the pair of spins $\vec{S}_i$ and $\vec{S}_j$ and it is proportional to the shift $(\vec{x}_{ij})$ of the ligand atom [16],

$$\vec{D}_{ij} \propto \vec{x}_{ij} \times \vec{e}_{ij} \qquad (6)$$

If the ligand atom is already shifted in the spin pair, then the Dzyaloshinskii vector $\vec{D}_{ij}$ would be non-zero and thus the DM interaction would cant these spins. The same phenomenon can occur in the opposite way, which is known as inverse DM interaction mechanism. If the spin arrangement is already canted due to some effects such as magnetic frustration, the ligand atom would shift in order to gain the DM interaction energy (Figure 1.8). In some particular spiral spin configurations, the shifts of the ligand atoms occur in a same direction and thus produce a macroscopic electric polarization [16,33,34,49].

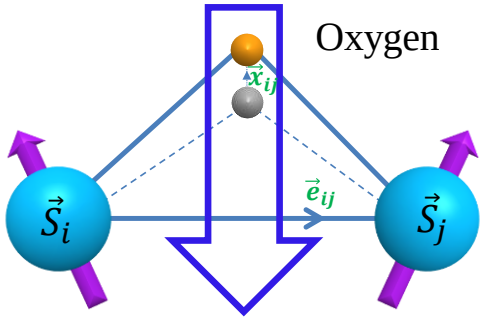

Figure 1.8 Shift of the oxygen ion due to the inverse DM interaction.

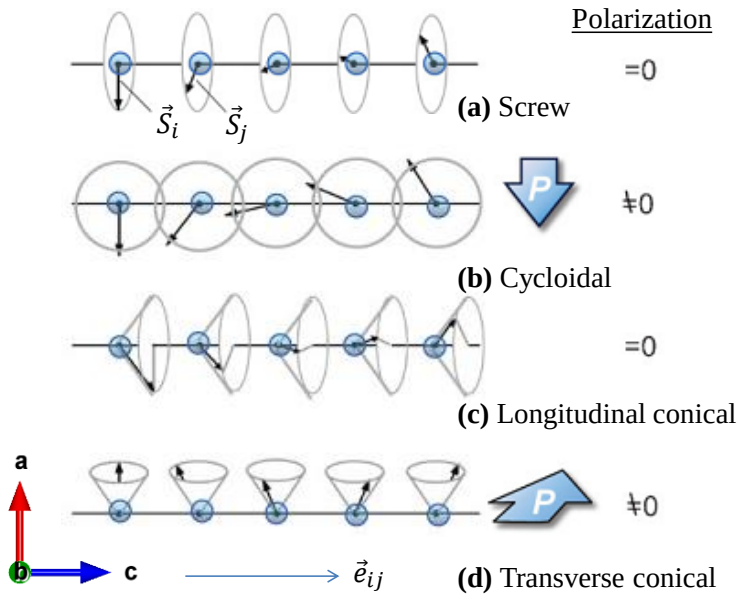

Figure 1.9 Different types of noncollinear spiral magnetic structure and the allowed electric polarization directions due to inverse DM interaction mechanism (adapted with permission from Ref. [49], © (2009) by John Wiley and Sons).

The possible spiral magnetic structures are shown in Figure 1.9 [49]. As shown in Figure 1.9(a), for the screw spin arrangements, $\vec{S}_i \times \vec{S}_j$ is parallel to $\vec{e}_{ij}$ and thus it does not allow electric polarization. Figure 1.9(b) displays the cycloidal magnetic structure, where $\vec{S}_i \times \vec{S}_j$ is perpendicular to $\vec{e}_{ij}$ and according to the second term in Equation (4) it results an electric polarization in a direction perpendicular to both to $\vec{e}_{ij}$ and $\vec{S}_i \times \vec{S}_j$. Longitudinal and transverse conical spin arrangements are shown in Figure 1.9(c) and (d), respectively. The antiferromagnetic components of the spins of longitudinal conical magnetic structure lie in *ab* plane and form a screw structure and thus do not allow electric polarization [16]. On the other hand, for the transverse conical spin structure, the antiferromagnetic components of the spins form a cycloidal structure in *bc* plane and thus it can induce electric polarization [16]. Therefore, only cycloidal and transverse spin arrangement can break inversion center and produce electric polarization.

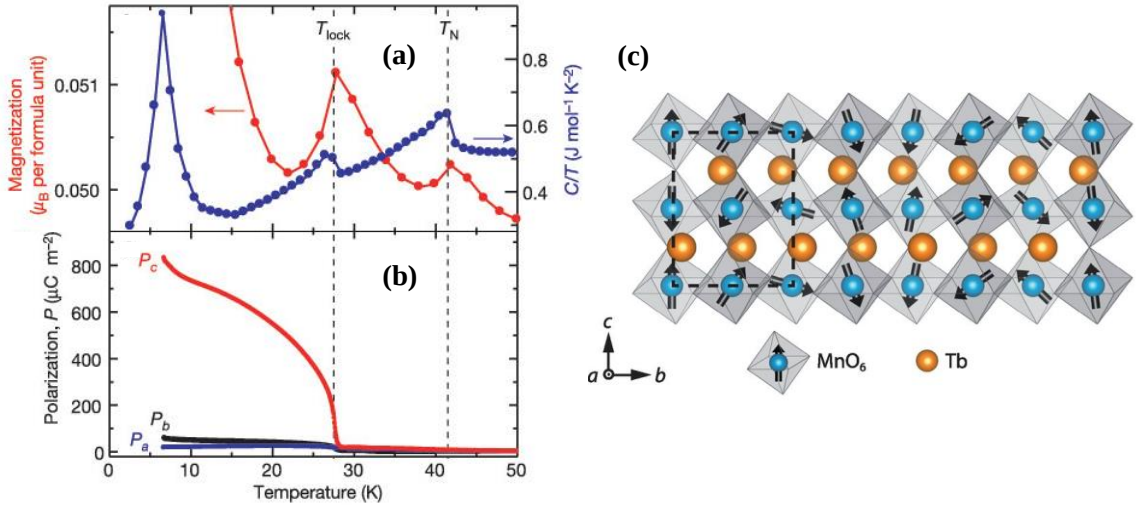

Figure 1.10 (a, b) Electric polarization below cycloidal magnetic ordering at 28 K in $TbMnO_3$ (adapted with permission from Ref. [50], © (2003) by the Nature Publishing Group). (c) Cycloidal magnetic structure of $TbMnO_3$ (adapted with permission from Ref. [51], © (2014) by the AAAS).

$TbMnO_3$ is the best example of cycloidal magnetic structure driven ferroelectricity and in fact, it is the first discovered spin-driven multiferroic [50]. It crystallizes in a centrosymmetric orthorhombic structure with space group *Pbnm*. As shown in Figure 1.10(a), upon lowering temperature, it first undergoes to a collinear sinusoidal magnetic ordering at T_N ~ 41 K and then it exhibits a cycloidal magnetic ordering below T_C ~ 28 K,

where Mn^{3+} moments form the cycloids in *bc* plane (Figure 1.10(c)) [50,51]. This cycloidal magnetic structure induces electric polarization along *c* direction according to the inverse DM model, as shown in Figure 1.10(b) [50].

One drawback of the cycloidal magnetic structure is that it does not have any spontaneous magnetization or ferromagnetic components. On the other hand, the transverse conical magnetic structure has both antiferromagnetic components forming a cycloidal structure and a ferromagnetic component. Transverse conical spin structure induced ferroelectricity is first observed in the spinel oxide $CoCr_2O_4$ (Figure 1.11) [52]. The incommensurate transverse conical magnetic structure of Cr^{3+} spins, as shown in Figure 1.11(a), is observed below ~ 26 K, where one component of the spins is ferromagnetic along *z* direction and the other component of the moments forms a cycloidal structure in a plane perpendicular to *z* direction. As discussed before, this magnetic structure breaks inversion symmetry due to the cycloidal components and thus it induces electric polarization below 26 K along *y* direction as indicated by the inverse DM interaction model (Figure 1.11(b, c)) [52]. However, since the spin cycloids in the transverse conical magnetic structure is formed by the components of the spins, the electric polarization induced by transverse conical magnetic structure is found to be very small compared to that of cycloidal magnetic structure.

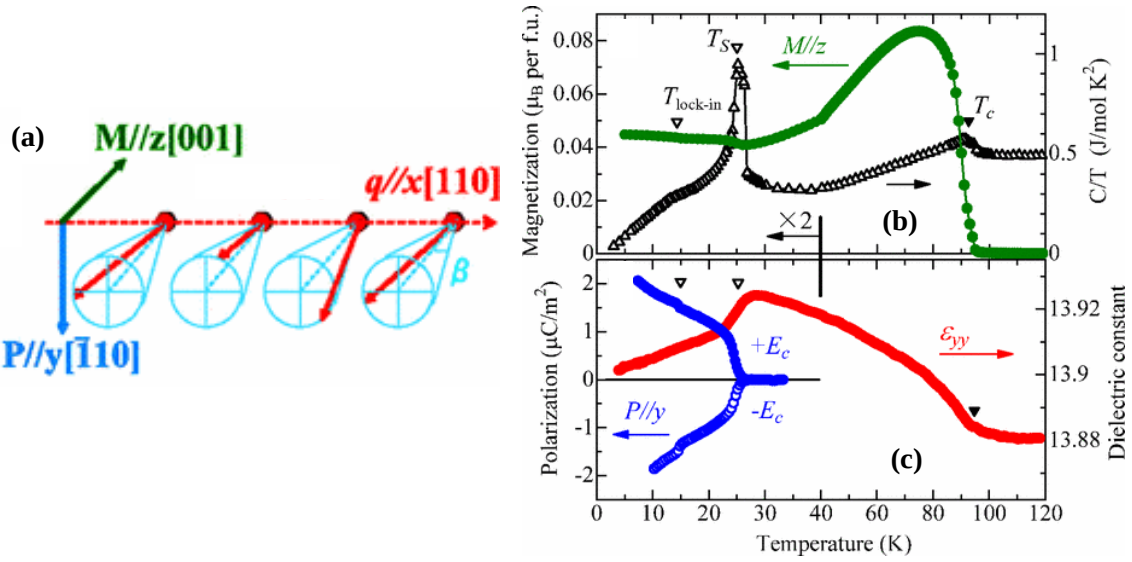

Figure 1.11 (a) Transverse conical magnetic structure in $CoCr_2O_4$, (b, c) Electric polarization due to the transverse conical magnetic ordering in $CoCr_2O_4$ (adapted with permission from Ref. [52], © (2006) by the American Physical Society).

1.2.2.3 *d-p* hybridization

According to the inverse DM interaction model, a screw-type magnetic structure cannot induce electric polarization. However, few materials have been discovered, which crystallize in a low symmetric structure such as triclinic or monoclinic and possess a proper screw-type magnetic structure, exhibit magnetism induced electric polarization [16,17,33,34]. Below the antiferromagnetic ordering with screw-type spin arrangement, the *d-p* hybridization between the metal and ligand ions induces electric polarization in such materials, where the magnetic ion occupies a low symmetric crystal environment. The allowed direction of the electric polarization is only along $\vec{e}_{ij}$, because all other directions are equivalent. However, if there exists a two-fold rotation axis along a direction perpendicular to $\vec{e}_{ij}$, under this two-fold rotation the polarization would be reversed, which indicates that there would be no spontaneous electric polarization. This suggests that a proper screw-type magnetic structure can induce a spontaneous electric polarization, if the crystal system does not contain any two-fold rotational axis perpendicular to the direction of the $\vec{e}_{ij}$ [16,34]. Multiferroicity in some delafossite oxides, such as $CuFeO_2$, $ACrO_2$ (A = Ag, Cu) is reported to be governed by this mechanism [53,54].

1.3 Symmetry aspect of magnetoelectrics and multiferroics

Symmetry is an important deciding factor for magnetoelectric effect and multiferroicity [1,2]. Spatial inversion (I) and time reversal (T) are the main governing symmetry elements in ferroelectrics and magnetic materials, respectively. Electric polarization ($\vec{P}$), which is defined by dipole moment per unit volume, is a polar vector, since the dipole moment is simply $q\vec{r}$, where $\vec{r}$ is the distance between the charges $\pm q$. Under spatial inversion and time reversal symmetry operations, electric polarization ($\vec{P}$) transforms as [16],

$$\vec{P'}_I = I\vec{P} = -\vec{P}$$

$$\vec{P'}_T = T\vec{P} = \vec{P}$$

Neumann's principle states that "the symmetry of any physical property of a crystal must include the symmetry elements of the point group of the crystal", which means that if a crystal has some symmetry element, all physical properties of this crystal

would remain invariant with respect to that symmetry element [13]. As shown above, the electric polarization changes its sign under spatial inversion symmetry while it remains invariant under time reversal operation. Thus, according to the Neumann's principle, to have a spontaneous electric polarization, spatial inversion symmetry has to be broken. This is the reason why the pyroelectric or ferroelectric properties are absent in all centrosymmetric materials. Out of the 32 crystallographic point groups, only 10 point groups are polar, which can be either pyroelectric or ferroelectric [55]. Using Neumann's principle, the symmetry allowed direction of the spontaneous electric polarization can be determined. For example, the orthorhombic point group *mm*2 is polar, where two mirror planes are perpendicular to the *x* and *y* axis and two-fold rotation axis is along *z* axis. If the polarization is directed along *x* or *y* direction, then it would be reversed under the operation of two-fold rotation, while if the electric polarization is along z axis, it would remain invariant under all the symmetry operation of this point group. Thus the symmetries of the point group *mm*2 allow electric polarization only along *z* direction. All the polar point groups and the symmetry allowed direction of the electric polarization are given in Table 1.1 [55].

Table 1.1 List of the polar point groups and the symmetry allowed direction of electric polarization

Crystal systems	Polar point groups	Allowed polarization ($\vec{P}$)
Triclinic	1	(p_x, p_y, p_z)
Monoclinic	2	(0, p_y, 0)
	m	(p_x, 0, p_z)
Orthorhombic	*mm*2	(0, 0, p_z)
Tetragonal	4, 4*mm*	(0, 0, p_z)
Triclinic	3, 3*m*	(0, 0, p_z)
Hexagonal	6, 6*mm*	(0, 0, p_z)

On the other hand, the magnetization ($\vec{M}$) is an axial vector. The best way to understand the symmetry operations on magnetization is by considering a magnetic moment created by a circular current loop of radius $\vec{r}$. The magnetization $\vec{M}$ is given by

$\vec{M} \sim \vec{r} \times \vec{J}$, where $\vec{J} = e\vec{v} = e\frac{d\vec{r}}{dt}$ is the current density [16]. Under spatial inversion (I) and time reversal (T), the magnetization ($\vec{M}$) changes as,

$$\vec{M}'_I = I\vec{M} = \vec{M}$$

$$\vec{M}'_T = T\vec{M} = -\vec{M}$$

This indicates that the magnetization changes its sign under time reversal and remains invariant under spatial inversion (Figure 1.12). Thus, in ferromagnetic materials, spontaneous magnetization appears by breaking time reversal symmetry. Even in case of conventional antiferromagnetic materials, magnetic ordering breaks time reversal symmetry. In this case the antiferromagnetic order parameter, which is given by $\vec{L} = \vec{S}_i - \vec{S}_j$, transforms under time reversal symmetry (T) as,

$$\vec{L}'_T = T\vec{L} = T\vec{S}_i - T\vec{S}_j = -(\vec{S}_i - \vec{S}_j) = -\vec{L}$$

Thus, upon time reversal, the antiferromagnetic order parameter changes its sign, which indicates that antiferromagnetic ordering also breaks time reversal symmetry.

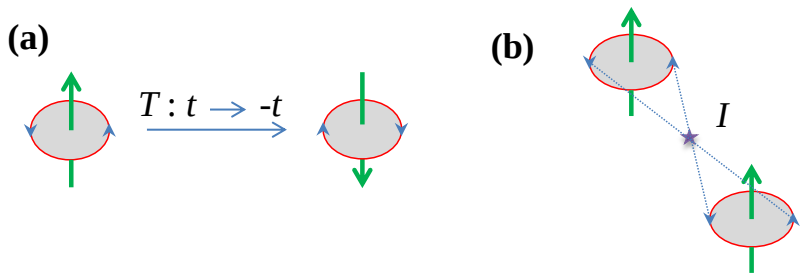

Figure 1.12 (a) Time reversal operation on a magnetic moment (b) Inversion of a magnetic moment.

The magnetoelectric materials, where magnetization (or electric polarization) appears under electric field (or magnetic field), should be odd under both spatial inversion (I) and time reversal (T) symmetry [1,16,17]. In the magnetoelectric materials, some particular types of magnetic ordering break inversion center and allow electric polarization. In this regard, the presence of linear magnetoelectric effect in Cr_2O_3 can be compared with Fe_2O_3 [17]. In the paramagnetic region, both these two oxides possess a corundum structure with centrosymmetric space group $R\bar{3}c$. The time reversal symmetry

is broken in both the cases below antiferromagnetic ordering. However, the arrangements of the spins are different in these oxides (Figure 1.13) and the magnetic point groups are $\bar{3}m$ and $\bar{3}'m'$ in Fe_2O_3 and Cr_2O_3, respectively. As shown in Figure 1.13(a), Fe_2O_3 holds the spatial inversion center, as the spin direction remains invariant under spatial inversion. On the other hand, as shown in Figure 1.13(b) in case of Cr_2O_3, the inversion center is absent; because the spins are reversed with respect to the center and they cannot be connected by inversion. Therefore, both the spatial inversion and time reversal symmetries are broken in Cr_2O_3 and thus it is magnetoelectric, while in Fe_2O_3, although the time reversal symmetry is broken by the magnetic ordering, but it cannot break the spatial inversion symmetry and thus it is not magnetoelectric [17]. This comparison indicates the importance of the magnetic structure or magnetic symmetry in inducing magnetoelectric effect. If the magnetic point group of a system is known, one can calculate the linear magnetoelectric coefficient (α_{ij}) using Neumann's principle, and show that whether it is magnetoelectric or not [13]. In Table 1.2, the magnetoelectric coefficients (α_{ij}) of 58 magnetoelectric point groups are given [13].

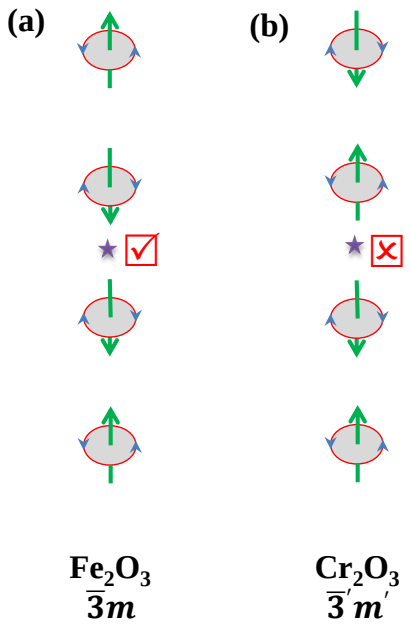

Figure 1.13 Presence and absence of inversion center in Fe_2O_3 and Cr_2O_3, respectively.

According to the symmetry ground itself, one can distinguish between magnetoelectric and multiferroic materials [16]. As mentioned before, in magnetoelectric materials, both the spatial inversion (*I*) and time reversal (*T*) symmetries should be

broken. However, the product (*TI*) of the time reversal (*T*) and spatial inversion (*I*) symmetry elements remains invariant in the magnetoelectric materials. This can be visualized for Cr_2O_3 as shown in Figure 1.13(b), the structure does not change under the operation of *TI* i.e., the simultaneous operation of spatial inversion (*I*) and time reversal (*T*). In case of multiferroic materials on the other hand, in addition to the breaking of both space inversion (*I*) and time reversal (*T*) symmetries, the system should be odd under the

Table 1.2 Magnetoelectric point groups and their magnetoelectric coefficients (α_{ij})

Magnetoelectric point groups	Allowed magnetoelectric coefficients (α_{ij})
1, $\bar{1}'$	$\begin{pmatrix} \alpha_{11} & \alpha_{12} & \alpha_{13} \\ \alpha_{21} & \alpha_{22} & \alpha_{23} \\ \alpha_{31} & \alpha_{32} & \alpha_{33} \end{pmatrix}$
2, m', $2/m'$	$\begin{pmatrix} \alpha_{11} & 0 & \alpha_{13} \\ 0 & \alpha_{22} & 0 \\ \alpha_{31} & 0 & \alpha_{33} \end{pmatrix}$
$2'$, m, $2'/m$	$\begin{pmatrix} 0 & \alpha_{12} & 0 \\ \alpha_{21} & 0 & \alpha_{23} \\ 0 & \alpha_{32} & 0 \end{pmatrix}$
222, $m'm'2$, $m'm'm'$	$\begin{pmatrix} \alpha_{11} & 0 & 0 \\ 0 & \alpha_{22} & 0 \\ 0 & 0 & \alpha_{33} \end{pmatrix}$
$22'2'$, $2mm$, $m'm2'$, $m'mm$	$\begin{pmatrix} 0 & 0 & 0 \\ 0 & 0 & \alpha_{23} \\ 0 & \alpha_{32} & 0 \end{pmatrix}$
3, $\bar{3}'$, 4, $\bar{4}'$, $4/m'$, 6, $\bar{6}'$, $6/m'$	$\begin{pmatrix} \alpha_{11} & \alpha_{12} & 0 \\ -\alpha_{12} & \alpha_{11} & 0 \\ 0 & 0 & \alpha_{33} \end{pmatrix}$
$4'$, $\bar{4}$, $4'/m'$	$\begin{pmatrix} \alpha_{11} & \alpha_{12} & 0 \\ \alpha_{12} & -\alpha_{11} & 0 \\ 0 & 0 & 0 \end{pmatrix}$
32, $3m'$, $\bar{3}'m'$, 422, $4m'm'$, $\bar{4}'2m'$, $4/m'm'm'$, 622, $6m'm'$, $\bar{6}'m'2$, $6/m'm'm'$	$\begin{pmatrix} \alpha_{11} & 0 & 0 \\ 0 & \alpha_{11} & 0 \\ 0 & 0 & \alpha_{33} \end{pmatrix}$
$4'22$, $4'mm'$, $\bar{4}2m$, $\bar{4}2'm'$, $4'/m'mm'$	$\begin{pmatrix} \alpha_{11} & 0 & 0 \\ 0 & -\alpha_{11} & 0 \\ 0 & 0 & 0 \end{pmatrix}$
$32'$, $3m$, $\bar{3}'m$, $42'2'$, $4mm$, $\bar{4}'2'm$, $4/m'mm$, $62'2'$, $6mm$, $\bar{6}'m2'$, $6/m'mm$	$\begin{pmatrix} 0 & \alpha_{12} & 0 \\ -\alpha_{12} & 0 & 0 \\ 0 & 0 & 0 \end{pmatrix}$
23, $m'3$, 432, $\bar{4}'3m'$, $m'3m'$	$\begin{pmatrix} \alpha_{11} & 0 & 0 \\ 0 & \alpha_{11} & 0 \\ 0 & 0 & \alpha_{11} \end{pmatrix}$

operation of the product (*TI*) of time reversal (*T*) and spatial inversion (*I*) [16]. As for example, the simple magnetic structure of the multiferroic Ca_3CoMnO_6, as shown in Figure 1.6(a), does not remain invariant under the operation of spatial inversion (*I*), time reversal (*T*) and the symmetry associated with the product of these two (*TI*) [16]. Thus, knowing the crystal and magnetic symmetry helps a lot in understanding magnetoelectric and multiferroic properties.

1.4 Applications

Magnetoelectric multiferroic materials find many applications in modern technology [1,18,56,57]. Among these, the most promising use of multiferroics would be in a four state random access memory (RAM) devices [57]. Earlier, nano-sized capacitor and transistor were used in dynamic RAM (DRAM) and static RAM (SRAM), respectively [57]. However, the drawback of the DRAM device is that the capacitor discharges slowly with time resulting loss of data. While there is no data loss in the SRAM devices, however it is composed of complex structure with few transistors per bit elements. Further, these memory devices are volatile in nature. In the present days, mainly two types of nonvolatile random access memory devices are used; these are ferroelectric random access memory (FRAM) and magnetic random access memory (MRAM) [57]. Both these two have advantages and disadvantages. In FRAM, the data is stored in a ferroelectric capacitor by the remanent electric polarization. However, FRAMs are not widely used due to the destructive read and reset operation. On the other hand, MRAM stores data using magnetoresistive elements with low and high resistance state as 0 and 1 bit, respectively. However, the write procedure requires magnetic field generated by a current and thus the power consumption and thermal issues limit its applications [57]. Using a multiferroic material in random access memory, these problems can be overcome. In multiferroic random access memory (MFRAM) devices, the data can be stored electrically and read magnetically. Further, it can be used as a four state memory device with different states of electric polarization (*P*) and magnetization (*M*): (*+P*, *+M*), (*+P*, *–M*), (*–P*, *+M*) and (*–P*, *–M*) [57]. Martin Gajek et *al.*, has shown the operation of four state memory device at low temperature using a thin film of $Bi_{0.9}La_{0.1}MnO_3$ [58]. Other than the memory devices, Wood and Austin proposed many possible applications of room temperature magnetoelectric multiferroic materials [59]. They can be used in devices such as magnetic field sensors, spin wave generator, microwave resonators,

domain wall devices, phase shifter, photovoltaic solar cells, oxide electronics, thermal energy harvesting etc. [1,57,59]. All these applications require the magnetoelectric and multiferroic properties of the material at room temperature with strong magnetoelectric coupling. However the magnetoelectric effect and multiferroicity discovered so far in most of the single phase materials occur at low temperature. Further the magnetoelectric coupling is also very weak which is not sufficient for application. This is due to the fact that the linear magnetoelectric coefficient (α_{ij}) is limited by the relation [1],

$$\alpha_{ij} < \varepsilon_0 \mu_0 \varepsilon_{ij} \mu_{ij}$$

where ε_{ij} and μ_{ij} are the electric and magnetic susceptibility, respectively. Thus to have a high value of magnetoelectric coefficient, the material has to be both ferroelectric and ferromagnetic. However, most of the magnetoelectric multiferroics are ferroelectric and antiferromagnetic (or ferrimagnetic) and thus the linear magnetoelectric coefficient is small. Because of this difficulty, scientists have made composite multiferroics, where ferromagnetic and ferroelectric materials are combined together to generate magnetoelectric effect [60,61]. The magnetoelectric coefficient of the composite material is higher than the single phase multiferroic materials and these can operate even at room temperature. Recently, electric field controlled magnetization, which is only possible with the magnetoelectric multiferroics, has received tremendous interest in spintronic devices. Magnetization reversal induced by an electric field at room temperature is observed in a $BiFeO_3$-CoFe heterostructure [62].

1.5 Scope of the thesis

After more than one decades of the discovery of magnetism-driven ferroelectricity, finding a new magnetoelectric or multiferroic material is still a challenging task to the research community. This is mainly because of the lack of sufficient understanding of magnetism that drives ferroelectricity and the available mechanisms. In this thesis, we focus on finding new magnetoelectric and multiferroic materials. We have worked on four different types of materials. First, we have investigated the properties of a series of compounds, $Bi_{1-x}Sm_xMnFe_2O_6$ (x = 0, 0.1 and 0.2), which could be a potential host for multiferroicity. However, our detailed study shows that these oxides are not multiferroics. We found some interesting magnetodielectric effects and magnetic properties in these oxides. Subsequently, we have

explored experimentally the linear magnetoelectric effect in *A*-site magnetic spinels, Co_3O_4 and $CoAl_2O_4$ for the first time and we address the magnetic ground state of $CoAl_2O_4$, which has been a controversial issue, with the magnetoelectric study. Further, we have discovered type-II multiferroicity in a series of compounds, $RFeWO_6$ (*R* = Dy, Eu, Tb and Y), which crystallizes in an ordered aeschynite-type structure. In addition, we have investigated the structure and properties of a chromium based aeschynite-type oxide, $DyCrWO_6$. Although magnetodielectric effect is observed, electric polarization is not detected in our experimental resolution limit. Also, we have investigated multiferroic and magnetic properties in another complex oxide, $BaYFeO_4$.

References

[1] M. Fiebig, *J. Phys. D: Appl. Phys.* **38,** R123 (2005).

[2] W. Eerenstein, N. Mathur, and J. F. Scott, *Nature* **442,** 759 (2006).

[3] B. Wang, *Mechanics of advanced functional materials* (Springer Science & Business Media, 2013).

[4] K. H. J. Buschow, *Handbook of magnetic materials*, Vol. 19 (Elsevier, 2011).

[5] P. Curie, *J. Physique* **3,** 393 (1894).

[6] P. Debye, *Z. Phys.* **36,** 300 (1926).

[7] J. H. Van Vleck, *The theory of electric and magnetic susceptibilities* (Oxford University Press, 1932).

[8] L. Landau and E. Lifshitz, *English edition: Pergamon Press, Oxford* (1960).

[9] I. Dzyaloshinskii, *Soviet Physics Jetp-Ussr* **10,** 628 (1960).

[10] D. Astrov, *Sov. Phys. JETP* **11,** 708 (1960).

[11] D. Astrov, *Sov. Phys. JETP* **13,** 729 (1961).

[12] G. Rado and V. Folen, *Phys. Rev. Lett.* **7,** 310 (1961).

[13] R. E. Newnham, *Properties of materials: anisotropy, symmetry, structure* (Oxford University Press on Demand, 2005).

[14] D. Khomskii, *Physics* **2,** 20 (2009).

[15] C. RayanáSerrao, *J. Mater. Chem.* **17,** 4931 (2007).

[16] D. Khomskii, *arXiv preprint arXiv:1510.05174* (2015).

[17] D. Khomskii, *Transition metal compounds* (Cambridge University Press, 2014).

[18] M. Fiebig, T. Lottermoser, D. Meier, and M. Trassin, *Nat. Rev. Mater.* **1,** 16046 (2016).

[19] G. Smolenskiĭ and I. Chupis, *Sov. Phys. Usp.* **25,** 475 (1982).

[20] J. Wang, J. Neaton, H. Zheng, V. Nagarajan, S. Ogale, B. Liu, D. Viehland, V. Vaithyanathan, D. Schlom, and U. Waghmare, *Science* **299,** 1719 (2003).

[21] A. M. Dos Santos, S. Parashar, A. Raju, Y. Zhao, A. Cheetham, and C. Rao, *Solid State Commun.* **122,** 49 (2002).

[22] Z. Chi, H. Yang, S. Feng, F. Li, R. Yu, and C. Jin, *J. Magn. Magn. Mater.* **310,** e358 (2007).

[23] A. A. Belik, *J. Solid State Chem.* **195,** 32 (2012).

[24] B. B. Van Aken, T. T. Palstra, A. Filippetti, and N. A. Spaldin, *Nat. Mater.* **3,** 164 (2004).

[25] M. Eibschütz, H. Guggenheim, S. Wemple, I. Camlibel, and M. DiDomenico, *Phys. Lett. A* **29,** 409 (1969).

[26] C. Ederer and N. A. Spaldin, *Phys. Rev. B* **74,** 024102 (2006).

[27] J. Scott and R. Blinc, *J. Phys. Condens. Matter* **23,** 113202 (2011).

[28] J. Van Den Brink and D. I. Khomskii, *J. Phys. Condens. Matter* **20,** 434217 (2008).

[29] N. Ikeda, H. Ohsumi, K. Ohwada, K. Ishii, T. Inami, K. Kakurai, Y. Murakami, K. Yoshii, S. Mori, and Y. Horibe, *Nature* **436,** 1136 (2005).

[30] A. Ruff, S. Krohns, F. Schrettle, V. Tsurkan, P. Lunkenheimer, and A. Loidl, *EPJ B* **85,** 290 (2012).

[31] J. d. de Groot, T. Mueller, R. Rosenberg, D. Keavney, Z. Islam, J.-W. Kim, and M. Angst, *Phys. Rev. Lett.* **108,** 187601 (2012).

[32] S.-W. Cheong and M. Mostovoy, *Nat. Mater.* **6,** 13 (2007).

[33] T. Kimura, *Annu. Rev. Condens. Matter Phys.* **3,** 93 (2012).

[34] Y. Tokura, S. Seki, and N. Nagaosa, *Rep. Prog. Phys.* **77,** 076501 (2014).

[35] Y. Choi, H. Yi, S. Lee, Q. Huang, V. Kiryukhin, and S.-W. Cheong, *Phys. Rev. Lett.* **100,** 047601 (2008).

[36] I. A. Sergienko, C. Şen, and E. Dagotto, *Phys. Rev. Lett.* **97,** 227204 (2006).

[37] V. Y. Pomjakushin, M. Kenzelmann, A. Dönni, A. B. Harris, T. Nakajima, S. Mitsuda, M. Tachibana, L. Keller, J. Mesot, and H. Kitazawa, *New J. Phys.* **11,** 043019 (2009).

[38] S. Picozzi, K. Yamauchi, B. Sanyal, I. A. Sergienko, and E. Dagotto, *Phys. Rev. Lett.* **99,** 227201 (2007).

[39] J. Kanamori, *J. Phys. Chem. Solids* **10,** 87 (1959).

[40] J. B. Goodenough, *Phys. Rev.* **100,** 564 (1955).

[41] J. B. Goodenough, *J. Phys. Chem. Solids* **6,** 287 (1958).

[42] N. Hur, S. Park, P. Sharma, J. Ahn, S. Guha, and S. Cheong, *Nature* **429,** 392 (2004).

[43] Y. Noda, H. Kimura, M. Fukunaga, S. Kobayashi, I. Kagomiya, and K. Kohn, *J. Phys. Condens. Matter* **20,** 434206 (2008).

[44] Y. Tokunaga, S. Iguchi, T. Arima, and Y. Tokura, *Phys. Rev. Lett.* **101,** 097205 (2008).

[45] Y. Tokunaga, N. Furukawa, H. Sakai, Y. Taguchi, T.-h. Arima, and Y. Tokura, *Nat. Mater.* **8,** 558 (2009).

[46] H. Katsura, N. Nagaosa, and A. V. Balatsky, *Phys. Rev. Lett.* **95,** 057205 (2005).

[47] I. Dzyaloshinsky, *J. Phys. Chem. Solids* **4,** 241 (1958).

[48] T. Moriya, *Phys. Rev.* **120,** 91 (1960).

[49] Y. Tokura and S. Seki, *Adv. Mater.* **22,** 1554 (2010).

[50] T. Kimura, T. Goto, H. Shintani, K. Ishizaka, T. Arima, and Y. Tokura, *Nature* **426,** 55 (2003).

[51] T. Kubacka, J. Johnson, M. Hoffmann, C. Vicario, S. De Jong, P. Beaud, S. Grübel, S.-W. Huang, L. Huber, and L. Patthey, *Science* **343,** 1333 (2014).

[52] Y. Yamasaki, S. Miyasaka, Y. Kaneko, J.-P. He, T. Arima, and Y. Tokura, *Phys. Rev. Lett.* **96,** 207204 (2006).

[53] T. Kimura, J. Lashley, and A. Ramirez, *Phys. Rev. B* **73,** 220401 (2006).

[54] S. Seki, Y. Onose, and Y. Tokura, *Phys. Rev. Lett.* **101,** 067204 (2008).

[55] C. Giacovazzo, *Fundamentals of crystallography* (Oxford university press, USA, 2000).

[56] J. Scott, *J. Mater. Chem.* **22,** 4567 (2012).

[57] M. M. Vopson, *Crit. Rev. Solid State Mater. Sci.* **40,** 223 (2015).

[58] M. Gajek, M. Bibes, S. Fusil, K. Bouzehouane, J. Fontcuberta, A. Barthélémy, and A. Fert, *Nat. Mater.* **6,** 296 (2007).

[59] V. E. Wood and A. Austin, *Int. J. Magn* **5,** 303 (1974).

[60] C.-W. Nan, M. Bichurin, S. Dong, D. Viehland, and G. Srinivasan, *J. Appl. Phys.* **103,** 1 (2008).

[61] J. Ma, J. Hu, Z. Li, and C. W. Nan, *Adv. Mater.* **23,** 1062 (2011).

[62] J. Heron, J. Bosse, Q. He, Y. Gao, M. Trassin, L. Ye, J. Clarkson, C. Wang, J. Liu, and S. Salahuddin, *Nature* **516,** 370 (2014).

Chapter 2

Experimental techniques

In this chapter, method of sample preparation, characterization and detailed experimental techniques used in the present thesis work are discussed.

2.1 Sample preparation

All the samples investigated in this thesis are polycrystalline in nature. High temperature solid state reaction method is used in preparing these samples [1]. In the solid state reaction method, the starting materials are mixed according to their cation ratio and ground thoroughly for long time. The mixed powder (or pellet) is heated at few different temperatures for 12 - 24 hours with intermittent grindings. The high temperature provides the necessary energy for the reaction which occurs by the diffusion of ions [1]. The important factor in this reaction mechanism is the diffusion coefficient (*D*), which is given by the Fick's law [2], $J = -D\frac{d\varphi}{dx}$, where *J* is the flux of diffusing elements and $\frac{d\varphi}{dx}$ is the concentration gradient. The diffusion coefficient (*D*) depends on the temperature of the reaction. For a good solid state reaction, the diffusion coefficient should be greater than 10^{-12} cm^2/s. The reaction temperature can be decided by using the Tamman's rule, which states that the reaction temperature should be at least 2/3 of the melting point of one or more precursor materials for a proper reaction [3]. However, this rule is not always true, particularly in case of the volatile starting materials.

2.2 Structural analysis

The structural investigations are carried out by the Rietveld refinement of powder X-ray and neutron diffraction data.

2.2.1 X-ray and neutron diffraction

X-ray diffraction is the simplest and widely used technique in structural analysis. X-ray diffraction experiments are performed on powder samples with a laboratory Bruker D8 Advance X-ray diffractometer and PANalytical Empyrean alpha 1 diffractometer

(monochromatic CuKα1). In general, an X-ray diffractometer consists of an X-ray tube, which produces X-ray and a detector, which detects the scattered X-rays from the sample placed in a sample platform. When X-rays are incident on a powder sample, which consists of grains arranged randomly in all possible orientation, some of the X-rays will be scattered by the atoms of the first layer or plane (Figure 2.1), and the rest of the X-rays will pass through the first layer and will be scattered by the succeeding layers. For this scattering to occur, the spacing between the atomic layers or crystallographic planes has to be of the order of the wavelength of the incident X-ray beam. Constructive interference will happen when these scattered rays coming from two different planes are in same phase and it will result a peak in the X-ray diffraction pattern. If these two scattered X-rays are out phase, no such peak will appear. According to the Bragg's law [1,4], the constructive interference will occur only if,

$$2d\ sin\theta = \lambda$$

where d is the spacing between the consecutive planes, λ is the wavelength of the incident X-rays, θ is the incident angle of the X-ray (Figure 2.1). Thus, when Bragg's law is satisfied by some particular sets of planes, many peaks will appear at different 2θ positions and results an X-ray diffraction pattern, which is unique for each material. The obtained X-ray diffraction data can be treated differently in order to get different information.

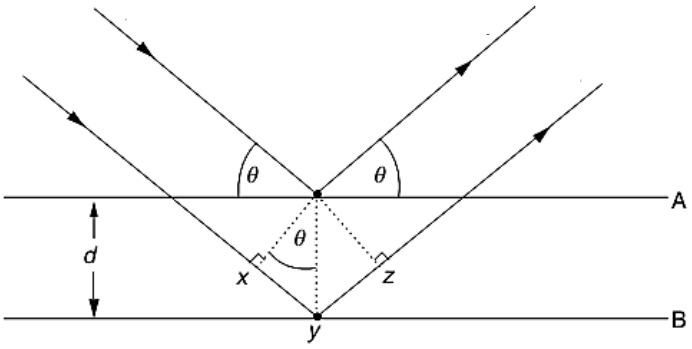

Figure 2.1 Schematic of X-ray diffraction - Bragg's law (Adapted with permission from Ref. [1], © (2014) by John Wiley and Sons).

Since the peak positions depend on the spacing between the planes (d), which is a function of the lattice parameters, one can determine the lattice parameters by indexing

the X-ray diffraction pattern. The phase purity of a known compound can be checked by comparing its X-ray diffraction data with the pattern available in some database such as Inorganic Crystal Structure Database (ICSD). In the same way, the phase of the impurity present in some compound can be determined. Most importantly, the complete crystal structure can be determined using powder X-ray diffraction data. For some particular compounds, it is difficult to index the laboratory X-ray diffraction pattern due to the overlap of two or more close peaks and thus the resulting crystal structure obtained from laboratory X-ray diffraction would be erroneous. The synchrotron X-ray diffraction experiments can resolve this issue, which has the ability to tune the wavelength. The synchrotron X-rays can provide better counting statistics i.e. high intense peak due to the higher intensity of the synchrotron X-ray beams and better resolution of the peaks and thus it has better signal to noise ratio. Therefore, synchrotron data can be indexed properly and can provide a much accurate structural parameters. Synchrotron X-ray diffraction experiments are performed at the Materials Science Powder Diffraction (BL04-MSPD) beamline of the ALBA synchrotron facility at Barcelona (Spain) [5,6].

Neutron diffraction experiment is necessary in the crystal structure determination, when the compound contains some light elements such as oxygen. The X-rays cannot detect the position of the light elements, since X-ray scattering occurs by the electron cloud only. On the other hand, neutrons interact with the nucleus of the atom and can determine accurately the position of the light elements. Further, since neutron possesses an intrinsic magnetic moment, it can interact with the moment of an atom in a compound and thus in addition to crystal structure, neutron diffraction experiments can be used in determining the magnetic structure of the compound. Neutron diffraction experiments are carried out at D2B beam line at the Institut Laue-Langevin (ILL), Grenoble, France. This neutron beam line has the high flux and resolution, which are essential to get the accurate crystal and particularly magnetic structure.

2.2.2 Rietveld refinement

Rietveld refinement is a technique by which, the complete structural parameters can be obtained from the powder X-ray and neutron diffraction data [7]. In this method, a diffraction (X-ray or neutron) pattern is compared with a calculated model pattern by adjusting certain number of parameters. In the process of refinement, the intensity y_{io} at each point of the experimental data is compared with the corresponding calculated point

y_{ic} in the model. This comparison is performed by minimizing a residual function *S* by least square process. The residual function S is given by [4,7],

$$S = \sum_i w_i |y_{io} - y_{ic}|^2$$

where w_i is an weight factor, which depends on the standard deviation in the peak intensity and background intensity. The intensity y_{ic} of the model pattern is given by [4],

$$y_{ic} = s \sum_k m_k L_k |F_k|^2 G(\Delta\theta_{ik}) + y_{ib}$$

where *s* is a scale factor, m_k is the multiplicity factor, L_k is the Lorentz polarization factor for reflection *k*, F_k is the structure factor, $G(\Delta\theta_{ik})$ is the reflection profile function where $\Delta\theta_{ik} = 2\theta_i - 2\theta_k$ and $2\theta_k$ is the calculated position of the Bragg peak, y_{ib} is the background intensity.

Among these, the important parameters are the reflection profile function $G(\Delta\theta_{ik})$ and structure factors (F_k). The shape of the peak depends on many parameters such as the radiation source, wavelength distribution, detector etc. Different functional form can be used for the peak shape function. Among these, the pseudo-Voigt (*pV*) function is mostly used,

$$pV = \eta L + (1 - \eta) G; \qquad with\ 0 \leq \eta \leq 1$$

where *L* is the Lorentzian function and *G* is the Gaussian function, which are given by,

$$L = \frac{C_1^{\frac{1}{2}}}{\pi H_k} \left\{ 1 + C_1 \left(\frac{\Delta\theta_{ik}}{H_k} \right)^2 \right\}^{-1}$$

$$G = \frac{C_0^{\frac{1}{2}}}{\sqrt{\pi} H_k} e^{-C_0 \left(\frac{\Delta\theta_{ik}}{H_k} \right)^2}$$

where C_0 and C_1 are constants and H_k is the full width at half maxima (FWHM) of the k^{th} reflection.

The FWHM (H_k) for Gaussian and Lorentzian peak function are given by [4],

$$(H_k)_G = (U \tan^2\theta + V \tan\theta - W)^{1/2}$$

$$(H_k)_L = X \tan\theta + \frac{Y}{\cos\theta}$$

The parameters *U*, *V*, *W* and *X*, *Y* can be refined during pattern matching of the diffraction data.

The structure factor F_{hkl} (= F_k for k^{th} reflection) is given by,

$$F_{hkl} = \sum_{j=1}^{m} N_j f_j e^{2\pi i(hx_j + ky_j + lz_j)}$$

$$|f|^2 = e^{\frac{-B\sin^2\theta}{\lambda^2}}$$

where *f* is the atomic form factor and the factor *B* is the Debye-Waller temperature factor.

In the refinement process, the background can be selected manually or as a polynomial function of 2θ [4], as

$$y_{ib} = \sum_{n} a_n (2\theta_i)^n$$

This background is refined during pattern matching by refining the coefficient a_n.

The quality of the refinement can be understood by the values of some parameters (*R*-factors) [4,7]. These are,

$$R_P(\text{Profile}) = \frac{\sum|y_{io} - y_{ic}|}{\sum y_{io}}$$

$$R_{wp}(\text{weigted profile}) = \left(\frac{w_i(y_{io} - y_{ic})^2}{\sum w_i y_{io}^2}\right)^{1/2}$$

$$R_E(\text{expected}) = \left\{\frac{(N-P)}{\sum w_i y_{io}^2}\right\}^{1/2}$$

$$\chi^2(\text{goodness of fit}) = \left(\frac{R_{wp}}{R_E}\right)^2 = \frac{\sum w_i(y_{io} - y_{ic})^2}{(N-P)}$$

where *N* is the number of profile points and *P* is the number of refined parameters. Among these, the χ^2 is the most important parameter, which should approach to 1 as refinement progresses.

In technical point of view, the Rietveld refinement is performed in three steps. In the first step, the pattern matching is performed, where the lattice parameters and shape (FWHM) parameters (*U*, *V*, *W* and/or *X*, *Y* and asymmetry parameters) are refined. At the end of pattern matching, the background is refined. In the next step, the scale factor and atomic positions are refined. Finally, the bond lengths and bond angles are obtained from the crystal structure. All the Rietveld refinements are performed with FullProf software packages [8]. The crystal structures obtained from the refinements are drawn with Vesta software [9].

2.3 Physical property measurements

In this thesis work, we have investigated physical properties such as magnetization, dielectric and ferroelectric properties of some oxide materials.

2.3.1 Magnetization

2.3.1.1 DC magnetization

The basic principle of magnetic measurements is the Faraday's law of induction, which states that the induced voltage in a closed circuit is proportional to the rate of change of magnetic flux through the circuit. Since the magnetic flux (φ) through a coil of *n* turn with area *A* is $\varphi = AB$, where *B* is the magnetic field, the induced voltage (*V*) in this coil is given by,

$$V = -n\frac{d\varphi}{dt} = -nA\frac{dB}{dt}$$

DC magnetization measurements are carried out with a Magnetic Property Measurement System (MPMS3-SQUID), Quantum Design, USA. The different parts of the MPMS3 are shown in Figure 2.2(a) [10]. The main important unit of the MPMS3 is a Superconducting Quantum Interference Device (SQUID), which is an instrument that can detect extremely small magnetic field (shown in the schematic of Figure 2.2(b)) [10]. In MPMS3, the SQUID is connected to the superconducting detection coil by superconducting wires and forms a closed loop [10]. SQUID acts as an extremely sensitive current to voltage converter. In magnetization measurement process, the sample moves through the superconducting detection coil and induces a change in the flux passing through it. This change in magnetic flux produces a change in the persistent

current in the detection coil, which is proportional to the change in magnetic flux. Since SQUID acts as an extremely sensitive linear current to voltage converter, the change in current in the detection coil results a corresponding change in the SQUID output voltage, which is proportional to the magnetic moment of the sample. In this way, the magnetization of a sample is measured. In MPMS3, magnetization can be measured by two different modes - Vibrating sample magnetometer (VSM) mode and dc scan mode [10]. In VSM mode, the sample vibrates sinusoidally up and down with very high frequency while in dc scan mode the sample is moved up and down uniformly instead of oscillation. Thus, to get a good quality data, dc scan mode is preferred.

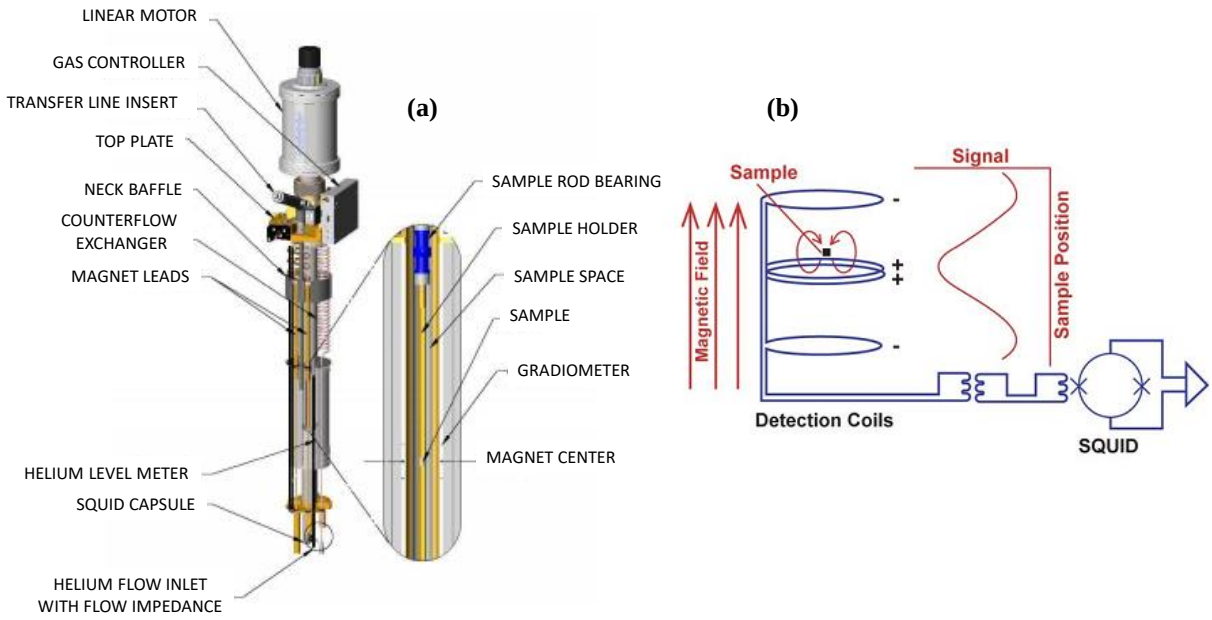

Figure 2.2 (a) Different parts of MPMS3 system, (b) Schematic diagram of superconducting detection coil and SQUID in MPMS3 (adapted from Ref. [10]).

2.3.1.2 AC susceptibility

AC susceptibility measurements are required particularly in the study of magnetization dynamics. DC magnetization cannot provide any information regarding magnetization dynamics, because dc magnetization remains constant during measurement

time. Study of magnetization dynamics is necessary particularly in spin glass systems, where the magnetization decays with time below spin glass transition temperature. Thus, ac susceptibility can provide the details of insight of the spin glass state.

In ac susceptibility measurements, sample's oscillation is not required, it remains static. A small ac magnetic field ($H = H_{ac}\sin(\omega t)$) is applied in the presence or absence of dc magnetic fields, where H_{ac} and ω are the amplitude and frequency of the applied ac magnetic field, respectively. A time-dependent magnetization in the sample is induced by this ac magnetic field, which causes a change in the current in the detection coil. The magnetization under a small ac magnetic field (with low frequency range) is given by [11],

$$M_{ac} = \frac{dM}{dH} H_{ac}\sin(\omega t)$$

where $\chi = \frac{dM}{dH}$ is the slope of the magnetization (M) *vs.* magnetic field (H) data. Since the ac magnetization depends on the slope ($\frac{dM}{dH}$) of *M vs. H* curve, it is very sensitive compared to the dc magnetization and it can probe small changes in magnetization.

On the other hand, in case of higher frequency of the applied ac magnetic field, the ac magnetization of the sample cannot follow the driving frequency and lags behind the applied ac field [11]. This lag can be detected by the ac magnetometer. Thus, the ac magnetic susceptibility has two components,

$$\chi' = \chi\cos(\phi)$$

$$\chi'' = \chi\sin(\phi)$$

$$\chi'^2 + \chi''^2 = \chi^2$$

$$\phi = tan^{-1}\frac{\chi''}{\chi'}$$

where χ' and χ'' are the real and imaginary part of the ac susceptibility, ϕ is the phase shift. The real part of the ac susceptibility χ' is simply the slope of the *M vs. H* curve in the low frequency limit.

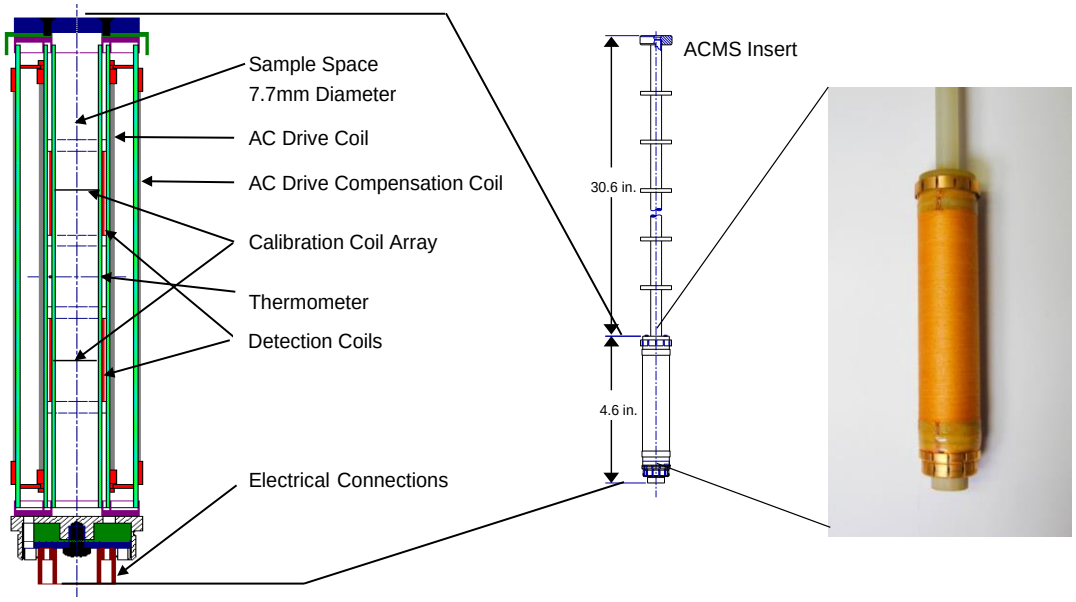

Figure 2.3 Schematic diagrams of the different parts of ACMS coil [12].

AC susceptibility is measured with Physical Property Measurement System (PPMS). In PPMS, the sample is placed in an ACMS coil (Figure 2.3) [12]. The measurements are performed by five-point BTBCC (bottom-top-bottom-center-center) measurement process [12]. First three reading are recorded by placing the sample at center of the bottom detection coil, at center of the top detection coil and again at center of the bottom detection coil [12]. After these three positions, the sample is placed at the center of the top and bottom detection coil and two more readings are taken with opposing polarities of the calibration coil switched into the detection circuit. The signals from the detection coil in first three readings are amplified and digitized by an analog to digital (A/D) converter and saved as response waveform. The real and imaginary components of each response waveform are obtained by fitting the data and comparing with the driving signal. Finally, the calibration readings are used in order to get the real and imaginary part of the ac susceptibility of the sample [12].

2.3.2 Heat capacity

Heat capacity is measured in PPMS. In Figure 2.4, a schematic of heat capacity measurement platform in PPMS is shown [13]. Before measuring heat capacity of the sample, addenda measurement is performed, where a small amount of Apiezon grease is

applied to the sample platform and heat capacity is measured without sample. After addenda measurement, the sample (small pellet) is placed in the sample platform, where the Apiezon grease holds the sample and total heat capacity is measured, which includes the heat capacity of the sample, grease and sample platform. The sample heat capacity is then obtained by subtracting addenda heat capacity from total heat capacity, which is performed automatically by the MultiVu software in PPMS [13].

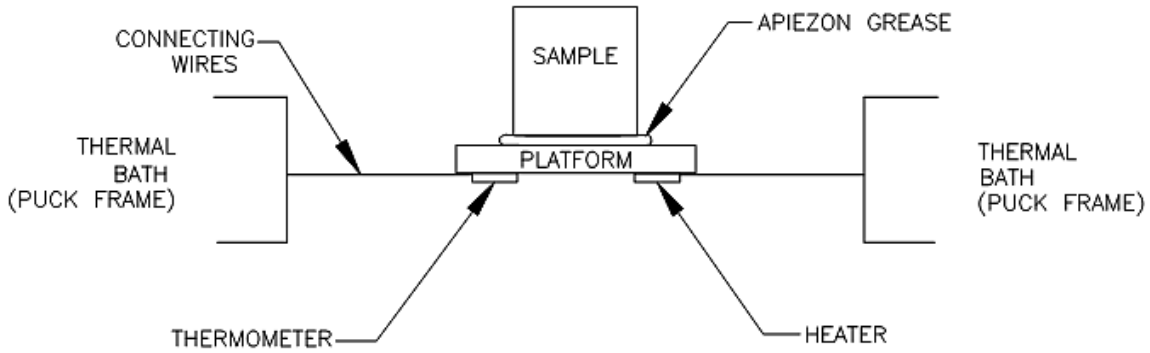

Figure 2.4 Heat capacity measurement platform in PPMS (adapted from Ref. [13]).

The PPMS uses a relaxation technique to measure heat capacity [13]. A high vacuum is maintained in the sample chamber, so that the heat cannot dissipate. During heat capacity measurements, a cycle of consecutive heating and cooling of the sample is performed. A known amount of heat is supplied to the sample for a constant time. After that, the sample is allowed to cool for the same time. Temperature response is recorded during each cycle and the program available in MultiVu software fits the temperature response for the full cycle with a model and finally provides the heat capacity of the sample [13].

In general, the heat capacity data exhibits a peak at the long-range magnetic ordering temperature. The change in magnetic entropy associated with the long-range magnetic ordering can be calculated by subtracting lattice contribution from total heat capacity. The lattice contribution can be obtained by measuring heat capacity of an isostructural nonmagnetic sample or by using a Debye-Einstein model.

2.3.3 Dielectric properties

Dielectric properties are investigated with an Agilent LCR meter (model no. E4980A). The complex dielectric constant (ε_r) is given by,

$$\varepsilon_r = \varepsilon_r' - i\varepsilon_r''$$

$$\text{loss} = \tan(\delta) = \frac{\varepsilon_r''}{\varepsilon_r'}$$

Here ε_r' and ε_r'' are the real and imaginary parts of dielectric constant, respectively. The real part ε_r' is proportional to the capacitance (C) of the material. For a parallel plate capacitor of thickness d and area A, the real part of dielectric constant is given by,

$$\varepsilon_r' = \frac{d}{\varepsilon_0 A} C$$

where ε_0 is the permittivity of the free space. The real part of dielectric constant (ε_r') indicates the charge storing capacity of the dielectric media. On the other hand, the imaginary part (ε_r'') indicates the dielectric loss, which is normally high in the less insulating materials.

The dielectric constant is determined by measuring impedance Z of the material under an electric field ($E_0 \sin \omega t$), where the capacitance C (complex) is obtained by [14],

$$C = \frac{1}{i\omega Z}$$

Although there are many methods for measuring impedance of the material, the Agilent LCR meter (model E4980A) uses an auto-balancing bridge method (Figure 2.5(a)) [14]. Here the voltage (V_x) across the terminal High and ground and the voltage V_r across the range resistor R_r and ground are measured, maintaining the Low terminal at zero volt. The impedance of the sample (DUT) is calculated by [14],

$$\frac{V_x}{Z_x} = I_x = I_r = \frac{V_r}{R_r}$$

$$Z_x = \frac{V_x}{I_x} = R_r \frac{V_x}{V_r}$$

Temperature and magnetic field dependent dielectric measurements are performed in PPMS with the help of a multifunctional probe (shown in Figure 2.5(b)) provided by Quantum Design, USA.

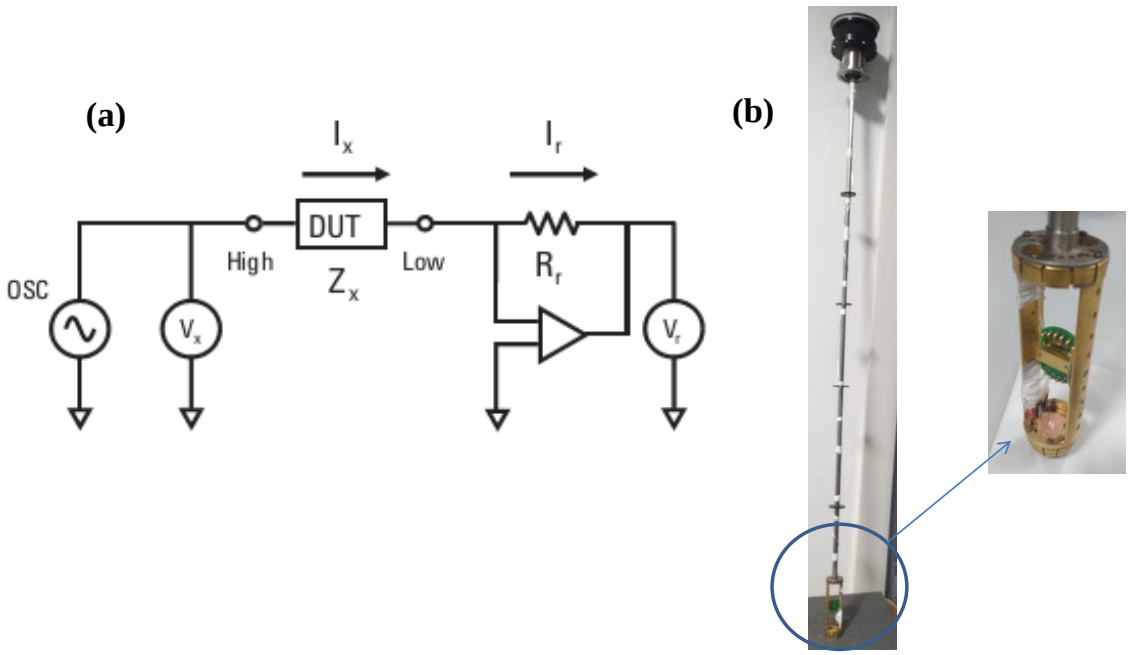

Figure 2.5 (a) An auto-balancing bridge method used for impedance measurements (adapted from the Ref. [14]). DUT (device under test) represents the sample. (b) Multifunctional probe used for dielectric and pyroelectric current measurements in PPMS.

2.3.4 Pyroelectric current measurements

In ferroelectric materials, the electric polarization can be obtained by measuring pyroelectric current. The pyroelectric current exhibits a sharp asymmetric peak at the ferroelectric transition. In pyroelectric current measurements, the sample is cooled across the ferroelectric transition temperature under an electric field. After that, the electric field is removed and the sample is kept shorted for long time in order to remove stray charges. The pyroelectric current is then recorded during heating. The electric polarization P (T) is calculated by integrating the pyroelectric current I (T) data with the measurement duration,

$$P(T) = \frac{1}{A}\int Idt$$

In most of the magnetoelectric multiferroic materials, the value of the electric polarization is small compared to the conventional ferroelectrics. In some cases, it is difficult to observe electric polarization from the pyroelectric current measurements, where the pyroelectric current peak remains below the background noise level. Thus, a very high electric field is required to observe the pyroelectric current peak. However, if the sample is not highly insulating, it cannot take high electric field. The main important factor in this case is the heating rate used in measurement. As the heating rate is increased, the pyroelectric current peak will increase. Thus, to detect a very small electric polarization, a high heating rate is necessary in pyroelectric current measurement.

One has to be very conscious while determining electric polarization from pyroelectric current measurements in polycrystalline samples [15]. As mentioned before, a ferroelectric transition is indicated by a sharp asymmetric peak in the pyroelectric current data. However, sometimes thermally stimulated depolarization current (TSDC) due to free or trapped charges can results a peak in the pyroelectric current data, which is in general broad and symmetric [16,17]. Such peaks should not be attributed to the ferroelectric transition. This peak can be distinguished from the peak associated with a ferroelectric transition by measuring it under different heating rates. If the peak is due to the TSDC, it shifts to higher temperature with increasing heating rates, while if it is associated with a ferroelectric transition, it doesn't shift with increasing heating rate [17].

Recently, a simple dc-biased current measurement has been proposed, which can clearly distinguish between these two origins [18]. In dc-biased current measurement, the sample is cooled to lowest temperature without applying electric field. The electric field is then applied and the current is measured during heating in the presence of electric field. If the pyroelectric current peak is due to intrinsic ferroelectric transition, the dc-biased current exhibits two peaks - one upward peak due to the polarization of the ferroelectric dipoles and then a downward peak due to the depolarization of these polarized dipoles. However, such typical feature is not observed in the case of TSDC peak. This dc-biased current measurement is necessary particularly in polycrystalline samples. Pyroelectric current and dc-biased current are measured in PPMS with a Keithley 6517A electrometer with the help of a multifunctional probe provided by Quantum Design.

2.3.5 *P* - *E* hysteresis loop

Another way of measuring electric polarization is the conventional *P* - *E* loop measurement. The *P* - *E* loop is measured using a Radiant Technology precision workstation, which uses a Sawyer-Tower circuit. The basic Sawyer-Tower circuit is shown in Figure 2.6(a). In *P* - *E* loop measurement, a triangular voltage pulse with a known frequency is applied to the sample. Since the sample is connected in series with a known capacitor (sense capacitor) of capacitance C_1, same charge (Q) will be stored in the sample and in the sense capacitor. Thus, the electric polarization (P) in the sample (with area A) can be obtained by,

$$P = \frac{Q}{A} = \frac{C_1 V_1}{A}$$

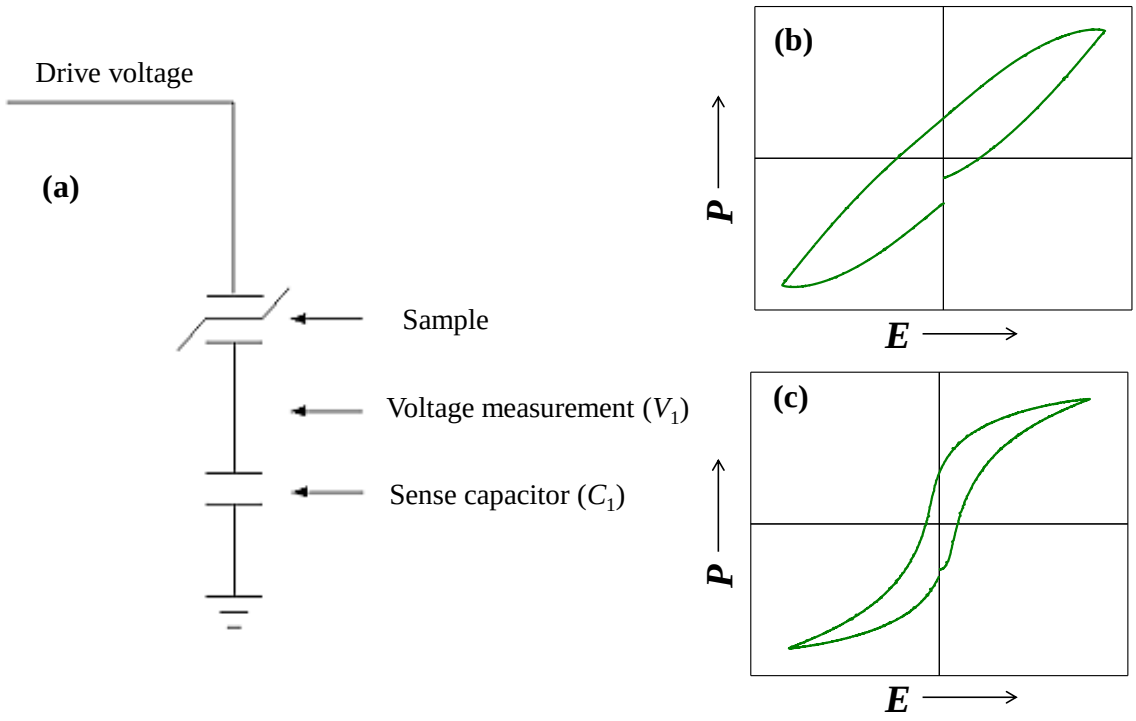

Figure 2.6 (a) A basic Sawyer-Tower circuit, (b) a leaky *P* - *E* hysteresis loop, (c) a proper ferroelectric *P* - *E* hysteresis loop.

Note that a hysteresis in *P* - *E* loop does not always indicate that the material is ferroelectric [19]. The hysteresis may arise in a nonferroelectric leaky material also. A typical leaky hysteresis loop is shown in Figure 2.6(b), while a hysteresis loop resembling a real ferroelectric behavior is shown in Figure 2.6(c). If the ferroelectric material is itself

not highly insulating, it is difficult to measure the conventional *P* - *E* loop, because the material will not take enough voltage. In order to avoid the leakage contribution, a modified *P* - *E* loop measurement technique is proposed, which is known as a positive-up-negative-down (PUND) method or double wave method (DWM) [20]. In PUND method, instead of a single positive and negative triangular pulse, two successive positive pulse followed by two successive negative pulses are applied to the sample. In first positive pulse, all the electric polarization (ferroelectric and leakage contribution) will get saturated. The ferroelectric contribution will not be affected by the second positive pulse and will change only in the presence of negative pulse. Thus, the contribution from the second positive pulse will have only leakage part. Upon subtraction, only ferroelectric contribution (half of the *P* - *E* loop) can be obtained. Similar way, ferroelectric contribution in another half of the *P* - *E* loop can be obtained from the negative pulses [20].

References

[1] A. R. West, *Solid State Chemistry and its Applications*, 2nd ed. (John Wiley & Sons, 2014).

[2] R. C. Ropp, *Solid state chemistry* (Elsevier, 2003).

[3] N. K. C. Muniraju, *Crystal and spin structure and their relation to physical properties in some geometrical and spin spiral multiferroics*, Vol. 44 (Forschungszentrum Jülich, 2012).

[4] C. Giacovazzo, *Fundamentals of crystallography* (Oxford university press, USA, 2000).

[5] F. Fauth, I. Peral, C. Popescu, and M. Knapp, *Powder Diffraction* **28,** S360 (2013).

[6] F. Fauth, R. Boer, F. Gil-Ortiz, C. Popescu, O. Vallcorba, I. Peral, D. Fullà, J. Benach, and J. Juanhuix, *EPJ Plus* **130,** 160 (2015).

[7] H. Rietveld, *J. Appl. Crystallogr.* **2,** 65 (1969).

[8] J. Rodriguez-Carvajal, in *FULLPROF: a program for Rietveld refinement and pattern matching analysis*, 1990 (Toulouse, France:[sn]).

[9] K. Momma and F. Izumi, *J. Appl. Crystallogr.* **41,** 653 (2008).

[10] *Magnetic Property Measurement System - MPMS 3 User's Manual (Quantum Design)*.

[11] D. Martien, *Introduction to AC susceptibility (Quantum Design)* (2002).

[12] *Physical Property Measurement System - AC Measurement System (ACMS) Option - User's Manual (Quantum Design)*.

[13] *Physical Property Measurement System - Heat Capacity Option - User's Manual (Quantum Design)*.

[14] *Agilent Impedance Measurement Handbook - A guide to measurement technology and techniques (Agilent Technologies)*.

[15] M. Maglione and M. Subramanian, *Appl. Phys. Lett.* **93,** 032902 (2008).

[16] S. McKeever and D. Hughes, *J. Phys. D: Appl. Phys.* **8,** 1520 (1975).

[17] Y. Kohara, Y. Yamasaki, Y. Onose, and Y. Tokura, *Phys. Rev. B* **82,** 104419 (2010).

[18] C. De, S. Ghara, and A. Sundaresan, *Solid State Commun.* **205,** 61 (2015).

[19] J. Scott, *J. Phys. Condens. Matter* **20,** 021001 (2007).

[20] M. Fukunaga and Y. Noda, *J. Phys. Soc. Jpn.* **77,** 064706 (2008).

Chapter 3

Magnetic properties and magnetodielectric effect in $Bi_{1-x}Sm_xMnFe_2O_6$ (x = 0, 0.1 and 0.2)*

Summary

We have investigated detailed magnetic and electrical properties of a complex oxide, $BiMnFe_2O_6$, which crystallizes in a centrosymmetric orthorhombic structure (space group *Pbcm*). It exhibits a spiral antiferromagnetic ordering at 212 K with a peak in magnetization at 35 K. We have shown that this peak in magnetization is due the appearance of a re-entrant spin glass state, which suggests that the magnetic ground state is a coexistence of spin glass state and spiral antiferromagnetc ordering. Further, a magnetic anomaly is found around 170 K, where a dielectric anomaly with significant intrinsic magnetodielectric effect is observed. However, these anomalies are not due to ferroelectricity. We have tried to modify the magnetic structure by substituting Bi^{3+} ions with Sm^{3+} ions and found that the magnetic anomaly at 170 K becomes prominent upon Sm^{3+} substitution, which is associated with a weak ferromagnetic state. Magnetodielectric effect is observed below T_N in 20% Sm^{3+}-substituted sample. We have shown that the magnetodielectric effect below weak ferromagnetic region has an intrinsic capacitive origin, while it is governed by the extrinsic magnetoresistive effect in the weak ferromagnetic region.

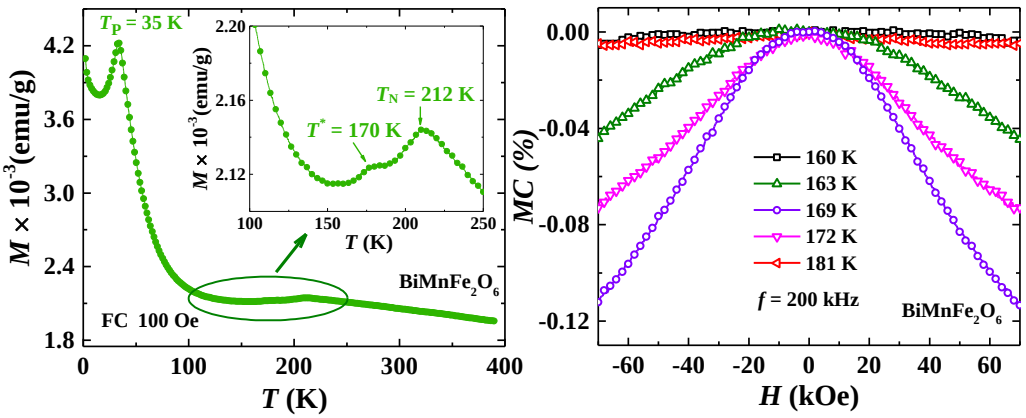

.....

*This work has appeared in *Phys. Rev. B*, **90**, 024413 (2014), © (2014) by the American Physical Society and *J. Appl. Phys.* **118**, 164103 (2015), © (2015) by the AIP Publishing.

3.1 Introduction

Bismuth based oxides are one of the potential candidates for exploring ferroelectricity due to the presence of stereochemically active lone pair electrons ($6s^2$), as discussed in Chapter 1 [1-4]. However, Bi^{3+} ions cannot always induce electric polarization [5]. But, in addition to the presence of Bi^{3+} ions, if the compound possesses a spiral magnetic ordering, it is highly possible that the compound can host multiferroicity. One important aspect of multiferroics (mainly type-II) is the presence of strong intrinsic magnetodielectric effect, where dielectric constant and magnetization are strongly coupled with each other. The magnetodielectric effect in this class of materials arises due to the magnetoelectric coupling. However, there are some materials, where strong magnetodielectric effect is observed without magnetoelectric coupling [6]. The origin of magnetodielectric effect in this type of materials has been suggested to be due to intrinsic effects (spin-phonon coupling, magnetostriction etc.) or extrinsic effects (magnetoresistance, Maxwell-Wagner relaxation etc.) [6]. For example, in MCuO$_3$ (M = Se and Te), a dielectric anomaly around the long-range magnetic ordering temperatures is observed, which is strongly effected by applied magnetic fields, although these are not magnetoelectrics [7,8]. The magnetodielectric effect in these oxides has been demonstrated to be intrinsic and it is explained in terms of spin-phonon coupling. Similarly, spin-phonon coupling induced intrinsic magnetodielectric effect is observed in $YFe_{1-x}Mn_xO_3$ [9]. On the other hand, magnetoresistance driven extrinsic magnetodielectric effect is found in γ-Fe_2O_3 [10].

Recently, a bismuth-based complex oxide $BiMnFe_2O_6$ is discovered, which crystallizes in a centrosymmetric orthorhombic structure (*Pbcm*) [11]. This compound has two potential mechanisms for inducing ferroelectricity. These are (a) the presence of stereochemically active lone-pair electrons of Bi^{3+} ions and (b) long-range spiral antiferromagnetic ordering of Mn^{3+}/Fe^{3+} spins at T_N ~ 212 K [12]. However, both these mechanisms do not seem to induce ferroelectricity as suggested by the neutron diffraction experiments [11,12]. Consistent with the centrosymmetric structure (*Pbcm*), the polar Bi^{3+} ions are arranged in an antiferroelectric manner and thus produce no net polarization [11]. On the other hand, a disorder arrangement of magnetic ions (Mn^{3+}/Fe^{3+}) in two different crystallographic sites (4*a* and 8*e*) results frustrated magnetic interactions that leads to a spiral antiferromagnetic ordering at T_N ~ 212 K which remains down to 7 K. A

peak in magnetization was observed around T_P ~ 34 K which has been attributed to a possible magnetic phase separation [11]. Based on the neutron diffraction experiments and density functional theory (DFT), it was shown that the resulting magnetic structure is of screw-type where the spins lying in the *ac* plane propagate along the *b*-axis [12]. This screw-type arrangement of Fe^{3+}/Mn^{3+} spins does not allow any electric polarization according to the inverse Dzyaloshinskii-Moriya (DM) interaction. Thus, it has been reported that $BiMnFe_2O_6$ remains non-ferroelectric.

One possibility to induce ferroelectricity in this compound is to modify the nature of the spiral magnetic ordering by substituting rare earth elements or other transition metal ions for Bi^{3+} or Mn^{3+}/Fe^{3+} ions, respectively. Batuk *et al.* have tried to modify the magnetic structure by substitution Cr^{3+} in the place of Mn^{3+} in $BiMn_{1-x}Cr_xFe_2O_6$ ($x \leq 0.3$) and investigated the structure and magnetic properties [13]. However, they have shown that Cr^{3+}-substitution does not have much effect on the bulk magnetic behavior, only a minor shift in T_N is observed, which decreases from 212 K in $x = 0$ to 165 K in $x = 0.3$.

In this chapter, we present the results of detailed magnetic and electrical measurements on the $Bi_{1-x}Sm_xMnFe_2O_6$ (x = 0, 0.1 and 0.2). In the first section, which deals with the results on the parent compound, we have shown that the magnetic peak at T_P ~ 34 K is associated with a re-entrant spin glass transition. Further, we observe a magnetic and dielectric anomaly at a temperature (T^* ~ 170 K) which is lower than the spiral antiferromagnetic ordering (T_N ~ 212 K) temperature. Significant magnetodielectric effect with intrinsic origin is observed around this dielectric and magnetic anomaly. Although, temperature dependent pyroelectric current exhibits a peak with the onset around T^* ~ 170 K, pyroelectric current measurements with different ramping rates and *P-E* loop measurements based on positive-up-negative-down (PUND) method suggest that the dielectric anomaly and the pyroelectric current peak around the magnetic anomaly at T^* ~ 170 K are not related to ferroelectricity. In the second section, we discuss the results on Sm^{3+}-substituted $Bi_{1-x}Sm_xMnFe_2O_6$ (x = 0.1 and 0.2). Temperature and magnetic field dependent magnetization data suggest that with increasing Sm^{3+} content, the magnetization anomaly grows into a weak ferromagnetism. Particularly, for x = 0.2, the weak ferromagnetism is observed in a wide temperature range (90 K to 201 K) and it enters into an antiferromagnetic state below 90 K upon further cooling. On the other hand, the dielectric anomaly shifts to lower temperatures and it occurs at 72 K for x = 0.2. In contrast to the parent compound, in the sample with x = 0.2, magnetodielectric effect is

observed both in the antiferromagnetic region (T < 90 K) and weak ferromagnetic region (90 K to 201 K). Our study reveals that the magnetodielectric effect in the antiferromagnetic region has an intrinsic capacitive origin while that observed at the weak ferromagnetic region originates from magnetoresistance.

3.2 Experimental section

Polycrystalline samples of $Bi_{1-x}Sm_xMnFe_2O_6$ (x = 0, 0.1 and 0.2) were prepared by solid state synthesis technique. Bi_2O_3, Sm_2O_3, Mn_2O_3, and Fe_2O_3 were mixed stoichiometrically and heated at 800 ^{0}C (6 hours) and 850 ^{0}C (18 hours) with intermittent grindings. The obtained powder was pressed into pellets and sintered at 900 ^{0}C, 920 ^{0}C and 940 ^{0}C for x = 0, 0.1 and 0.2, respectively for 12 hours. The rare earth oxide, Sm_2O_3 was preheated at 900 ^{0}C for 12 hours in air before use. To confirm the phase purity, room temperature X-ray diffraction data were collected with PANalytical Empyrean alpha-1 diffractometer using monochromatized Cu Kα_1 radiation. Structural analysis was carried out by Rietveld refinement method using FullProf software [14,15].

Temperature dependent dc magnetization measurements were carried out with a rate of 3 K/min under different magnetic fields. Magnetic field dependent measurements at different temperatures were performed with stable at each field mode. AC susceptibility was measured with the PPMS. Dielectric constant and dielectric loss were measured during warming the samples with a heating rate of 1 K/min. In pyroelectric current measurements, the poling was performed 200 K to 50 K under electric field and the pyroelectric current was recorded during warming with different heating rates (2, 3, 4 and 5 K/min). DC resistivity was measured by measuring current in the presence of an electric field of E = +3.9 kV/cm during warming using an electrometer. The conventional *P-E* loop and PUND measurements were performed [16]. The details of the measurements and instruments are already discussed in Chapter 2.

3.3 Results and discussion

In this section, we will discuss first the results on the parent compound $BiMnFe_2O_6$. Then, we will discuss the effect of Sm^{3+} substitution in $Bi_{1-x}Sm_xMnFe_2O_6$ (x = 0.1 and 0.2).

3.3.1 Results on $BiMnFe_2O_6$

3.3.1.1 Crystal structure

Figure 3.1 shows the room temperature powder X-ray diffraction (XRD) pattern of $BiMnFe_2O_6$, which confirms the pure phase of the sample. Rietveld refinement is performed with the centrosymmetric orthorhombic space group *Pbcm* and the detailed structural parameters are given in Table 1.1. The crystal structure viewed along [100] direction is displayed in Figure 3.2(a). It is found that, both of the Mn^{3+} and Fe^{3+} ions are randomly distributed in two different crystallographic sites, *A*1 (4*a*) and *A*2 (8*e*), which form distorted octahedral coordination with oxygen ions. Since X-ray cannot distinguish between Fe^{3+} and Mn^{3+} ions, the occupancies of Fe^{3+} and Mn^{3+} ions in these two sites are kept fixed to the values obtained from the neutron diffraction experiment, as given in Table 1.1 [11]. As shown in Figure 3.2(b-e), the *A*1-site octahedra are connected by all type of sharing, namely, face, edge and corner sharing and form a layer in *bc*-plane, while the *A*2-site octahedra are connected only by corner sharing and form a zigzag chain along *b*-axis. These two octahedra, *A*1 and *A*2 are interconnected by a further complicated arrangement involving corner and edge sharing. It is to be noted that, the high values of

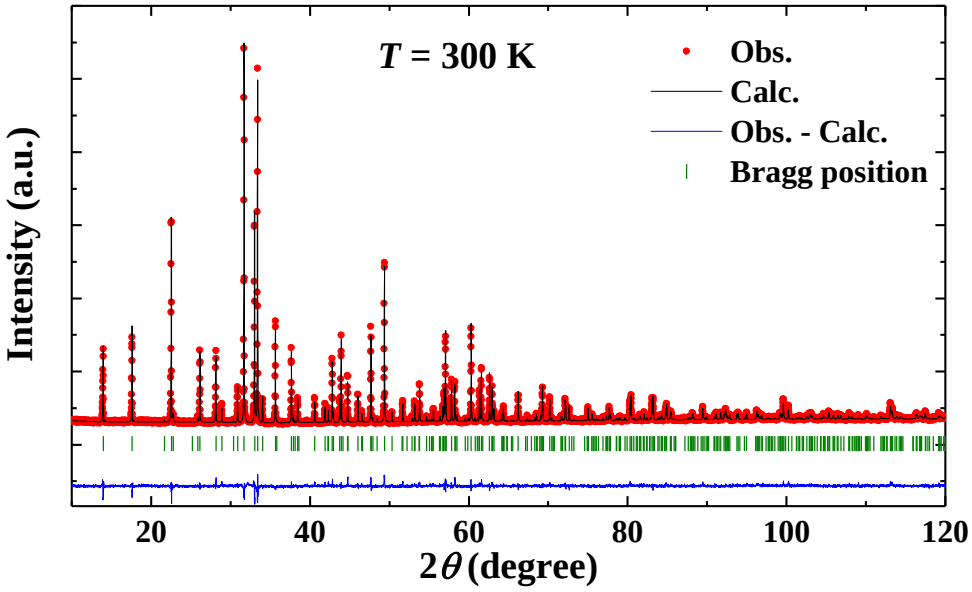

Figure 3.1 Rietveld refinement of room temperature X-ray diffraction data of $BiMnFe_2O_6$.

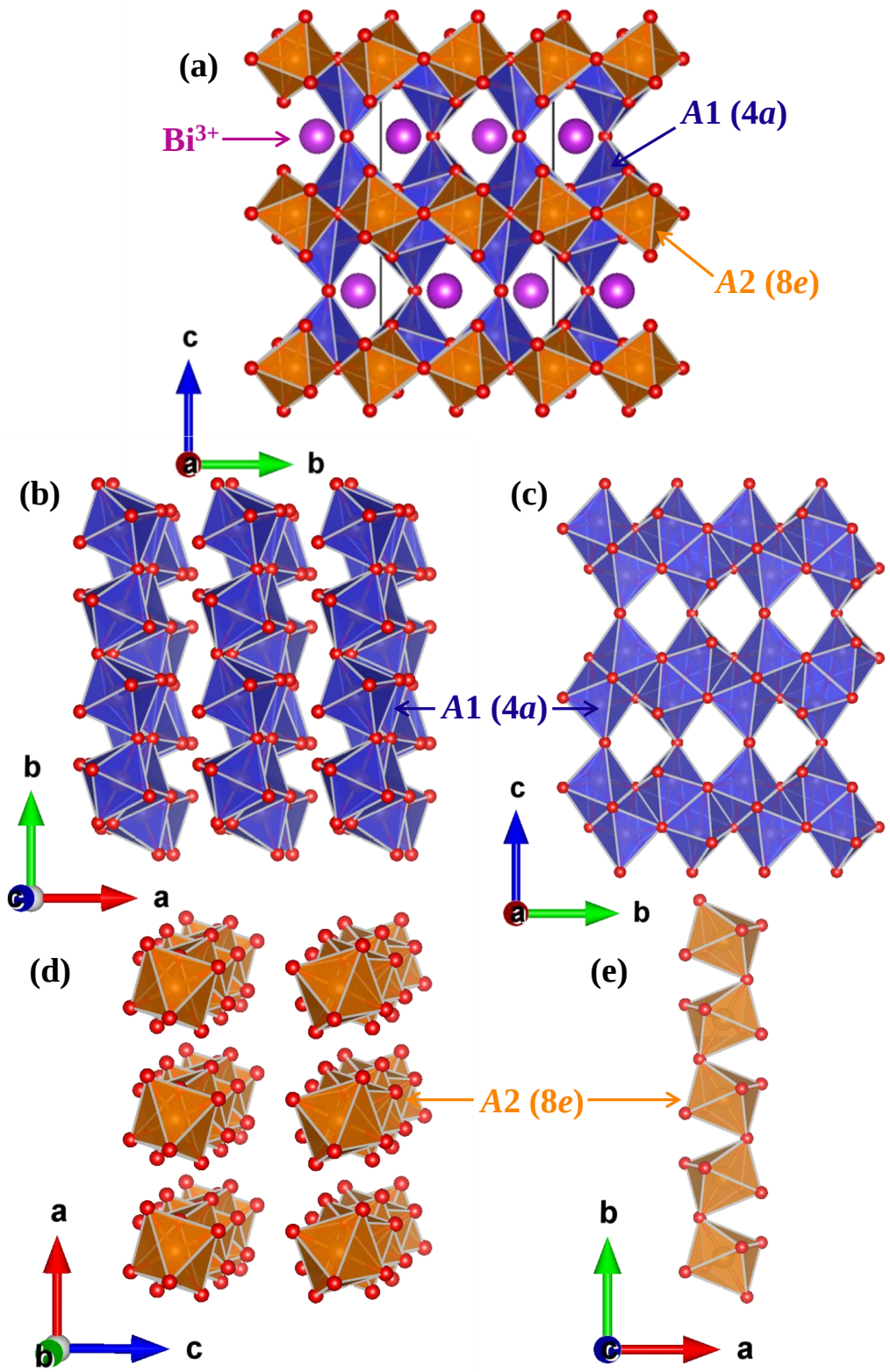

Figure 3.2 (*a*) Crystal structure of $BiMnFe_2O_6$ consisting of two types of octahedra (*A*1 and *A*2) of Mn^{3+}/Fe^{3+} ions. (*b*-*c*) Edge and corner sharing of *A*1 octahedra, which form a layer in *bc* plane. (*d*-*e*) Corner-shared *A*2 octahedra forming a zigzag chain along *b* axis.

Table 1.1 Crystallographic parameters of $BiMnFe_2O_6$ obtained from Rietveld refinement of room temperature X-ray diffraction data

Space group: *Pbcm*; a = 5.03283(4) Å, b = 7.06949(5) Å, c = 12.66413(8) Å, V = 450.584(5) Å^3; χ^2 = 2.26

Atom	Wyckoff position	x	y	z	B_{iso} (Å^2)	Occupancy
Bi	4*d*	0.9711(2)	0.3694(2)	1/4	1.25(3)	1
Mn1	8*e*	0.4903(8)	0.3399(4)	0.6014(1)	1.44(6)	0.3
Fe1	8*e*	0.4903(8)	0.3399(4)	0.6014(1)	1.44(6)	0.7
Mn2	4*a*	0	1/2	1/2	1.26(8)	0.4
Fe2	4*a*	0	1/2	1/2	1.26(8)	0.6
O1	8*e*	0.1627(17)	0.9468(15)	0.6255(6)	1.00	1
O2	8*e*	0.6640(15)	0.0995(19)	0.5683(6)	1.00	1
O3	4*c*	0.7881(26)	3/4	1/2	1.00	1
O4	4*d*	0.3539(24)	0.1886(19)	1/4	1.00	1

isotropic thermal parameter (B_{iso}) for Fe and Mn atoms could be due to the effect of fluorescence. Bi^{3+} cations occupy the cavity formed by the *A*1 and *A*2-site octahedra, which is asymmetric because of the displacement of Bi^{3+} ions in opposite directions due to the lone pair effect (Figure 3.2(a)). Thus, there is no net electric polarization in overall crystal structure.

3.3.1.2 DC magnetization

Temperature evolution of the dc magnetization measured under a magnetic field of 100 Oe is shown in Figure 3.3(a). The magnetization is measured under field-cooled (FC) condition, where the sample was cooled to lowest temperature under a magnetic field and the magnetization data was recorded during warming the sample in the presence of same magnetic field. As reported earlier by Yang *et al.*, two anomalies, one at T_N ~ 212 K and another at a lower temperature T_P ~ 34 K, are observed in magnetization [11]. The anomaly at 212 K is related to the long-range spiral antiferromagnetic ordering of Fe^{3+}/Mn^{3+} spins. In addition to these two magnetic anomalies (at T_N and T_P), we also observe a weak magnetic anomaly at T^* ~ 170 K at low field (100 Oe), which is shown in the left inset of Figure 3.3(a). This anomaly is so weak that it was remained unnoticed in

the earlier study [11]. However, while we measure FC magnetization under high magnetic field (70 kOe), it becomes clear and prominent, which can be seen in Figure 3.3(b).

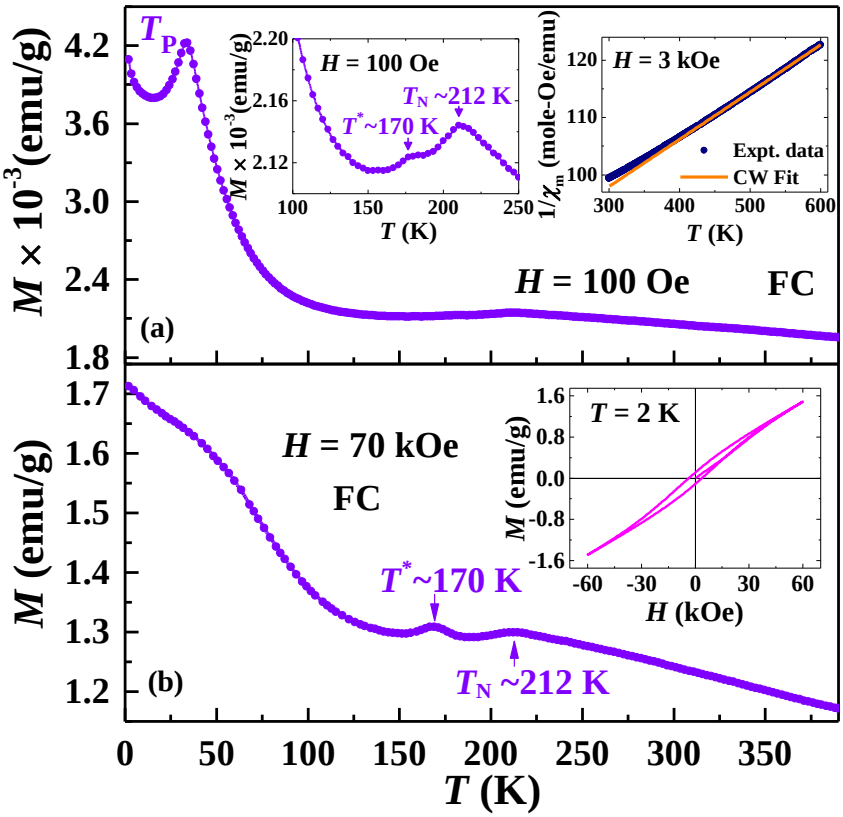

Figure 3.3 Temperature dependent field-cooled (FC) magnetization of $BiMnFe_2O_6$ measured under magnetic fields of (a) 100 Oe and (b) 70 kOe. The left inset of figure (a) shows a magnified-view of FC magnetization data and the right inset shows the Curie-Weiss Fit of $1/\chi_m$ *vs.* T data. Magnetic field dependent magnetization at 2 K is shown in the inset of figure (b).

Though the present compound exhibits a long-range antiferromagnetic ordering at T_N ~ 212 K, the magnetic susceptibility does not follow Curie-Weiss behavior at room temperature, suggesting the presence of a short-range spin correlation above T_N, which is consistent with the results of neutron diffraction data [11]. Thus, to understand the nature of the magnetic interactions, we have performed high temperature magnetization measurements from 300 K to 600 K in the presence of a magnetic field of 3 kOe. It is observed that the magnetic susceptibility follows the Curie-Weiss law only above 450 K. The results of Curie-Weiss fit of $1/\chi_m$ *vs.* T data is shown in the right inset of Figure 3.3(a). The effective paramagnetic moment (μ_{eff}) obtained from the fit is 9.89 μ_B/f.u. which is close to the calculated value (9.69 μ_B/f.u.). The obtained value of Curie-Weiss

temperature (θ_{CW}) is -890 K. The negative sign of θ_{CW} is consistent with the antiferromagnetic interactions, while the value is much higher than T_N indicating the presence of magnetic frustration. The frustration parameter f (= $|\theta_{CW}|/T_N$) is found to be 4.2 which suggests that the magnetic structure is moderately frustrated [17].

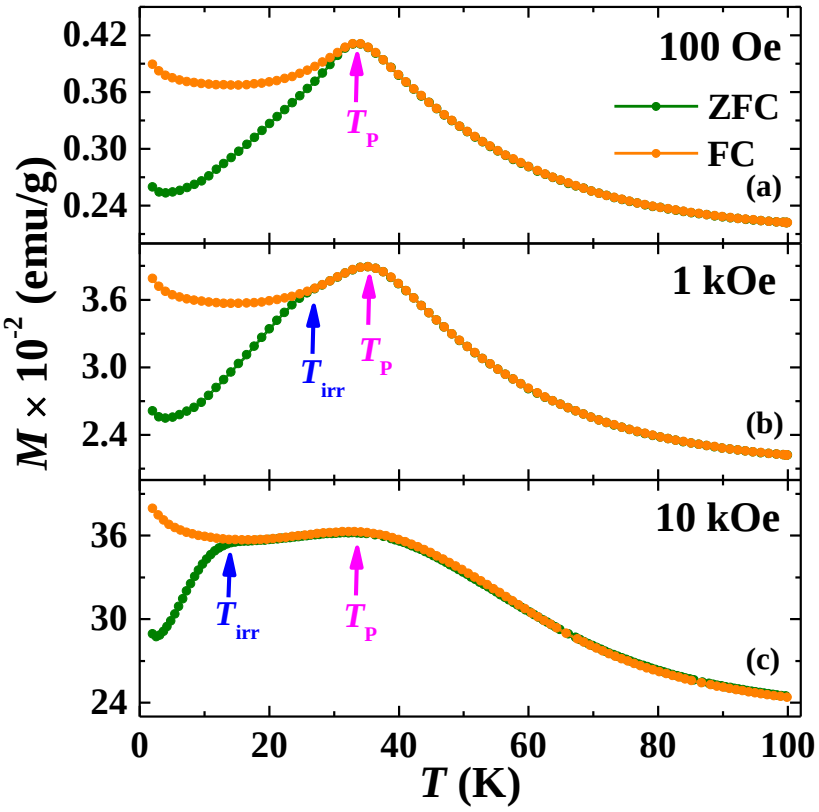

Figure 3.4 Temperature dependent zero-field-cooled (ZFC) and field-cooled (FC) magnetization of $BiMnFe_2O_6$ measured under different magnetic fields.

Temperature dependent field-cooled (FC) and zero-field-cooled (ZFC) magnetizations under magnetic fields of 100 Oe, 1 kOe and 10 kOe are shown in Figure 3.4(a-c), respectively. In ZFC mode, the sample was cooled to lowest temperature without any magnetic field and the magnetization was measured during heating in the presence of applied magnetic field. Both FC and ZFC magnetizations exhibit a peak around T_P ~ 34 K and bifurcate below a temperature (T_{irr}), which is the onset of the thermomagnetic irreversibility (TMI). The influence of applied magnetic fields on these two temperatures (T_{irr} and T_P) are different. As shown in Figure 3.4(a-c), T_{irr} is found to shift to lower temperature with increasing applied magnetic fields, while T_P initially increases and then decreases with increasing magnetic fields.

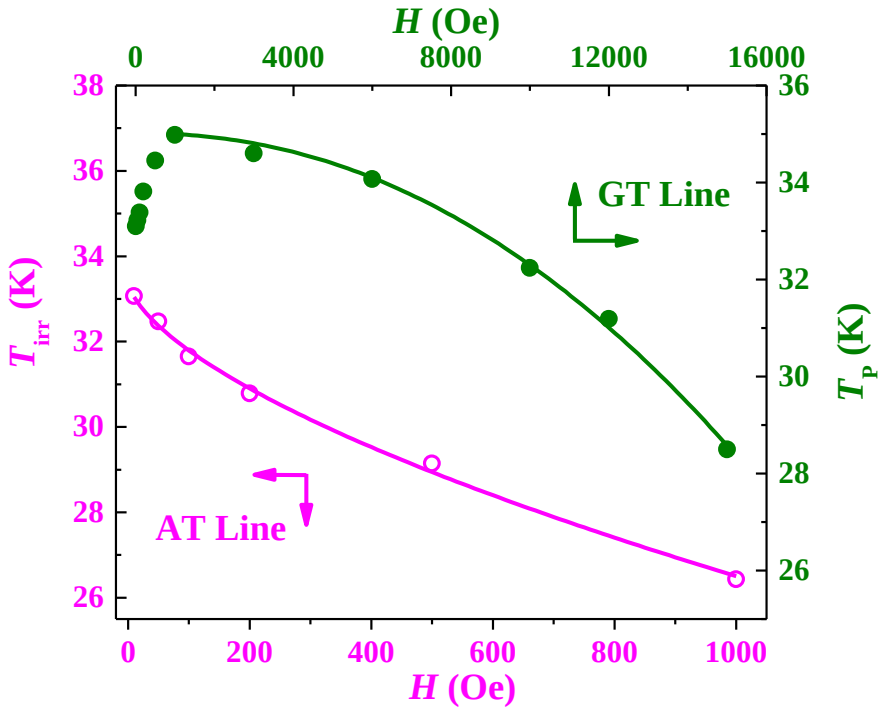

Figure 3.5 Magnetic field dependencies of T_{irr} and T_P. Solid lines represent the fit to the de Almeida-Thouless (AT) line and Gabay-Toulouse (GT) line for T_{irr} (H) and T_P (H), respectively.

In a typical Heisenberg spin glass system, two different lines, correspond to strong and weak irreversibility temperatures, have been observed in *H-T* phase diagram, which are known as de Almeida-Thouless (AT) line and Gabay-Toulouse (GT) line, respectively [18,19]. For the present system, it is observed that T_{irr} (H) and T_P (H) follow AT and GT line, respectively. These two lines can be represented by the following equations,

$$T_{irr}(H) = T_{irr}(0)(1 - CH^n); n = 2/3 \quad (1)$$

$$T_P(H) = T_P(0)(1 - C'H^m);\ m = 2 \quad (2)$$

where C and C′ are constants and T_{irr} (0) and T_P (0) are the T_{irr} and T_P at zero magnetic field. The dependencies of T_{irr} and T_P on applied magnetic fields are shown in Figure 3.5. The experimental data of T_{irr} (H) can be fitted with Equation (1). A best fit is obtained only at low field region (H < 1000 Oe). The value of T_{irr} (0) obtained from the fit is 33.4 K and the obtained value of n is 0.62 (± 0.06) which is close to the theoretical value of n (= $\frac{2}{3}$) for the AT line for a spin glass system [18]. On the other hand, as shown in Figure 3.5, the dependence of T_P on magnetic field is quite unusual compared to the theoretical

suggestion. Initially T_P increases with increasing magnetic fields, and above a critical magnetic field, it decreases and follows the Gabay-Thouless (GT) line [19]. The value of *m* obtained from a fit with Equation (2) is 2.12 (± 0.09) which is almost equal to the theoretical value of $m = 2$ for spin glass systems. The initial linear increase of T_P (*H*) data at low fields may arise from the uniaxial anisotropy as observed in $La_{0.9}Sr_{0.1}CoO_3$ [20]. The presence of AT and GT lines in *H-T* phase diagram have been observed in other spin glass systems [20-24]. Thus, the bifurcation between ZFC and FC magnetization and the presence of AT and GT lines in *H-T* phase diagram are indications of Heisenberg-like spin glass state below 34 K. Magnetic field-dependent magnetization measured at 2 K (inset of Figure 3.3(b)) shows a tiny hysteresis loop which is similar to that of a typical spin glass systems [25].

3.3.1.3 AC susceptibility

We have carried out ac susceptibility measurements in order to confirm the presence of spin glass state below T_P ~ 34 K. Figure 3.6(a) shows the temperature variation of the real part of ac susceptibility $\chi'(T)$ measured with different frequencies. A peak is found around 34 K in χ' (*T*) and the peak position, which is known as freezing temperature (T_f), shifts to higher temperature with increasing frequency of the applied ac magnetic field. This frequency-dependent peak-shift confirms the presence of spin glass state below T_P ~ 34 K. The spin glass state appears well below the long-range spiral antiferromagnetic ordering temperature (T_N ~ 212 K), indicating a re-entrant spin glass state [25].

To get more insight into the nature of glassy state, we further analyzed ac susceptibility data. The frequency-dependent peak-shift can be quantified by a parameter (*S*) defined by [25],

$$S = \frac{\Delta T_f}{T_f\{\Delta log_{10}(f)\}} \qquad (3)$$

where $\Delta T_f = T_{f_1} - T_{f_2}$ and $\Delta log_{10}(f) = log_{10} f_1 - log_{10} f_2$. The parameter (*S*) is used to distinguish a spin glass from a superparamagnet. For a spin glass, *S* should remain between $0.005 < S < 0.08$, while $S > 0.2$ for a superparamagnetic state [25]. The obtained value of *S* for the present system is 0.0175, which suggests that the glassy state is due to (re-entrant) spin glass transition.

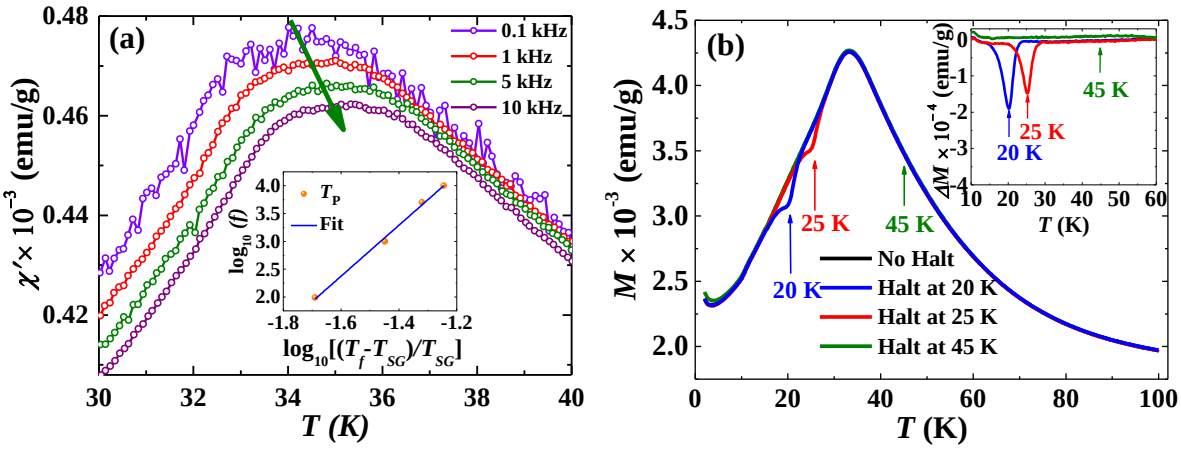

Figure 3.6 (a) Temperature dependent real part of the ac susceptibility measured with different frequencies. The inset shows the critical slowing down behavior of freezing temperatures. (b) Results of memory effect experiments performed by halting at different temperatures. Inset shows the difference between the halt and without-halt magnetization $\Delta M = M_{ZFC(\text{with halt})} - M_{ZFC(\text{without halt})}$.

It is well known that T_f follows critical slowing down behavior for a spin glass system, which is given by the following equation [25-27],

$$\tau = \tau_0 \left(\frac{T_f - T_{SG}}{T_{SG}}\right)^{-z\nu} \qquad (4)$$

where τ is the characteristic time corresponds to the excitation frequency f, T_{SG} is the freezing temperature at f = 0 Hz, τ_0 is a characteristic time-constant, which is related to the spin-flipping time and $z\nu$ is a dynamical critical exponent. In the inset of Figure 3.6(a), $\log_{10} f$ *vs.* $\log_{10}[(T_f - T_{SG})/T_f]$ is plotted, which can be fitted with the Equation (4) with T_{SG} = 33.4 K, which is same as T_{irr} (0) obtained from the results of the fit of AT line. For a spin glass system, τ_0 and $z\nu$ are typically ~ 10^{-12} - 10^{-13} sec and 4 - 12, respectively [22,28]. The values of τ_0 and $z\nu$ obtained from the best fit to a straight line are 3.147 × 10^{-11} sec and 4.58, respectively. Thus, the obtained value of $z\nu$ further suggests the presence of spin glass state below 34 K. However, the value of the characteristic time-constant (τ_0) is one order higher than that of typical spin glass system but smaller than that of a typical cluster glass system (~ 10^{-7} - 10^{-10} sec) [22,28]. This indicates the possibility of the presence of some interacting spin-cluster in the re-entrant spin glass state.

3.3.1.4 Memory effect

Memory and rejuvenation effects are important features of spin glasses [29-31]. DC magnetic memory effect experiment was performed with the following procedure [32]: The sample was cooled to a particular temperature (T_H) in a ZFC condition, where the sample was halted for a duration of t_H = 6000 sec. Then the sample was cooled to the lowest possible temperature and the magnetization was measured during heating the sample in the presence of a magnetic field of 100 Oe. In Figure 3.6(b), the ZFC magnetizations without-halt and with-halt at three different temperatures T_H = 20, 25 and 45 K are shown. When T_H is less than T_P, the magnetization shows a clear dip at the halt-temperature (T_H = 20 K and 25 K). In the inset of Figure 3.6(b), $\Delta M = M_{ZFC(\text{with halt})} - M_{ZFC(\text{without halt})}$ is shown, where the memory effect is clearly indicated by a sharp peak. However, such a dip is not observed when $T_H > T_P$. The dip associated with the memory effect experiment further confirms the presence of metastable glassy state below T_P.

3.3.1.5 Magnetization relaxation

It is a well-known and interesting fact that the magnetization of a spin glass system relaxes with time. To study the magnetization relaxation, the sample was cooled to different temperatures below 34 K under FC conditions with a magnetic field of 100 Oe and magnetization was recorded with time after switching off the field to zero and keeping the temperature fixed. In Figure 3.7(a), normalized magnetizations, $m(t) = M_t / M_{t=0}$, measured at 5, 10, 15 and 20 K, are shown as a function of time (t). The $m(t)$ *vs.* time data can be fitted well with the stretched exponential equation [33-36], which is given by,

$$m(t) = m_0 - m_g e^{-\left(\frac{t}{\tau}\right)^{\beta}} \qquad (5)$$

where β is the stretching exponent, τ is the characteristic relaxation time constant, m_g is related to the glassy component of magnetization and m_0 is related to an initial remanent magnetization which is required to fit the decay of magnetization of a re-entrant spin glass system. For a spin glass, β should remain in the range of $0 < \beta < 1$. As shown in Table 1.2, the obtained value of β from the fit of $m(t)$ *vs.* time with the Equation 5 remains between 0.42 - 0.51 for all temperatures. The value of relaxation time constant (τ)

increases continuously with decreasing temperature. This result also suggests the presence of spin-cluster in the spin glass state, which grows upon further cooling.

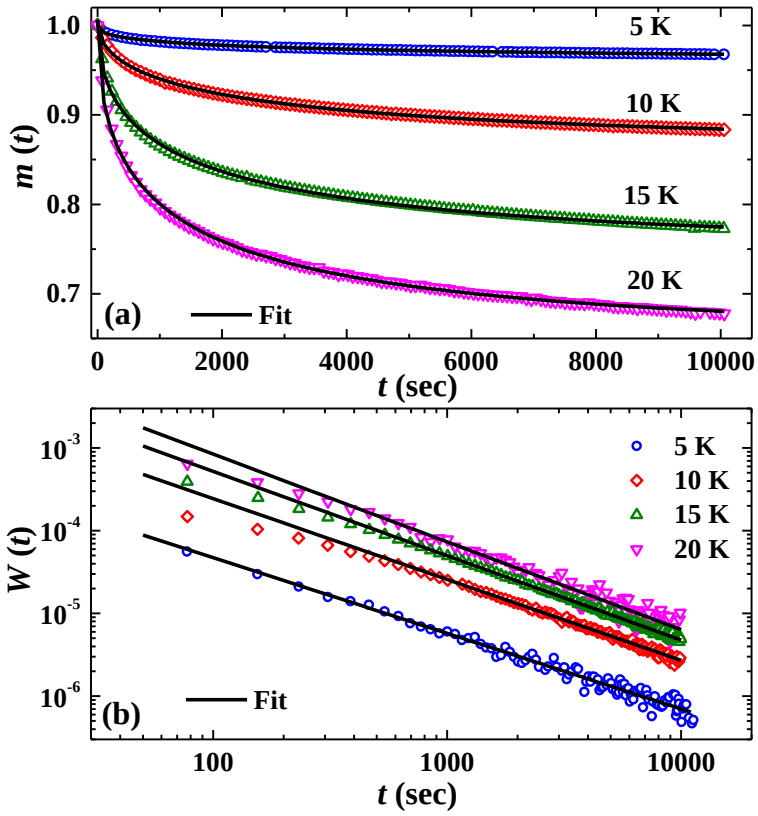

Figure 3.7 (a) Magnetization relaxation data recorded at different temperatures after a field-cooled cooling under a magnetic field of 100 Oe and setting the magnetic field to zero. The fits with the stretched exponential equation are shown by the solid lines. (b) $W(t)$ vs. time plot at different temperatures. Solid lines represent the fit to a power law.

To confirm the presence of spin-cluster, we have further analyzed the relaxation data using the model proposed by Ulrich [37]. According to this model, after a crossover time, the rate of change of normalized thermoremanent magnetization $m(t)$, defined by, $W(t) = -\frac{d}{dt}[\ln m(t)]$, of a system of magnetic particles, should decay with time as a power law [37],

$$W(t) \sim At^{-n} \tag{6}$$

The value of n is very important and depends on the density of the magnetic particles and interaction between them. For an ideal spin glass system, the value of n should remain constant throughout the temperature below the spin glass transition. For the present

system, $W(t)$ *vs.* time at different temperatures is plotted in Figure 3.7(b) and we have fitted these data with the Equation 6. As shown in Table 1.2, we found that the value of n obtained from the fit increases continuously from 0.91(2) to 1.06(2) with increasing temperature from 5 K to 20 K. This analysis strongly suggests that the glassy state is not a simple atomic spin glass; rather it includes some strongly interacting spin-clusters as well. Using this model, the presence of spin-cluster glass state was confirmed in manganites and cobaltites [38-40].

Table 1.2 Characteristic relaxation time constant (τ) and stretching exponent (β) obtained from fitting $M(t)$ vs. time data with a stretch exponential equation at different temperatures. The parameter n at different temperatures obtained from fitting $W(t)$ *vs.* time with a power law, $W(t) \sim At^{-n}$ are also given.

T (K)	τ (sec)	β	n
5	3584(104)	0.42(1)	0.91(2)
10	2589(70)	0.51(1)	0.97(1)
15	1728(43)	0.47(1)	1.01(1)
20	1347(33)	0.46(1)	1.06(2)

3.3.1.6 Coexistence of spin glass and long-range antiferromagnetic ordered state

According to the results of the neutron diffraction experiments performed at 7 K, the long-range antiferromagnetic ordering is present down to at least 7 K [11]. Thus, the above results suggest that the long-range antiferromagnetic ordered state and spin glass state coexist below $T_P \sim 34$ K. Coexistence of long-range collinear antiferromagnetic ordering and glassy state has been reported in systems such as $Fe_{0.55}Mg_{0.45}Cl_2$, $Fe_xMn_{1-x}TiO_3$, and $PbFe_{0.5}Nb_{0.5}O_3$ [41-44]. It is important to note that the spiral ordering coexist with spin glass state which is seldom observed. The existence of glassy state in the present compound is consistent with the disordered arrangement of Fe^{3+} and Mn^{3+} ions in two different crystallographic sites in the complex crystal structure. The emergence of the glassy state does not destroy the long-range spiral ordering at low temperature. Further, since the ordered magnetic moment of the two sites of Fe^{3+}/Mn^{3+} ions increases continuously down to 7 K, as discussed in earlier study [12], it is possible

that the glassy state and the spiral ordering develop almost independently. Further investigation is required for a more detailed microscopic origin of this mixed state.

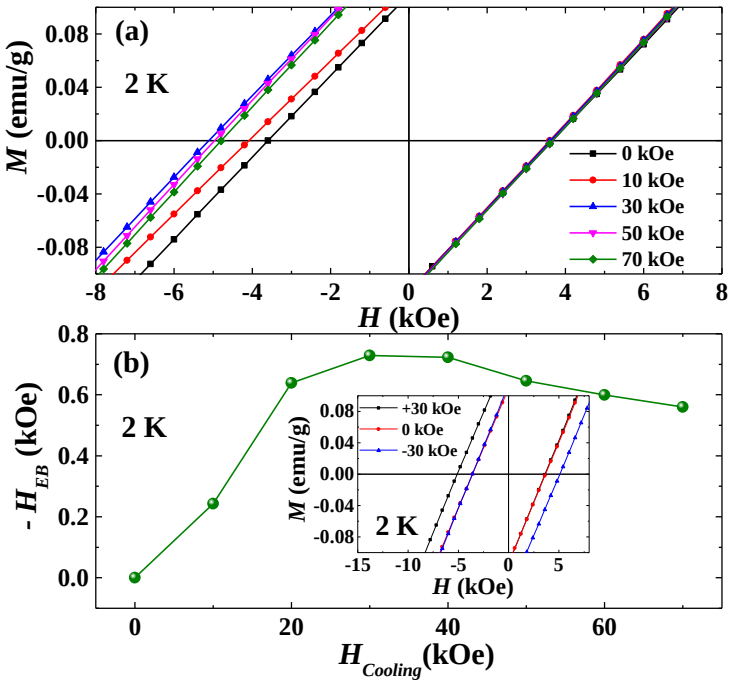

Figure 3.8 (a) Magnetic field dependent magnetizations at 2 K measured after cooling the sample under different magnetic fields (b) Cooling-field ($H_{Cooling}$) dependent exchange bias field (- H_{EB}) at 2 K. The reversible shift of the *M vs. H* loops upon cooling under opposite magnetic fields is shown in the inset.

3.3.1.7 Exchange bias

The coexistence of the long-range antiferromagnetic ordering and the spin-cluster glass state is further evidenced from the observation of exchange bias effect at low temperature. To investigate exchange bias effect, magnetic field dependent magnetizations are measured at 2 K after cooling the sample in the presence of different cooling magnetic fields, which are shown in Figure 3.8(a). It is evident from this figure that, the *M vs. H* hysteresis loops shift asymmetrically along the field-axis in the direction opposite to the applied magnetic field upon field cooling. The shift increases with increasing cooling field up to 30 kOe and then decreases above 30 kOe. As shown in the inset of Figure 3.8(b), the shift can be reversed by applying opposite cooling-field of ± 30 kOe. In Figure 3.8(b), the cooling-field ($H_{Cooling}$) dependent exchange-bias field (-H_{EB}) is shown. These results indicate the presence of exchange bias effect in the present system,

which further supports the coexistence of the ordered antiferromagnetic and spin-cluster glass states at low temperature [45-47].

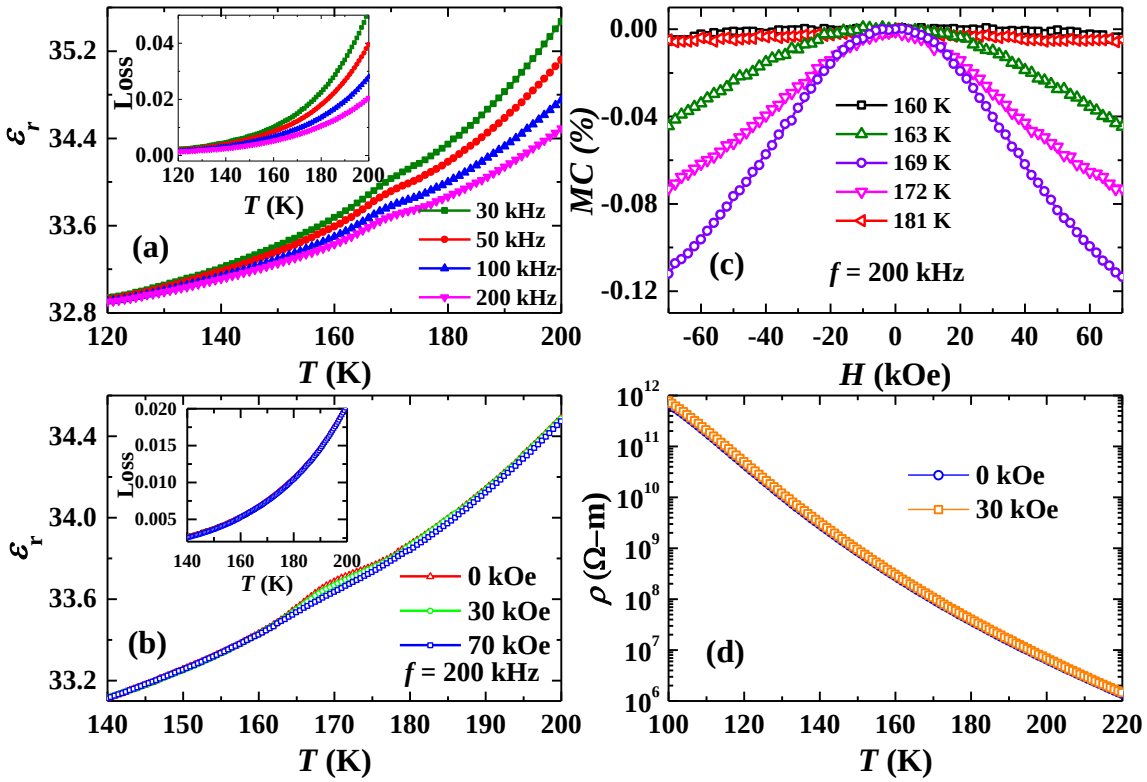

Figure 3.9 (a) Temperature variation of dielectric constant (ε_r) measured with different frequencies. Temperature dependent dielectric loss is shown in the inset. (b) Temperature dependent dielectric constant measured with 200 kHz under different magnetic fields. The associated dielectric loss is shown in the inset. (c) Magnetic field dependent magnetocapacitance, *MC* (%), measured at different temperatures around the dielectric anomaly with 200 kHz. (d) Variation of resistivity with temperature measured under 0 and 30 kOe are shown.

3.3.1.8 Magnetodielectric effect

Temperature dependent dielectric constant data measured with different frequencies are shown in Figure 3.9(a). In contrast to the earlier report [11], we observed a frequency-independent broad dielectric anomaly around T^* ~ 170 K as shown in Figure 3.9(a), where we found a weak anomaly in magnetization. The occurrence of dielectric and magnetic anomaly at the same temperature suggests the presence of magnetodielectric effect. On the other hand, as shown in the inset of Figure 3.9(a), we did

not observe any noticeable anomaly in the dielectric loss which remains as low as 0.01 at 170 K. Further, the dielectric constant was measured under various applied magnetic fields and the data is shown in Figure 3.9(b). Interestingly, it is found that the dielectric anomaly is suppressed under external magnetic fields. Magnetic field dependent capacitance is measured with 200 kHz around the dielectric anomaly by varying the magnetic field from +70 kOe to -70 kOe and the obtained magnetocapacitance, $\{MC(\%) = \frac{C_H - C_{H=0}}{C_{H=0}} \times 100\}$, are shown in Figure 3.9(c). As expected from the results of Figure 3.9(b), magnetocapacitance is observed only around the dielectric anomaly. We note that a similar broad dielectric anomaly and magnetocapacitance effect have been found in $BiMnO_3$ around the ferromagnetic transition temperature (T_C ~ 100 K), which has been attributed to the intrinsic magnetoelectric coupling between the ferromagnetic and ferroelectric ordering [48].

To probe the origin of the observed magnetocapacitance, we have measured dc electrical resistivity with conventional two probe method under an electric field of + 3.9 kV/cm and magnetic fields of 0 and 30 kOe. Temperature dependent resistivity is shown in Figure 3.9(d). The resistivity is as high as ~ 10^8 Ohm-m at 170 K and there is no anomaly in resistivity around this temperature. As shown in Figure 3.9(d) and in the inset of Figure 3.9(b), we did not observe any magnetoresistance effect and magneto-loss around 170 K. Further, at such a high frequency (~ 200 kHz), the resistive part or extrinsic effect (such as grain boundary, space charge, etc.) hardly contributes to the magnetodielectric effect, since those are mostly sensitive to low frequency ac signal only [6]. Therefore, the observed magnetodielectric effect should be intrinsic or purely capacitive in nature. The presence of magnetodielectric effect is an indication of existence of possible spin-phonon coupling. However, other experimental study (such as Raman spectroscopy) is necessary for further understanding.

3.3.1.9 Pyroelectric current and positive-up-negative-down method

Pyroelectric current measurements were performed to know whether or not the observed dielectric anomaly around the magnetic anomaly (T^* ~ 170 K) is associated with the ferroelectric transition. As shown in Figure 3.10(a), a broad and symmetric pyroelectric current peak is observed with the onset around the dielectric anomaly (T^* ~ 170 K). Since the pyroelectric current in a polycrystalline sample may appear from other effects, such as leakage and space charge due to an electric field poling, pyroelectric

current was measured with different warming rates. We observe that the pyroelectric current peak shifts to higher temperature with increasing warming rate, as shown in Figure 3.10(a). This indicates that the pyroelectric current peak originates from thermally stimulated depolarization current and cannot be attributed to a ferroelectric transition [49]. For further confirmation, we have performed the conventional *P-E* hysteresis loop and PUND measurements at 77 K and 170 K. The hysteresis loop obtained from the conventional *P-E* loop measurements at 77 K is shown in the inset of Figure 3.10(b), which resembles a leaky behavior. Further, PUND measurement does not show any noticeable ferroelectric polarization at 77 K, which is shown in Figure 3.10(b). Similar results are observed at 170 K also. Thus, these results confirm that the observed magnetic anomaly, dielectric anomaly and pyroelectric current peak around 170 K are not due to ferroelectric transition.

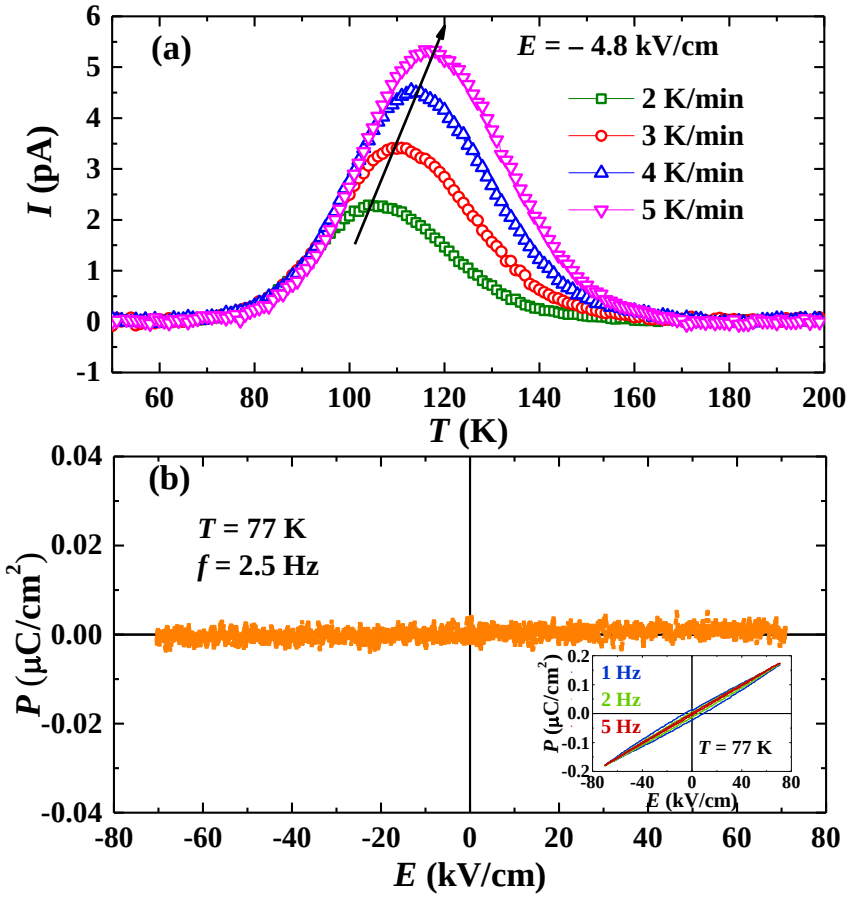

Figure 3.10 (a) Temperature dependent pyroelectric current data measured with different heating rates after poling the sample with an electric field of - 4.8 kV/cm. (b) *P-E* loop obtained from the PUND measurements at 77 K. Inset shows the conventional *P-E* loop measured at 77 K.

3.3.2 Results on $Bi_{1-x}Sm_xMnFe_2O_6$ (x = 0.1 and 0.2)

In this section, we discuss the results on Sm^{3+}-substituted samples. For comparison, we have shown here some results of the parent compound also.

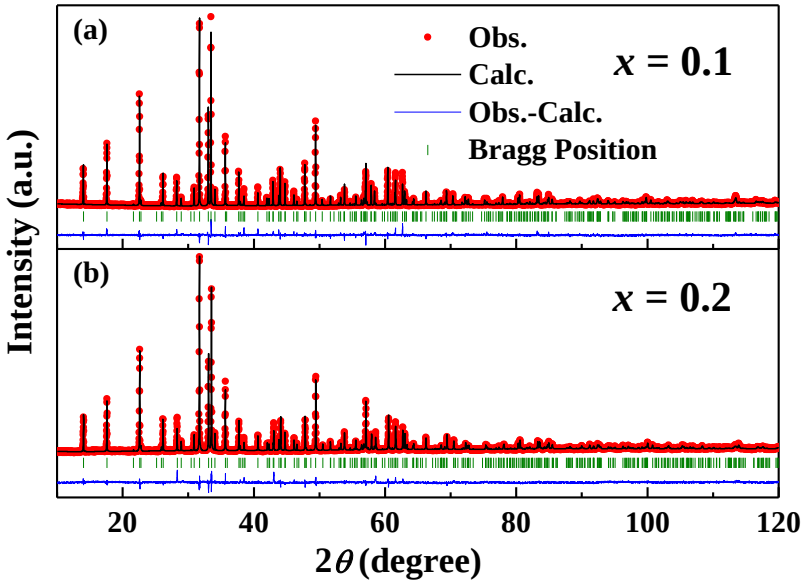

Figure 3.11 Rietveld refinements of room temperature X-ray diffraction data of $Bi_{1-x}Sm_xMnFe_2O_6$ (x = 0.1 and 0.2).

3.3.2.1 Crystal structure

Figure 3.11 shows room temperature powder X-ray diffraction patterns of the samples, $Bi_{1-x}Sm_xMnFe_2O_6$ (x = 0.1 and 0.2). Rietveld refinements were performed for structural analysis and it is observed that the crystal structures remain same (space group *Pbcm*) as parent compound up to a substitution of 20% Sm^{3+}at Bi^{3+} site. We have tried to substitute more Sm^{3+} also, but we could not stabilize the pure phase. The lattice parameters and volume of the unit cell of the Sm^{3+}-substituted samples obtained from Rietveld refinements are shown in Table 1.3. It is found that with increasing x, the lattice parameters a and c decrease, whereas the parameter b increases slightly. Volume (V) of the unit cell decreases monotonically with increasing x. Bi^{3+} ion in the parent compound is surrounded by eight oxygen atom and the ionic radius of Bi^{3+} is 1.17 Å in eight coordination site, while that of Sm^{3+} is 1.079 Å. Thus, the observed systematic decrease

of the volume of the unit cell is consistent with the Sm^{3+} substitution at Bi^{3+} site in $BiMnFe_2O_6$.

Table 1.3 Lattice parameters and volume of $Bi_{1-x}Sm_xMnFe_2O_6$ (x = 0, 0.1 and 0.2) obtained from Rietveld refinements of X-ray diffraction data collected at room temperature

x	a (Å)	b (Å)	c (Å)	V (Å^3)
0	5.0325(0)	7.0690(0)	12.6634(1)	450.493(6)
0.1	5.0319(1)	7.0700(1)	12.6316(1)	449.378(9)
0.2	5.0313(1)	7.0708(1)	12.5991(2)	448.216(10)

3.3.2.2 DC magnetization

The variation of magnetizations with temperature measured under a field-cooled-warming (FCW) condition with a magnetic field of 100 Oe for x = 0, 0.1 and 0.2 are shown in Figure 3.12(a-c), respectively. In the FCW magnetization measurements, we have followed the same procedure of FC measurements as discussed before. Upon substitution of Sm^{3+}, the long-range antiferromagnetic ordering temperature (T_N) decreases from 212 K (for parent compound) to 201 K (for x = 0.2). Interestingly, the weak magnetic anomaly, that is observed around T^* ~ 170 K in the parent compound, becomes prominent in Sm^{3+}-substituted samples even at low magnetic fields. Particularly, in the case of x = 0.2, the magnetization increases rapidly below T_N = 201 K and drops below 165 K. This broad peak between 90 K and 201 K suggests a weak ferromagnetic (WFM) state which is confirmed by the nature of *M vs. H* loops as discussed later. Upon further cooling, the weak ferromagnetism disappears below 90 K and the compound enters into an antiferromagnetic (AFM) state. This WFM-AFM transition around 90 K in x = 0.2 sample is so robust that it is not suppressed even under a high magnetic field of 70 kOe, which is shown in the right inset of Figure 3.12(c). As observed in the parent compound, the anomaly due to re-entrant spin glass (RSG) transition is present in both x = 0.1 and 0.2 as shown in Figure 3.12(b) and (c).

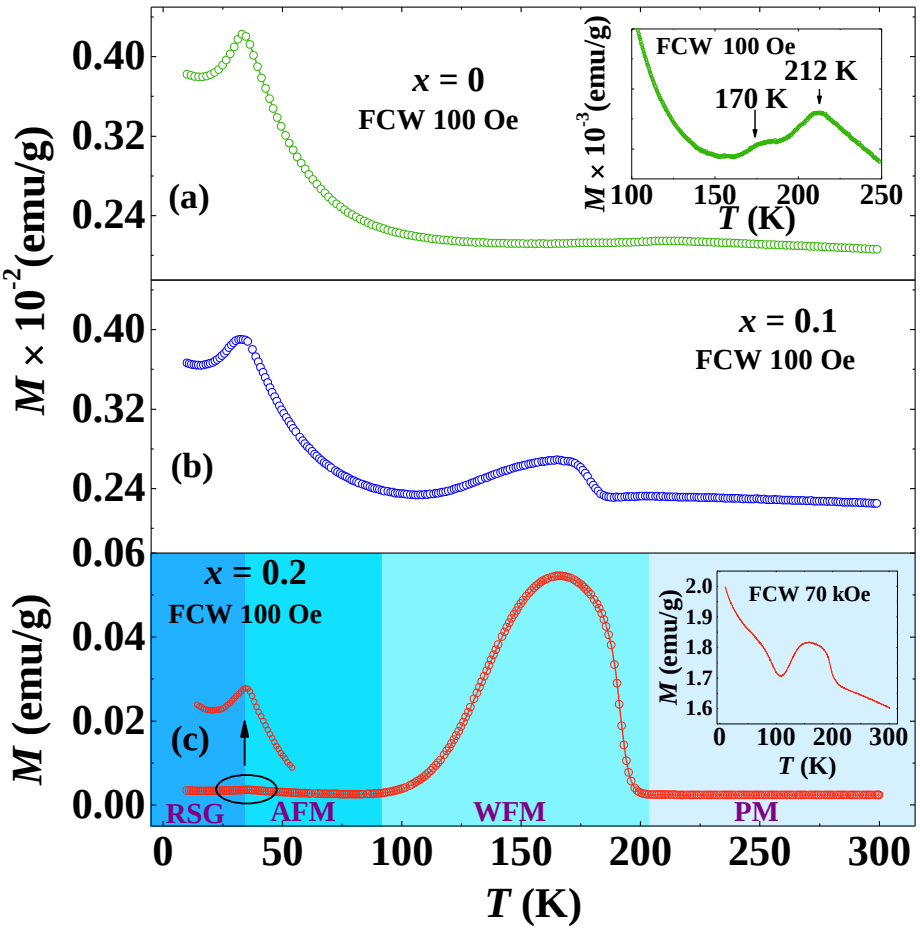

Figure 3.12 (a-c) Temperature dependent magnetization measured with a filed-cooled-warming condition under a magnetic field of 100 Oe for x = 0, 0.1 and 0.2, respectively. Inset of (a) shows the magnified view of the magnetization of x = 0.The left inset of (c) shows magnified view of the magnetization of x = 0.2 at low temperature, while right inset shows the magnetization with field-cooled-warming under a magnetic field of 70 kOe.

Further, we have measured magnetization for x = 0.2 sample under field-cooled-cooling (FCC) with a magnetic field of 100 Oe, where the magnetization data was recorded during cooling in the presence of applied magnetic field. In Figure 3.13(a), we have shown both FCC and FCW magnetization of x = 0.2 sample, where a clear thermal hysteresis is observed between these two magnetizations, which suggests that the WFM-AFM transition is first order in nature. We have used the Banerjee criterion to further confirm the first order nature of this transition by analyzing magnetization data [50,51]. According to Banerjee criterion, a first order magnetic phase transition is accompanied by a negative slope in H/M *vs.* M^2 plots around the transition temperature. We have measured magnetic field dependent magnetization at several temperatures and in Figure 3.13(b), H/M *vs.* M^2 plots at different temperatures are shown. A clear negative slope of

these curves is observed around the WFM-AFM transition temperature and thus confirms the first order nature of this transition.

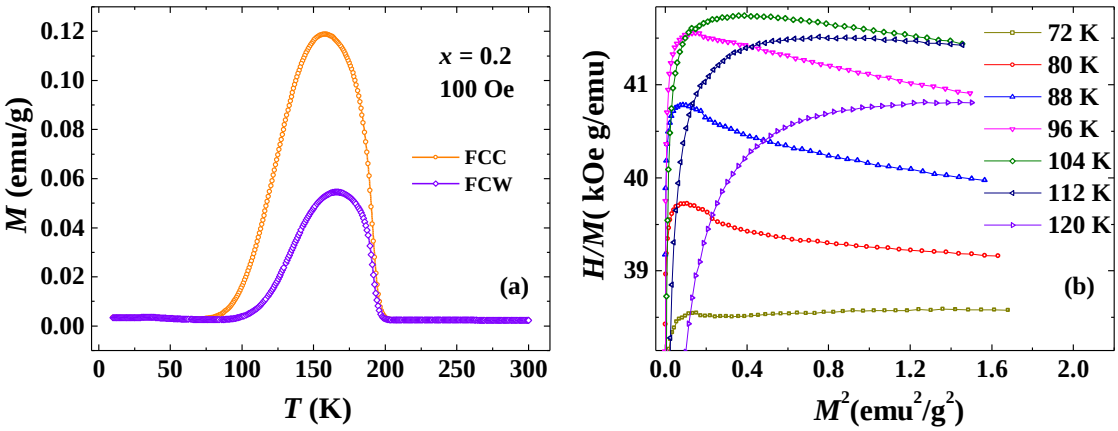

Figure 3.13 (a) Temperature dependent field-cooled-cooling and field-cooled-warming magnetization for x = 0.2 sample measured under a magnetic field of 100 Oe. (b) H/M vs. M^2 plots at different temperatures.

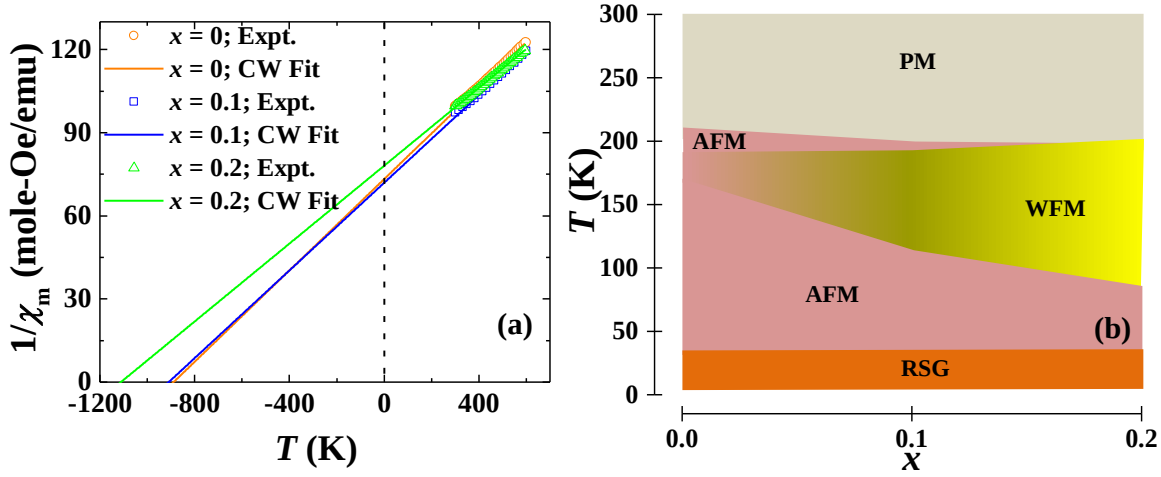

Figure 3.14 (a) Curie-Weiss fit of $1/\chi_m$ *vs.* T data for all the samples. (b) Magnetic phase diagram of $Bi_{1-x}Sm_xMnFe_2O_6$ (x = 0, 0.1 and 0.2).

Similar to the parent compound, a short-range interaction is observed above T_N in Sm^{3+} substituted samples, as indicated by the deviation from Curie-Weiss behavior of $1/\chi_m$ *vs.* T plots up to 450 K. We have fitted the high temperature (450 K - 600 K) magnetization data well above T_N with the Curie-Weiss law and the results are shown in Figure 3.14(a). The parameters obtained from the fit are given in Table 1.4. For x = 0.2,

the Curie-Weiss temperature (θ_{CW}) increases to -1111 K and the frustration parameter (f) becomes 5.52, which is higher than that of parent compound. This indicates that the substitution of Sm^{3+} results more frustrated magnetic interactions. Similar to the parent compound, for x = 0.1, the experimental effective paramagnetic moment (μ_{exp}) remains very close to the calculated value (μ_{cal}), but for x = 0.2, μ_{exp} is found to be slightly higher than μ_{cal}.

Table 1.4 Magnetic parameters obtained from the Curie-Weiss fit of $1/\chi_m$ *vs.* T data at high temperatures of $Bi_{1-x}Sm_xMnFe_2O_6$ (x = 0, 0.1 and 0.2)

x	T_N (K)	θ_{CW} (K)	$f = \lvert\theta_{CW}\rvert/T_N$	μ_{cal} (μ_B/f.u.)	μ_{exp} (μ_B/f.u.)
0	212	-890	4.20	9.69	9.89
0.1	204	-910	4.46	9.71	10.10
0.2	201	-1111	5.52	9.72	10.71

3.3.2.3 Magnetic phase diagram of $Bi_{1-x}Sm_xMnFe_2O_6$ ($0 \le x \le 0.2$)

Based on the temperature and magnetic field dependent magnetization measurements, we have shown the magnetic phase diagram of $Bi_{1-x}Sm_xMnFe_2O_6$ ($0 \le x \le 0.2$) in Figure 3.14(b). The different magnetic states are shown with different colors. In the phase diagram, it can be clearly seen the emergence of weak ferromagnetic region with increasing Sm^{3+} content in a parent antiferromagnetic compound. However, the re-entrant spin glass state persists in all the samples. It would be interesting to stabilize the phase with more Sm^{3+} content using other method, such as chemical routes or solid state synthesis technique under high pressure, to know whether the weak ferromagnetic phase become the ground state.

3.3.2.4 Dielectric properties

Figure 3.15 shows temperature dependent dielectric constant of all the samples measured with 50 kHz. With Sm^{3+} substitution, the broad dielectric anomaly shifts to lower temperatures and it occurs at 135 K for x = 0.1 and 72 K for x = 0.2. Similar to the parent compound, the temperature of the dielectric anomaly is independent of frequency, as shown in the inset of Figure 3.15 for x = 0.2 and correspondingly there is no anomaly

in the dielectric loss. This suggests that the dielectric anomaly is not associated with relaxation phenomena.

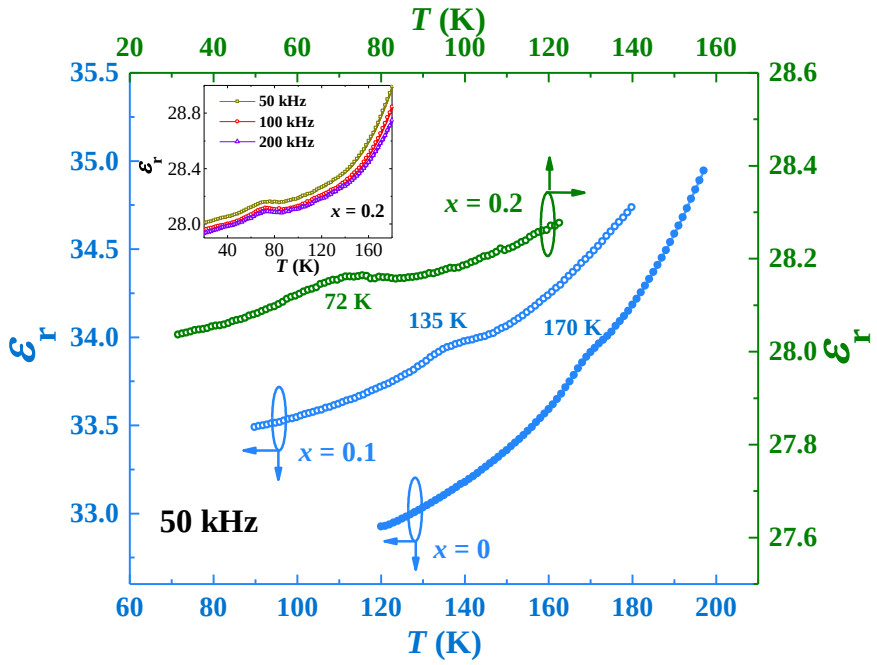

Figure 3.15 Temperature dependent dielectric constant of all the samples measured at 50 kHz. Inset shows the temperature dependent dielectric constant of x = 0.2 measured with different frequencies.

3.3.2.5 Magnetodielectric effect

For further investigations, we have measured magnetic field dependent magnetization, capacitance and resistivity at different temperatures in x = 0.2 sample. In Figure 3.16, we show a correlation between magnetization with magnetocapacitance and magnetic field dependent dc resistivity. Magnetic field dependent magnetization, M (H), measured at several temperatures (T = 72, 130, 165, 185 and 220 K) in different magnetic states are shown in Figure 3.16(a). The linear behavior of M (H) plot at 220 K is consistent with the paramagnetic (PM) state. At T = 130, 165 and 185 K, a clear hysteresis loop but without saturation is observed, which indicates the presence of weak ferromagnetic (WFM) state, whereas a linear behavior observed at 72 K resembles an antiferromagnetic (AFM) behavior. Thus, magnetic field dependent magnetizations along with temperature variation of magnetization confirm that the weak ferromagnetism

appears in x = 0.2 in a wide temperature range (90 K - 201 K). The derivatives of M (H) data with respect to H are shown in Figure 3.16(b), where the peak position corresponds to the slope-change in M (H) curves as seen in Figure 3.16(a).

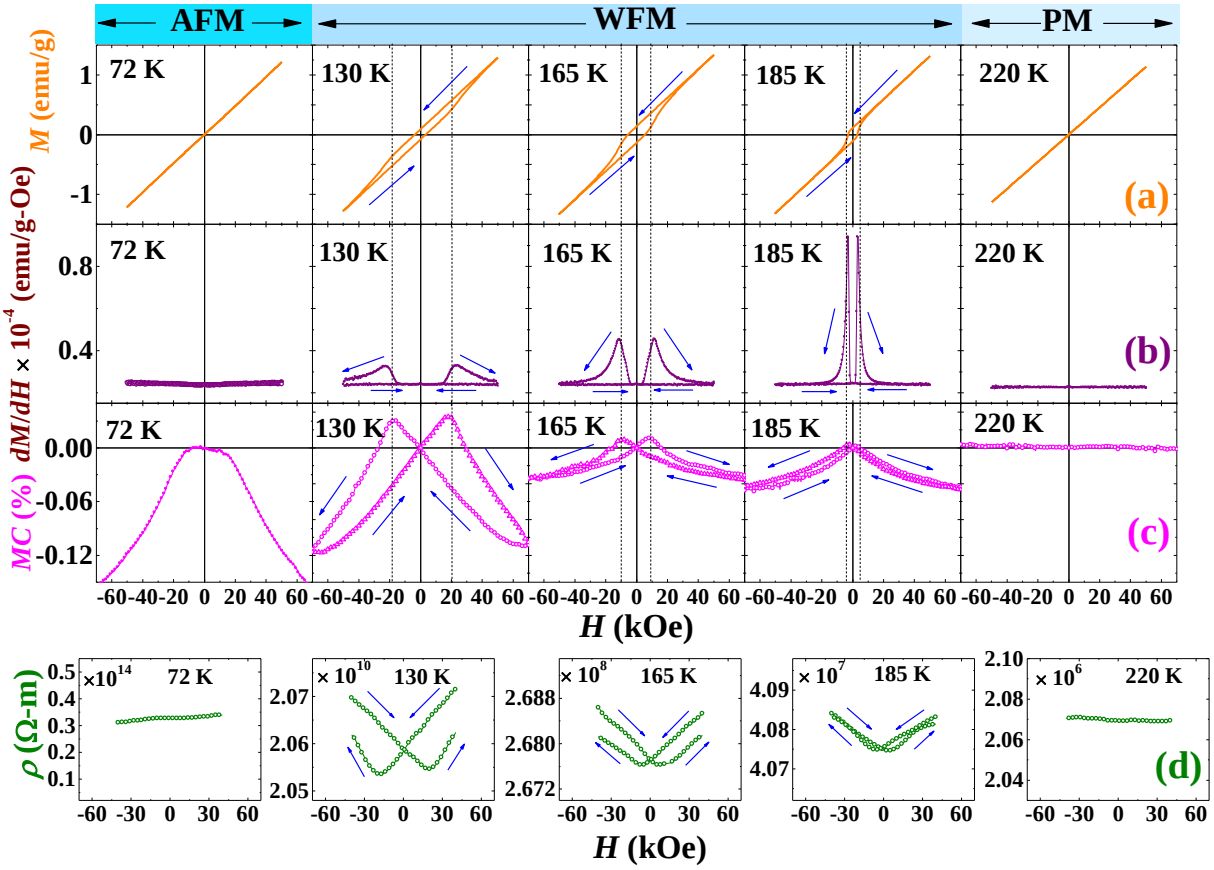

Figure 3.16 (a-d) Magnetic field dependent magnetization (M), dM/dH, magnetocapacitance and resistivity, respectively measured at different temperatures in the sample with x = 0.2.

Magnetocapacitances measured at the same temperatures are shown in Figure 3.16(c). Interesting observation is that, in contrast to the parent compound, where magnetocapacitance is observed only around the magnetic/dielectric anomaly at T^* ~ 170 K, magnetocapacitance in x = 0.2 sample is observed in the entire temperature range below T_N = 201 K. However, the nature and origin of magnetocapacitance are different in the AFM (T < 90 K) and WFM region (90 K < T < 201 K). A non-hysteretic magnetocapacitance is observed in the AFM region (T < 90 K) including the spin-glass state and a maximum value of magnetocapacitance is found around the dielectric anomaly (72 K), whereas the magnetocapacitance is found to exhibit a symmetrical butterfly-

hysteresis loop in the WFM region. It should be noticed that the kink of the butterfly loop in the magnetocapacitance corresponds to the change in slope of M (H) loops or the peak in dM/dH, which are indicated by the vertical dotted lines in Figure 3.16. Thus, the one-to-one-correspondence between the magnetization and magnetocapacitance in the WFM region as well as the presence of magnetocapacitance in the AFM region demonstrate the presence of strong coupling between magnetization and dielectric constant.

However, the observed magnetodielectric effect can be intrinsic or extrinsic [6]. To find out the origin of magnetodielectric effect, we have measured magnetic field dependent electrical resistivity ρ (H) at the same temperatures, which are shown in Figure 3.16(d). Interestingly, we found that resistivity changes with magnetic field in the WFM region indicating the presence of magnetoresistance. However, resistivity is independent of magnetic field below and above the WFM region. Thus, the presence of magnetoresistance is consistent with the weak ferromagnetism. Further, in the WFM region (90 K < T < 201 K), ρ (H) curves show a typical hysteresis loop and corresponding to the kink in magnetocapacitance, there is a minimum in ρ (H) curves which indicates that the butterfly-loop observed in the magnetocapacitance is directly related to the hysteresis in magnetoresistance. On the other hand, the magnetocapacitance observed in the AFM region (T < 90 K) is not associated with the magnetoresistance. These experimental results suggest that the magnetodielectric effect observed in the AFM region originates from intrinsic capacitive contribution, but in the WFM region it is mainly governed by the magnetoresistance effect. Further study is necessary to understand whether there is any role of 3*d*-4*f* interactions between Mn^{3+}/Fe^{3+} and Sm^{3+} moments in inducing the changes in magnetic and electrical properties.

3.3.2.6 *P-E* loop and PUND

Certainly, the magnetic structure of Sm^{3+}-substituted samples are different from that of the parent compound and the resulting magnetic structure may induce ferroelectricity. The pyroelectric current data of x = 0.2 sample show a broad peak with the onset around 170 K (not shown), similar to the parent compound, which we cannot attribute to the ferroelectricity. For further investigation, we have performed *P-E* loop and positive-up-negative-down (PUND) measurements at 150 K in WFM region, which are shown in Figure 3.17(a) and (b), respectively. The conventional *P-E* loop shows a leaky non-ferroelectric behavior and the *P-E* loop obtained from PUND method does not show

any measurable polarization at 150 K. PUND measurements performed at 50 K (below dielectric anomaly) also shows a similar non-ferroelectric behavior (not shown).

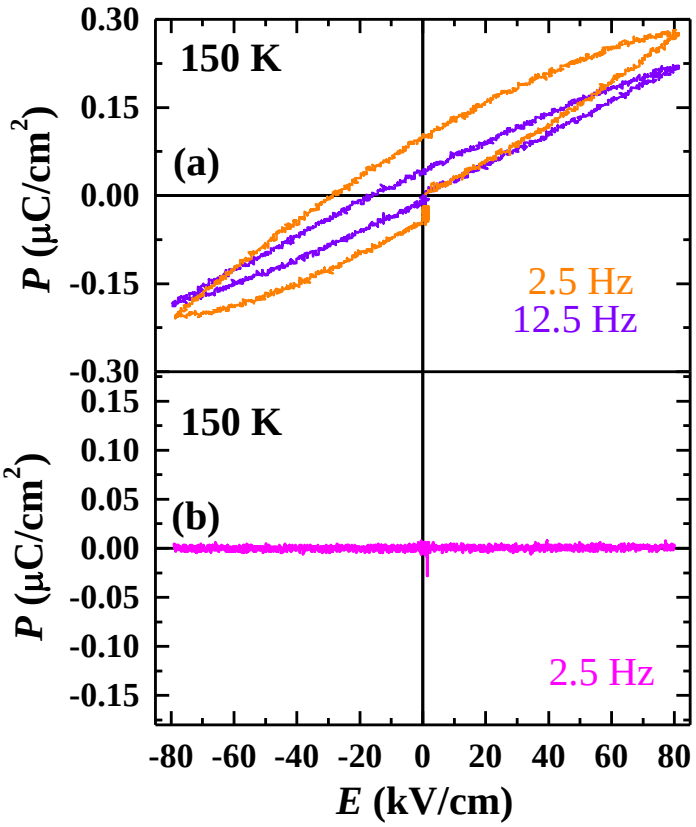

Figure 3.17 (a) Conventional *P-E* hysteresis loop of x = 0.2 measured at 150 K. (b) *P-E* loop obtained from PUND method at 150 K.

3.4 Conclusion

We have investigated detailed magnetic, dielectric and magnetodielectric properties in $Bi_{1-x}Sm_xMnFe_2O_6$ (x = 0.1 and 0.2). Our studies on the parent compound show that a re-entrant spin glass state coexist with the long-range spiral antiferromagnetic ordering below T_P ~ 34 K. We found two distinct irreversibility anomalies, T_{irr} and T_P, in field-cooled and zero-field-cooled magnetization, which follow AT and GT lines, respectively in the *H-T* phase diagram. Magnetization relaxation and ac susceptibility data reveal the presence of spin-cluster in the glassy state. The spin glass state appears due to the disorder arrangements of Fe^{3+} and Mn^{3+} spins at two different crystallographic sites in such a complex crystal structure. Further, we found a magnetic anomaly around T^* ~ 170 K, where a dielectric anomaly with a significant magnetocapacitance is observed,

indicating the presence of magnetodielectric effect. We have shown that the observed magnetodielectric effect is intrinsic in nature. Pyroelectric current and positive-up-negative-down measurements confirm that these anomalies are not associated with ferroelectricity. On the other hand, the substitution of Sm^{3+} in $Bi_{1-x}Sm_xMnFe_2O_6$ (x = 0.1 and 0.2) induces drastic changes in magnetic and dielectric properties. Upon 20% Sm^{3+} substitution, a weak ferromagnetic state is induced in a broad temperature range (90 K - 201 K), below which it undergoes to an antiferromagnetic state. The broad dielectric anomaly is found to shift to lower temperature with increasing x. In x = 0.2, an intrinsic magnetodielectric effect is observed in the antiferromagnetic region with a maximum around the dielectric anomaly, whereas an extrinsic magnetodielectric effect is observed in the weak ferromagnetic region with a butterfly-hysteresis loop, which is attributed to the presence of magnetoresistance, that is found only in the weak ferromagnetic region. Thus, depending on temperature, the magnetodielectric effect is governed by intrinsic and extrinsic contributions in x = 0.2 sample. Our results demonstrate that the present system is an example of having different origin of magnetodielectric effect in the same material. However, Sm^{3+} substitution in $Bi_{1-x}Sm_xMnFe_2O_6$ (x = 0.1 and 0.2) does not induce ferroelectricity.

References

[1] G. Smolenskiĭ and I. Chupis, *Sov. Phys. Usp.* **25,** 475 (1982).

[2] J. Wang, J. Neaton, H. Zheng, V. Nagarajan, S. Ogale, B. Liu, D. Viehland, V. Vaithyanathan, D. Schlom, and U. Waghmare, *Science* **299,** 1719 (2003).

[3] A. M. Dos Santos, S. Parashar, A. Raju, Y. Zhao, A. Cheetham, and C. Rao, *Solid State Commun.* **122,** 49 (2002).

[4] R. Seshadri and N. A. Hill, *Chem. Mater.* **13,** 2892 (2001).

[5] A. A. Belik, *J. Solid State Chem.* **195,** 32 (2012).

[6] G. Catalan, *Appl. Phys. Lett.* **88,** 102902 (2006).

[7] G. Lawes, A. P. Ramirez, C. M. Varma, and M. A. Subramanian, *Phys. Rev. Lett.* **91,** 257208 (2003).

[8] G. Lawes, T. Kimura, C. Varma, M. Subramanian, N. Rogado, R. Cava, and A. Ramirez, *Prog. Solid State Chem.* **37,** 40 (2009).

[9] P. Mandal, V. S. Bhadram, Y. Sundarayya, C. Narayana, A. Sundaresan, and C. Rao, *Phys. Rev. Lett.* **107,** 137202 (2011).

[10] T. Bonaedy, Y. Koo, K. Sung, and J. Jung, *Appl. Phys. Lett.* **91,** 132901 (2007).

[11] T. Yang, A. M. Abakumov, J. Hadermann, G. Van Tendeloo, I. Nowik, P. W. Stephens, J. Hemberger, A. A. Tsirlin, K. V. Ramanujachary, and S. Lofland, *Chem. Sci.* **1,** 751 (2010).

[12] A. M. Abakumov, A. A. Tsirlin, J. M. Perez-Mato, V. Petříček, H. Rosner, T. Yang, and M. Greenblatt, *Phys. Rev. B* **83,** 214402 (2011).

[13] D. Batuk, C. De Dobbelaere, A. A. Tsirlin, A. M. Abakumov, A. Hardy, M. K. Van Bael, M. Greenblatt, and J. Hadermann, *Mater. Res. Bull.* **48,** 2993 (2013).

[14] H. Rietveld, *J. Appl. Crystallogr.* **2,** 65 (1969).

[15] J. Rodriguez-Carvajal, in *FULLPROF: a program for Rietveld refinement and pattern matching analysis*, 1990 (Toulouse, France:[sn]).

[16] M. Fukunaga and Y. Noda, *J. Phys. Soc. Jpn.* **77,** 064706 (2008).

[17] A. Ramirez, *Annu. Rev. Mater. Sci.* **24,** 453 (1994).

[18] J. De Almeida and D. J. Thouless, *J. Phys. A: Math. Gen.* **11,** 983 (1978).

[19] M. Gabay and G. Toulouse, *Phys. Rev. Lett.* **47,** 201 (1981).

[20] N. Khan, A. Midya, P. Mandal, and D. Prabhakaran, *J. Appl. Phys.* **113,** 183909 (2013).

[21] Z. Fu, Y. Zheng, Y. Xiao, S. Bedanta, A. Senyshyn, G. G. Simeoni, Y. Su, U. Rücker, P. Kögerler, and T. Brückel, *Phys. Rev. B* **87,** 214406 (2013).

[22] J. Lago, S. J. Blundell, A. Eguia, M. Jansen, and T. Rojo, *Phys. Rev. B* **86,** 064412 (2012).

[23] M. K. Singh, R. S. Katiyar, W. Prellier, and J. Scott, *J. Phys. Condens. Matter* **21,** 042202 (2008).

[24] S. Chatterjee and A. K. Nigam, *Phys. Rev. B* **66,** 104403 (2002).

[25] J. A. Mydosh, *Spin glasses* (Taylor and Francis, 1993).

[26] P. C. Hohenberg and B. I. Halperin, *Rev. Mod. Phys.* **49,** 435 (1977).

[27] K. Binder and A. P. Young, *Rev. Mod. Phys.* **58,** 801 (1986).

[28] A. Malinowski, V. L. Bezusyy, R. Minikayev, P. Dziawa, Y. Syryanyy, and M. Sawicki, *Phys. Rev. B* **84,** 024409 (2011).

[29] R. Mathieu, M. Hudl, and P. Nordblad, *EPL (Europhysics Letters)* **90,** 67003 (2010).

[30] K. Jonason, E. Vincent, J. Hammann, J. P. Bouchaud, and P. Nordblad, *Phys. Rev. Lett.* **81,** 3243 (1998).

[31] P. Koželj, S. Jazbec, S. Vrtnik, A. Jelen, J. Dolinšek, M. Jagodič, Z. Jagličić, P. Boulet, M. C. de Weerd, J. Ledieu, J. M. Dubois, and V. Fournée, *Phys. Rev. B* **88,** 214202 (2013).

[32] D. Choudhury, P. Mandal, R. Mathieu, A. Hazarika, S. Rajan, A. Sundaresan, U. V. Waghmare, R. Knut, O. Karis, P. Nordblad, and D. D. Sarma, *Phys. Rev. Lett.* **108,** 127201 (2012).

[33] A. Bhattacharyya, S. Giri, and S. Majumdar, *Phys. Rev. B* **83,** 134427 (2011).

[34] S. Chattopadhyay, S. Giri, and S. Majumdar, *EPL (Europhysics Letters)* **98,** 27004 (2012).

[35] R. S. Freitas, L. Ghivelder, F. Damay, F. Dias, and L. F. Cohen, *Phys. Rev. B* **64,** 144404 (2001).

[36] R. V. Chamberlin, *J. Appl. Phys.* **57,** 3377 (1985).

[37] M. Ulrich, J. García-Otero, J. Rivas, and A. Bunde, *Phys. Rev. B* **67,** 024416 (2003).

[38] F. Rivadulla, M. A. López-Quintela, and J. Rivas, *Phys. Rev. Lett.* **93,** 167206 (2004).

[39] Y.-k. Tang, Y. Sun, and Z.-h. Cheng, *Phys. Rev. B* **73,** 012409 (2006).

[40] K. Manna, D. Samal, A. Bera, S. Elizabeth, S. Yusuf, and P. A. Kumar, *J. Phys. Condens. Matter* **26,** 016002 (2013).

[41] P.-z. Wong, S. von Molnar, T. T. M. Palstra, J. A. Mydosh, H. Yoshizawa, S. M. Shapiro, and A. Ito, *Phys. Rev. Lett.* **55,** 2043 (1985).

[42] H. Yoshizawa, S. Mitsuda, H. Aruga, and A. Ito, *Phys. Rev. Lett.* **59,** 2364 (1987).

[43] G. M. Rotaru, B. Roessli, A. Amato, S. N. Gvasaliya, C. Mudry, S. G. Lushnikov, and T. A. Shaplygina, *Phys. Rev. B* **79,** 184430 (2009).

[44] W. Kleemann, V. V. Shvartsman, P. Borisov, and A. Kania, *Phys. Rev. Lett.* **105,** 257202 (2010).

[45] S. Karmakar, S. Taran, E. Bose, B. K. Chaudhuri, C. P. Sun, C. L. Huang, and H. D. Yang, *Phys. Rev. B* **77,** 144409 (2008).

[46] S. Giri, A. Poddar, and T. Nath, *AIP Advances* **1,** 032110 (2011).

[47] M. Ali, P. Adie, C. H. Marrows, D. Greig, B. J. Hickey, and R. L. Stamps, *Nat. Mater.* **6,** 70 (2007).

[48] T. Kimura, S. Kawamoto, I. Yamada, M. Azuma, M. Takano, and Y. Tokura, *Phys. Rev. B* **67,** 180401 (2003).

[49] Y. Kohara, Y. Yamasaki, Y. Onose, and Y. Tokura, *Phys. Rev. B* **82,** 104419 (2010).

[50] B. Banerjee, *Phys. Lett.* **12,** 16 (1964).

[51] J. Mira, J. Rivas, F. Rivadulla, C. Vázquez-Vázquez, and M. A. López-Quintela, *Phys. Rev. B* **60,** 2998 (1999).

Chapter 4

Linear magnetoelectric effect in *A*-site magnetic spinels, Co_3O_4 and $CoAl_2O_4$*

Summary

The present chapter deals with the experimental discovery of linear magnetoelectric effect in two different *A*-site magnetic spinels, Co_3O_4 and $CoAl_2O_4$, which is explained based on the mechanism of local noncentrosymmetry of the magnetic ions. In case of Co_3O_4, a clear long-range collinear antiferromagnetic ordering is observed below T_N ~ 30 K. Magnetic field induced dielectric anomaly and electric polarization below T_N confirm the presence of linear magnetoelectric effect. On the other hand, the magnetic ground state of $CoAl_2O_4$ has been a controversial issue. The ground state was suggested to be either a spiral spin-liquid state or a long-range collinear antiferromagnetic ordered state. Using different disordered samples of $Co_{1-x}Al_x[Al_{2-x}Co_x]O_4$ (x = 0.05, 0.07, 0.11 and 0.14), it is found that the samples with less disorder ($x \leq 0.11$) exhibit linear magnetoelectric effect, which indicates that the magnetic ground state is a long-range collinear antiferromagnetic ordered state. In contrast, the sample with x = 0.14 exhibits a spin glass state without magnetoelectric effect. These experimental finding are further supported by Monte Carlo calculations.

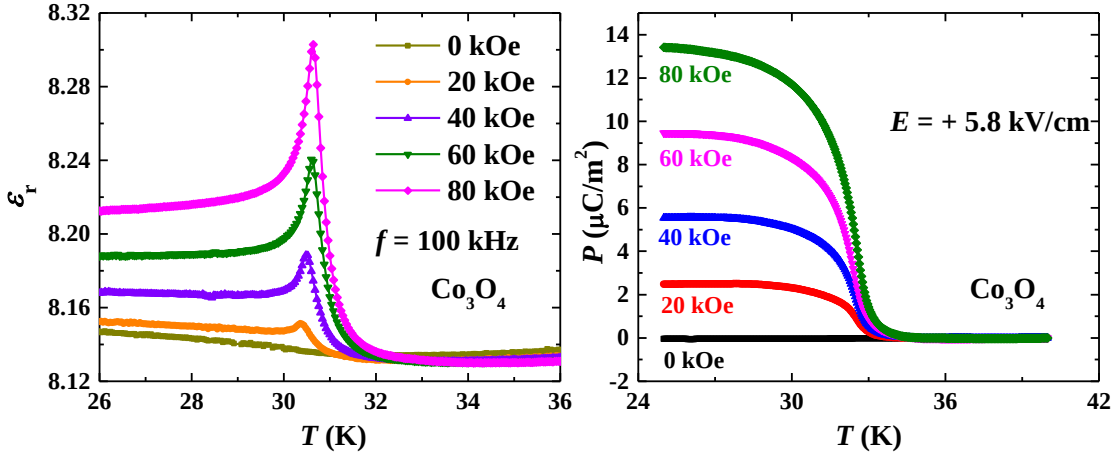

*Papers based on this work are published in *Phys. Rev. B*, **94**, 14428 (2016) and *Phys. Rev. B*, **95**, 94404 (2017), © 2016 and 2017 by the American Physical Society.

4.1 Introduction

Magnetoelectric materials, in which electric polarization is induced by a magnetic field and magnetization is induced by an electric field, find many applications in modern spintronic technology, as discussed in Chapter 1. Apart from the application point of view, magnetoelectric materials have attracted much attention to the research community in the last few decades due to its interesting mechanisms, which help in understanding the fundamental physics of materials. Recently, a microscopic model suggests that a single-ion contribution of the magnetic ions, located at the local noncentrosymmetric sites, which have spin-dependent electric dipole moments, can cause magnetoelectric effect [1]. This proposed model can explain properly the magnetoelectric effect in some well-known compounds, such as $MnWO_4$, $MnPS_3$, and $LiNiPO_4$, in which the magnetic ions are located in local noncentrosymmetric crystal environments. Using this microscopic model, it has been proposed that the *A*-site magnetic spinels possessing long-range collinear antiferromagnetic ordered state may exhibit a linear magnetoelectric effect [2].

In a normal cubic spinel $A^{2+}[B_2^{3+}]X_4$, A^{2+} ions occupy tetrahedral site and form a lattice similar to the diamond lattice and B^{3+} ions remain in octahedral site and form a pyrochlore lattice. The diamond lattice of *A*-site magnetism spinel with magnetic ions at (0, 0, 0) and (1/4, 1/4, 1/4) is composed of two interpenetrating face-centered cubic (fcc) lattices. Thus, as shown in Figure 4.1, two exchange paths are possible, namely, the nearest-neighbor interaction (J_1), which couples ions between two fcc lattices and next-nearest-neighbor interaction (J_2), which couples ions within same fcc lattice. Four nearest-neighbor interaction (J_1) and twelve next-nearest-neighbor interaction (J_2) are present in a unit cell of the diamond lattice of the *A*-site magnetic spinel. The magnetic diamond lattice with only nearest-neighbor interaction (J_1) is not frustrated and results a collinear antiferromagnetic ordering. However, the magnetic interaction becomes frustrated when J_2 is significant, which suppresses the long-range collinear antiferromagnetic ordering and results a spin liquid ground state. From the theoretical calculation, it has been reported that for any *A*-site magnetic spinel, if $0 < J_2/J_1 < 1/8$, the magnetic ground state is a collinear Neel antiferromagnetic ordered state, while $J_2/J_1 > 1/8$ results a degenerate spiral spin liquid ground state [3]. This theoretical proposed model is consistent with the experimental observation on few spinel compounds. For example, Co_3O_4 and $MnAl_2O_4$ have a ratio of $J_2/J_1 \sim 0.019$ and 0.09, respectively and

exhibit a well-defined long-range collinear antiferromagnetic ordering. In contrast, $MnSc_2S_4$ has $J_2/J_1 \sim 0.85$ and exhibits a spiral spin liquid ground state [4-8].

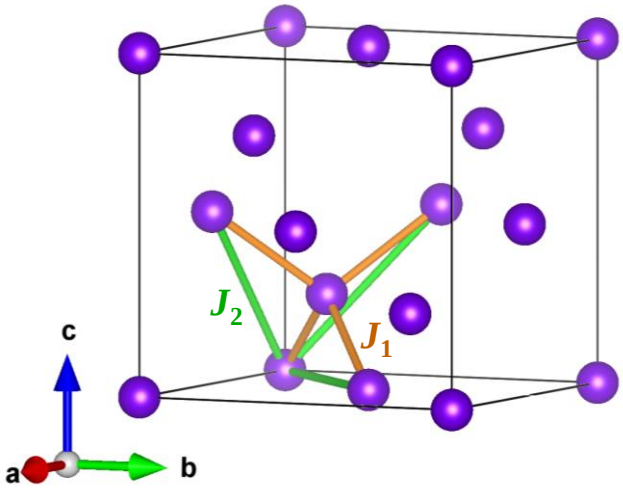

Figure 4.1 Diamond lattice formed by the *A*-site magnetic ions in the normal spinel $A^{2+}[B_2^{3+}]X_4$. The nearest-neighbor (J_1) and next-nearest-neighbor (J_2) exchange interactions are shown.

There exists another *A*-site magnetic spinel, $CoAl_2O_4$, which has a very interesting magnetic property. The true nature of the magnetic ground state of $CoAl_2O_4$ at low temperature is not very clear and there is no consensus in the literature. This is because of the fact that the strengths of the exchange interactions in $CoAl_2O_4$ is such that, the ratio of J_2/J_1 (~ 0.109) is close to the critical ratio of 1/8, which separates the collinear antiferromagnetic and the spiral spin liquid states [3,4]. Thus, many contradicting theoretical as well as experimental results have been reported regarding the magnetic ground state of $CoAl_2O_4$. Further, in addition to the competing exchange interactions, the anti-site disorder (x) between *A* and *B* site in $Co_{1-x}Al_x(Al_{2-x}Co_x)O_4$ also plays a major role in determining the magnetic ground of this compound [9].

In an earlier report, a collinear antiferromagnetic ordering of Co^{2+} spins has been proposed from the observation of a weak (200) magnetic Bragg peak in neutron diffraction pattern recorded at 4.2 K on a polycrystalline sample of $Co_{1-x}Al_x(Al_{2-x}Co_x)O_4$ with site disorder $x = 0.05$ [7]. The antiferromagnetic ordering of Co^{2+} spins in $CoAl_2O_4$ has been proposed to be similar to that of Co_3O_4. In a recent report by Roy *et al.*, a similar collinear antiferromagnetic ordering of Co^{2+} has been suggested using nuclear magnetic

resonance and neutron diffraction experiments performed on a polycrystalline sample with x = 0.057 [10]. In contrast, based on inelastic neutron diffraction experiments on a sample with x = 0.07- 0.08, it has been shown that $J_2/J_1 \sim 0.17 > 1/8$ indicating the presence of spiral spin liquid state with a very strong but short-range spin interactions [5]. The presence of spin liquid like state is also supported by the results of the neutron diffraction experiments on single crystal with disorder x = 0.08 [4]. On the other hand, MacDougall *et al.* reported that $CoAl_2O_4$ possesses a first order magnetic phase transition, where a true long-range order is inhibited by the frozen magnetic domain walls, which cannot grow even at lowest temperature, using single crystal neutron diffraction experiments on a sample with x = 0.02 [11]. Further, Tristan *et al.* have demonstrated the presence spin glass state using magnetic, electron spin resonance and heat capacity measurements on a sample with disorder x = 0.08, where the spin glass state is caused by the strong geometric and spin frustration [12].

In this chapter, we discuss the discovery of linear magnetoelectric effect in two different *A*-site magnetic spinels, Co_3O_4 and $CoAl_2O_4$ and address the magnetic ground state of the latter compound. In case of Co_3O_4, which has a clear long-range antiferromagnetic ordering (T_N = 30 K), magnetic field induced dielectric anomaly is found around T_N, where an emergence of electric polarization under magnetic field is observed. The electric polarization varies linearly with magnetic field, confirming the presence of linear magnetoelectric effect. On the other hand, the magnetoelectric studies on $CoAl_2O_4$ with different degrees of anti-site disorder show that the less disordered $CoAl_2O_4$ exhibits a linear magnetoelectric effect, while the highest disordered sample exhibits a spin glass behavior without magnetoelectric effect. Thus, the observation of magnetoelectric effect, along with the dc and ac magnetization, heat capacity measurements and Monte Carlo simulations, suggests that the magnetic ground state of $CoAl_2O_4$ with less disorder ($x \leq 0.11$) is a long-range collinear antiferromagnetic state.

4.2 Experimental section

Commercially available polycrystalline Co_3O_4 was pressed into pellets and heated at 800 °C for 24 hour in air and then the sample was cooled to room temperature with a cooling rate of 1 °C/min. On the other hand, polycrystalline samples of $CoAl_2O_4$ were synthesized by the conventional high temperature solid state reaction method. Co_3O_4 and Al_2O_3 were mixed according to the cation stoichiometry and heated at 1000 °C (for 12

hour) and 1050 °C (for 12 hour) with intermittent grindings. The obtained powders were pressed into pellets and sintered at 1130 °C for 24 hour in air. The different cooling rates, 0.2 °C/min, 1 °C/min and 2 °C/min, were adapted to prepare different anti-site disordered samples. The highest disordered sample was prepared by a quenching process. Temperature dependent magnetization data were recorded under zero-field-cooled (ZFC) and field-cooled (FC) conditions with a heating rate of 3 K/min. In ZFC condition, the sample was cooled to lowest temperature without magnetic field and magnetization was recorded during heating under an applied magnetic field. On the other hand, in case of FC condition, sample was cooled under an applied magnetic field and magnetization was measured during heating under the same magnetic field. AC susceptibility and heat capacity were measured in PPMS. To study magnetoelectric effect, dielectric constant and pyroelectric current were measured in the presence of various magnetic fields. In pyroelectric current measurements, the magnetoelectric poling were performed across the magnetic transition temperature under electric fields of E_P = + 5.8 kV/cm and + 6.5 kV/cm for Co_3O_4 and $CoAl_2O_4$, respectively and pyroelectric current was recorded with a heating rate of 8 K/min. DC-biased current measurements on $CoAl_2O_4$ samples were carried out in the presence of an electric field of E_{Bias} = + 6.5 kV/cm and a magnetic field of 80 kOe with a heating rate of 8 K/min. The details of these measurements are discussed in Chapter 2.

4.3 Results and discussion

4.3.1 Results on Co_3O_4

4.3.1.1 Crystal structure

The room temperature X-ray diffraction pattern is shown in Figure 4.2(a). The Rietveld refinement was performed with the space group $Fd\bar{3}m$ and the obtained crystal structure is displayed in Figure 4.2(b). Co_3O_4 crystallizes in a normal cubic spinel structure, which consists of a diamond lattice formed by the Co^{2+} ions located at tetrahedral sites and a pyrochlore lattice composed of Co^{3+} ions occupying octahedral sites, as shown in Figure 4.2(c-d). The structural parameters are given in Table 4.1. The high values of the isotropic thermal parameters (B_{iso}) of cobalt atoms could be due to the effect of fluorescence.

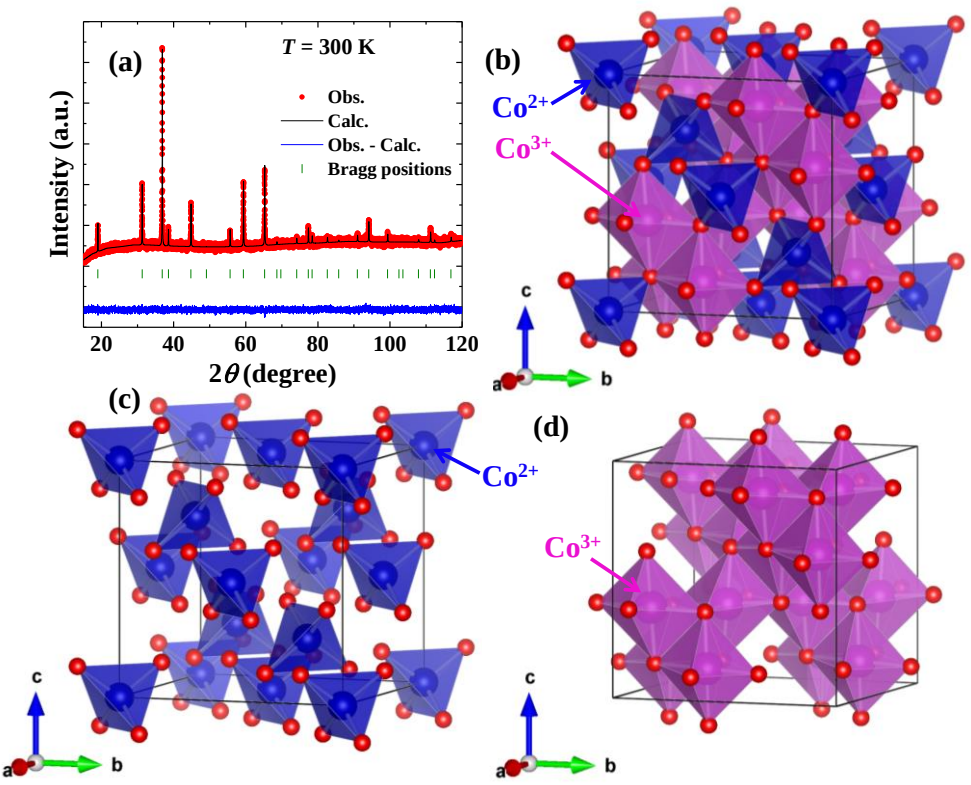

Figure 4.2 (a) Room temperature X-ray diffraction data of Co_3O_4. (b) The cubic spinel crystal structure of Co_3O_4. (c, d) The diamond lattice and pyrochlore lattice formed by the Co^{2+} and Co^{3+} ions, respectively.

Table 4.1 Structural parameters of Co_3O_4 obtained from Rietveld refinements of the room temperature X-ray diffraction data with *Fd*-3*m* space group

a = 8.0851 (3) Å, χ^2 = 1.08

Atom	Wyckoff position	*x*	*y*	*z*	B_{iso} (Å^2)	Occupancy
Co	8*a*	1/8	1/8	1/8	1.48 (9)	1
Co	16*d*	1/2	1/2	1/2	1.30 (8)	1
O	32*e*	0.2614 (4)	0.2614 (4)	0.2614 (4)	1.00	1

It is worth mentioning here that the crystal field splits the degeneracy of five *d* orbitals, as shown in Figure 4.3 [13,14]. Under octahedral crystal field, the *d* orbitals are split into two sets, one is triply degenerate t_{2g} (d_{xy}, d_{yz} and d_{xz}) orbitals and another is doubly degenerate e_g (d_z^2 and $d_{x^2-z^2}$) orbitals. The energy difference between the t_{2g} and e_g

sets of orbitals is Δ_o, which depends on the repulsion by the bonding electrons on *d* electrons. The orientation of the t_{2g} orbitals is away from the bonding direction between the metal and ligands resulting less interaction between bonding electrons and 3*d* electrons and thus the energy of t_{2g} orbitals will be lower (by an amount of $-\frac{2}{5}\Delta_o$). On the other hand, since the e_g orbitals are oriented along the bonds, the repulsion between bonding and *d* electrons will be more and as a result the energy of e_g level is higher by an amount of $\frac{3}{5}\Delta_o$. A similar but opposite picture of degeneracy breaking of the five *d* orbitals is observed in tetrahedral crystal fields, as shown in Figure 4.3. In the present case, Co^{3+} ions has $3d^6$ electronic configuration and occupy octahedral site. As shown in the Figure 4.3, the gain in orbital energy in low spin state compared to high spin state is $2\Delta_o$. Thus, Co^{3+} ions in the octahedral site in Co_3O_4 remain in the low spin state without unpaired electrons, indicating that Co^{3+} ions are nonmagnetic. On the other hand, Co^{2+} ions in the tetrahedral site remains in high spin state with three unpaired electrons and thus Co^{2+} ions are magnetic in nature [13,15].

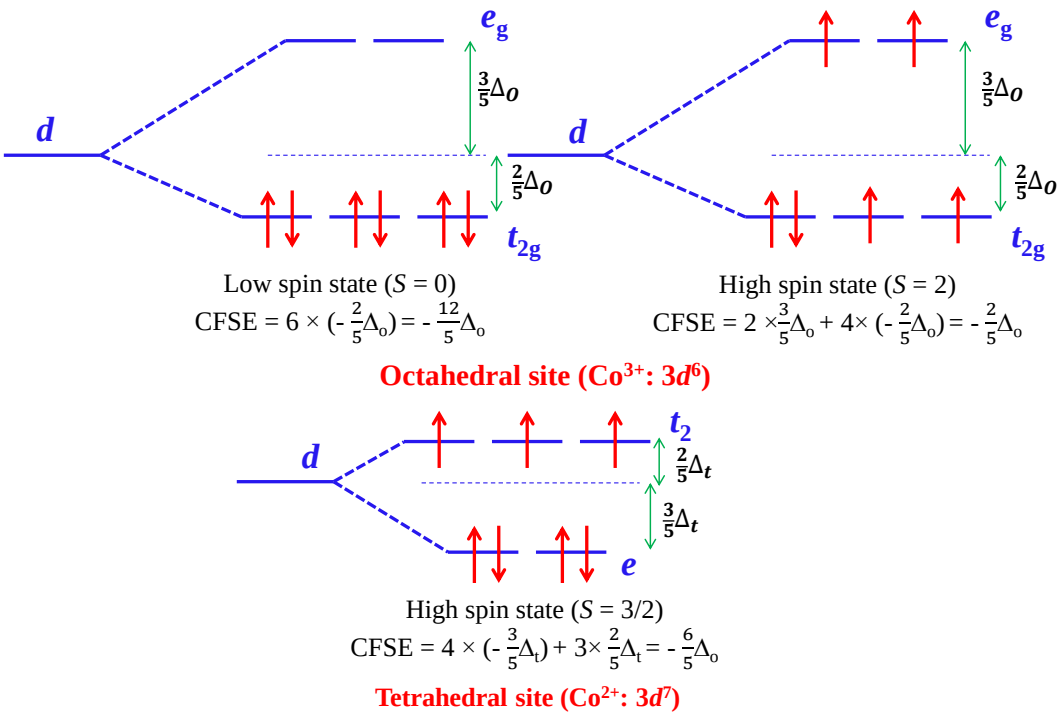

Figure 4.3 Crystal field splitting of the *d* orbitals of Co^{2+} ions in tetrahedral site and Co^{3+} ions in octahedral sites.

4.3.1.2 DC magnetization and heat capacity

Temperature variation of magnetization data M (T) measured under a field-cooled (FC) condition with a magnetic field of 1 kOe is shown in Figure 4.4(a). A broad peak is observed around T_N = 30 K in M (T), where a sharp peak is found in dM/dT, which is shown in the inset of Figure 4.4(a). The heat capacity data C_P (T) exhibits a clear λ-type peak around 30 K (Figure 4.4(b)), which indicates the long-range antiferromagnetic ordering of Co^{2+} spins. A linear behavior is observed in magnetic field dependent magnetization data recorded at 2 K, as shown in the inset of Figure 4.4(b), which is consistent with the antiferromagnetic behavior. The inverse susceptibility ($1/\chi_m$) data against temperature is shown in Figure 4.4(a), where the solid lines represent the fit with the Curie-Weiss law in the paramagnetic region. The effective paramagnetic moment (μ_{eff}) obtained from the fit is found to be 4.8 μ_B/Co^{2+}, while the calculated spin-only moment of a free Co^{2+} ion is 3.87 μ_B. This indicates that there is an orbital contribution to the effective moment. The obtained Curie-Weiss temperature (θ_{CW}) is - 90 K, where the negative sign is consistent with the antiferromagnetic interaction and the obtained frustration parameter ($f = |\theta_{CW}|/T_N$) is 3, which suggest that the spin structure in Co_3O_4 is moderately frustrated. The presence of moderate frustration is consistent with the ratio of exchange interactions, $J_2/J_1 \sim 0.019 < 1/8$.

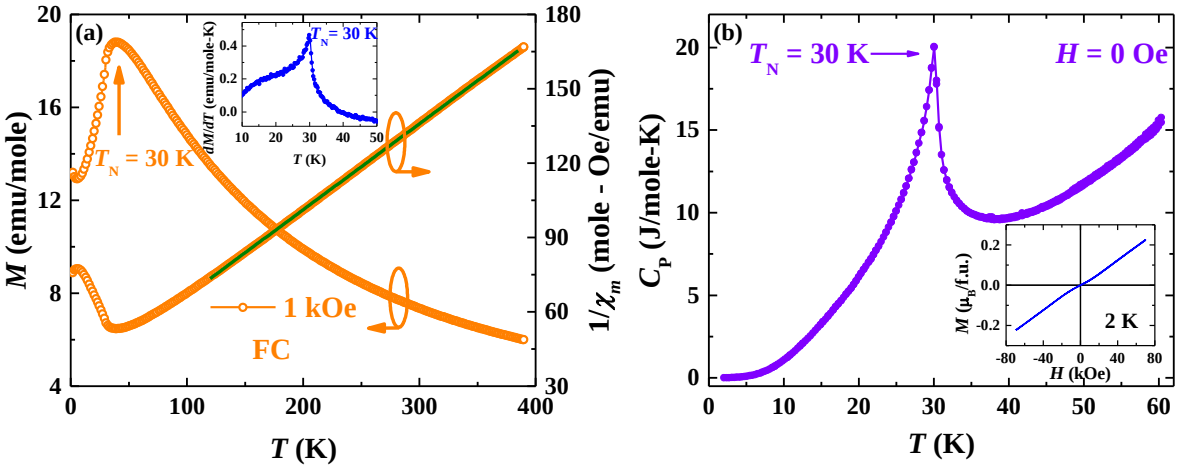

Figure 4.4 (a) Temperature dependent field-cooled (FC) magnetization measured under a magnetic field of 1 kOe (left scale). Curie-Weiss fit (solid line) of $1/\chi_m(T)$ data (right scale). Inset shows dM/dT plot. (b) Temperature dependent heat capacity C_P (T) measured without magnetic field. Inset shows the magnetic field dependent magnetization measured at 2 K.

4.3.1.3 Magnetodielectric effect

The temperature dependence of dielectric constant ε_r (T) measured at 100 kHz under different magnetic fields is shown in Figure 4.5(a). The ε_r (T) does not exhibit any anomaly around T_N under zero-magnetic field. However, a sharp peak appears at T_N under applied magnetic field, suggesting the presence of magnetodielectric effect. Further, as shown in Figure 4.5(a), the peak increases with increasing magnetic fields. In Figure 4.5(b), magnetic field dependent magnetocapacitance, $\left(MC(\%) = \frac{\varepsilon_r(H)-\varepsilon_r(0)}{\varepsilon_r(0)} \times 100\%\right)$ measured at different temperatures is shown. Magnetocapacitance is observed throughout the temperature below T_N and its maximum value (~ 1.8 %) is found around T_N. The origin of magnetodielectric effect in Co_3O_4 can be attributed to the presence of magnetoelectric coupling between the magnetic and electrical order parameters, as discuss in next section.

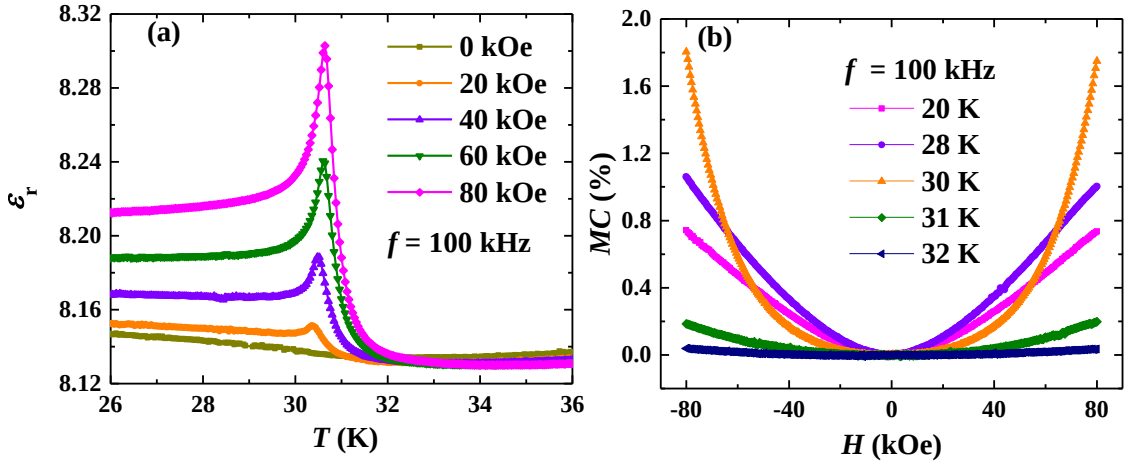

Figure 4.5 (a) Temperature variation of dielectric constant ε_r (T) measured under different magnetic fields. (b) Magnetocapacitance MC (%) at different temperatures.

4.3.1.4 Magnetoelectric effect

Temperature dependent pyroelectric current data measured under an electric field of E = + 4.5 kV/cm and different magnetic fields are shown in the inset of Figure 4.6. It can be seen that, there is no peak in pyroelectric current data under zero magnetic fields. However, a sharp pyroelectric current peak is observed around the antiferromagnetic ordering temperature (T_N = 30 K) under magnetic fields and it increases with increasing

magnetic fields. The electric polarization is calculated by integrating pyroelectric current with measurement time and the obtained result is shown in Figure 4.6. It is clear that the electric polarization appears below long-range antiferromagnetic ordering temperature under applied magnetic field and the value of electric polarization increases with increasing magnetic fields, suggesting the presence of a strong magnetoelectric effect.

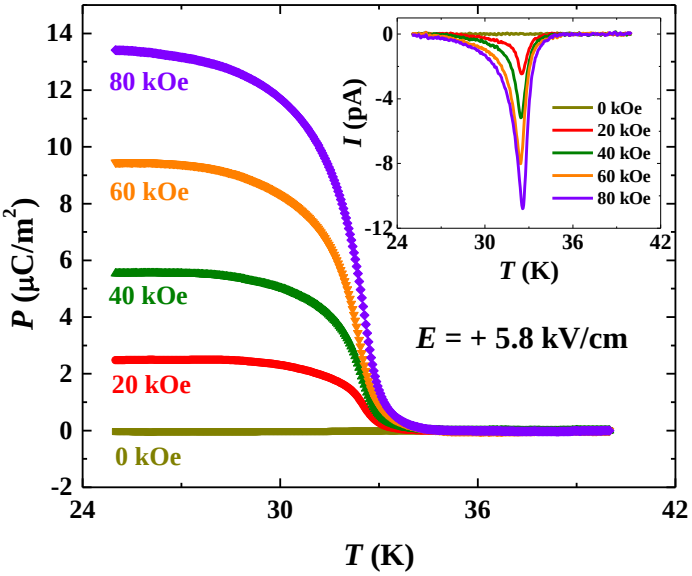

Figure 4.6 Temperature evolution of electric polarization induced by magnetic fields. Inset shows corresponding pyroelectric current data.

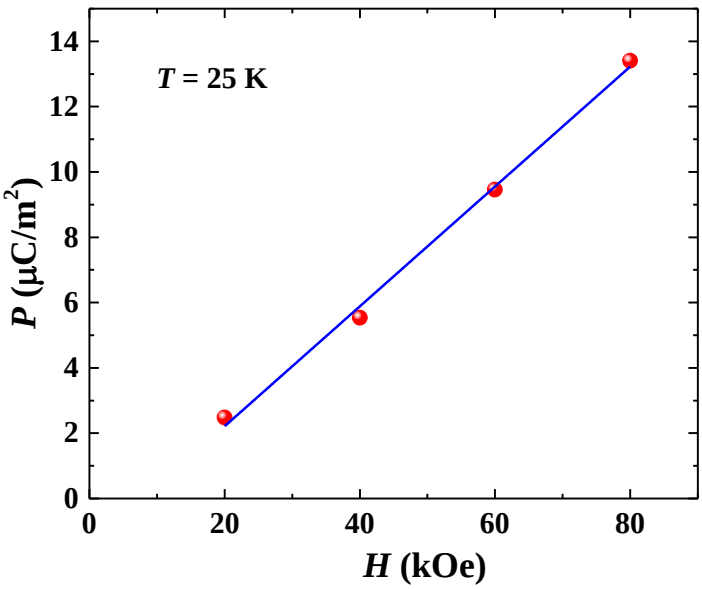

Figure 4.7 The linear behaviour of *P vs. H* data at 25 K.

Magnetic field dependent electric polarization data at 25 K is shown in Figure 4.7. It is evident from this figure that the electric polarization varies linearly with magnetic field, suggesting the linear magnetoelectric effect. The magnetoelectric coefficient is calculated from the slope of the *P vs. H* data, $\alpha = \frac{dP}{dH} = 2.6$ ps/m. The value of α is comparable to that of Cr_2O_3 (α = 2.8 ps/m), but higher than that of another magnetoelectric $NdCrTiO_5$ (α = 0.54 ps/m) [16,17].

4.3.1.5 Magnetic control of electric polarization

Magnetoelectric materials offer a platform for controlling magnetization by electric field and electric polarization by magnetic field. We have performed the pyroelectric current measurements under two different protocols in order to control electric polarization by magnetic field. In first case, the sample was poled under an electric field of *E* = + 5.8 kV/cm and a magnetic field of *H* = + 80 kOe. The electric field

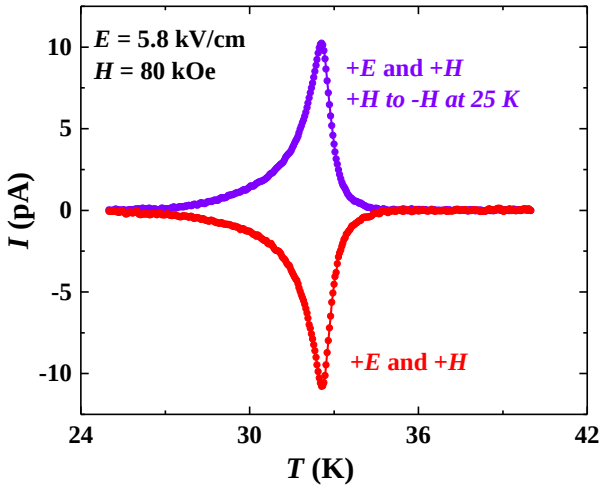

Figure 4.8 Pyroelectric current data measured with two different protocols.

was then removed and the sample was kept shorted for long time, after that the current was recorded during heating under the same magnetic field. The obtained data is shown by red curve in Figure 4.8. In the second protocol, the sample was cooled to lowest temperature under same electric and magnetic field. After removing the electric field and shorting, the magnetic field was reversed from +80 kOe to - 80 kOe. Then the current was measured during heating under - 80 kOe magnetic field and the obtained data is shown by blue curve in the same figure. Interestingly, after switching the polarity of the magnetic

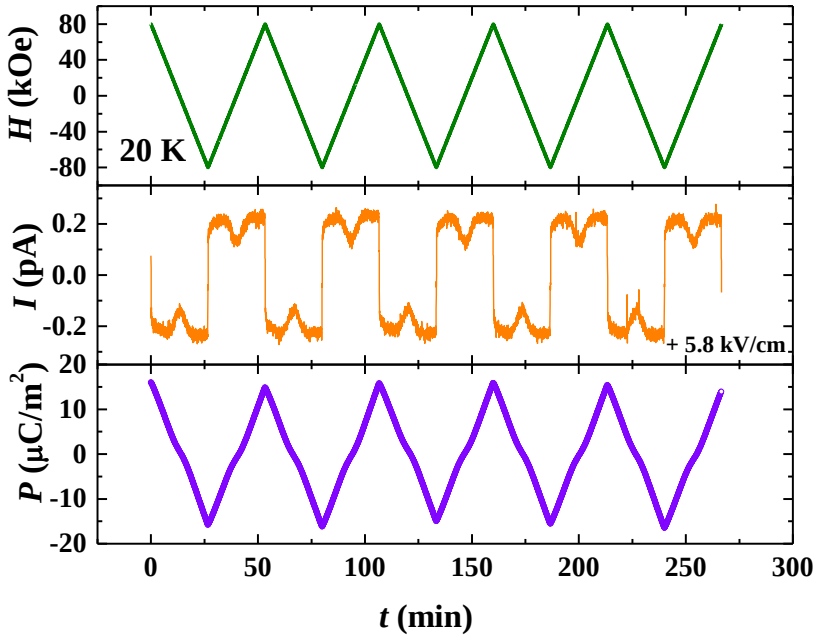

Figure 4.9 Magnetic control of electric polarization in the presence of an oscillating magnetic field of ± 80 kOe at 20 K.

field, the pyroelectric current peak is reversed, although the polarity of the electric fields used in poling is same in these two measurements. This observation suggests that the electric polarization of a magnetoelectric material can be reversed by only magnetic field. This motivates us to investigate magnetic control of electric polarization at fixed temperature. In this measurement, the sample was poled across T_N under a magnetic field of + 80 kOe and an electric field of + 5.8 kV/cm. After removing the field and shorting, the current was measured at 20 K by oscillating magnetic field between + 80 kOe and - 80 kOe. The obtained electric polarization is shown in Figure 4.9. It can be seen that the electric polarization is switched from positive to negative value with switching the polarity of magnetic field at fixed temperature. Thus, only magnetic field is sufficient to control the electric polarization in magnetoelectric materials. The magnetic field control electric polarization reversal can be explained by the phenomenological model using the equation,

$$P = \alpha H \propto \lambda G H$$

where λ is the coupling constant, G is an order parameter used in magnetoelectric material [16]. The sign of G completely depends on the polarity of applied poling electric

effect. In case of the poling under $+E$ and $+H$, the initial electric polarization remains positive. Now if the polarity of the magnetic field changes, since the sign of G remains invariant, the electric polarization is reversed from positive to negative.

4.3.1.6 Microscopic mechanism of magnetoelectric effect

Microscopic origin of linear magnetoelectric effect can be understood from a phenomenological theory. It is already proposed that the magnetoelectric interaction in *A*-site magnetic spinel with collinear antiferromagnetic ordering is given by [2],

$$I_{ME} = L_x\left(M_yP_z + M_zP_y\right) + L_y(M_zP_x + M_xP_z) + L_z\left(M_xP_y + M_yP_x\right) \quad (1)$$

where $\vec{L}$ = (L_x, L_y, L_z) is the antiferromagnetic order parameter, $\vec{M}$ = (M_x, M_y, M_z) is the magnetization and $\vec{P}$ = (P_x, P_y, P_z) is the electric polarization.

It is known that the primitive unit cell of the normal cubic spinel contains two A^{2+} ions located at $\left(\frac{1}{8},\frac{1}{8},\frac{1}{8}\right)$ and $\left(\frac{7}{8},\frac{7}{8},\frac{7}{8}\right)$ and four B^{3+} ions at $\left(\frac{1}{2},\frac{1}{2},\frac{1}{2}\right)$, $\left(\frac{1}{2},\frac{3}{4},\frac{3}{4}\right)$, $\left(\frac{3}{4},\frac{1}{2},\frac{3}{4}\right)$, and $\left(\frac{3}{4},\frac{3}{4},\frac{1}{2}\right)$. Assuming $\vec{S}_{Ai}$ $(i = 1,2)$ and $\vec{S}_{Bj}$ $(j = 1,2,3,4)$ are the spins of atoms at *A* and *B* sites, respectively, the antiferromagnetic order parameter can be written as $\vec{L} = \vec{S}_{A1} - \vec{S}_{A2}$. The magnetization of the *A* and *B* site can be written as $\vec{M}_A = \vec{S}_{A1} + \vec{S}_{A2}$ and $\vec{M}_B = \vec{S}_{B1} + \vec{S}_{B2} + \vec{S}_{B3} + \vec{S}_{B4}$, respectively. Using these relations in equation (1), the obtained magnetoelectric interaction become a sum of two terms,

$$2P_x\left(S_{A1y}S_{A1z} - S_{A2y}S_{A2z}\right) + 2P_y(S_{A1x}S_{A1z} - S_{A2x}S_{A2z}) + 2P_z\left(S_{A1x}S_{A1y} - S_{A2x}S_{A2y}\right), \quad (2)$$

and

$$\sum_{j=1,2,3,4}\left(\vec{S}_{A1}\otimes\vec{S}_{Bj} - \vec{S}_{A2}\otimes\vec{S}_{Bj}\right)\vec{P} \quad (3)$$

Here the symbol $\otimes$ represents $\vec{V}_1\otimes\vec{V}_2 = \left(V_{1y}V_{2z} + V_{1z}V_{2y}; V_{1z}V_{2x} + V_{1x}V_{2z}; V_{1x}V_{2y} + V_{1y}V_{2x}\right)$. Equation (2) represents the magnetoelectric interaction due to the single-ion effect of the *A*-sites, whereas magnetoelectric interaction represented by the equation (2) is governed by the interaction between the *A* and *B* atoms.

As it is mentioned before that only Co^{2+} ion located at the *A* site is magnetic and Co^{3+} ions located at *B* site is nonmagnetic. Therefore, magnetoelectric polarization in

Co_3O_4 can only be induced by single-ion contribution according to equation (2). The calculated magnetoelectric polarization in Co_3O_4 by considering only single-ion contribution is found to be 1-10 μC/m^2, which agrees well with the experimental value.

Further, the site symmetry of the magnetic ions (Co^{2+}) is $\bar{4}3m$, which is noncentrosymmetric. Thus, each tetrahedral site with Co^{2+} ions has a diploe moment. However the overall electric polarization is zero because the overall crystal structure is centrosymmetric ($Fd\bar{3}m$). Under magnetic field, due to spin-orbit coupling the orientation of dipole moments changes, resulting a net electric polarization.

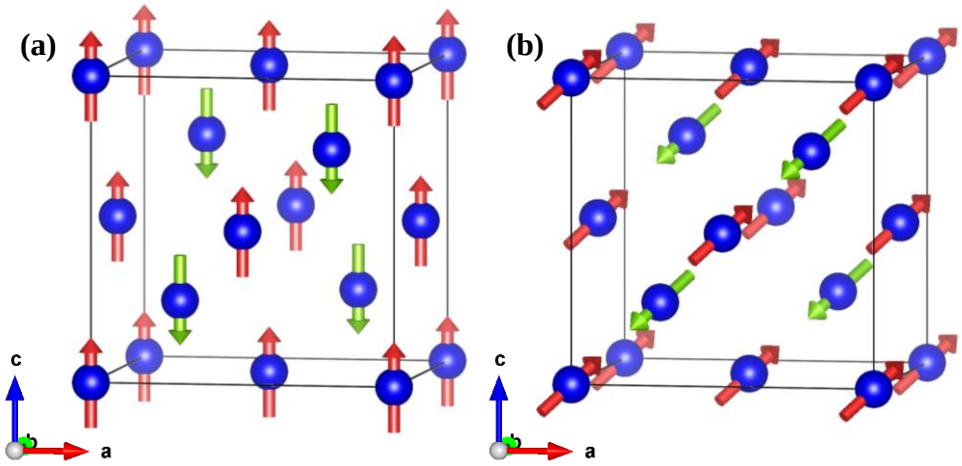

Figure 4.10 Two possible magnetic structures of Co_3O_4. Co^{2+} spins are aligned (a) along [001] direction, which is associated with the magnetic space group $I4'_1/a'm'd$, (b) along [111] direction associated with and $R\bar{3}'m'$.

4.3.1.7 Magnetic structure

The magnetic structure of Co_3O_4 was determined by Roth *et al.* using a neutron diffraction experiment at 4.2 K on a polycrystalline sample [6]. It was shown that each Co^{2+} spins are tetrahedrally surrounded by four opposite Co^{2+} spins, which are directed along any of the cubic edges, such as along [001] as shown in Figure 4.10(a). The magnetic space group associated with this spin configuration is $I4'_1/a'm'd$ (magnetic point group $4'/m'm'm$). It is to be noted that because of the cubic symmetry of the crystal structure, in addition to the cubic edges, another principle axis [111] is also equally probable for an easy axis, as reported in the case of $MnGa_2O_4$, which is another *A*-site magnetic spinel, using powder neutron diffraction experiments [18]. However, it is not

possible to distinguish these two using a polycrystalline sample. In the absence of single crystal of Co_3O_4, we have grown single crystal of $MnGa_2O_4$ and using magnetic and magnetoelectric measurements, we have shown that the easy axis of $MnGa_2O_4$ is indeed directed along [111] of the cubic unit cell. The magnetic space group associated with this easy axis is $R\bar{3}'m'$ (magnetic point group $\bar{3}'m'$). Interestingly, both of these two magnetic symmetries allow linear magnetoelectric effect [19]. Thus, the magnetic space group of Co_3O_4 can be any one of these two, as shown in Figure 4.10(a) and (b). Neutron diffraction study or a similar magnetic and magnetoelectric study on a single crystal of Co_3O_4 is necessary to find out the exact magnetic space group.

4.3.2 Results on $CoAl_2O_4$

4.3.2.1 Crystal structure

Figure 4.11(a-d) shows the result of Rietveld refinements of X-ray diffraction data collected at room temperature of all the samples. The structural parameters are given in

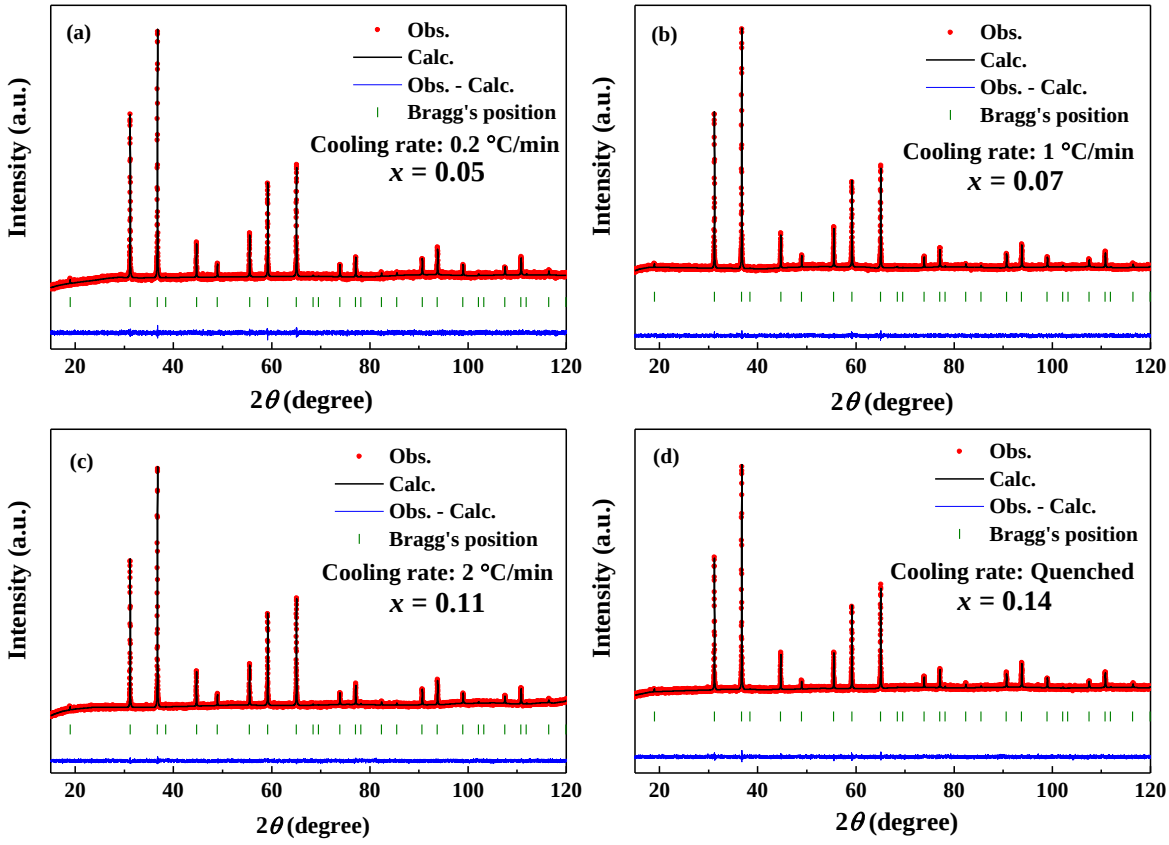

Figure 4.11 (a-d) Rietveld refinements of the room temperature X-ray diffraction data of $Co_{1-x}Al_x[Al_{2-x}Co_x]O_4$ prepared using different cooling rates in the synthesis process.

Table 4.2 Structural parameters of $Co_{1-x}Al_x[Al_{2-x}Co_x]O_4$ obtained from Rietveld refinements of the room temperature X-ray diffraction data with *Fd*-3*m* space group

x = 0.05; *a* = 8.1069 (1) Å, χ^2 = 1.10

Atom	Wyckoff position	*x*	*y*	*z*	B_{iso} (Å^2)	Occupancy
Co	8*a*	1/8	1/8	1/8	0.33 (7)	0.95 (1)
Co	16*d*	1/2	1/2	1/2	0.33 (7)	0.02 (1)
Al	8*a*	1/8	1/8	1/8	0.32 (11)	0.05 (1)
Al	16*d*	1/2	1/2	1/2	0.32 (11)	0.98 (1)
O	32*e*	0.2645 (3)	0.2645 (3)	0.2645 (3)	0.14 (11)	1.00

x = 0.07; *a* = 8.1070 (1) Å, χ^2 = 1.11

Atom	Wyckoff position	*x*	*y*	*z*	B_{iso} (Å^2)	Occupancy
Co	8*a*	1/8	1/8	1/8	0.40 (7)	0.93 (1)
Co	16*d*	1/2	1/2	1/2	0.40 (7)	0.03 (1)
Al	8*a*	1/8	1/8	1/8	0.38 (10)	0.07 (1)
Al	16*d*	1/2	1/2	1/2	0.38 (10)	0.97 (1)
O	32*e*	0.2643 (2)	0.2643 (2)	0.2643 (2)	0.27 (10)	1.00

x = 0.11; *a* = 8.1072 (1) Å, χ^2 = 1.12

Atom	Wyckoff position	*x*	*y*	*z*	B_{iso} (Å^2)	Occupancy
Co	8*a*	1/8	1/8	1/8	0.24 (6)	0.89 (1)
Co	16*d*	1/2	1/2	1/2	0.24 (6)	0.05 (1)
Al	8*a*	1/8	1/8	1/8	0.58 (11)	0.11 (1)
Al	16*d*	1/2	1/2	1/2	0.58(11)	0.95 (1)
O	32*e*	0.2643 (2)	0.2643 (2)	0.2643 (2)	0.41(9)	1.00

x = 0.14; *a* = 8.1075 (2) Å, χ^2 = 1.10

Atom	Wyckoff position	*x*	*y*	*z*	B_{iso} (Å^2)	Occupancy
Co	8*a*	1/8	1/8	1/8	0.18 (8)	0.86 (1)
Co	16*d*	1/2	1/2	1/2	0.18 (8)	0.07 (1)
Al	8*a*	1/8	1/8	1/8	0.19 (12)	0.14 (1)
Al	16*d*	1/2	1/2	1/2	0.19 (12)	0.93 (1)
O	32*e*	0.2634 (3)	0.2634 (3)	0.2634 (3)	0.31 (11)	1.00

Table 4.2. Similar to Co_3O_4 (Figure 4.2(b)), $CoAl_2O_4$ crystallizes in a cubic normal spinel structure (space group $Fd\bar{3}m$). However, unlike Co_3O_4 where the cations Co^{2+} and Co^{3+} entirely occupy the tetrahedral and octahedral sites, respectively, it is seen that there is a tendency of cation disorder between tetrahedral and octahedral sites in $CoAl_2O_4$. The samples with different degree of cation disorder are prepared by using different cooling

rates in the synthesis process. We have varied the relative occupancies of Co and Al atoms in these two sites in the refinement process and found that the slowly cooled samples are prone to have less inversion than the rapidly cooled sample. Thus, the sample, which was cooled with the slowest cooling rate of 0.2 °C/min, has a degree of inversion (x) is 0.05, on the other hand, the sample that was quenched to room temperature has an inversion (x) of 0.14.

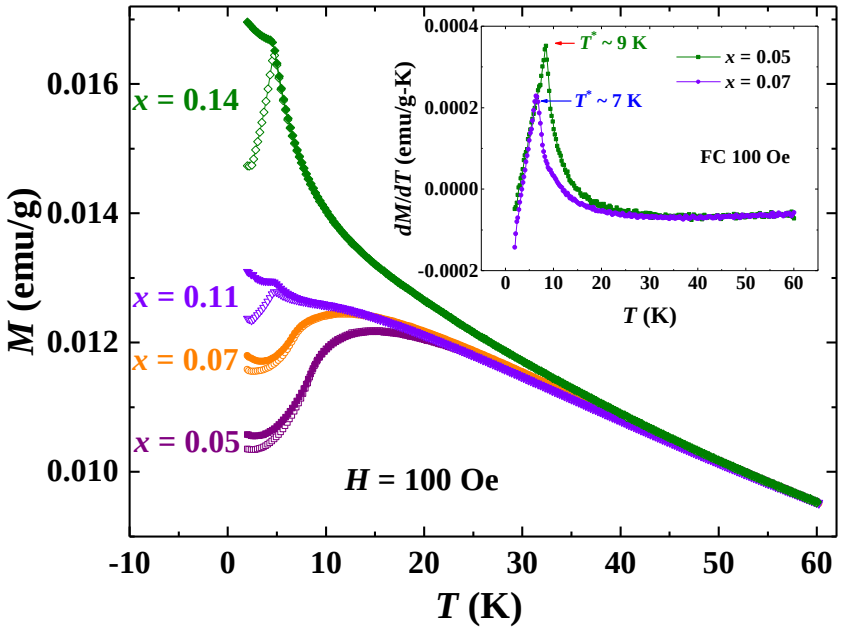

Figure 4.12 Zero-field-cooled (ZFC) and field-cooled (FC) magnetization data of all the samples measured with a magnetic field of 100 Oe. Closed symbols represent FC data and open symbols represent ZFC data. Inset shows dM/dT plots of FC magnetizations of x = 0.05 and 0.07 samples.

4.3.2.2 DC magnetization

Magnetization data M (T) of all the samples measured at a magnetic field of 100 Oe under zero-field-cooled (ZFC) and field-cooled (FC) conditions are shown in Figure 4.12. A broad peak is observed around 14 K in both of ZFC and FC magnetization for x = 0.05 sample. First order derivative of magnetization (FC) with temperature shows a sharp peak around T^* ~ 9 K as shown in the inset of Figure 4.12. It has been suggested that this broad peak is due to a transition to either a spiral spin liquid state or a long-range ordered antiferromagnetic state [10,20]. Further, a bifurcation is observed in ZFC and FC magnetization at lower temperature, which is due to the presence of minor inversion (x =

0.05) in the sample [20]. With increasing inversion (x), the broad peak shifts to lower temperature and is suppressed. A new peak is observed at a further lower temperature (~ 5 K) in x = 0.11 sample. For the highest disordered sample (x = 0.14), the broad peak disappears and the peak around 5 K becomes a sharp peak. The bifurcation between ZFC and FC magnetization is increased with increasing x. Using ac susceptibility measurements (discussed later), we have confirmed that this sharp peak around 5 K is due to the appearance of spin glass state, which is consistent with the earlier report [20].

$1/\chi_m$ *vs.* T data for all the samples measured under FC condition with 1 kOe magnetic fields are shown in Figure 4.13. The data at high temperature region are fitted with the Curie-Weiss law (solid lines) and the obtained parameters are shown in Table 4.3. The obtained effective paramagnetic moments (μ_{eff}) remain around 4.6 μ_B/Co^{2+} for all the samples. The calculated spin-only value of the effective paramagnetic moment (μ_{cal}) is 3.87 μ_B/Co^{2+}, while it is 6.5 μ_B/Co^{2+} considering both spin and orbital contribution. Thus, the observation of an intermediate value of μ_{eff} suggests the presence of orbital contribution. Further, μ_{eff} remains same for all the samples, irrespective of the amount of inversion, which suggests that the cobalt ions that occupy the octahedral sites due to inversion remain in same oxidation state (+2). The obtained Curie-Weiss temperature (θ_{CW}) for all samples is close to - 95 K and it does not vary much with inversion. The value of θ_{CW} is very high compared to T^* and the frustration parameter ($f = |\theta_C|/T^*$) is found to be ~ 10 (for x = 0.05 sample). For Co_3O_4, the frustration parameter (f) is found to be ~ 3. As mentioned earlier, the ratio of exchange interactions J_2/J_1 is 0.019 < 1/8 for Co_3O_4 and 0.109 (~ 1/8) for $CoAl_2O_4$. Thus, the next-nearest-neighbor interaction (J_2) is significant in $CoAl_2O_4$ and results magnetic frustration.

Table 4.3 Results of the fit of $1/\chi_m$ *vs.* T data from 150 K to 390 K with the Curie - Weiss law for all samples of $Co_{1-x}Al_x[Al_{2-x}Co_x]O_4$

x	μ_{eff} (μ_B/Co^{2+})	θ_{CW} (K)
0.05	4.6	-94.4
0.07	4.6	-96.9
0.11	4.5	-95.4
0.14	4.6	-94.8

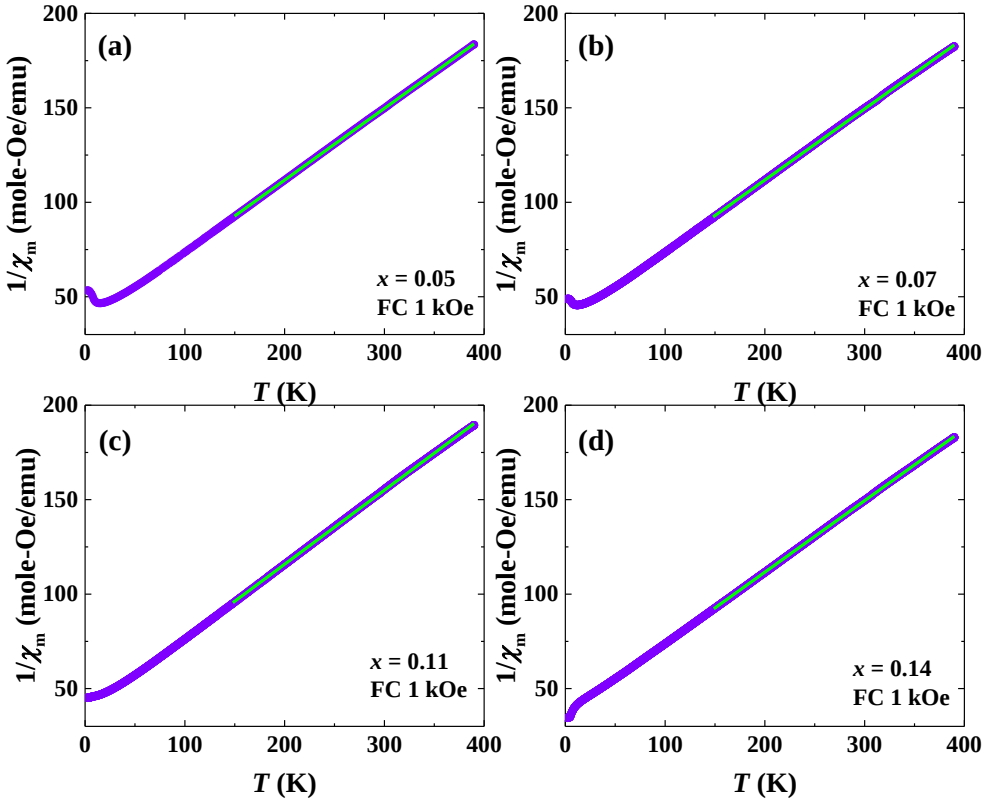

Figure 4.13 $1/\chi_m$ (T) data of all samples measured with a magnetic field of 1 kOe. Solid green lines represent the linear fit with the Curie-Weiss law.

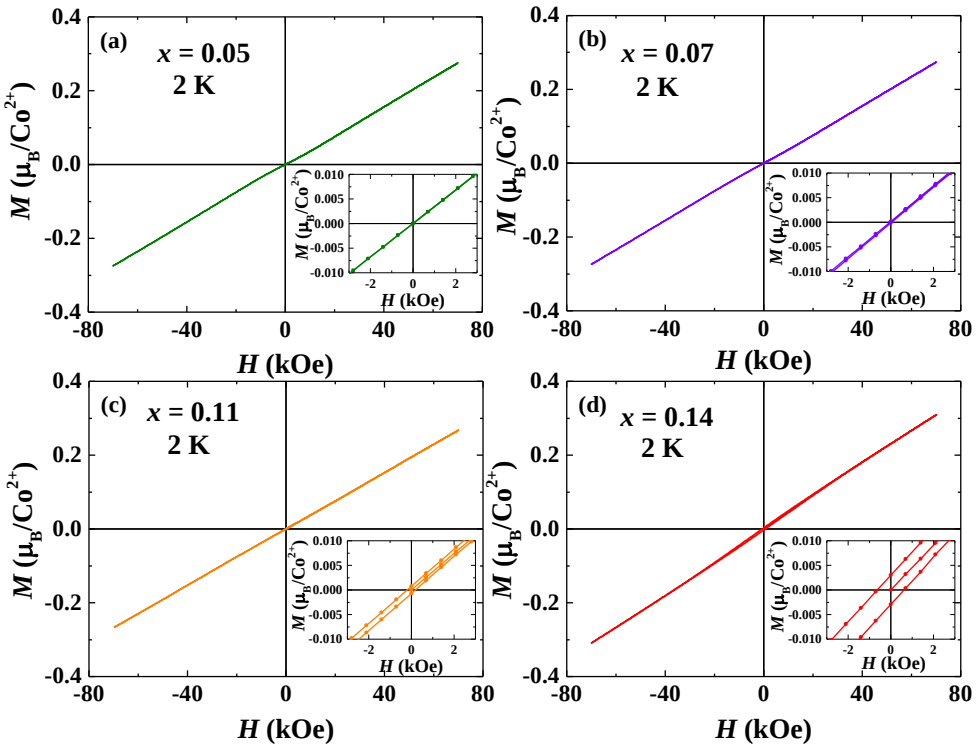

Figure 4.14 Magnetic field dependent magnetization M (H) of all samples measured at 2 K. Inset shows the magnified view of magnetization at low magnetic fields.

Figure 4.14 shows the magnetic field dependence of magnetizations M (H) measured at 2 K of all the samples. The insets show the magnified view of magnetization at low fields. The overall behavior of M (H) data is linear for all the samples, except x = 0.14, where a tiny hysteresis loop is observed. The insets clearly show that the tiny hysteresis loop is developed from a linear behavior with increasing x from x = 0.05 to 0.14. The typical shape of the tiny hysteresis loop as observed in x = 0.14 is a characteristic of a spin glass state, while the linear behavior in x = 0.05 is consistent with the antiferromagnetic nature.

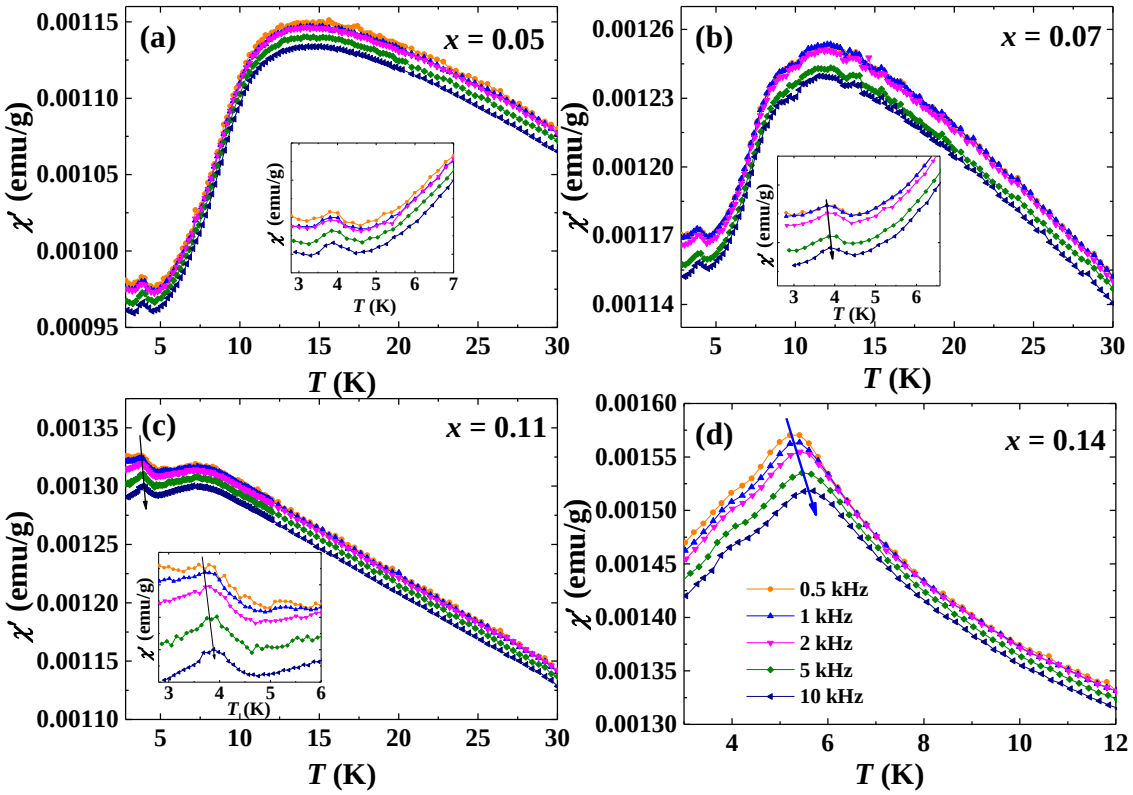

Figure 4.15 AC susceptibility χ' (T) data of all the samples. The inset shows the magnified view of the peak at low temperature.

4.3.2.3 AC susceptibility

In Figure 4.15(a-d), we show the temperature dependence of the real part of ac susceptibility (χ') for all the samples. For x = 0.05 sample, a broad frequency independent peak is observed around 14 K, while a weak kink is found around 4 K, which is also frequency independent (shown in the inset of Figure 4.15(a)). The broad peak is similar to

that of dc magnetization. With increasing disorder (x), the broad peak shifts to lower temperature and is suppressed, while the weak kink becomes prominent. In the sample with x = 0.14, the broad peak is completely suppressed and the weak kink becomes a sharp peak around 5 K, which shifts to higher temperature with increasing frequency. These results confirm that a spin glass state appears in $CoAl_2O_4$ with increasing anti-site disorder [21].

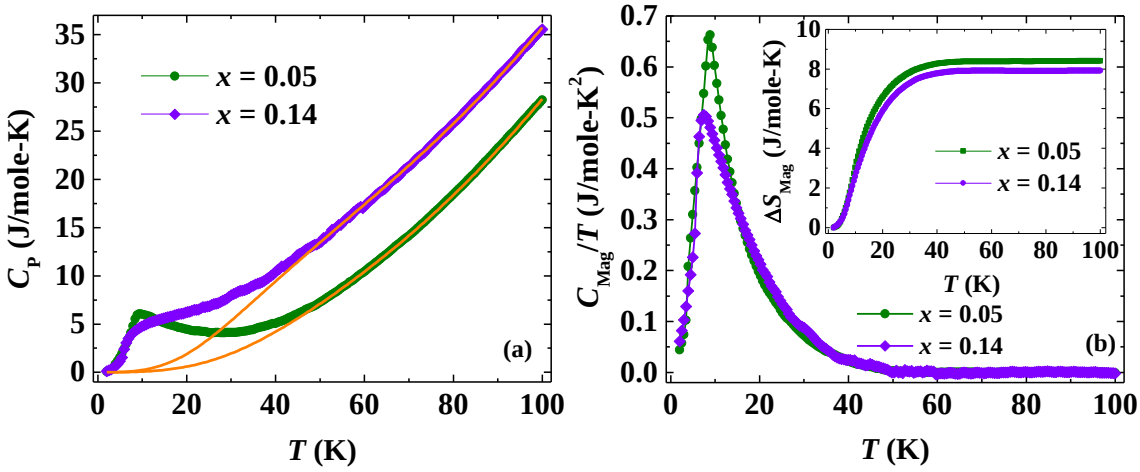

Figure 4.16 (a) Temperature dependence of heat capacity (C_p) of the samples with x = 0.05 and 0.14 measured without magnetic field. The phonon contributions to the total heat capacity obtained using a Debye-Einstein model are shown by solid lines. (b) Magnetic contributions to the total heat capacity (C_{Mag}/T) for x = 0.05 and 0.14. The entropy-changes associated with the magnetic transitions for x = 0.05 and 0.14 are shown in the inset.

4.3.2.4 Heat Capacity

For further investigations, heat capacity (C_P) was measured on x = 0.05 and 0.14 sample. Figure 4.16(a) shows the temperature variation of heat capacity (C_p) of these samples. In x = 0.05 sample, a peak is found around T^* ~ 9 K, suggesting the presence of a possible long-range magnetic ordering of Co^{2+} spins. However, the peak is broad and it is not like a conventional λ-type peak, as seen in the case of Co_3O_4 (Figure 4.4(b)). It is worth mentioning here that similar to $CoAl_2O_4$, the frustrated spinel $FeSc_2S_4$ remains at the boundary, which separates the long-range spin-orbital ordering and spin-orbital liquid state. A similar broad peak was found in C_P (T) around 8 K in $FeSc_2S_4$ and it has been suggested recently that it remains in the near but in the long-range ordered side of the

boundary [22]. Upon increasing disorder in the present compound, the peak becomes broad and shifts to lower temperature (~ 7.5 K for x = 0.14). It is well-known that, for a spin glass system with spin glass transition temperature T_{SG}, C_P (T) exhibits such a broad peak at ~ 1.4 T_{SG} [21]. Thus, for x = 0.14 sample, the broad peak in C_P (T) around 7.5 K and the sharp peak in M (T) around 5 K are consistent with the appearance of spin glass state.

To estimate the magnetic contribution $C_{Mag}(T)$ to the heat capacity, phonon contribution (C_{Ph}) is calculated using a combined Debye-Einstein model, as given by [23-25],

$$C_{Ph} = C_{Debye} + C_{Einstein} = \frac{9Ra_1}{x_D^3}\int_0^{x_D}\frac{x^4e^x}{(e^x-1)^2}dx + 3R\sum_{n=1}^{2}b_n\frac{x_{E,n}^2e^{x_{E,n}}}{(e^{x_{E,n}}-1)^2}$$

where R is the universal gas constant, $x_{D,E}$ = $\Theta_{D,E}/T$ where $\Theta_{D,E}$ are the Debye and Einstein temperature, respectively. C_P (T) data in the temperature range of 50 K to 100 K are fitted with the above equation. We found that one Debye and two Einstein terms are sufficient to fit the present data. The used values of Debye and Einstein coefficients a_1, b_1 and b_2 are 1, 1 and 5, respectively, since total number of modes in the Debye-Einstein model is equal to the number of atoms in the formula unit [23,24]. The values of Θ_D, Θ_{E1} and Θ_{E2} were found to be 295, 432 and 706 K for x = 0.05 and 200, 368 and 685 K for x = 0.14, respectively. The obtained phonon contribution C_{Ph} (T) is then extrapolated down to lowest temperature and is shown by the solid lines in the same figure. $C_{Mag}(T)$ is obtained by subtracting $C_{Ph}(T)$ from the total heat capacity. In Figure 4.16(b), temperature dependent C_{Mag}/T is shown for x = 0.05 and 0.14. It is evident from the figure that the magnetic contribution to the heat capacity decreases with increasing inversion. The entropy-change $\Delta S_{Mag}(T)$ associated with the magnetic transition in both the samples is calculated by using the following equation [23],

$$\Delta S_{\mathrm{Mag}}(T) = \int_0^T \frac{C_{\mathrm{Mag}}(T)}{T}dT$$

The obtained ΔS_{Mag} (T) is shown in the inset of the Figure 4.16(b). The expected change in entropy due to magnetic ordering of Co^{2+} spins with S = 3/2, is $\Delta S_{Mag} = R\,ln(2S+1)$ = 11.5 J/mole-K at high temperature limit. For x = 0.05, the observed ΔS_{Mag} ~ 8.4 J/mole-K at 100 K, which is almost ~ 73% of the expected total entropy. On the other hand,

ΔS_{Mag} (= 7.9 J/mole-K) for x = 0.14 is decreased further as expected for the appearance of spin glass state. Note that even in Co_3O_4, which exhibits a well-defined long-range collinear antiferromagnetic ordering at 30 K, the observed ΔS_{Mag} is ~ 70% of the expected value [23]. Thus, the observed less values of entropy change cannot be attributed to the appearance of possible spiral spin liquid state.

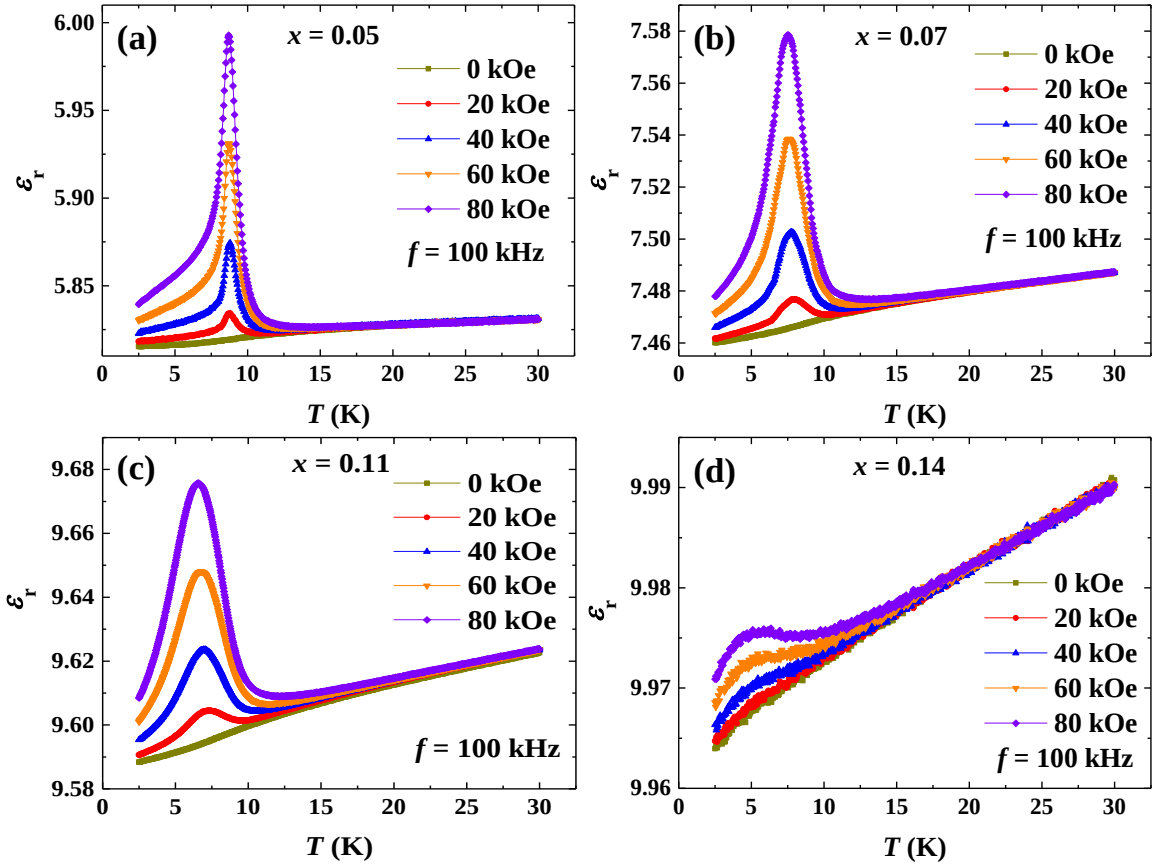

Figure 4.17 Temperature dependence of dielectric constant measured with 100 kHz under different magnetic fields for all the samples.

4.3.2.5 Magnetodielectric effect

Temperature dependent dielectric constant data ε_r (T) of all the samples measured at 100 kHz under different magnetic fields (0, 20, 40, 60 and 80 kOe) are shown in Figure 4.17(a-d). Similar to Co_3O_4, no dielectric anomaly is observed around T^* in the absence of magnetic field in x = 0.05 sample, while a sharp λ-type peak appears around T^* under external magnetic field and its magnitude increases continuously with increasing magnetic field. These results suggest the presence of a strong magnetodielectric effect. A

peak in dielectric loss associated with the peak in ε_r (T) is also observed only in the presence of magnetic field and it remains as low as 0.02 throughout the measurement temperature window (not shown). The magnetic field induced dielectric peak is observed in all the samples (Figure 4.17(a-d)), however their natures are different. With increasing anti-site disorder (x), the peak in ε_r (T) becomes broad and the λ-type nature of the peak is vanished. Further, the peak shifts to lower temperature with increasing x, which is consistent with the shift of the broad peak in dc and ac magnetization.

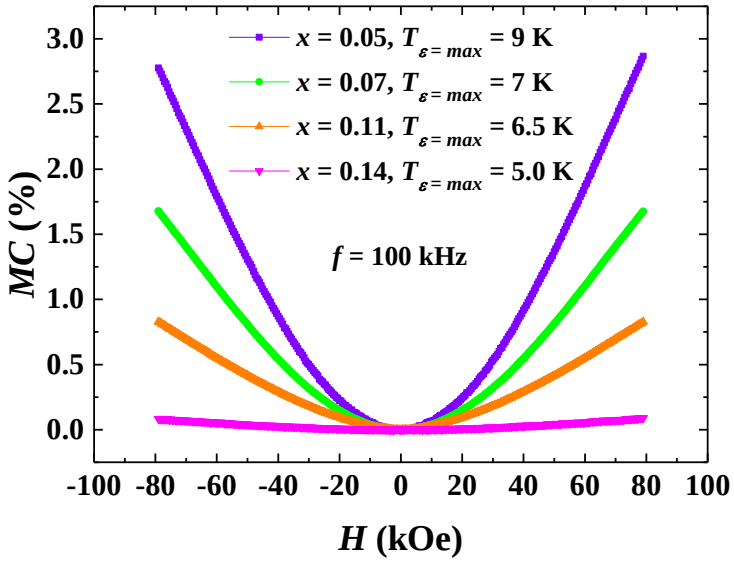

Figure 4.18 Magnetocapacitances of all the samples measured with 100 kHz at the temperatures, where magnetic field induced peak in ε_r (T) is observed.

Magnetocapacitance $\{MC(\%) = \frac{C_H - C_{H=0}}{C_{H=0}} \times 100\}$ is measured for all the samples at the temperatures where the magnetic field induced peak in ε_r (T) is observed and is shown in Figure 4.18. It can be seen that, the magnetocapacitance decreases with increasing x. The maximum magnetocapacitance ($MC(\%)$ = 2.8 %) observed in x = 0.05 sample is higher than that of Co_3O_4. On the other hand, the magnetocapacitance is almost vanished in the highest disordered sample (x = 0.14).

4.3.2.6 Linear magnetoelectric effect

In order to find out whether or not the magnetic field induced dielectric peak is associated with the magnetoelectric effect, pyroelectric current was measured under different applied magnetic fields in all the samples. Insets of Figure 4.19(a-c) show the

pyroelectric current data under different magnetic fields for the samples with x = 0.05, 0.07 and 0.11, respectively. As observed in Co_3O_4, the sample with x = 0.05 exhibits a sharp peak around the dielectric peak under magnetic field. The pyroelectric current peak under magnetic field is observed in all the samples, except x = 0.14 sample. Electric polarization obtained from pyroelectric current data is shown in Figure 4.19(a-c), which indicates that the electric polarization appears below the magnetic transition temperature under external magnetic fields in all the samples with $x \leq 0.11$. However, the natures of the pyroelectric current peaks are different for different samples, similar to the behavior of magnetic field induced dielectric peak. For x = 0.05, the pyroelectric current peak is very sharp and asymmetric. With increasing x, the peak becomes broad and symmetric and finally it is vanished for the x = 0.14 sample. These results indicate the presence of magnetoelectric effect in the samples with $x \leq 0.11$.

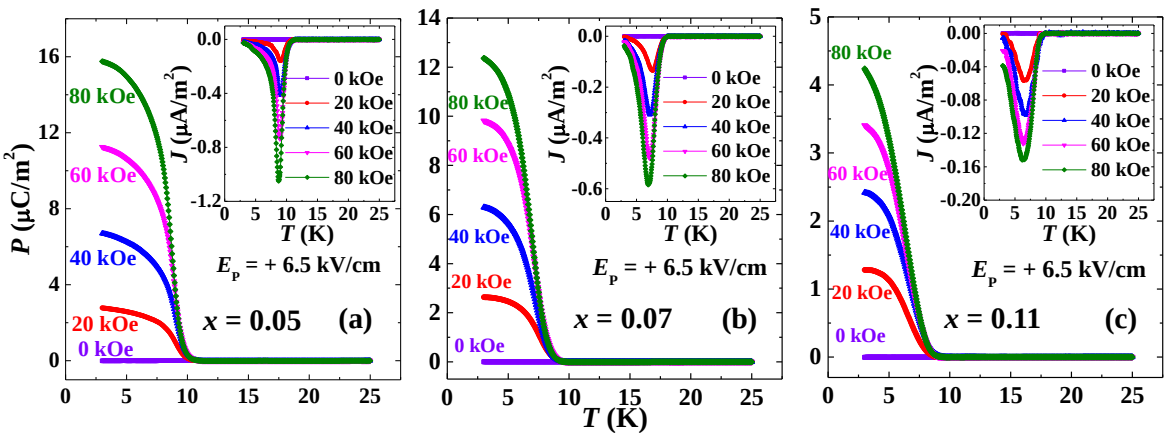

Figure 4.19 (a-c) Evolution of electric polarizations with temperature obtained from pyroelectric current measurements under different magnetic fields for the samples with x = 0.05, 0.07 and 0.11, respectively. The insets show the corresponding pyroelectric current data, which are measured in the presence of different magnetic field after a magnetoelectric poling with an electric field of E_P = + 6.5 kV/cm and same magnetic field.

Electric polarization *vs.* magnetic field data is shown in Figure 4.20. Similar to Co_3O_4, the electric polarization varies linearly with magnetic fields, indicating the linear magnetoelectric effect. The linear magnetoelectric coefficient (α) calculated from the slope of the linear fit of the P *vs.* H data is found to be 2.7 ps/m for x = 0.05 sample, which is slightly higher than that of Co_3O_4. With increasing disorder, the value of α is decreased as mentioned in Figure 4.20.

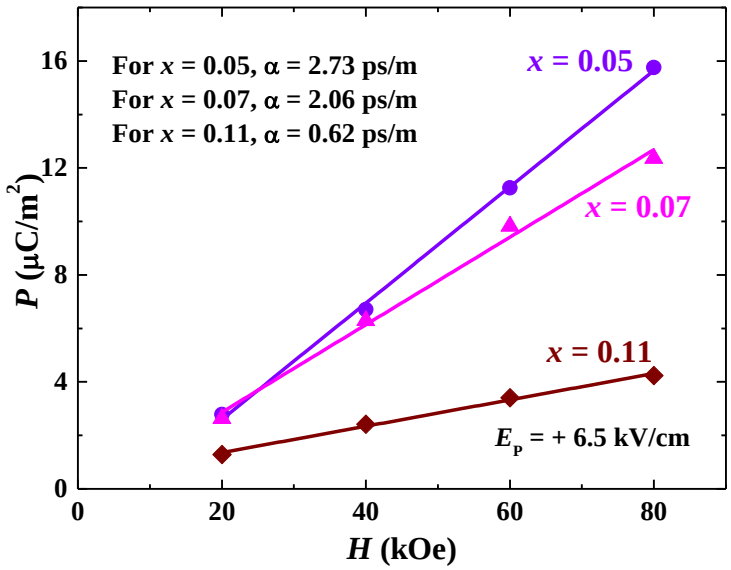

Figure 4.20 *P vs. H* data at 3 K of the samples with x = 0.05, 0.07 and 0.11.

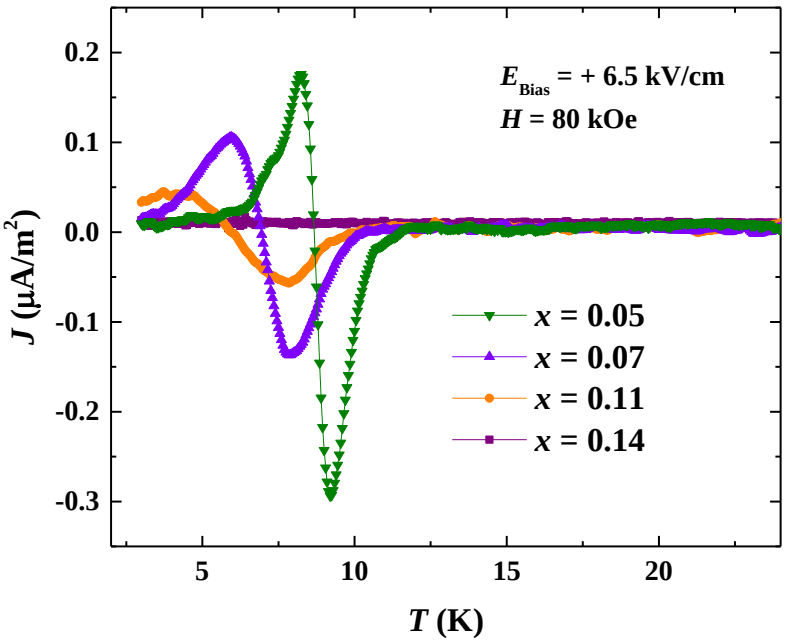

Figure 4.21 Results of dc-biased current measurements on all the samples with an electric field of E_{Bias} = + 6.5 kV/cm and a magnetic field of 80 kOe.

4.3.2.7 DC-biased current

It has been recently suggested that a dc-biased current measurement can differentiate the pyroelectric current peak associated with the ferroelectric transition from the thermally stimulated free charge current (TSFC) in multiferroics [26]. The results of dc-biased current measurements on all the samples with a magnetic field of 80 kOe and

an electric field of E_{Bias} = + 6.5 kV/cm are shown in Figure 4.21. For the sample with x = 0.05, the dc-biased current exhibits an upward peak due to magnetoelectric polarization and a downward peak due to the depolarization of these polarized dipoles. With increasing disorder (x), these peaks become broad and shift to lower temperature and finally disappears for x = 0.14. The dc-biased current data are consistent with the results of pyroelectric current measurements and further confirm the magnetoelectric effect.

4.3.2.8 Magnetic ground state of $CoAl_2O_4$

The emergence of electric polarization associated with a peak in dielectric constant under magnetic fields in the samples with x = 0.05, 0.07 and 0.11 suggest that $CoAl_2O_4$ with less anti-site disorder is a magnetoelectric. As mentioned before, the symmetry criterion of the magnetoelectric effect requires the breaking of space inversion and time reversal symmetry. Thus, the broken time reversal symmetry indicates the presence of long-range magnetic ordering. Further, to the best of our knowledge, till today there is no material reported to exhibit magnetoelectric effect without long-range magnetic ordering. Therefore, the observation of linear magnetoelectric effect in $CoAl_2O_4$ indicates that the broad peaks in dc/ac magnetization and heat capacity in the less disordered samples are associated with a long-range collinear antiferromagnetic ordering. However, the broad natures of these peaks could be due to combined effect of frustration caused by competing exchange interactions and anti-site disorder. Further, as discussed in case of Co_3O_4, the magnetic space group of $CoAl_2O_4$ could be any one of $I4'_1/a'm'd$ and $R\bar{3}'m'$, both of which allow linear magnetoelectric effect. A further study on single crystal of $CoAl_2O_4$ is necessary to distinguish between these two. On the other hand, the sample with highest disorder (x = 0.14) exhibits a spin glass state without magnetoelectric effect.

4.3.2.9 Result of Monte Carlo simulations

4.3.2.9.1 Long-range AF order parameter and magnetoelectric polarization

The experimental results were compared with the calculated antiferromagnetic (AF) order parameter (L) and electric polarization (P) in these samples using Monte Carlo simulations. We have used equation (2) for calculating electric polarization. In the simulation technique, the effect of cation disorder was modeled as voids in the magnetic

diamond lattice and we did not consider possible Co^{2+} spins at the *B*-sites. The ratio of the exchange interactions $J_2/J_1 = 0.11$ calculated from neutron diffraction study was used, while the exchange constant $J_1 = 3.14$ meV close to experimentally determined value 2.1 meV yielded better agreement for the temperature of magnetic phase transition [27]. The Monte Carlo simulations were performed using the Metropolis algorithm, where a system with dimensions of 20×20×20 cubic unit cells ($N = 64000$ Co atoms) and periodic boundary conditions are used. The system was allowed to relax at each temperature for 1000 Monte Carlo steps per spin (MCs), after which the statistics were recorded.

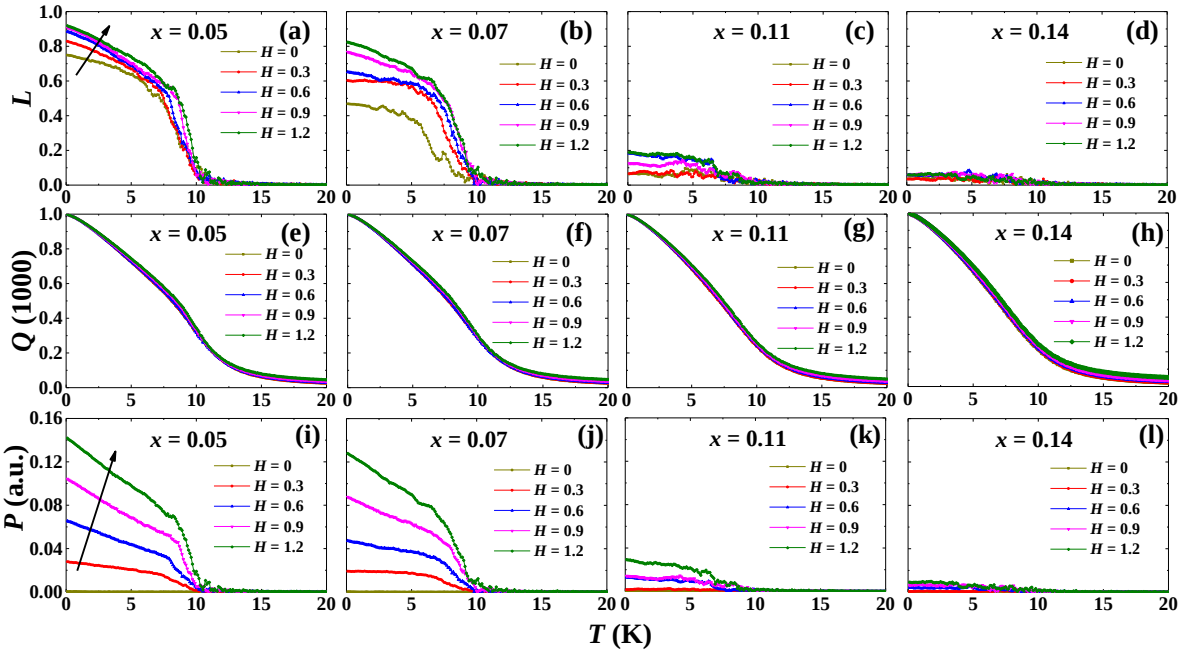

Figure 4.22 Results of the Monte Carlo simulations of (a-d) antiferromagnetic order parameter L, (e-h) Edwards-Anderson order parameter $Q(1000)$, and (i-l) electric polarization for all samples.

The results of Monte Carlo simulations are shown in Figure 4.22. It can be seen from Figure 4.22(a-d) that the sample with x = 0.05 is almost completely ordered at low temperature (the value $L = 1$ corresponds to complete antiferromagnetic ordering). Further, the AF order parameter L increases under applied magnetic field. With increasing x, the AF order parameter decreases and finally disappears for x = 0.14 sample. In Figure 4.22(e-h), the Edwards-Anderson order parameter for all the samples are shown, which is

given by [28,29],

$$Q(t) = \frac{1}{N}\sum_{i=1}^{N}\left|\frac{1}{t}\int_0^t \vec{S}_i(t')dt'\right|^2,$$

where integration is replaced by summation over MCs in simulations. The Edwards-Anderson order parameter is normally used in spin glasses to calculate the local magnetization. It follows that for the sample with x = 0.05, the appearance of AF order is accompanied by the growth of Q (1000). On the other hand, the samples with x = 0.14 do not show AF order upon decreasing temperature, nevertheless Q (1000) increases similarly to x = 0.05 sample, which indicates that the spins are frozen at low temperature in x = 0.14 sample. As shown in Figure 4.22(i-l), electric polarization appears in x = 0.05 sample in the presence of magnetic field when AF order sets in. The electric polarization varies linearly with magnetic field. With increasing disorder (x), the magnetic field induced electric polarization is decreased, which is consistent with the experimental observation.

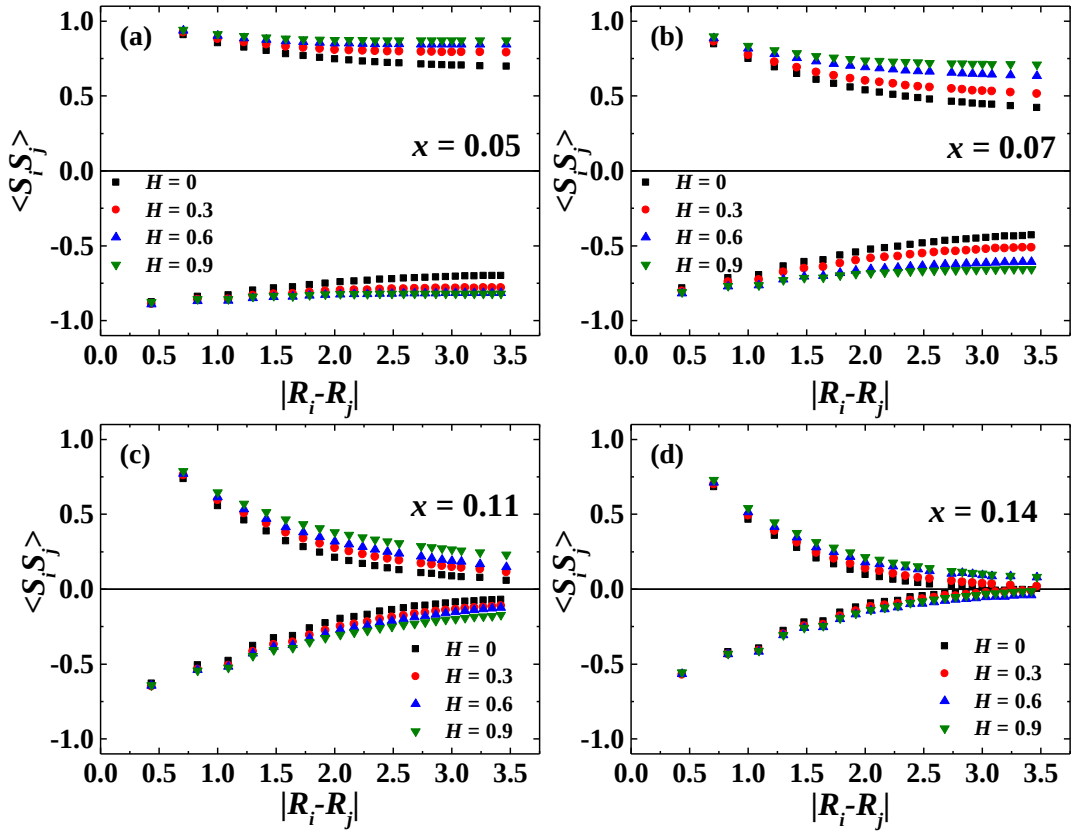

Figure 4.23 Spin-spin correlation functions $\langle \vec{S}_i \vec{S}_j \rangle$ as functions of relative distance measured in units of the cubic lattice constant for all x.

4.3.2.9.2 Spin-spin correlation

The correlation functions $\langle \vec{S}_i \vec{S}_j \rangle$ as functions of the relative distance $|\vec{R}_i - \vec{R}_j|$ in all the samples are shown in Figure 4.23. Consistent with the long-range AF order parameter L, the sample with x = 0.05 shows a saturation of spin-spin correlation function at a constant value for a large relative distances. The correlation length gradually decreases with increasing disorder. In case of x = 0.14 sample, the correlation length reaches a value that corresponds to the lattice constant, which indicates that the spins are not correlated beyond that distance and thus there is no long-range order.

4.3.2.10 Theoretical discussion

The present experimental results confirm that $CoAl_2O_4$ with less cation disorder exhibits linear magnetoelectric effect, which is further supported by MC calculations. $CoAl_2O_4$ lies at the boundary between the long-range AF and spin spiral ground states, which is the reason of contradicting experimental results obtained by various research groups. The possibility of electric polarization induced by the spiral spin states was theoretically suggested earlier [30]. However the existence of linear magnetoelectric effect in the spiral spin state, which is possibly suggested for $CoAl_2O_4$, is not possible due to the following reason. If the ratio of J_2/J_1 is slightly greater than 1/8, spin spiral state will appear, which can be described by spatially varying $\vec{L}$ and $\vec{M}$. Then macroscopically, the linear magnetoelectric effect would require the presence of macroscopic interactions of the form

$$\frac{\partial L_i}{\partial x_j} H_k P_l,$$

or

$$\frac{\partial M_i}{\partial x_j} H_k P_l,$$

However, both of them would average to zero upon integration over volume, since L and M are sine or cosine in the spiral. Thus, the observation of linear magnetoelectric effect in $CoAl_2O_4$ is the signature of the long-range AF ordering.

4.4 Conclusion

In conclusion, we have shown experimentally the presence of linear magnetoelectric effect in a simple cubic spinel oxide Co_3O_4, which exhibits a clear long-range collinear antiferromagnetic ordering at 30 K. Further, our study on different disordered samples of $CoAl_2O_4$ suggests that $CoAl_2O_4$ with low disorder ($\leq 11\%$) exhibits linear magnetoelectric effect, while the sample with 14% cation disorder exhibits a spin glass behavior without magnetoelectric effect. The observation of linear magnetoelectric effect in $CoAl_2O_4$ with low anti-site disorder indicates that the magnetic ground state is long-range collinear antiferromagnetic ordered state. The experimental findings are further supported by the results of Monte Carlo simulations. Thus, while Co_3O_4 lies far below the border of the long-range antiferromagnetic and spiral spin liquid state, the compound $CoAl_2O_4$ with low anti-site disorder can be placed on near the boundary ($J_2/J_1 \lesssim 1/8$) but in the long-range ordered side of the phase diagram.

References

[1] V. Sakhnenko and N. Ter-Oganessian, *J. Phys. Condens. Matter* **24,** 266002 (2012).

[2] N. V. Ter-Oganessian, *J. Magn. Magn. Mater.* **364,** 47 (2014).

[3] D. Bergman, J. Alicea, E. Gull, S. Trebst, and L. Balents, *Nat. Phys.* **3,** 487 (2007).

[4] O. Zaharko, N. B. Christensen, A. Cervellino, V. Tsurkan, A. Maljuk, U. Stuhr, C. Niedermayer, F. Yokaichiya, D. Argyriou, and M. Boehm, *Phys. Rev. B* **84,** 094403 (2011).

[5] A. Krimmel, H. Mutka, M. Koza, V. Tsurkan, and A. Loidl, *Phys. Rev. B* **79,** 134406 (2009).

[6] W. Roth, *J. Phys. Chem. Solids* **25,** 1 (1964).

[7] W. Roth, *Journal de Physique* **25,** 507 (1964).

[8] S. Gao, O. Zaharko, V. Tsurkan, Y. Su, J. S. White, G. S. Tucker, B. Roessli, F. Bourdarot, R. Sibille, D. Chernyshov, T. Fennell, A. Loidl, and C. Ruegg, *Nat Phys* **13,** 157 (2017).

[9] B. C. Melot, K. Page, R. Seshadri, E. Stoudenmire, L. Balents, D. L. Bergman, and T. Proffen, *Phys. Rev. B* **80,** 104420 (2009).

[10] B. Roy, A. Pandey, Q. Zhang, T. Heitmann, D. Vaknin, D. C. Johnston, and Y. Furukawa, *Phys. Rev. B* **88,** 174415 (2013).

[11] G. J. MacDougall, D. Gout, J. L. Zarestky, G. Ehlers, A. Podlesnyak, M. A. McGuire, D. Mandrus, and S. E. Nagler, *Proc. Natl. Acad. Sci. USA* **108,** 15693 (2011).

[12] N. Tristan, J. Hemberger, A. Krimmel, H. K. Von Nidda, V. Tsurkan, and A. Loidl, *Phys. Rev. B* **72,** 174404 (2005).

[13] U. Muller, *Inorganic Structural Chemistry* (Wiley).

[14] A. R. West, *Solid State Chemistry and its Applications*, 2nd ed. (John Wiley & Sons, 2014).

[15] J. Chen, X. Wu, and A. Selloni, *Phys. Rev. B* **83,** 245204 (2011).

[16] A. Iyama and T. Kimura, *Phys. Rev. B* **87,** 180408 (2013).

[17] J. Hwang, E. Choi, H. Zhou, J. Lu, and P. Schlottmann, *Phys. Rev. B* **85,** 024415 (2012).

[18] B. Boucher, A. Herpin, and A. Oles, *J. Appl. Phys.* **37,** 960 (1966).

[19] R. E. Newnham, *Properties of materials: anisotropy, symmetry, structure* (Oxford University Press on Demand, 2005).

[20] K. Hanashima, Y. Kodama, D. Akahoshi, C. Kanadani, and T. Saito, *J. Phys. Soc. Jpn.* **82,** 024702 (2013).

[21] J. A. Mydosh, *Spin glasses* (Taylor and Francis, 1993).

[22] K. W. Plumb, J. R. Morey, J. A. Rodriguez-Rivera, H. Wu, A. A. Podlesnyak, T. M. McQueen, and C. L. Broholm, *Phys. Rev. X* **6,** 041055 (2016).

[23] Y. Ikedo, J. Sugiyama, H. Nozaki, H. Itahara, J. Brewer, E. Ansaldo, G. Morris, D. Andreica, and A. Amato, *Phys. Rev. B* **75,** 054424 (2007).

[24] A. Yogi, A. K. Bera, A. Maurya, R. Kulkarni, S. M. Yusuf, A. Hoser, A. A. Tsirlin, and A. Thamizhavel, *Phys. Rev. B* **95,** 024401 (2017).

[25] B. Koteswararao, R. Kumar, P. Khuntia, S. Bhowal, S. Panda, M. Rahman, A. Mahajan, I. Dasgupta, M. Baenitz, and K. H. Kim, *Phys. Rev. B* **90,** 035141 (2014).

[26] C. De, S. Ghara, and A. Sundaresan, *Solid State Commun.* **205,** 61 (2015).

[27] G. J. MacDougall, A. A. Aczel, Y. Su, W. Schweika, E. Faulhaber, A. Schneidewind, A. D. Christianson, J. L. Zarestky, H. Zhou, and D. Mandrus, *Phys. Rev. B* **94,** 184422 (2016).

[28] S. F. Edwards and P. W. Anderson, *Journal of Physics F: Metal Physics* **5,** 965 (1975).

[29] K. Binder, *Zeitschrift für Physik B Condensed Matter* **26,** 339 (1977).

[30] S. Lee and L. Balents, *Phys. Rev. B* **78,** 144417 (2008).

Chapter 5

Ordered aeschynite-type polar magnets $RFeWO_6$ (R = Dy, Eu, Tb and Y): A new family of type-II multiferroics*

Summary

The magnetoelectric multiferroic properties of a series of oxides $RFeWO_6$ (R = Dy, Eu, Tb and Y) are demonstrated. Using synchrotron X-ray and neutron diffraction studies, we have shown that these oxides crystallize in a polar aeschynite-type structure ($Pna2_1$) with an ordered arrangement of Fe^{3+} and W^{6+} ions. Long-range antiferromagnetic ordering of Fe^{3+} spins at T_N^{Fe} ~ 15 - 18 K induces a dielectric anomaly, where a sudden change in electric polarization (ΔP) is observed in all the compounds. The electric polarizations in all these compounds are affected by applied magnetic field, where different R-ions influences the polarization to a different extent, demonstrating a strong coupling between magnetic R-ion and Fe-ion moments. A detailed neutron diffraction analysis in $DyFeWO_6$ reveals that a commensurate non-collinear antiferromagnetic ordering of Fe^{3+} spins is responsible for enhancing electric polarization below T_N^{Fe} ~ 18 K.

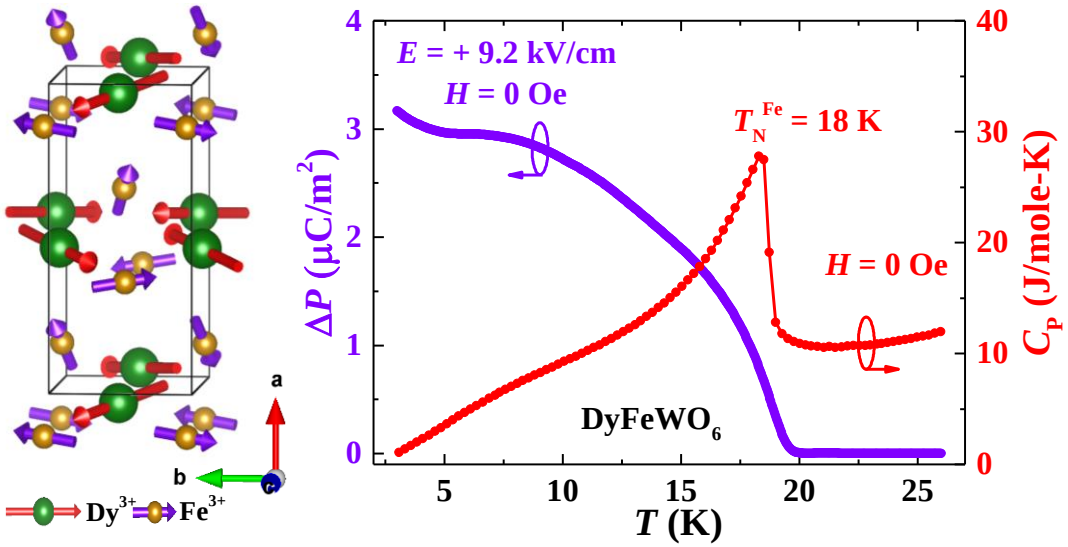

*Paper based on this work has appeared in *Phys. Rev. B*, **95**, 224416 (2017), © (2017) by the American Physical Society

5.1 Introduction

Among many exotic phenomena in condensed matter physics, multiferroicity, i.e. the coexistence of ferroelectricity and magnetism in a single-phase material, is one of the most investigated topics in the last two decades [1-3]. Though ferroelectricity and magnetism are incompatible in a single material according to the classical concept, different ways have been utilized in order to combine these two properties, which are discussed in Chapter 1 in details [1]. In one approach, multiferroicity results from independent sources of ferroelectricity and magnetism, and thus they are weakly-coupled with each other. These materials are classified as type-I multiferroics [1]. On the other hand, few materials have been discovered where ferroelectricity appears at the magnetic ordering temperature due to the breaking of inversion symmetry by certain types of collinear and noncollinear magnetic structures [4-7]. Because of the same origin of these two properties, they are strongly coupled with each other. These materials, known as type-II multiferroics, are usually centrosymmetric in the paramagnetic state. For practical application purpose, the multiferroic material should have a high transition temperature, a high value of polarization/magnetization and a strong magnetoelectric coupling. Thus, in this regards, type-II multiferroics are the promising candidates for application point of view. However, the collinear and noncollinear magnetic structures of type-II multiferroics, which induce ferroelectricity, mainly occur at low temperatures due to the presence of magnetic frustrations and thus these materials have very low transition temperatures.

The polar magnets offer a great possibility to have a room temperature multiferroics. In contrast to the nonpolar type-II multiferroics, in the polar magnets, the inversion symmetry is already broken above the magnetic ordering temperature while the time reversal symmetry is broken at the magnetic ordering temperature. Thus polar magnets can have magnetoelectric effect below magnetic ordering temperature. Further, two different cases may arise depending on the mechanism involved in the breaking of inversion symmetry. If the noncentrosymmetric crystal structure of the polar magnet is associated with a nonmagnetic ion, as in the case of type-I multiferroics, the magnetoelectric coupling will be very weak. The polar compounds $BiFeO_3$, BaMF$_4$ (M = Mn, Ni) belong to this type of multiferroics family [8-12]. On the other hand, recently, few polar magnets have been discovered where the noncentrosymmetry of the crystal

structure in the paramagnetic region is associated with the magnetic ions. Thus, in addition to a sudden enhancement in the electric polarization due to magnetic ordering, a strong magnetoelectric coupling is observed below the magnetic ordering temperature. Hence, these polar magnets can form a subclass of type-II multiferroics. The best example of this class of polar magnets is $A_2Mo_3O_8$ (*A* = Fe and Mn) [13-15]. These oxides crystallize in a hexagonal structure with a polar space group $P6_3mc$, which consists of *A*-O layers of corner-shared AO_4 tetrahedra and AO_6 octahedra. In each *A*-O layer, the AO_4 tetrahedra and AO_6 octahedra are shifted along *c*-axis with respect to each other, which results in long and short interlayer *A*-*A* distances. Both these two oxides exhibit an abrupt enhancement in the electric polarization below magnetic ordering temperatures, where a large magnetoelectric effect is observed [13-15]. Similar strong magnetoelectric effect is observed in another polar compound $CaBaCo_4O_7$, where a non-switchable spontaneous electric polarization appears below the ferrimagnetic ordering temperature [16-18]. The polar corundum oxide Ni_3TeO_6 exhibits a non-hysteretic magnetoelectric effect below collinear antiferromagnetic ordering [19]. Several polar corundum derivatives $A_2BB'O_6$ with space group $R3c$ have been reported to exhibit multiferroic properties [20-23].

There exists a family of oxides that belong to the aeschynite mineral group. The most common representative oxide in this structure is $CaTa_2O_6$, which has a centrosymmetric orthorhombic structure with space group *Pnma* (Figure 5.1). The crystal structure of $CaTa_2O_6$ consists of dimers of edge-shared $Ta^{5+}O_6$ octahedra, which are further connected by corner sharing [24]. The oxides $RTiTaO_6$ (*R* = La to Dy) also crystallize in the aeschynite-type structure, where Ti^{4+} and Ta^{5+} ions are disorderly arranged in a octahedral site, similar to the arrangement of $Ta^{5+}O_6$ octahedra in $CaTa_2O_6$ [25]. On the other hand, the series of compounds $RMWO_6$ (*R* = rare earth element and *M* = V, Cr, Fe) have been suggested to exhibit an ordered arrangement of M^{3+} and W^{6+} ions in the aeschynite-type structure with a polar space group $Pn2_1a$ [26]. However, the detailed structural parameters and physical properties of these oxides were not known so far.

In this chapter, the discovery of magnetoelectric multiferroicity in the series of compounds $RFeWO_6$ (*R* = Dy, Eu, Tb and Y) is discussed. Analysis of synchrotron X-ray and neutron diffraction data confirms that these oxides indeed crystallize in an ordered aeschynite-type structure with the polar space group $Pna2_1$. These oxides undergo a long-

range antiferromagnetic ordering of Fe^{3+} ions at T_N^{Fe} ~ 15-18 K, where a clear dielectric anomaly is observed. A sudden enhancement of electric polarization is found below T_N^{Fe}. The magnetic field strongly influences the dielectric anomaly and electric polarization. These results suggest that *R*FeWO$_6$ (*R* = Dy, Eu, Tb and Y) constitute a new family of type-II multiferroics. Using neutron diffraction study on DyFeWO$_6$, we have shown that a commensurate noncollinear magnetic structure of Fe^{3+} spins is responsible for enhancing electric polarization below T_N^{Fe}.

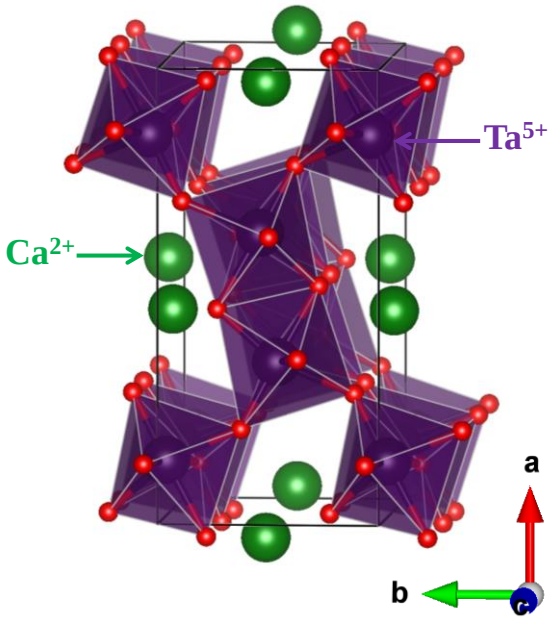

Figure 5.1 The aeschynite-type crystal structure of $CaTa_2O_6$. The structure is shown in *Pnam* setting.

5.2 Experimental section

Polycrystalline samples of *R*FeWO$_6$ (*R* = Dy, Eu and Tb) oxides were prepared by high temperature solid state reaction method through a two-step process. In the first step, *R*FeO$_3$ (*R* = Dy, Eu and Tb) were made by mixing stoichiometric amount of R_2O_3 (*R* = Dy and Eu) or Tb_4O_7 with Fe_2O_3, and heating at the final temperature of 1350 °C for 24 hour in air with several intermittent grindings. The rare earth oxides were preheated at 900 °C for 12 hour in air before use. In the second step, the obtained *R*FeO$_3$ and WO_3 were mixed stoichiometrically and the mixtures were heated at the final temperatures of 1020 °C, 1110 °C and 1060 °C for 12 hour in pure argon atmosphere for *R* = Dy, Eu and Tb,

respectively. The polycrystalline sample of $YFeWO_6$ was prepared at high pressure (4.5 Gpa) and high temperature (1000 °C) using a multi anvil cubic high pressure apparatus from the stoichiometric amounts of Y_2O_3, Fe_2O_3 and WO_3. Room temperature synchrotron X-ray diffraction data for all the samples were collected at the Materials Science Powder Diffraction (BL04-MSPD) beamline of the ALBA synchrotron facility (Barcelona, Spain) using the wavelengths λ = 0.3544 and 0.3171 Å [27,28]. Synchrotron X-ray diffraction data were also collected at low temperatures for $DyFeWO_6$. Neutron diffraction data were collected on $DyFeWO_6$ with D2B diffractometer at the Institut Laue-Langevin (ILL, Grenoble, France) with a wavelength of λ = 1.594 Å at different temperatures. Room temperature neutron diffraction data on $TbFeWO_6$ were also collected with the same wavelength on D2B diffractometer. Room temperature powder second harmonic generation (SHG) measurements were carried out on $DyFeWO_6$ and $EuFeWO_6$ using a modified Kurtz-NLO system with a pulsed Nd:YAG laser (λ = 1064 nm). The details of equipment and methodology can be found in the references [29-31]. The physical property measurements were carried out, which are discussed in Chapter 2. Pyroelectric and dc biased currents were recorded with a heating rate of 10 K/min for all the samples.

5.3 Results and discussion

5.3.1 Stability of *R*$FeWO_6$

In Figure 5.2, the phase formation temperatures of the compounds *R*$FeWO_6$ (*R* = Dy, Eu, Tb and Y) are shown. As discussed later, the crystal structure of *R*$FeWO_6$ compounds consists of edge shared octahedra of Fe^{3+} and W^{6+} ions. According to the Pauling's 3rd rule, the presence of edge-shared or face-shared polyhedra containing cations of high charges decreases the stability of the ionic compounds. This is because of the fact that the edge or face sharing of polyhedra decreases the distance between two cations and thus increases the cation-cation repulsion. Thus, the phase formation temperature windows of the present oxides are very narrow, as indicated by the error bars in the Figure 5.2. We have tried to prepare other oxides in this family with other rare earth elements, but we could not stabilize the pure phases using solid state reaction method.

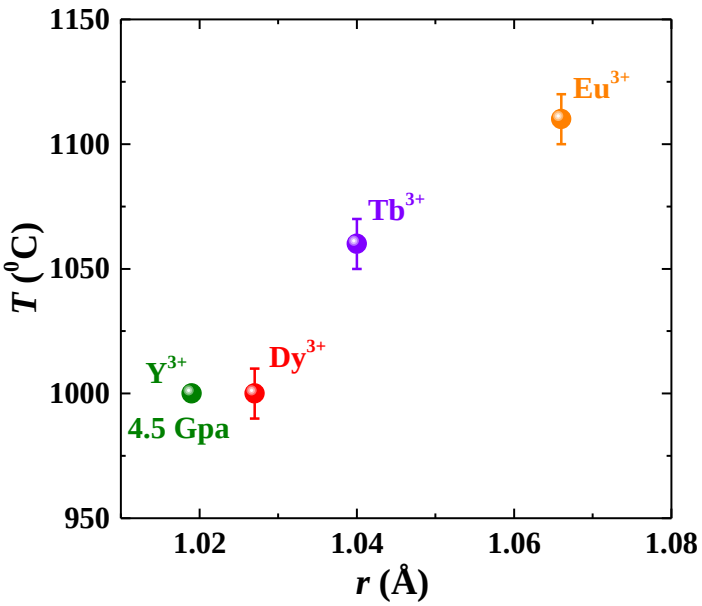

Figure 5.2 Phase formation temperatures of RFeWO$_6$ (R = Dy, Eu, Tb and Y).

5.3.2 Results on DyFeWO$_6$

5.3.2.1 Structure

In order to determine the crystal structure of DyFeWO$_6$, room temperature laboratory monochromatic X-ray diffraction pattern is indexed with the DICVOL program available in the FullProf Suite [32]. The reflection conditions obtained from indexing are:

$$0kl\text{: } k + l = 2n,$$

$$hk0\text{: } h = 2n,$$

These conditions suggest that the most probable space group could be either *Pnma* or $Pn2_1a$. Since the reflection conditions for both of these space groups are same, we could not distinguish between these two space group from the diffraction data. However, note that *Pnma* is centrosymmetric, while $Pn2_1a$ is a polar space group. Room temperature second harmonic generation (SHG) measurement revealed that the present material is SHG active with efficiency comparable to that of α-SiO$_2$, which indicates that the crystal structure is polar supporting the space group $Pn2_1a$. Finally, a combined Rietveld refinement analysis of the room temperature synchrotron X-ray and neutron diffraction

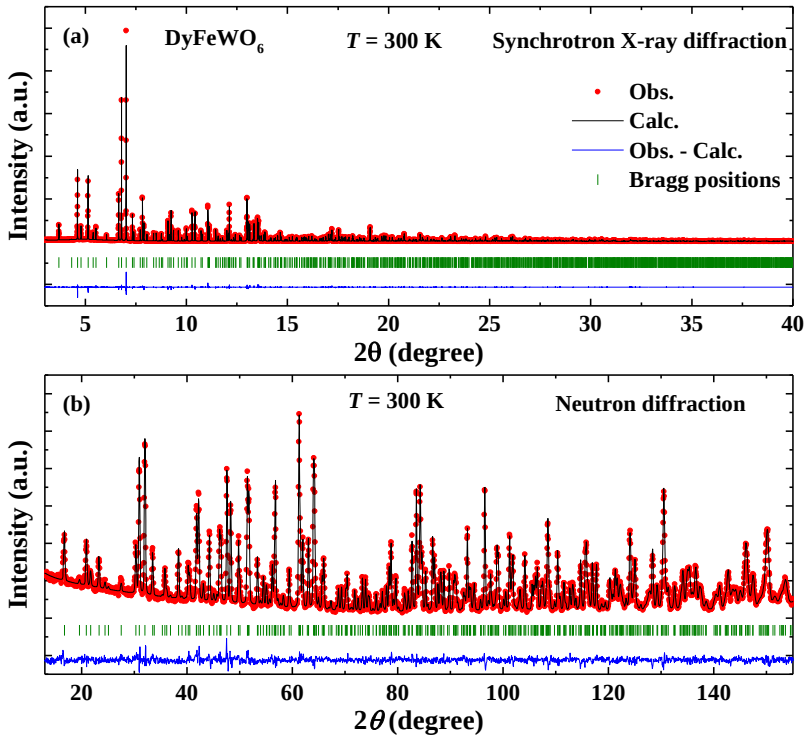

Figure 5.3 (a, b) Results of combined Rietveld refinement of room temperature synchrotron X-ray and neutron diffraction data of $DyFeWO_6$.

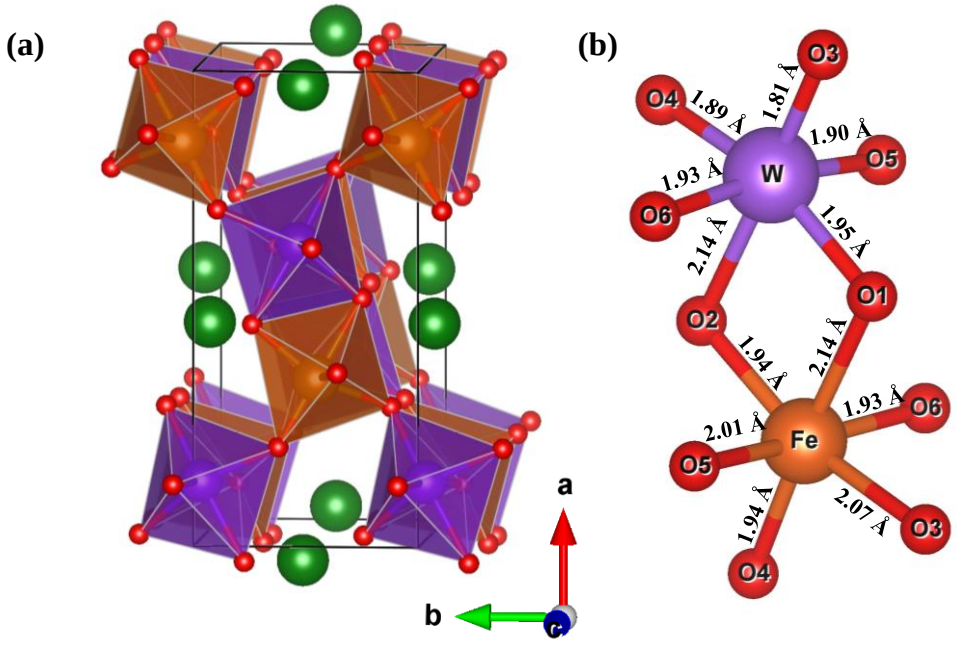

Figure 5.4 (a) The ordered aeschynite-type crystal structure (space group $Pna2_1$) of $DyFeWO_6$. (b) The edge-shared octahedra of Fe^{3+} and W^{6+} ions showing the bond distances.

Tables 5.1 Crystallographic parameters of $DyFeWO_6$ obtained from combined Rietveld refinement of synchrotron X-ray (λ = 0.3544 Å) and neutron diffraction data collected at of room temperature

Atom	Wyckoff position	*x*	*y*	*z*	B_{iso} (Å^2)	Occ.
Dy	4*a*	0.0426(1)	0.4570(2)	0.25	0.49(1)	1
Fe	4*a*	0.1378(2)	0.9661(5)	0.9925(5)	0.80(4)	1
W	4*a*	0.3539(1)	0.4519(2)	0.0057(3)	0.13(1)	1
O1	4*a*	0.9703(7)	0.7683(15)	0.0424(14)	0.77(17)	1
O2	4*a*	0.5221(7)	0.2542(16)	0.9610(15)	0.99(19)	1
O3	4*a*	0.2130 (8)	0.6145(19)	0.0622 (15)	1.24(19)	1
O4	4*a*	0.2919(8)	0.1278(17)	0.9333(13)	0.68(16)	1
O5	4*a*	0.1437(3)	0.0590(7)	0.2583(16)	0.94(6)	1
O6	4*a*	0.1197(3)	0.8289(6)	0.7500 (20)	0.83(6)	1

Space group: *Pna*2$_1$; *a* = 10.97992 (2) Å, *b* = 5.18849(1) Å, *c* = 7.34824(1) Å, $\alpha = \beta = \gamma = 90°$, *V* = 418.624(1) Å^3; χ^2 = 1.75 (for neutron), χ^2 = 1.07 (for synchrotron); Bragg *R*-factor = 3.66, R_f-factor = 2.36 (for neutron); Bragg *R*-factor = 3.67, R_f-factor = 2.80 (for synchrotron)

Tables 5.2 Selected bond lengths (Å) and bond valence sum (BVS) of $DyFeWO_6$ at room temperature

Cation	O1	O2	O3	O4	O5	O6
Dy	2.36(1) 2.45(1)	2.30(1) 2.40(1)	2.46(1)	2.43(1)	2.34(0)	2.32(0)
Fe	2.14(1)	1.94(1)	2.07(1)	1.94(1)	2.01(1)	1.93(1)
W	1.95(1)	2.14(1)	1.81(1)	1.89(1)	1.90 (1)	1.93(1)
	Dy_{BVS}				2.88(2)	
	Fe_{BVS}				3.15(4)	
	W_{BVS}				5.88(7)	

data is performed using FullProf software. In the refinement process, the standard setting *Pna*2$_1$ (space group no. 33) is used instead of the non-standard *Pn*2$_1$*a* setting. Since the atomic positions are not known and *Pna*2$_1$ is a subgroup of *Pnam* (another setting of *Pnma*), the atomic positions in $CaTa_2O_6$ in *Pnma* space group have been used and converted from the setting of *Pnma* to *Pna*2$_1$ using the program SUBGROUPGRAPH and TRANSTRU program provided by Bilbao Crystallographic Server [33].

The results of the combined Rietveld refinement of the synchrotron X-ray and neutron diffraction data are shown in Figure 5.3(a, b), respectively. The detailed structural parameters obtained from the refinements are given in Table 5.1 and the obtained crystal structure of $DyFeWO_6$ is displayed in Figure 5.4(a). It is found that the crystal structure of $DyFeWO_6$ with the polar space group $Pna2_1$ appears due to the splitting of the 8*d* octahedral site of the centrosymmetric *Pnam* structure (as shown in Figure 5.1 for $CaTa_2O_6$) into two 4*a* octahedral sites as a result of ordering of Fe^{3+} and W^{6+} ions. The cation ordering occurs because of the large differences in size and charge between Fe^{3+} and W^{6+} ions. The octahedra $Fe^{3+}O_6$ and $W^{6+}O_6$ are connected by edge sharing and form dimers which are connected through corner sharing to form a three dimensional network. The selected bond lengths obtained from refinement are given in Table 5.2. The obtained average <Dy-O>, <Fe-O> and <W-O> bond lengths, 2.38, 2.00, and 1.94 Å, respectively are consistent with those reported in $DyFeO_3$ and $MnWO_4$, indicating Dy^{3+}, Fe^{3+} and W^{6+} oxidation states [34,35]. Further, the bond valence sum calculations, as given in Table 5.2, confirm the +3 and +6 oxidation state of Dy/Fe and W ions, respectively. The edge-shared FeO_6 and WO_6 octahedra are shown in Figure 5.4(b), where the bond lengths are also given.

5.3.2.2 DC magnetization and magnetic structure

Field-cooled (FC) magnetization data M (T) as a function of temperature measured with an applied magnetic field of 100 Oe is shown Figure 5.5(a). A clear anomaly is seen in M (T) data around $T_N^{Fe} \sim 18$ K. Heat capacity C_P (T) exhibits a sharp λ-type peak around the same temperature, as shown in Figure 5.5(b), indicating the long-range antiferromagnetic ordering of Fe^{3+} spins. Upon further cooling, M (T) increases initially and exhibits a broad maximum around 12 K. At 5 K, a step is found in M (T) data, indicating a long-range cooperative antiferromagnetic ordering of Dy^{3+} moments. As discussed later, our neutron diffraction analysis reveals that the Fe^{3+} ordered moments induce Dy^{3+} moments to order at 18 K with the same propagation vector. Because of this, no anomaly is found in C_P (T) at the independent ordering temperature (5 K) of Dy^{3+} moments.

The inverse susceptibility ($1/\chi_{mol}$) *vs.* temperature data is plotted in Figure 5.6(a), which is fitted with the Curie - Weiss law at higher temperatures as shown by the solid

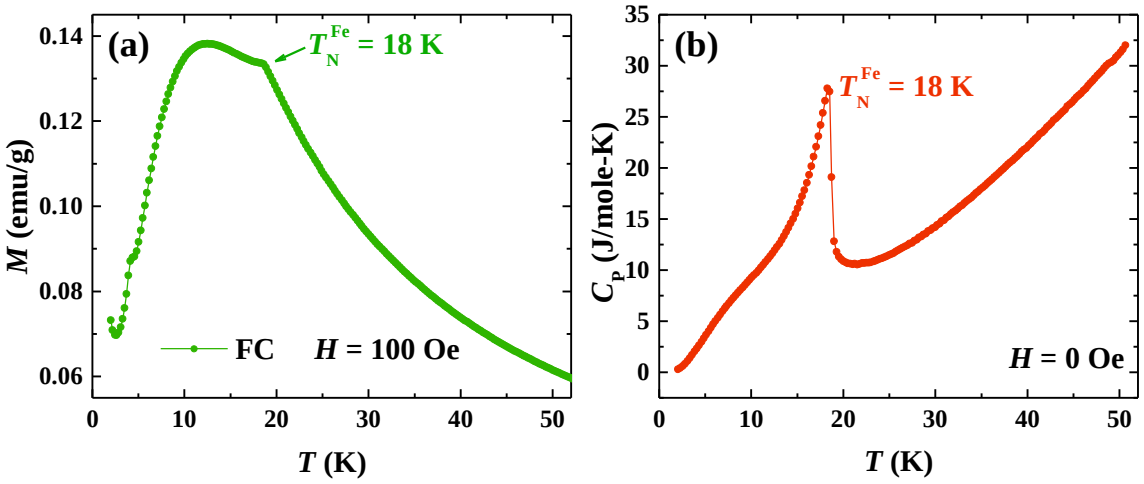

Figure 5.5 (a) Field-cooled (FC) magnetization M (T) of $DyFeWO_6$ as a function of temperature measured under a magnetic field of 100 Oe. (b) Temperature dependent heat capacity C_P (T) of $DyFeWO_6$.

line. The effective paramagnetic moment (μ_{eff}) obtained from the fitting is 12.5 μ_B/f.u., which is close to the theoretical moment (12.17 μ_B/f.u.). The obtained Curie-Weiss temperature (θ_{CW}) is – 21 K, which is consistent with the observed antiferromagnetic ordering at 18 K. Figure 5.6(b) shows the magnetic field dependent magnetization M (H) at different temperatures. The M (H) curve at 15 K is consistent with the antiferromagnetic behavior, while the M (H) curve at 2 K exhibits field-induced steps, indicating the meta-magnetic phase transitions associated with Dy^{3+} magnetism. Above 18 K, the M (H) curve resembles paramagnetic behavior.

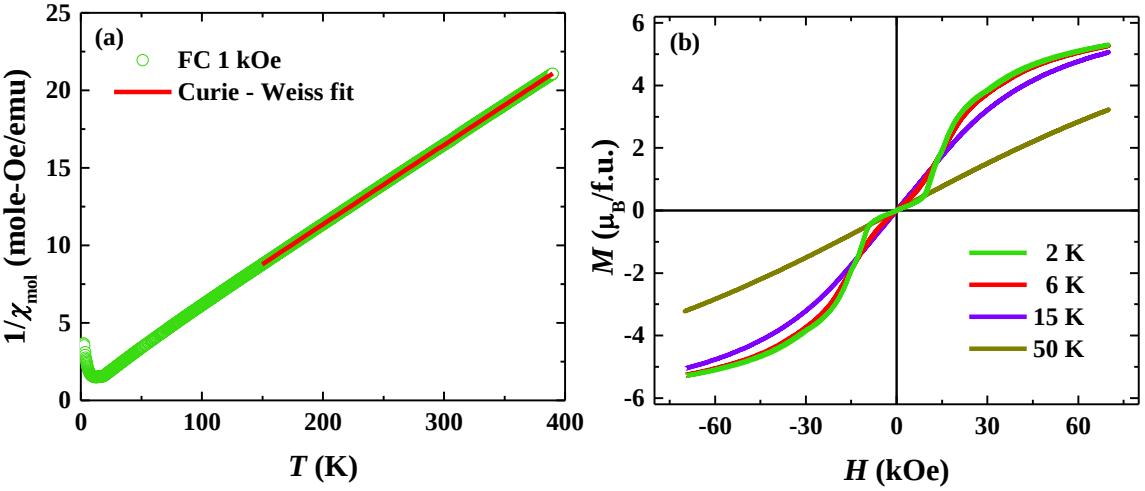

Figure 5.6 (a) Inverse susceptibility ($1/\chi_{mol}$) as a function of temperature. (b) Magnetic field dependent magnetization M (H) at different temperatures.

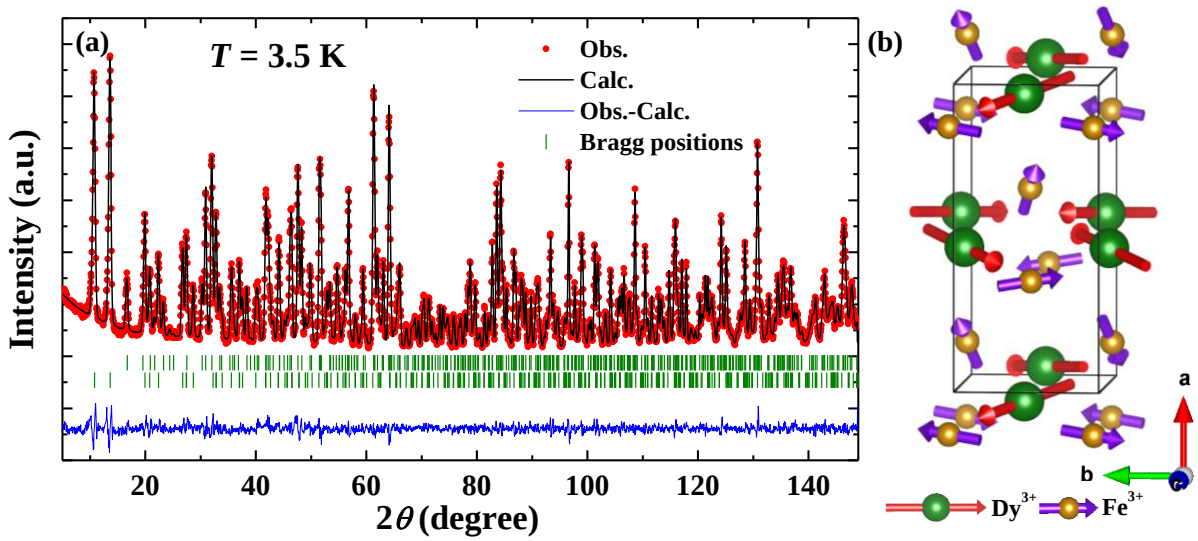

Figure 5.7 (a) Rietveld refinement of neutron diffraction data of $DyFeWO_6$ recorded at 3.5 K. The first and second rows of vertical bars represent the nuclear and magnetic Bragg peak positions, respectively. (b) The obtained magnetic structure of $DyFeWO_6$.

Tables 5.3 Crystallographic parameters of $DyFeWO_6$ at 3.5 K obtained from Rietveld refinement of neutron diffraction data. Ordered magnetic moments at different temperatures are shown at the bottom rows.

a = 10.97334(11) Å, b = 5.18423(5) Å, c = 7.33767(7) Å, $\alpha = \beta = \gamma = 90°$, V = 417.427(7) Å^3, χ^2 = 2.25; Bragg R-factor = 2.22, R_f-factor = 1.22

Name	Wyckoff position	x	y	z	B_{iso} (Å^2)	Occ.
Dy	4a	0.0424(1)	0.4576(2)	0.25	0.43(2)	1
Fe	4a	0.1363(4)	0.9642(10)	0.9936(10)	0.86(9)	1
W	4a	0.3530(6)	0.4572(16)	0.0095(15)	0.07(13)	1
O1	4a	0.9732(7)	0.7639(15)	0.0385(17)	0.23(14)	1
O2	4a	0.5234(10)	0.2579(20)	0.9550(22)	1.48(22)	1
O3	4a	0.2151(8)	0.6088(19)	0.0630(14)	1.47(20)	1
O4	4a	0.2938(6)	0.1290(13)	0.9342(11)	0.11(13)	1
O5	4a	0.1437(3)	0.0593(7)	0.2522(24)	0.83(5)	1
O6	4a	0.1204(3)	0.8290(6)	0.7466(20)	0.56(6)	1

Ordered magnetic moments

T (K)	$\mu_{Dy^{3+}}$ (μ_B)	$\mu_{Fe^{3+}}$ (μ_B)
3.5	7.90(4)	4.48(9)
10	5.71(6)	4.29(12)
15	3.57(9)	3.87(17)

In order to determine the magnetic structure, we have analyzed low temperature neutron diffraction data. In Figure 5.7(a), the neutron diffraction pattern collected at 3.5 K is shown, where Rietveld refinement is performed by considering both magnetic and nuclear structure model. The magnetic structure is solved using symmetry analysis with the programs BasIreps available in FullProf Suite and MAXMAGN provided by Bilbao Crystallographic Server [36]. The 12 basis functions obtained suggest that we have to impose special directions in the representation space (put constraints in the coefficients) in order to get more symmetric magnetic structures, otherwise we obtain triclinic structures. Using MAXMAGN, we obtain three maximal magnetic space groups compatible with the propagation vector **k** = (0, 1/2, 1/2), these are: C_ac, P_ac and P_S1. The magnetic space group C_ac describes correctly the diffraction data and corresponds to a particular selection of basis vectors obtained with BasIreps. Using the Belov-Neronova-Smirnova (BNS) notation, the transformation from the setting we use, related to the paramagnetic basis as (**a**, 2**b**, 2**c**; 0, 0, 0), to the standard BNS cell is (-**c**, **b**, **a**; 0, 1/8, 0), so the **b** - axis is kept and the glide plane *c* of C_ac is the original glide plane *a* perpendicular to the **b** - axis of $Pna2_1$ [37]. The small metric distortion due to the reduction of symmetry to monoclinic cannot be detected with the resolution of our present neutron and synchrotron data. Only an anomaly is seen at T_N^{Fe} in the evolution of the cell parameters as a function of temperature in the synchrotron data. However, very small changes in the intensities of Bragg peaks may contain information about the distortion of the crystal structure. From the symmetry point of view, the magnetic point group associated with the magnetic space group C_ac is $m1'$, where the mirror plane *m* is perpendicular to the **b** - axis of the paramagnetic space group and therefore all the macroscopic physical properties in the magnetically ordered state are driven by this point group. This indicates that the allowed electric polarization is constrained to be within the *m* - plane and thus the electric polarization should be of the form $\mathbf{P}_m = (p_x, 0, p_z)$ in the ordered magnetic state. On the other hand, in the paramagnetic phase where all the properties are driven by the symmetry of $Pna2_11'$, the allowed electric polarization, even if it is not detected experimentally, should be of the form of $\mathbf{P} = (0, 0, p_z)$. Therefore in the magnetic phase a new component is allowed.

In the analysis of neutron diffraction data, we found an unusual behavior of Dy^{3+} magnetism. The neutron diffraction pattern at 15 K could be refined by considering only Fe^{3+} moments, however the magnetic moment of Fe^{3+} becomes 5.7 μ_B which is too high.

This indicates that there should be a contribution from Dy^{3+} moments at 15 K probably induced by the ordering of Fe^{3+} moments. To confirm this, we refined the neutron diffraction data at different temperatures (15, 10 and 3.5 K) including the contribution from Dy^{3+} moments with the same propagation vector of Fe^{3+} spins. This model gave a best fit to the data with good reliability parameters and expected magnetic moments. The obtained crystallographic parameters (at 3.5 K) and the magnetic moments of Fe^{3+} and Dy^{3+} ions at different temperatures are given in Table 5.3.

Figure 5.7(b) shows the obtained magnetic structure at 3.5 K. Dy^{3+} and Fe^{3+} spins are arranged in an unusual manner. There are two different Fe^{3+} spin sites. The Fe^{3+} spins are aligned antiferromagnetically within each site, but between the sites (along the *a*-axis) they are nearly perpendicularly aligned with respect to each other and thus the magnetic structure is strongly non collinear. Similar non collinear arrangement of Dy^{3+} spins is found with a tendency to get nearly perpendicular Dy^{3+} moments at low temperature, which could be due to the single - ion anisotropy of Dy^{3+} ions. The magnetic structure remains same in the temperature range between 3.5 K and 18 K, despite the independent magnetic correlations developed among Dy^{3+} spins below 5 K. The obtained magnetic structure is essentially non-centrosymmetric as the underlying crystal structure is polar. This kind of magnetic structure is different from the known magnetic structures which induce spontaneous electric polarization. Further investigations are necessary to understand the observed spin configuration.

5.3.2.3 Magnetodielectric effect

Figure 5.8(a) shows the temperature dependence of dielectric constant ε_r (T) measured with different frequencies. A clear anomaly is observed around magnetic ordering temperature T_N^{Fe} = 18 K in ε_r (T), where an anomaly in dielectric loss (not shown) is also observed. These anomalies in ε_r (T) and loss do not shift with varying frequency. Further, the value of loss is very small (~ 0.02) at 50 kHz around T_N^{Fe}. The observation of dielectric anomaly at the magnetic ordering temperature indicates a strong correlation between magnetic and dielectric properties. This correlation is further supported by the temperature dependent dielectric constant measurements at 50 kHz under various magnetic fields, which is shown in Figure 5.8(b). The dielectric anomaly at T_N^{Fe} is strongly suppressed by applied magnetic fields. Thus, Figure 5.8(a, b) confirm that a strong magnetodielectric effect is present below T_N^{Fe} in the present system. At further

lower temperature, a broad peak is observed in ε_r (T) which increases with increasing magnetic fields, indicating possible field induced changes in magnetic structure of Dy^{3+} spins.

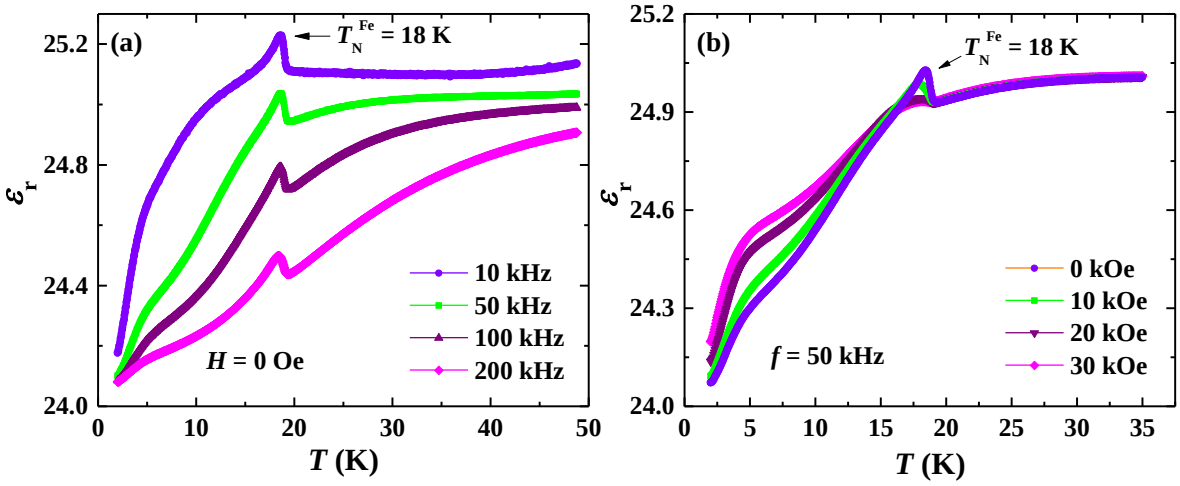

Figure 5.8 (a) Temperature dependence of dielectric constant ε_r (T) of $DyFeWO_6$ measured under different frequencies. (b) Temperature dependent dielectric constant at 50 kHz measured under different applied magnetic fields.

5.3.2.4 Magnetoelectric multiferroicity

The pyroelectric current measurements were carried out in order to investigate whether or not the dielectric anomaly is associated with the appearance of electric polarization. For pyroelectric current measurements, the sample was poled under an applied electric field of E = ± 9.2 kV/cm and different magnetic fields. A sharp asymmetric pyroelectric current peak is observed around T_N^{Fe} under zero magnetic field and the electric polarization ΔP (T) obtained by integrating the pyroelectric current with measurement duration is shown in Figure 5.9, which indicates the appearance of electric polarization below T_N^{Fe}. Note that the present compound is polar and thus there can be a non-zero electric polarization in the paramagnetic state. However, we could not detect measurable electric polarization above T_N^{Fe}, which indicates that the compound is either only pyroelectric or the electric polarization is too small to be detected. Thus, the observed electric polarization below T_N^{Fe} is the result of the possible enhancement of the high temperature electric polarization (p_z) and the emergence of a new component p_x of electric polarization due to magnetic ordering of Fe^{3+} ions, as discussed above. Further, as

shown in Figure 5.9, the electric polarization is also affected by the external magnetic fields, as observed in ε_r (T) in Figure 5.8(b), and is completely suppressed under a magnetic field of 40 kOe. Magnetic field dependent electric polarization ΔP (H) measured at 10 K is shown in the inset of Figure 5.9, where the magnetic field was varied from 0 kOe to 50 kOe with a rate of 120 Oe/sec at 10 K after poling the sample with an electric field of E = + 9.2 kV/cm. The ΔP (H) curve clearly demonstrates the suppression of electric polarization under applied magnetic field. Thus, the presence of dielectric anomaly and electric polarization below antiferromagnetic ordering temperature (T_N^{Fe}) of Fe^{3+} spins and their response under applied magnetic fields suggest that the compound $DyFeWO_6$ is a magnetoelectric multiferroic or type-II multiferroic. However the obtained magnetic point group $m1'$ does not allow the first order magnetoelectric effect, so only the second order inverse magnetoelectric tensor $\left(P_i = \alpha_{ijk}^{T} H_j H_k\right)$ is allowed. Though the pyroelectric current peak can be switched in the polycrystalline sample by applying opposite poling electric field (not shown), an experimental study on single crystal is necessary to confirm the switching of electric polarization.

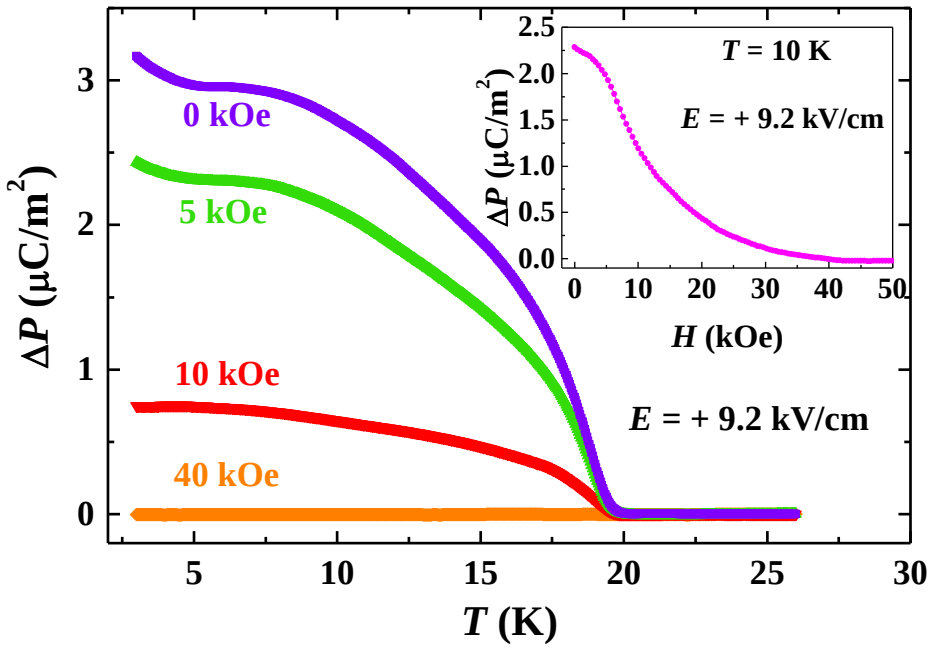

Figure 5.9 Temperate evolution of electric polarization ΔP (T) of $DyFeWO_6$ measured under various magnetic fields. The inset figure shows the change in electric polarization ΔP (H) with magnetic field at 10 K.

5.3.2.5 DC-biased current

DC-biased current measurements were carried out to confirm that the observed pyroelectric current peak near T_N^{Fe} is due to the depolarization current associated with electric dipoles and not due to the thermally stimulated free charge carriers. It is recently reported that a simple dc-biased current measurement can distinguish these two different origins [38]. The temperature dependence of dc-biased current measured under an applied electric field E_{dc} = + 9.2 kV/cm is shown in Figure 5.10, which exhibits a broad upward and then a sharp downward peak with increasing temperature. The upward broad peak appears due to the polarization of the material, which slowly increases with increasing temperature in the presence of electric field. The downward peak around T_N^{Fe} is associated with the depolarization of the polarized dipoles. A small shift of the depolarization current peak could be due to the higher warming rate (10 K/min). These results confirm the intrinsic nature of the electric polarization. Further, the typical feature of the dc-biased current is suppressed under a magnetic field of 40 kOe, which is consistent with the suppression of electric polarization by magnetic field as shown in Figure 5.9.

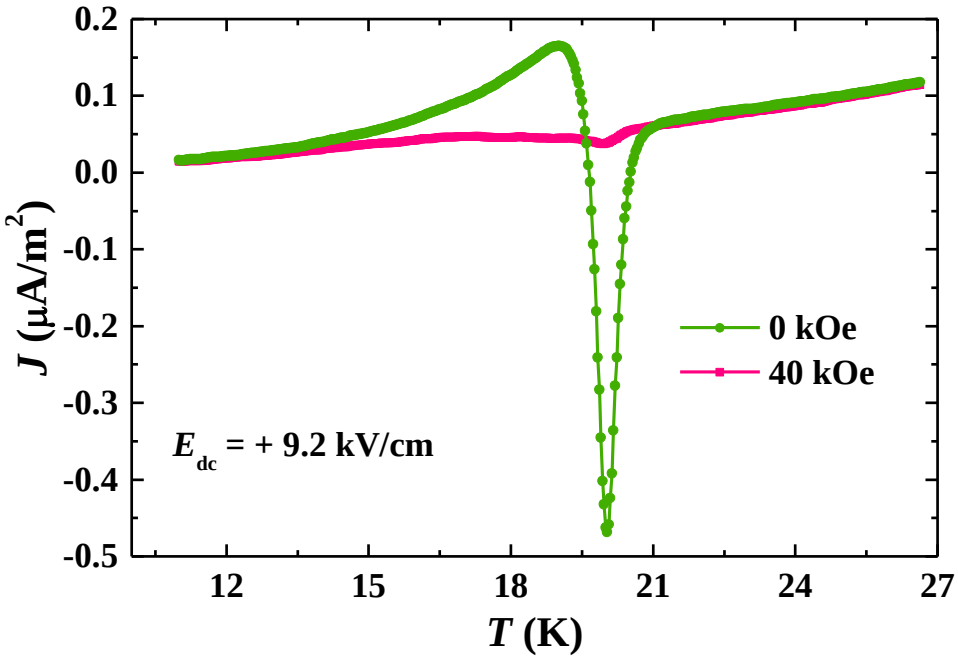

Figure 5.10 Temperature variation of dc-biased current of $DyFeWO_6$ measured with an electric field of E_{dc} = + 9.2 kV/cm and magnetic fields of 0 kOe and 40 kOe.

5.3.2.6 Effect of high magnetic fields

As discussed above, the electric polarization disappears under a magnetic field of 40 kOe. Some interesting results are observed under higher magnetic fields (> 60 kOe). As shown in Figure 5.11(a), the λ-type peak in heat capacity C_P (T), that is observed at zero magnetic field, is smeared out under high magnetic field and a new magnetic field induced peak is appeared around T^* ~ 15 K. An anomaly in dielectric constant ε_r (T) is observed at the same temperature under high magnetic fields (see Figure 5.11(b)). Interestingly, as shown in Figure 5.11(c), the electric polarization, which is disappeared at 40 kOe, is reappeared at T^* ~ 15 K under higher magnetic fields and increases with increasing magnetic field. The magnetic field induced reappearance of electric polarization is very unusual. Neutron diffraction under high magnetic field and single crystal study are necessary to understand this unusual phenomenon.

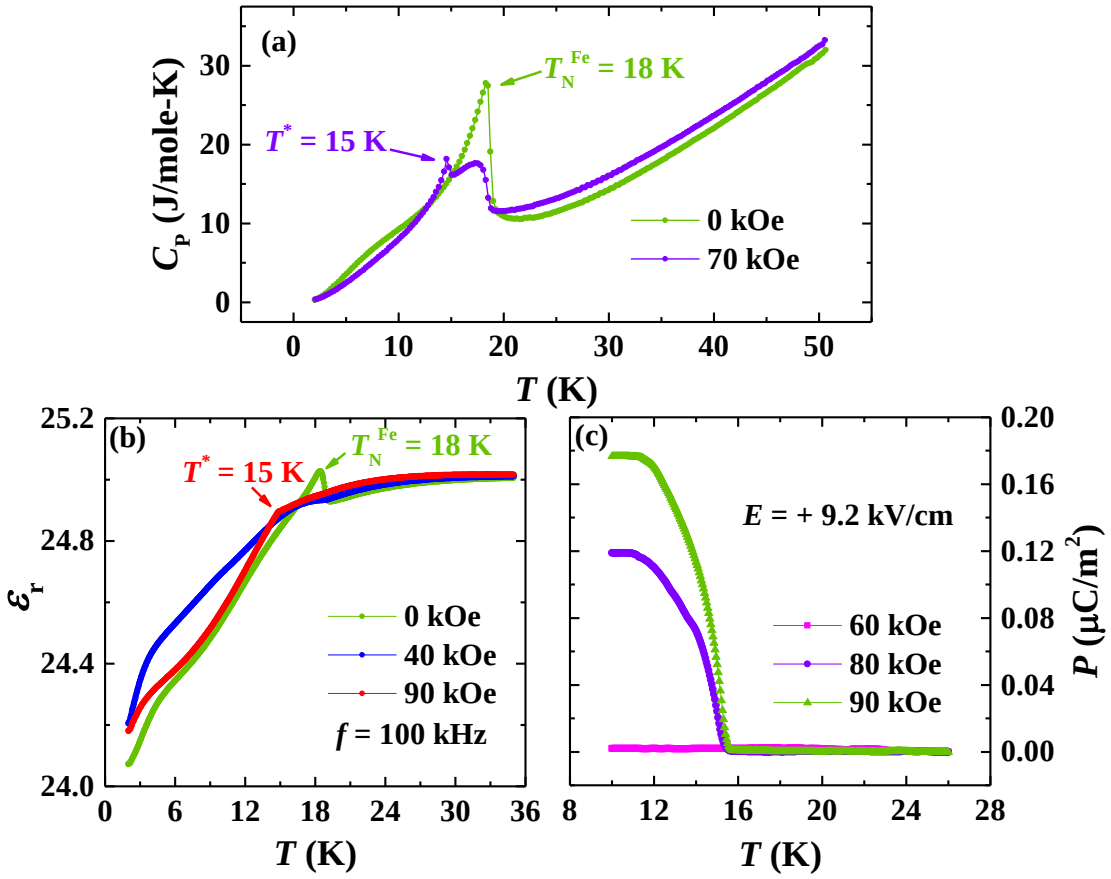

Figure 5.11 (a) Heat capacity C_P (T) of $DyFeWO_6$ under different magnetic fields, (b) Effect of high magnetic field on dielectric constant ε_r (T) of $DyFeWO_6$, (c) Reappearance of electric polarization ΔP (T) in $DyFeWO_6$ under higher magnetic fields.

5.3.2.7 Calculated electric polarization

We have refined the most relevant structural modes amplitudes in order to determine the most important structural change accompanying the magnetic ordering using the approach of symmetry modes analysis [39]. There are two active representations of the paramagnetic group $Pna2_11'$ for structural distortions, GM1 and GM4, and the global refined amplitudes for both representations are: A_GM1= 0.04(1) Å and A_GM4= 0.17(8) Å. The most important displacements correspond to the parent O2, O4, and O6 (which are split into two independent atoms each) with approximate displacements of 0.035 Å/atom with respect to the paramagnetic phase.

We have calculated ionic polarization assuming formal charges and experimental structural data with the help of CrysCalCon program available in FullProf. The calculated value of ionic polarization in the polar paramagnetic state at 30 K is 6300 $\mu C/m^2$ along the **c** - axis, which originates due to a shift of barycenter of the positive and negative charges by 0.0034 Å . Though this value of polarization should be measurable experimentally, we could not detect any polarization because of the fact that there is no polar-nonpolar phase transition in the accessible temperature range and also due to the polycrystalline nature of the sample. On the contrary, the same calculation performed in the magnetically ordered state (3.5 K) using the resulting crystal structure from the refinement of the symmetry mode amplitudes gives a value of an order of magnitude greater: 75,560 $\mu C/m^2$ with $\mathbf{P} \approx$ (-62,200, 0, 42,900) $\mu C/m^2$, where p_x arises solely due to magnetic ordering. However, the low value of electric polarization obtained from pyroelectric current measurements could be due to the polycrystalline nature of the sample [21].

5.3.3 Results on $EuFeWO_6$

Rietveld refinement is performed on the room temperature synchrotron X-ray diffraction data of $EuFeWO_6$ with the space group $Pna2_1$ and the result is shown in Figure 5.12, where the first row of vertical bars represents the Bragg positions of $EuFeWO_6$ and second row of vertical bars represents the Bragg positions of TiO_2 from cryostat. The polar crystal structure is further confirmed by the room temperature SHG measurements. The structural parameters obtained from Rietveld refinement are given in Table 5.4.

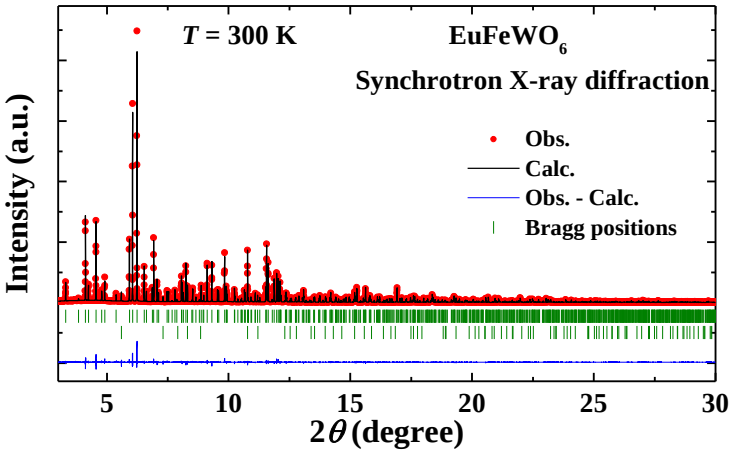

Figure 5.12 Rietveld refinement of synchrotron X-ray (λ = 0.3171 Å) diffraction data of $EuFeWO_6$ collected at room temperature. The second row of vertical bars represents the Bragg positions of TiO_2 from cryostat.

Tables 5.4 Structural parameters of $EuFeWO_6$ obtained from Rietveld refinement of synchrotron X-ray (λ = 0.3171 Å) diffraction data collected at room temperature

Name	Wyckoff position	*x*	*y*	*z*	B_{iso} (Å^2)	Occ.
Eu	4*a*	0.0421(1)	0.4574(2)	0.25	0.83(1)	1
Fe	4*a*	0.1387(3)	0.9658(5)	0.9943(10)	0.61(5)	1
W	4*a*	0.3536(1)	0.4523(2)	0.0053(3)	0.67(1)	1
O1	4*a*	0.9719(11)	0.7747(23)	0.0419(21)	0.78(8)	1
O2	4*a*	0.5215(11)	0.2601(24)	0.9652(21)	0.78(8)	1
O3	4*a*	0.2146(11)	0.6153(23)	0.0636(17)	0.78(8)	1
O4	4*a*	0.2903(12)	0.1344(25)	0.9442(17)	0.78(8)	1
O5	4*a*	0.1407(9)	0.0545(20)	0.2625(18)	0.78(8)	1
O6	4*a*	0.1204(9)	0.8369(19)	0.7487(24)	0.78(8)	1

Space group: $Pna2_1$; *a* = 10.97750(1) Å, *b* = 5.24939(1) Å, *c* = 7.39788(1) Å, $\alpha = \beta = \gamma = 90°$, *V* = 426.304(1) Å^3; χ^2 = 1.81, Bragg *R*-factor = 3.96, R_f-factor = 4.92

Cation	O1	O2	O3	O4	O5	O6
Eu	2.40(1) 2.49(1)	2.35(1) 2.41(1)	2.49(1)	2.51 (1)	2.37(1)	2.36(1)
Fe	2.12(1)	1.94(1)	2.08(1)	1.92(1)	2.04(1)	1.95(2)
W	1.95(1)	2.12(1)	1.80(1)	1.87(1)	1.88(1)	1.92(1)

Eu_{BVS}	3.16(4)
Fe_{BVS}	3.12(5)
W_{BVS}	6.10(9)

Temperature dependence of field-cooled (FC) magnetization M (T) is shown in Figure 5.13(a). A peak is found around T_N^{Fe} ~ 17 K indicating the long-range magnetic ordering of Fe^{3+} ions, which is further confirmed by a sharp λ-type peak in C_P (T), as shown in Figure 5.13(b). Magnetic field dependent magnetization M (H) at 2 K is consistent with antiferromagnetic ordering (shown in the inset of Figure 5.13(a)). The analysis of high temperature magnetization data with the Curie-Weiss law suggests that Eu^{3+} ions contribute to the effective paramagnetic moment, however it remains paramagnetic down to 2 K as suggested by M (T) and C_P (T) data. This paramagnetic behavior of Eu^{3+} ions is consistent with the increase in M (T) at low temperatures. Temperature dependent dielectric constant ε_r (T), as shown in Figure 5.13(c), possesses a

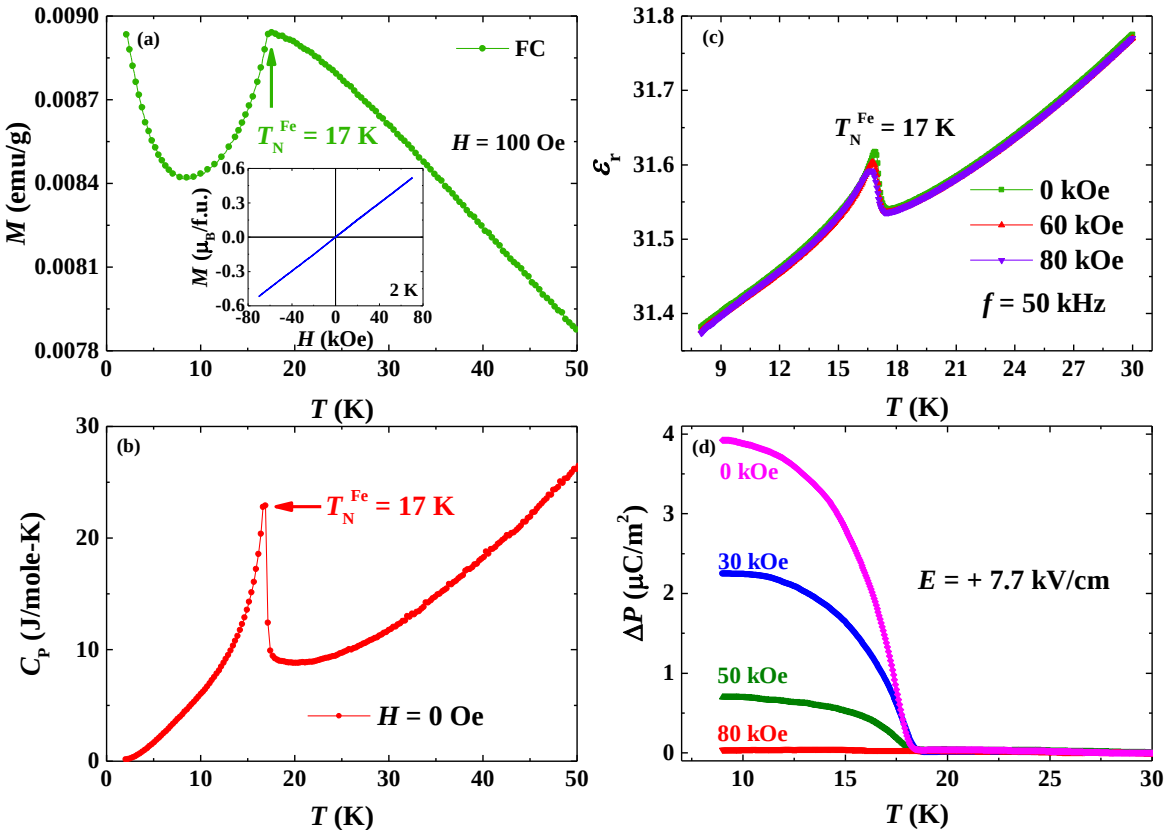

Figure 5.13 (a) FC magnetization M (T) as a function of temperature measured under a magnetic field of 100 Oe in $EuFeWO_6$. The inset shows magnetic field dependent magnetization at 2 K. (b) Temperature variation of heat capacity C_P (T) of $EuFeWO_6$. (c) Temperature dependent dielectric constant ε_r (T) of $EuFeWO_6$ measured with 50 kHz under various magnetic fields. (d) Electric polarization ΔP (T) as a function of temperature in $EuFeWO_6$ under measured different magnetic fields.

sharp peak around T_N^{Fe} under zero magnetic field. In the presence of applied magnetic fields, the dielectric peak seems to be smeared out. Similar to $DyFeWO_6$, electric polarization ΔP (T) is found below T_N^{Fe} in zero magnetic field as shown in Figure 5.13(d), which is suppressed with increasing magnetic field. However, unlike $DyFeWO_6$, the electric polarization in $EuFeWO_6$ is suppressed at relatively large magnetic field (80 kOe). These results suggest that $EuFeWO_6$ is also a type-II multiferroic.

5.3.4 Results on $TbFeWO_6$

In order to determine the crystal structure of $TbFeWO_6$, a combined Rietveld refinement of room temperature synchrotron X-ray and neutron diffraction is carried out and the results are shown in Figure 5.14(a, b). The structural parameters are given in Table 5.5. Similar to Dy and Eu - compound, $TbFeWO_6$ also crystallizes in an ordered aeschynite-type polar crystal structure ($Pna2_1$).

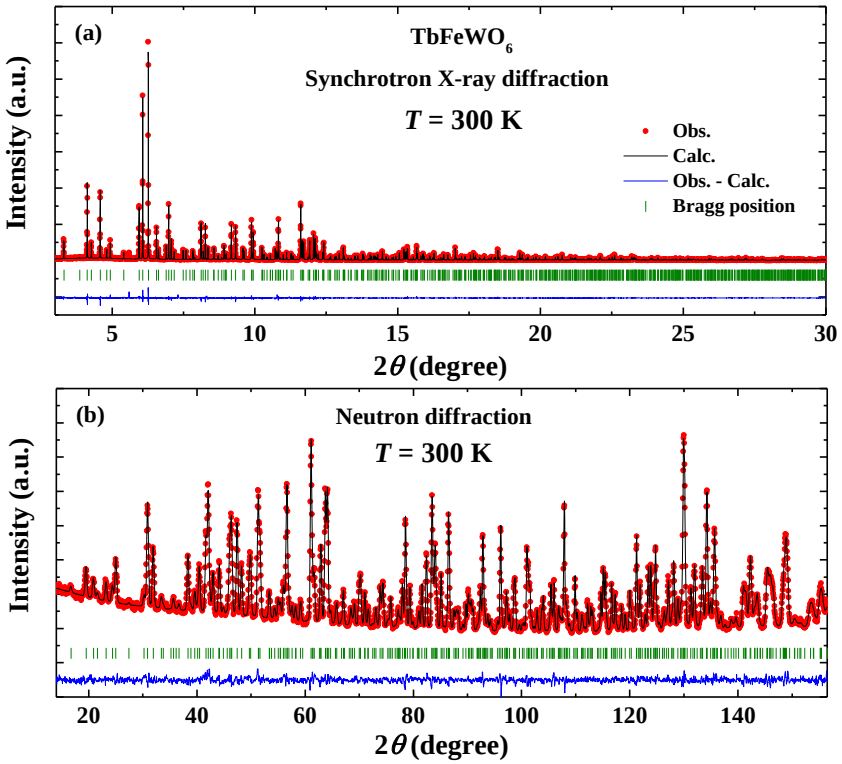

Figure 5.14 (a, b) Results of combined Rietveld refinements of synchrotron X-ray (λ = 0.3171 Å) and neutron (λ = 1.594 Å) diffraction data of $TbFeWO_6$ recorded at room temperature. The peaks of TiO_2 from cryostat in synchrotron X-ray diffraction data are not considered (kept in excluded region) in the refinement process.

Tables 5.5 Structural parameters of $TbFeWO_6$ obtained from combined Rietveld refinement of room temperature synchrotron X-ray (λ = 0.3171 Å) and neutron (λ = 1.594 Å) diffraction data

Name	Wyckoff position	*x*	*y*	*z*	B_{iso} (Å^2)	Occ.
Tb	4*a*	0.0424(1)	0.4570(3)	0.25	0.65(2)	1
Fe	4*a*	0.1377(2)	0.9658(3)	0.9924(6)	0.75(3)	1
W	4*a*	0.3539(1)	0.4516(3)	0.0056(5)	0.43(2)	1
O1	4*a*	0.9700(4)	0.7690(9)	0.0429(10)	0.70(8)	1
O2	4*a*	0.5215(4)	0.2550(10)	0.9625(10)	0.92(9)	1
O3	4*a*	0.2127(4)	0.6131(9)	0.0628(11)	0.95(8)	1
O4	4*a*	0.2922(4)	0.1313(9)	0.9338(10)	0.72(8)	1
O5	4*a*	0.1438(2)	0.0576(5)	0.2565(12)	0.88(4)	1
O6	4*a*	0.1206(2)	0.8301(5)	0.7462(13)	0.87(4)	1

Space group: $Pna2_1$; a = 10.97391(3) Å, b = 5.20805(1) Å, c = 7.36294(2) Å, $\alpha = \beta = \gamma = 90°$, V = 420.812(2) Å^3; χ^2 = 2.09 (for neutron), χ^2 = 1.54 (for synchrotron); Bragg R-factor = 3.01, R_f-factor = 1.89 (for neutron); Bragg R-factor = 5.88, R_f-factor = 5.64 (for synchrotron)

Cation	O1	O2	O3	O4	O5	O6
Tb	2.36(1) 2.46(1)	2.31(1) 2.40(1)	2.46(1)	2.44(1)	2.36(0)	2.33(0)
Fe	2.14(0)	1.95(0)	2.08(1)	1.95(1)	2.00(1)	1.95(1)
W	1.95(0)	2.13(0)	1.81(0)	1.88(1)	1.92(1)	1.90(1)
Tb_{BVS}					3.06(2)	
Fe_{BVS}					3.08(3)	
W_{BVS}					5.96(5)	

Figure 5.15(a) shows the field-cooled (FC) magnetization M (T) as a function of temperature data measured with 100 Oe magnetic field, where a sharp peak is observed at 2.4 K, while two sharp λ-type peak around 15 K and 2.4 K in heat capacity C_P (T) are observed, as shown in Figure 5.15(b), suggesting long-range antiferromagnetic ordering of Fe^{3+} and Tb^{3+} spins, respectively. No anomaly is found around the Fe^{3+} ordering temperature (T_N^{Fe} ~ 15 K) in M (T) because of relatively large paramagnetic moment of Tb^{3+} ions. Unlike $DyFeWO_6$, where the Dy^{3+} moments are induced by the ordered Fe^{3+} moments at T_N^{Fe}, the presence of the peak in C_P (T) at T_N^{Tb} ~ 2.4 K suggests that Tb^{3+}

moments may remain paramagnetic above T_N^{Tb} ~ 2.4 K. Low temperature neutron diffraction measurements are necessary to confirm this suggestion. *M* (*H*) data (shown in the inset of Figure 5.15(a)) suggest an antiferromagnetic behavior below T_N^{Fe} ~ 15 K, while a metamagnetic behavior at 2 K due to the field induced transitions associated with Tb^{3+} ordering. Temperature variation of dielectric constant ε_r (*T*) measured with 50 kHz under various magnetic fields are shown in Figure 5.15(c). Two sharp anomalies are observed around T_N^{Fe} ~ 15 K and T_N^{Tb} ~ 2.4 K in ε_r (*T*) under zero magnetic field. Under applied magnetic fields, the anomaly around T_N^{Fe} is suppressed and becomes broad, while the anomaly around T_N^{Tb} is disappeared at high magnetic field. Temperature evolution of the electric polarization ΔP (*T*) under different magnetic fields is shown in Figure 5.15(d).

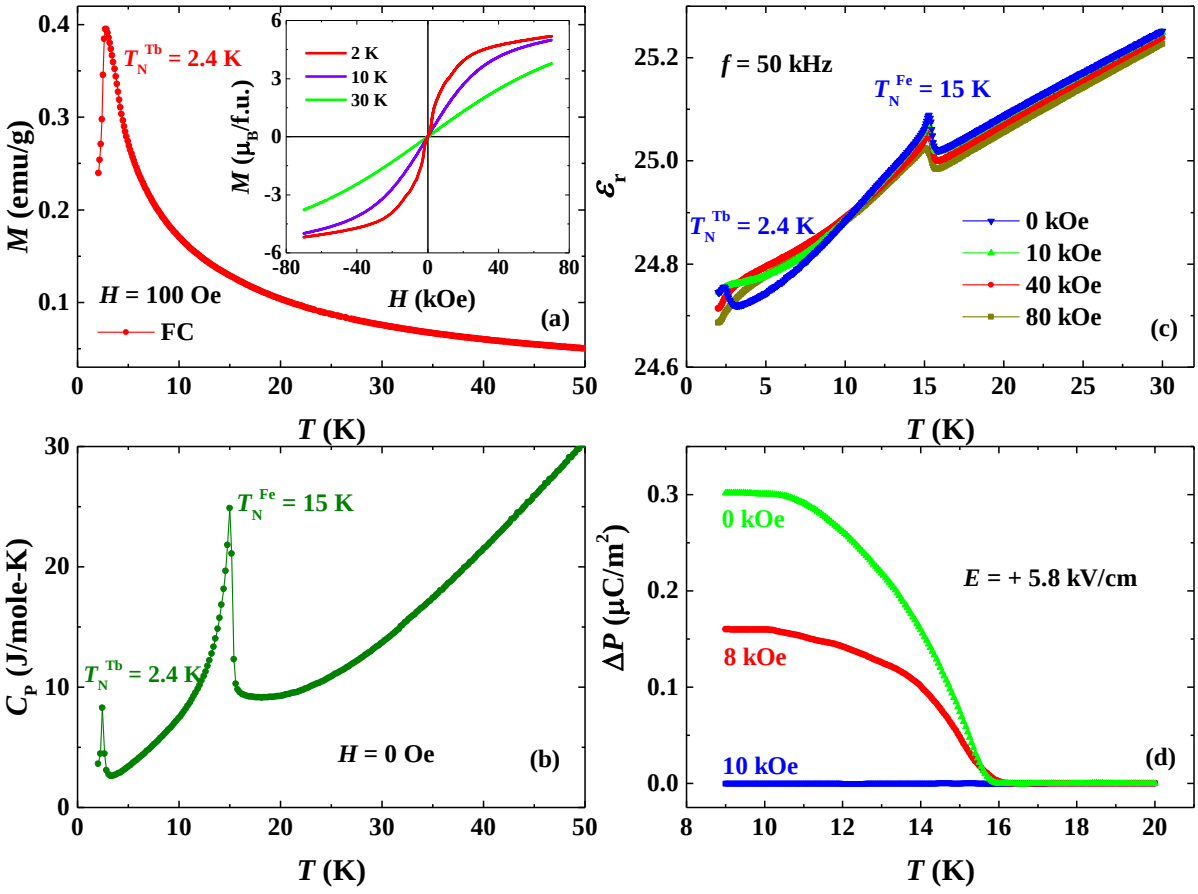

Figure 5.15 (a) FC magnetization *M* (*T*) *vs.* temperature data of $TbFeWO_6$ measured with a magnetic field of 100 Oe. Inset shows the *M* (*H*) data measured at different temperatures. (b) Temperature dependence of heat capacity C_P (*T*) of $TbFeWO_6$. (c) Temperature variation of dielectric constant ε_r (*T*) measured with 50 kHz under various magnetic fields. (d) Evolution of electric polarization ΔP (*T*) with temperature measured with an electric field of *E* = + 5.8 kV/cm and different magnetic fields in $TbFeWO_6$.

The appearance of non-zero electric polarization below T_N^{Fe} ~ 15 K under zero-magnetic field suggests the presence of multiferroicity in $TbFeWO_6$. Further, the electric polarization is vanished under an applied magnetic field of 10 kOe, indicating the presence of strong magnetoelectric effect.

5.3.5 Results on $YFeWO_6$

Unlike other compounds, in $YFeWO_6$ we do not have additional complexity due to the interplay between R^{3+} and Fe^{3+} ions, because Y^{3+} is nonmagnetic and therefore the magnetoelectric properties should arise from Fe-ions only. The result of Rietveld refinement of synchrotron X-ray diffraction data is shown in Figure 5.16 and the structural parameters are given in Table 5.6.

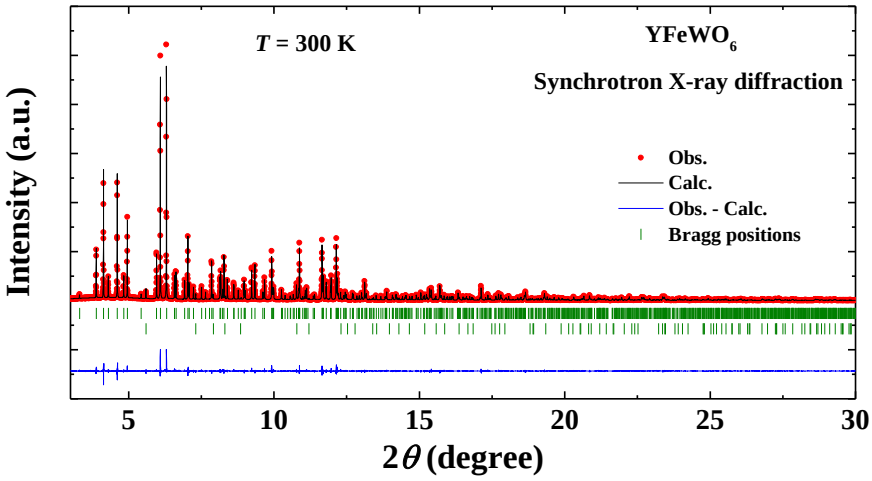

Figure 5.16 Synchrotron X-ray (λ = 0.3171 Å) diffraction data of $YFeWO_6$ collected at 300 K. The second row of vertical bars indicates the Bragg positions of TiO_2 in cryostat.

Temperature variation of field-cooled (FC) magnetization M (T) and heat capacity C_P (T) data are shown in Figure 5.17(a, b), respectively. Magnetic field dependent magnetization M (H) at 2 K is shown in the inset of Figure 5.17(a). An anomaly is observed around 15 K in M (T), where a sharp peak is found in C_P (T) data. These anomalies along with the linear behavior of M (H) data at 2 K suggest antiferromagnetic ordering of Fe^{3+} moments at T_N^{Fe} ~ 15 K. Dielectric constant ε_r (T) data measured under various magnetic fields are shown in Figure 5.17(c). A sharp dielectric anomaly is found in zero-magnetic field around T_N^{Fe} and it is not affected by the applied magnetic fields but

Tables 5.6 Crystallographic parameters of $YFeWO_6$ obtained from Rietveld refinement of room temperature synchrotron X - ray (λ = 0.3171 Å) diffraction data

Name	**Wyckoff position**	***x***	***y***	***z***	B_{iso} **(Å^2)**	**Occ.**
Y	4*a*	0.0427(1)	0.4584(3)	0.25	0.64(2)	1
Fe	4*a*	0.1377(2)	0.9656(4)	0.9929(11)	0.98(5)	1
W	4*a*	0.3542(1)	0.4515(1)	0.0057(4)	0.62(1)	1
O1	4*a*	0.9701(10)	0.7736(19)	0.0433(20)	0.89(8)	1
O2	4*a*	0.5214(10)	0.2487(19)	0.9648(21)	0.89(8)	1
O3	4*a*	0.2111(10)	0.6122(21)	0.0637(16)	0.89(8)	1
O4	4*a*	0.2883(11)	0.1362(23)	0.9358(16)	0.89(8)	1
O5	4*a*	0.1399(10)	0.0644(21)	0.2607(17)	0.89(8)	1
O6	4*a*	0.1198(10)	0.8235(20)	0.7427(21)	0.89(8)	1

Space group: *Pna*2$_1$; *a* = 10.96762(2) Å, *b* = 5.16523(1) Å, *c* = 7.33217(1) Å, $\alpha = \beta = \gamma = 90°$, *V* = 415.370(1) Å^3; χ^2 = 2.72, Bragg *R*-factor = 4.58, R_f-factor = 4.80

Cation	**O1**	**O2**	**O3**	**O4**	**O5**	**O6**
Y	2.37(1) 2.46(1)	2.28(1) 2.36(1)	2.43(1)	2.48(1)	2.30(1)	2.30(1)
Fe	2.12(1)	1.96(1)	2.06(1)	1.92(1)	2.03(1)	1.99(2)
W	1.92(1)	2.13(1)	1.82(1)	1.86(1)	1.89(1)	1.88(1)
	Y_{BVS}				3.13(4)	
	Fe_{BVS}				3.08(4)	
	W_{BVS}				6.18(8)	

shifts slightly to a lower temperature at 80 kOe. In Figure 5.17(d), temperature dependent electric polarization ΔP (T) data measured under different magnetic fields are shown. Similar to other compounds, the electric polarization is enhanced below T_N^{Fe} and it decreases with increasing magnetic fields. However, in contrast to other *R*FeWO$_6$ with magnetic *R*-ions, the electric polarization in YFeWO$_6$ does not disappear even at 80 kOe. The observation of electric polarization below T_N^{Fe} ~ 15 K in YFeWO$_6$ suggests that the emergence of electric polarization in all the *R*FeWO$_6$ compounds is solely due to the long-range magnetic ordering of Fe^{3+} moments. The magnetic *R*-ion moments only affect the polarization through the coupling between magnetic *R*- and Fe-spins. Though we have not determined the magnetic structure in compounds other than DyFeWO$_6$, the

appearance of electric polarization below T_N^{Fe} suggests that all the compounds should have a similar magnetic structure of Fe^{3+} spins. Neutron diffraction study on all the compounds is required to verify the magnetic structure.

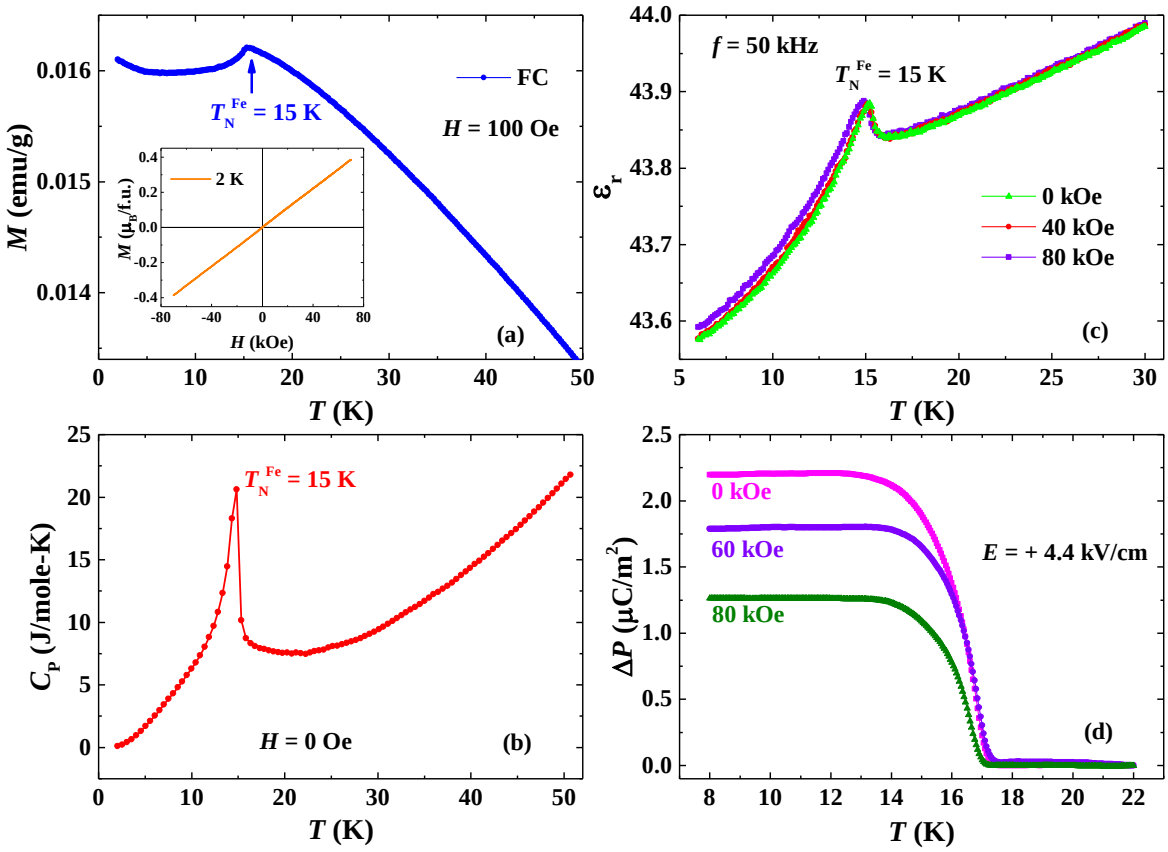

Figure 5.17 (a) Temperature dependent field-cooled (FC) magnetization of $YFeWO_6$ measured under a magnetic field of 100 Oe. M (H) data at 2 K is shown in the inset figure. (b) Heat capacity C_P (T) data of $YFeWO_6$. (c) Temperature dependence of dielectric constant ε_r (T) measured with 50 kHz under different magnetic fields (d) Variation of electric polarization ΔP (T) with temperature measured under different magnetic fields in $YFeWO_6$.

5.4 Conclusion

We have determined the complete crystal structure of a series of oxides, RFeWO$_6$ (R = Dy, Eu, Tb and Y), which belong to a polar aeschynite-type structure. It is demonstrated that these polar magnets constitute a new family of magnetoelectric multiferroics or type-II multiferroics. An unusual commensurate and noncollinear magnetic structure of Fe^{3+} spins, which is quite different from the known magnetic

structures giving rise to spontaneous electric polarization, is responsible for inducing a new component (p_x) of electric polarization below the magnetic ordering temperature. Further, the coupling between magnetic *R* and Fe-ions has a strong effect on the electric polarization. Theoretical investigations are required to understand the mechanism of the enhancement of electric polarization associated with magnetic ordering and magnetoelectric effect. These results of type-II multiferroicity in RFeWO$_6$ will help to design and predict new polar magnets for magnetoelectric multiferroic properties.

References

[1] D. Khomskii, *Physics* **2,** 20 (2009).

[2] W. Eerenstein, N. Mathur, and J. F. Scott, *Nature* **442,** 759 (2006).

[3] N. A. Spaldin, S.-W. Cheong, and R. Ramesh, *Phys. Today* **63,** 38 (2010).

[4] S.-W. Cheong and M. Mostovoy, *Nat. Mater.* **6,** 13 (2007).

[5] Y. Tokura and S. Seki, *Adv. Mater.* **22,** 1554 (2010).

[6] Y. Tokura, S. Seki, and N. Nagaosa, *Rep. Prog. Phys.* **77,** 076501 (2014).

[7] T. Kimura, *Annu. Rev. Mater. Res.* **37,** 387 (2007).

[8] G. Smolenskiĭ and I. Chupis, *Sov. Phys. Usp.* **25,** 475 (1982).

[9] J. Wang, J. Neaton, H. Zheng, V. Nagarajan, S. Ogale, B. Liu, D. Viehland, V. Vaithyanathan, D. Schlom, and U. Waghmare, *Science* **299,** 1719 (2003).

[10] J. Scott and R. Blinc, *J. Phys. Condens. Matter* **23,** 113202 (2011).

[11] M. Eibschütz, H. Guggenheim, S. Wemple, I. Camlibel, and M. DiDomenico, *Phys. Lett. A* **29,** 409 (1969).

[12] C. Ederer and N. A. Spaldin, *Phys. Rev. B* **74,** 024102 (2006).

[13] T. Kurumaji, S. Ishiwata, and Y. Tokura, *Phys. Rev. X* **5,** 031034 (2015).

[14] Y. Wang, G. L. Pascut, B. Gao, T. A. Tyson, K. Haule, V. Kiryukhin, and S.-W. Cheong, *Sci. Rep.* **5** (2015).

[15] T. Kurumaji, S. Ishiwata, and Y. Tokura, *Phys. Rev. B* **95,** 045142 (2017).

[16] V. Caignaert, A. Maignan, K. Singh, C. Simon, V. Pralong, B. Raveau, J. F. Mitchell, H. Zheng, A. Huq, and L. Chapon, *Phys. Rev. B* **88,** 174403 (2013).

[17] R. Johnson, K. Cao, F. Giustino, and P. Radaelli, *Phys. Rev. B* **90,** 045129 (2014).

[18] R. Fishman, S. Bordács, V. Kocsis, I. Kézsmárki, J. Viirok, U. Nagel, T. Rõõm, A. Puri, U. Zeitler, and Y. Tokunaga, *Phys. Rev. B* **95,** 024423 (2017).

[19] Y. S. Oh, S. Artyukhin, J. J. Yang, V. Zapf, J. W. Kim, D. Vanderbilt, and S.-W. Cheong, *Nat. Commun.* **5,** 3201 (2014).

[20] M. R. Li, D. Walker, M. Retuerto, T. Sarkar, J. Hadermann, P. W. Stephens, M. Croft, A. Ignatov, C. P. Grams, and J. Hemberger, *Angew. Chem. Int. Ed.* **52,** 8406 (2013).

[21] M.-R. Li, P. W. Stephens, M. Retuerto, T. Sarkar, C. P. Grams, J. Hemberger, M. C. Croft, D. Walker, and M. Greenblatt, *J. Am. Chem. Soc.* **136,** 8508 (2014).

[22] M. R. Li, M. Retuerto, D. Walker, T. Sarkar, P. W. Stephens, S. Mukherjee, T. S. Dasgupta, J. P. Hodges, M. Croft, and C. P. Grams, *Angew. Chem. Int. Ed.* **53,** 10774 (2014).

[23] M. R. Li, M. Croft, P. W. Stephens, M. Ye, D. Vanderbilt, M. Retuerto, Z. Deng, C. P. Grams, J. Hemberger, and J. Hadermann, *Adv. Mater.* **27,** 2177 (2015).

[24] L. Jahnberg, *Acta Chem. Scand.* **71,** 2548 (1963).

[25] G. J. Thorogood, M. Avdeev, and B. J. Kennedy, *Solid State Sci* **12,** 1263 (2010).

[26] R. Salmon, H. Baudry, J. Grannec, and G. Le Flem, *Revue de Chimie Minerale* **11,** 71 (1974).

[27] F. Fauth, I. Peral, C. Popescu, and M. Knapp, *Powder Diffraction* **28,** S360 (2013).

[28] F. Fauth, R. Boer, F. Gil-Ortiz, C. Popescu, O. Vallcorba, I. Peral, D. Fullà, J. Benach, and J. Juanhuix, *EPJ Plus* **130,** 160 (2015).

[29] S. Kurtz and T. Perry, *J. Appl. Phys.* **39,** 3798 (1968).

[30] K. E. Rieckhoff and W. L. Peticolas, *Science* **147,** 610 (1965).

[31] K. M. Ok, E. O. Chi, and P. S. Halasyamani, *Chem. Soc. Rev.* **35,** 710 (2006).

[32] J. Rodriguez-Carvajal, in *FULLPROF: a program for Rietveld refinement and pattern matching analysis*, 1990 (Toulouse, France:[sn]).

[33] S. Ivantchev, E. Kroumova, G. Madariaga, J. Perez-Mato, and M. Aroyo, *J. Appl. Crystallogr.* **33,** 1190 (2000).

[34] V. A. Streltsov and N. Ishizawa, *Acta Crystallogr., Sect. B: Struct. Sci* **55,** 1 (1999).

[35] A. Kuzmin and J. Purans, *Radiation measurements* **33,** 583 (2001).

[36] J. Perez-Mato, S. Gallego, E. Tasci, L. Elcoro, G. de la Flor, and M. Aroyo, *Annu. Rev. Mater. Res.* **45,** 217 (2015).

[37] Belov, *Sov. Phys. Crystallogr.* **2,** 311 (1957).

[38] C. De, S. Ghara, and A. Sundaresan, *Solid State Commun.* **205,** 61 (2015).

[39] B. J. Campbell, H. T. Stokes, D. E. Tanner, and D. M. Hatch, *J. Appl. Crystallogr.* **39,** 607 (2006).

Chapter 6

Structural, magnetic and dielectric properties of the aeschynite-type polar magnet $DyCrWO_6$*

Summary

The crystal structure and physical properties of $DyCrWO_6$ are investigated in the present work. Using synchrotron X-ray and neutron diffraction study at room temperature, $DyCrWO_6$ is found to be isostructural with the multiferroic compound $DyFeWO_6$ crystallizing in the ordered aeschynite-type structure with the polar space group ($Pna2_1$). It undergoes a long-range antiferromagnetic ordering at T_N ~ 25 K, indicating that it belongs to the polar magnet groups. Further, it exhibits negative magnetization below 4 K and a large magnetocaloric effect at low temperature. A weak dielectric anomaly is found around antiferromagnetic ordering temperature, corroborating magnetodielectric effect. However, electric polarization is not detected in the present experimental detection limit.

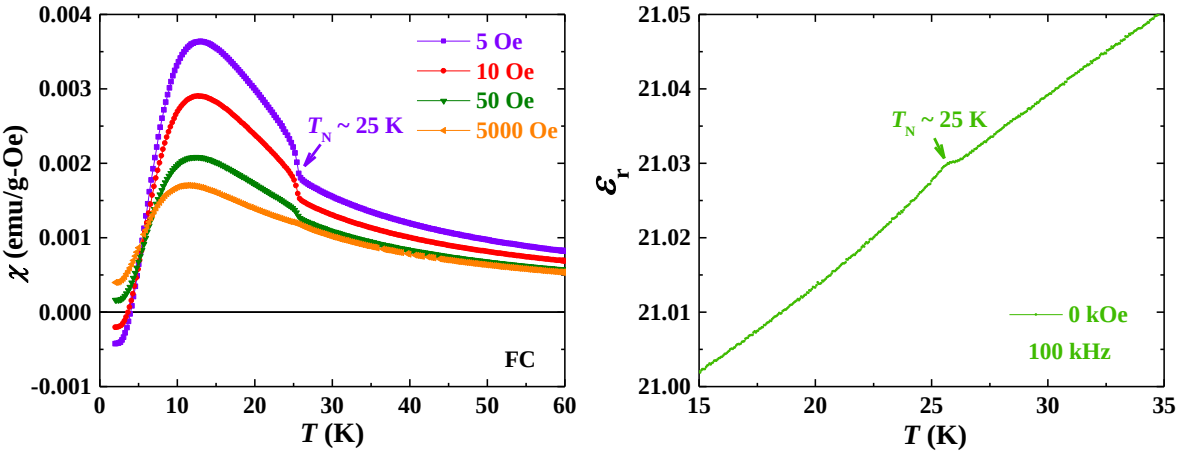

.....

*Manuscript based on this work is under preparation.

6.1 Introduction

In the previous chapter, we have demonstrated that the iron (Fe^{3+}, $3d^5$) based oxides, RFeWO$_6$ (R = Dy, Eu, Tb and Y), which crystallize in an ordered aeschynite-type polar structure ($Pna2_1$), constitute a new family of magnetoelectric multiferroics. Using a neutron diffraction study on DyFeWO$_6$, it is shown that a noncollinear magnetic structure of Fe^{3+} spins is responsible for a sudden enhancement of electric polarization at the antiferromagnetic ordering temperature. In this chapter, motivated by the results of RFeWO$_6$, we have investigated a Cr^{3+} ($3d^3$)-based aeschynite-type oxide, DyCrWO$_6$. Although DyCrWO$_6$ was proposed to be isostructural with the DyFeWO$_6$ compound, the detailed physical properties were not known. Using a combined Rietveld refinement of room temperature synchrotron X-ray and neutron diffraction data, we have confirmed that it crystallizes in a similar ordered aeschynite-type structure ($Pna2_1$). Magnetic measurements reveal the occurrence of temperature induced magnetization reversal and the presence of large magnetocaloric effect at low temperature. A weak anomaly in dielectric constant is found around the long-range antiferromagnetic ordering temperature (T_N ~ 25 K), demonstrating magnetodielectric effect. However, the electric polarization is not found in our experimental detection limit.

6.2 Experimental section

Polycrystalline sample of DyCrWO$_6$ was prepared by conventional solid state reaction method. Stoichiometric amounts of Dy_2O_3, Cr_2O_3 and WO_3 were mixed, ground and heated at a final temperature of 1140 ^oC for 12 hour in air with intermittent grindings. The rare earth oxide Dy_2O_3 was preheated at 900 ^oC for 12 hour in air before use. Synchrotron X-ray diffraction data were collected at room temperature at the Materials Science Powder Diffraction beamline (BL04-MSPD) of the ALBA synchrotron facility at Barcelona, Spain using a wavelength of λ = 0.3171Å [1,2]. Neutron diffraction data were recorded at room temperature on D2B diffractometer at the Institut Laue-Langevin (ILL), Grenoble, France with a wavelength of λ = 1.594 Å. We have carried out physical property measurements, as performed on RFeWO$_6$ compounds (mentioned in the previous chapter).

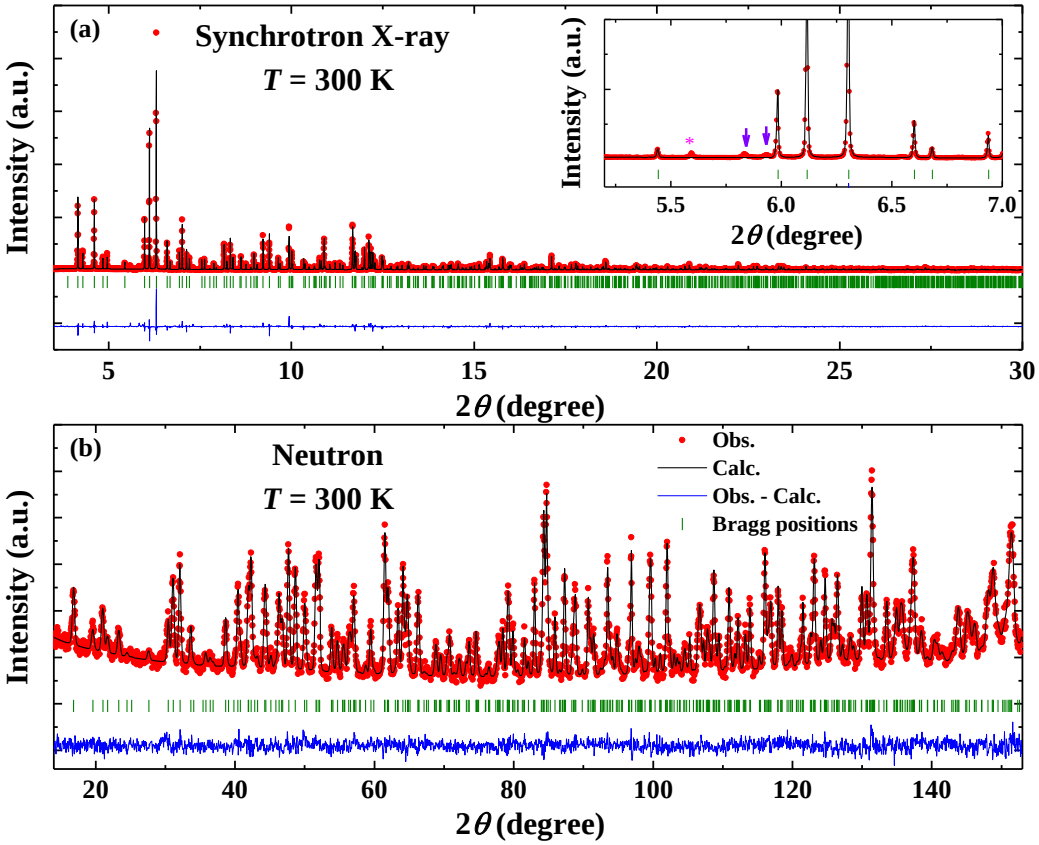

Figure 6.1 (a, b) Results of combined Rietveld refinement of synchrotron X-ray and neutron diffraction data collected at room temperature. The arrows in the inset figure represent the peak positions of the minor impurity phase of Dy_2WO_6. The peaks from TiO_2 (cryostat) in synchrotron X-ray diffraction data are marked with the * symbol. These peaks are not included in the refinement process.

6.3 Results and discussion

6.3.1 Structure

The crystal structure of $DyCrWO_6$ is determined by a combined Rietveld refinement of room temperature synchrotron X-ray and neutron diffraction data using FullProf software [3]. Since the detailed structure of $DyCrWO_6$ was not known, the structural parameters of $DyFeWO_6$ were used in the refinement process. The results of combined Rietveld refinement with the space group $Pna2_1$ are shown in Figure 6.1 and the obtained structural parameters are given in Table 6.1. The aeschynite-type crystal structure obtained from the refinement is shown in Figure 6.2(a). Since there is a large difference in the sizes and charges between Cr^{3+} and W^{6+} ions, these two ions are

arranged in an ordered manner, similar to the ordered arrangement of Fe^{3+} and W^{6+} ions in *R*$FeWO_6$. The octahedra formed by Cr^{3+} and W^{6+} ions are interconnected by corner and edge sharing. The bond diagram of the edge shared Cr^{3+} and W^{6+} octahedra is shown in Figure 6.2(b). In the synchrotron X-ray data, a minor impurity phase of Dy_2WO_6 is observed, as indicated by the arrows in the inset of Figure 6.1(a). It is reported that the Dy_2WO_6 remains paramagnetic down to lowest temperature [4]. For further confirmation, we have prepared Dy_2WO_6 and found that it indeed remains paramagnetic down to 2.5 K. Thus, it will not affect any results of the present investigation. Further, as indicated in the inset of Figure 6.1(a), the symbol (*) represents the peak from TiO_2 (cryostat). The peaks from both TiO_2 and Dy_2WO_6 are not included in the refinement process. We have tried to prepare the compounds *R*$CrWO_6$ with other rare earth elements, but we couldn't stabilize the pure phase. This is because of the less stability of these phases due to the presence of the edge-shared octahedra of cations with high charges, as discussed in the previous chapter.

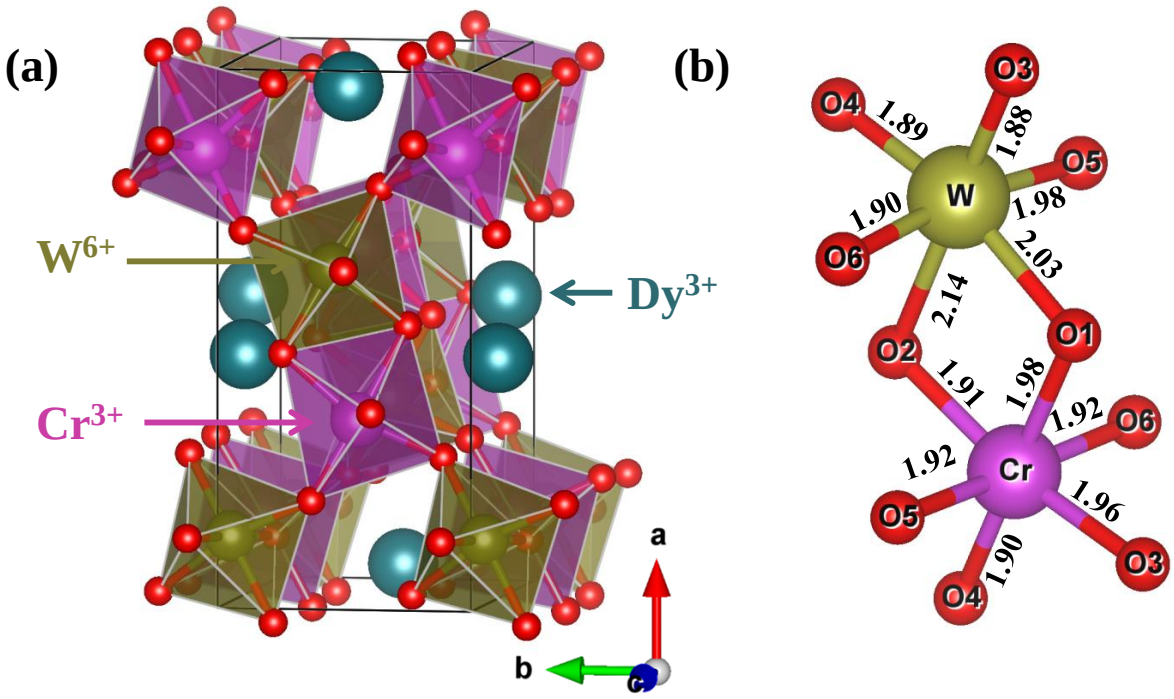

Figure 6.2 (a) The ordered aeschynite-type crystal structure of $DyCrWO_6$ (b) The edge-shared Cr^{3+} and W^{6+} octahedra showing the bond lengths.

Tables 6.1 Atomic positions, bond lengths and the result of bond valence sum (BVS) calculation in $DyCrWO_6$ obtained from combined Rietveld refinement of room temperature synchrotron X-ray (λ = 0.3171 Å) and neutron diffraction (λ = 1.594 Å) data

Space group: *Pna*2_1; a = 10.87855(2) Å, b = 5.18328(1) Å, c = 7.32152(2) Å, $\alpha = \beta = \gamma = 90°$, V = 412.836(1) Å^3; χ^2 = 1.40 (for neutron), χ^2 = 3.92 (for synchrotron); Bragg R-factor = 5.35, R_f-factor = 3.56 (for neutron); Bragg R-factor = 7.01, R_f-factor = 6.68 (for synchrotron)

Atom	**Wyckoff position**	***x***	***y***	***z***	B_{iso} **(Å^2)**	**Occ.**
Dy	4*a*	0.0430(1)	0.4542(3)	0.25	0.48(2)	1
Cr	4*a*	0.1340(4)	0.9513(10)	0.9962(17)	0.11(7)	1
W	4*a*	0.3531(1)	0.4443(3)	0.0044(6)	0.44(2)	1
O1	4*a*	0.9773(13)	0.7688(29)	0.0465(24)	0.67(31)	1
O2	4*a*	0.5273(13)	0.2588(30)	0.9647(26)	0.99(35)	1
O3	4*a*	0.2053(12)	0.6161(26)	0.0607(23)	0.75(27)	1
O4	4*a*	0.2822(12)	0.1263(25)	0.9349(21)	0.47(24)	1
O5	4*a*	0.1429(5)	0.0585(13)	0.2473(35)	0.66(9)	1
O6	4*a*	0.1202(6)	0.8340(12)	0.7492(40)	0.75(10)	1

Cation	**O1**	**O2**	**O3**	**O4**	**O5**	**O6**
Dy	2.32(1) 2.47(1)	2.36(2) 2.37(0)	2.39(1)	2.50(1)	2.32(1)	2.32(1)
Cr	1.98(1)	1.91(2)	1.96(2)	1.90(1)	1.92(0)	1.92(0)
W	2.03(1)	2.14(1)	1.88(1)	1.89(1)	1.98 (0)	1.90(0)

Dy_{BVS}	2.90(4)
Cr_{BVS}	3.42(8)
W_{BVS}	5.34(12)

6.3.2 DC magnetization

6.3.2.1 Long-range antiferromagnetic ordering

Figure 6.3(a) shows the temperature variation of field-cooled (FC) susceptibility χ (T) measured with a magnetic field of 100 Oe. A tiny anomaly is observed around T_N ~ 25 K in χ (T), where a sharp λ-type peak is found around 25 K in heat capacity C_P

(T) data, as shown in the inset of Figure 6.3(a), suggesting a long range magnetic ordering of Cr^{3+} moments. The absence of anomalies at further lower temperature in χ (T) and C_P (T), respectively suggests that probably Dy^{3+} moments are polarized by the ordered Cr^{3+} moments at 25 K, as found in $DyFeWO_6$. Below 25 K, χ (T) increases initially because of the high paramagnetic moment of Dy^{3+} spins and then it decreases below 12 K, which could be due to the competition between the polarized Dy^{3+} and ordered Cr^{3+} moments.

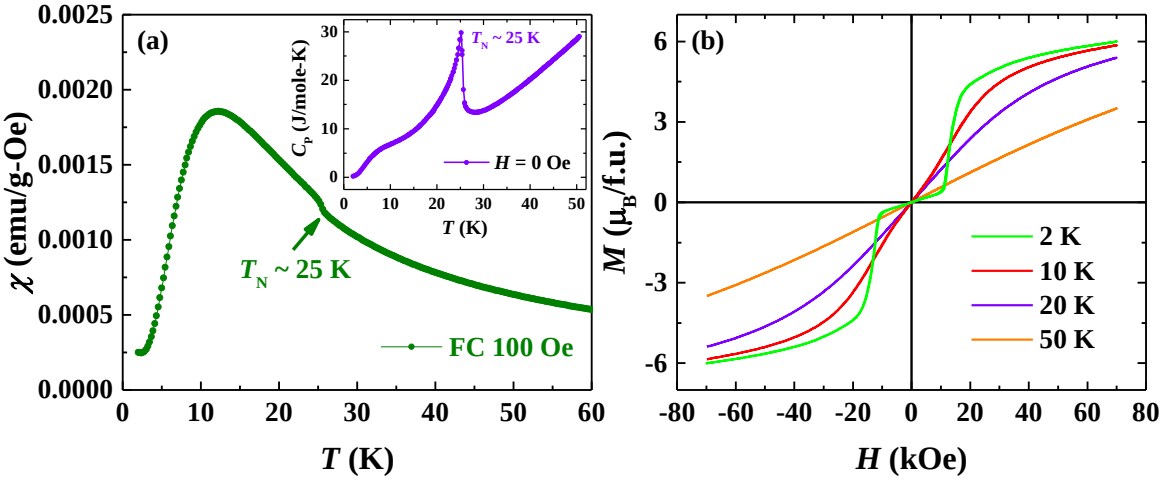

Figure 6.3 (a) Temperature variation of field-cooled (FC) magnetic susceptibility χ (T) measured under a magnetic field of 100 Oe. The inset shows temperature dependent heat capacity C_P (T). (b) Magnetic field dependent magnetization M (H) measured at different temperatures.

In Figure 6.3(b), magnetic field dependent magnetization M (H) data measured at different temperature are shown. As observed in $DyFeWO_6$, the M (H) loop at 2 K exhibits field induced steps, indicating metamagnetic transitions due to the appearance of complex magnetic states associated with Dy^{3+}-magnetism. Above 6 K, these steps are disappeared and show antiferromagnetic nature. Neutron diffraction study is necessary to understand this complex behavior.

6.3.2.2 Magnetization reversal

Temperature dependent field-cooled (FC) susceptibility χ (T) data measured with different magnetic fields are shown in Figure 6.4(a). Surprisingly, it is found that the magnetization measured under a low magnetic field of + 5 Oe becomes negative below a

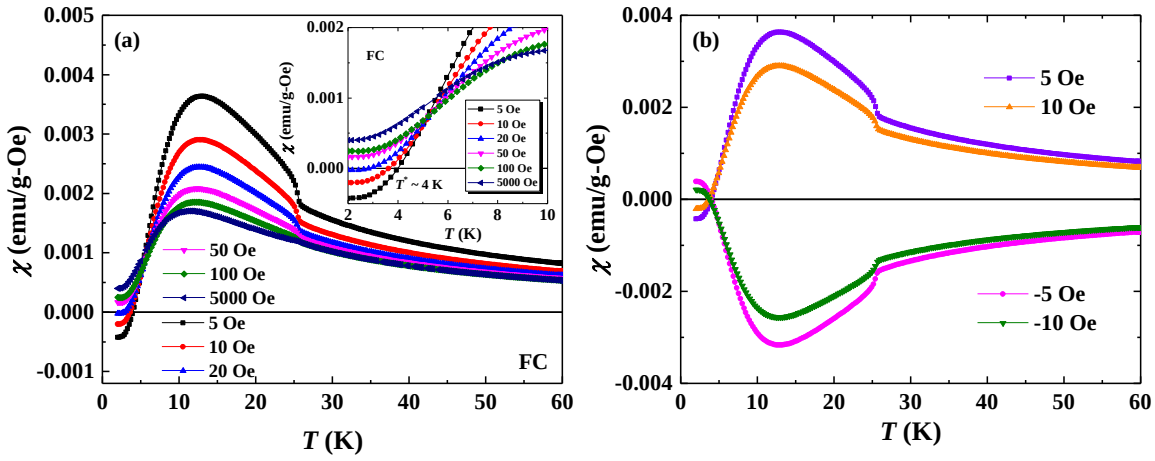

Figure 6.4 (a) Temperature dependent field cooled (FC) susceptibility χ (T) measured with different positive magnetic fields. Inset shows the magnified view of χ (T) at low temperature. (b) Magnetization reversal under positive and negative magnetic fields.

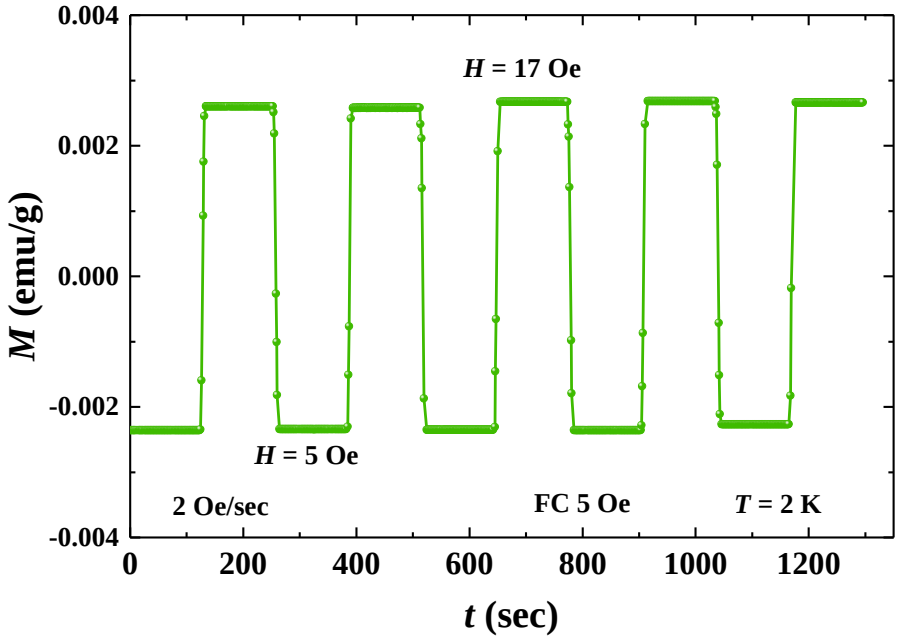

Figure 6.5 Magnetization switching at 2 K under an oscillating magnetic field between +5 Oe and +17 Oe.

compensation temperature T^* ~ 4 K. With increasing magnetic field, the compensation temperature T^* shifts to lower temperature (inset of Figure 6.4(a)) and the magnetization becomes positive above H > 20 Oe. The opposite behavior is observed under negative magnetic fields, as shown in Figure 6.4(b). These results demonstrate the presence of temperature induced magnetization reversal in the present system, which indicates the

crucial role of the competition between Dy^{3+} and Cr^{3+} moments at low temperature. Note that, magnetization reversal is not observed in the isostructural compound $DyFeWO_6$. Temperature induced magnetization reversal is observed in several compounds, such as $BiFe_{0.5}Mn_{0.5}O_3$, $YFe_{1-x}Mn_xO_3$, YVO_3 etc. [5-7].

For further investigation, isothermal magnetization switching experiment was performed at 2 K. In this measurement, the sample was cooled to 2 K under a magnetic field of +5 Oe and then the magnetization was measured with time by oscillating the magnetic field between +5 Oe and +17 Oe with a rate of 2 Oe/sec. The result of magnetization switching experiment is shown in Figure 6.5. It is clear from the figure that the magnetization can be switched from negative to positive value by changing the field from +5 Oe to + 17 Oe. Note that, in ferromagnetic materials, the magnetization can only be reversed by changing the polarity of the magnetic field. In the present case, the magnetization can be reversed by changing the magnetic field in the same direction.

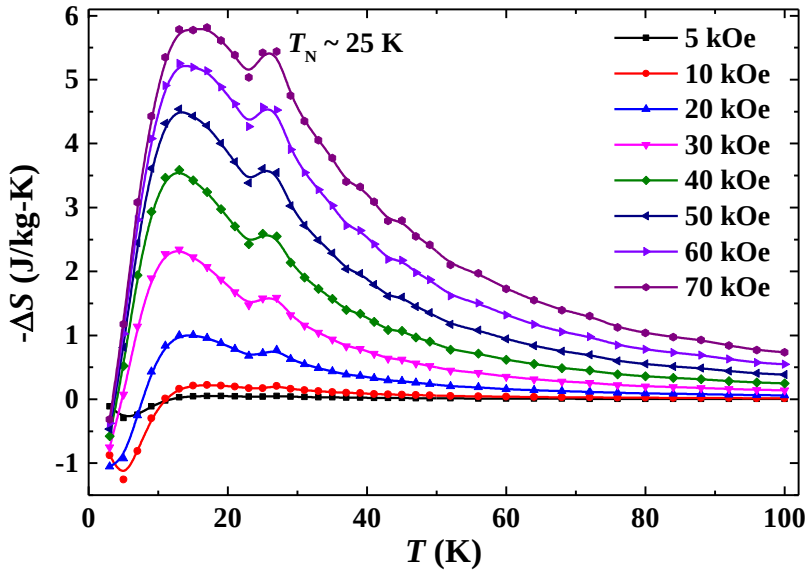

Figure 6.6 Temperature dependent entropy-changes ΔS under different magnetic fields.

6.3.3 Magnetocaloric effect

The entropy of a magnetic material changes while it is placed in a changing magnetic field in adiabatic condition, which results a change in temperature of the material. This phenomenon is known as magnetocaloric effect. In order to estimate the

change in magnetic entropy, magnetic field dependent magnetization at several temperatures were measured. The change in entropy is calculated using the following equation,

$$\Delta S(T,H) = \int_0^H \left(\frac{\partial M}{\partial T}\right)_H dH$$

The entropy-change under various magnetic fields is shown in Figure 6.6. A large value of entropy-change is observed at low temperature with a maximum value of 6 J/kg-K around 12 K. This value is quite high in oxides. A clear anomaly is observed in ΔS around T_N. Upon cooling, the ΔS changes its sign at a further lower temperature. Understanding the origin of this behavior requires further investigations.

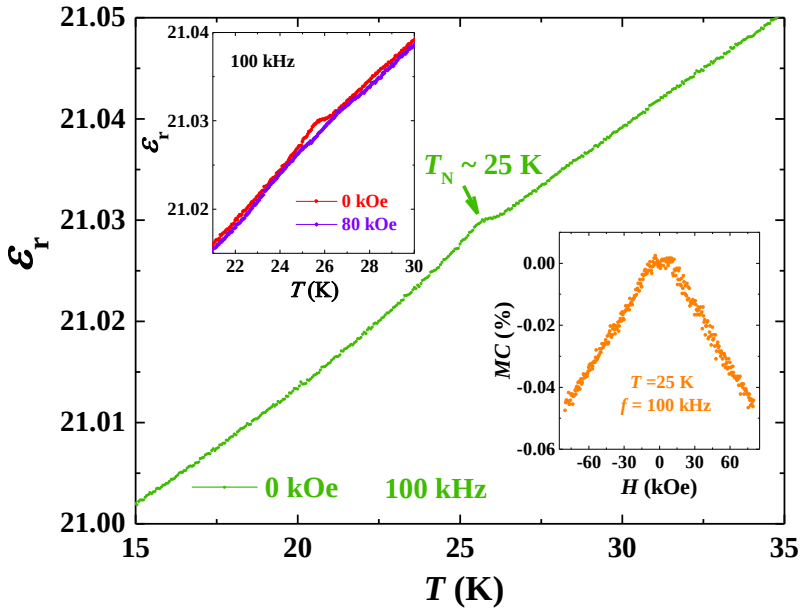

Figure 6.7 Temperature variation of dielectric constant ε_r (T) at 100 kHz under zero-magnetic field. Inset at the top panel shows the suppression of the dielectric anomaly under a magnetic field of 80 kOe, while the inset at the bottom panel shows magnetocapacitance MC (%) measured at T_N ~ 25 K.

6.3.4 Magnetodielectric effect and absence of measureable electric polarization

Temperature dependent dielectric constant ε_r (T) data measured with 100 kHz is shown in Figure 6.7(a). An anomaly is observed in ε_r (T) at the antiferromagnetic

ordering temperature T_N ~ 25 K, indicating the presence of magnetodielectric effect. However, this dielectric anomaly is very weak compared to the RFeWO$_6$ systems. No anomaly is found in dielectric loss data at T_N. Under magnetic field, the anomaly in ε_r (T) is completely suppressed as shown in the top inset of Figure 6.7(a). Magnetocapacitance measured at T_N ~ 25 K shows the presence of a small but finite value, as shown in bottom inset of Figure 6.7(a).

Pyroelectric current measurements were carried out across the antiferromagnetic ordering temperature. However, we could not detect any electric polarization. This indicates that either the electric polarization is beyond our instrumental detection limit or the magnetic structure is different from that of RFeWO$_6$ compounds.

6.4 Conclusion

In summary, we have determined the complete crystal structure of DyCrWO$_6$. Our analysis shows that it crystallizes in an ordered aeschynite-type structure with a polar space group ($Pna2_1$). The occurrence of long-range antiferromagnetic ordering at 25 K suggests that this compound also belongs to the polar magnet family. A weak dielectric anomaly is observed around T_N, however electric polarization is not found, which suggests that the present compound is either only a pyroelectric or the spontaneous electric polarization is very small. Although multiferroicity is not observed in DyCrWO$_6$, other interesting results, such as magnetization reversal and magnetocaloric effect are observed at low temperature.

References

[1] F. Fauth, R. Boer, F. Gil-Ortiz, C. Popescu, O. Vallcorba, I. Peral, D. Fullà, J. Benach, and J. Juanhuix, *EPJ Plus* **130,** 160 (2015).

[2] F. Fauth, I. Peral, C. Popescu, and M. Knapp, *Powder Diffraction* **28,** S360 (2013).

[3] H. Rietveld, *J. Appl. Crystallogr.* **2,** 65 (1969).

[4] P. Urbanowicz, E. Tomaszewicz, T. Groń, H. Duda, A. Pacyna, and T. Mydlarz, *Physica B: Condensed Matter* **404,** 2213 (2009).

[5] P. Mandal, A. Sundaresan, C. Rao, A. Iyo, P. Shirage, Y. Tanaka, C. Simon, V. Pralong, O. Lebedev, and V. Caignaert, *Phys. Rev. B* **82,** 100416 (2010).

[6] P. Mandal, C. Serrao, E. Suard, V. Caignaert, B. Raveau, A. Sundaresan, and C. Rao, *J. Solid State Chem.* **197,** 408 (2013).

[7] Y. Ren, T. Palstra, D. Khomskii, E. Pellegrin, A. Nugroho, A. Menovsky, and G. Sawatzky, *Nature* **396,** 441 (1998).

Chapter 7

Multiferroic properties and re-entrant spin glass behavior in $BaYFeO_4$*

Summary

The oxide $BaYFeO_4$ crystallizing in a complex orthorhombic structure with centrosymmetric space group *Pnma* exhibits two successive antiferromagnetic phase transitions. Upon cooling, it undergoes a spin density wave (SDW)-like antiferromagnetic ordering at T_{N1} ~ 48 K and a cycloidal ordering at a further lower temperature (T_{N2} ~ 35 K). In this work, we have investigated detailed magnetic and electrical properties of this oxide. We found that the cycloidal magnetic ordering at T_{N2} ~ 35 K induces an electric polarization, where a dielectric anomaly is also observed. The dielectric anomaly and electric polarization are strongly suppressed by external magnetic field. These results suggest that the present compound is a magnetoelectric multiferroic. Interestingly, we observed another anomaly in magnetization around T^* ~ 17 K, which is attributed to a re-entrant spin glass transition.

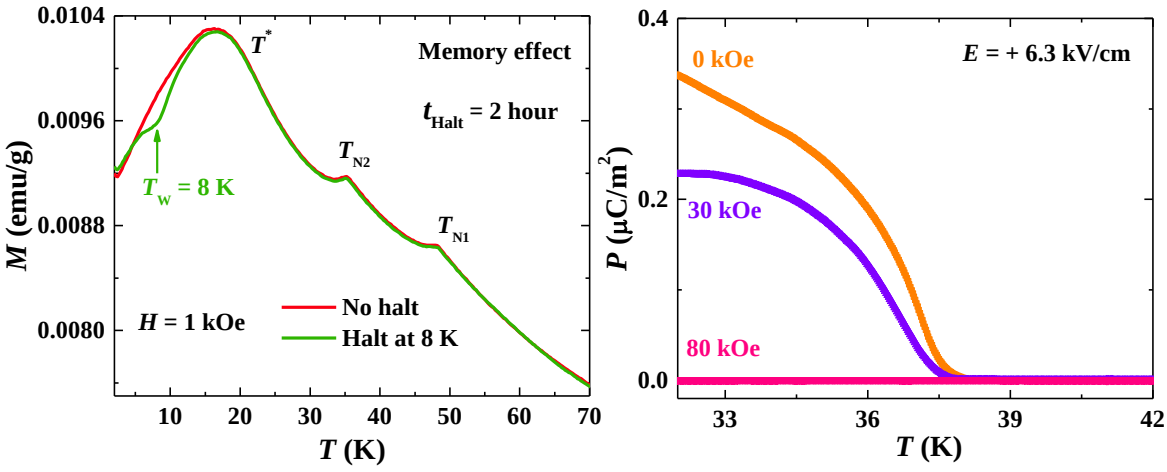

.....

*Manuscript based on this work is under preparation.

7.1 Introduction

Recently, a quaternary complex compound $BaYFeO_4$ has been reported to crystallize in an orthorhombic structure with a centrosymmetric space group (*Pnma*) [1]. The main building blocks of this complex crystal structure are two types of polyhedra - FeO_5 square pyramids and FeO_6 octahedra. These two polyhedra are interconnected by corner sharing and form a four-membered ring. Due to this unusual crystal structure, this compound exhibits interesting magnetic properties [1,2]. Using magnetization measurements, it has been shown that the compound undergoes multiple magnetic phase transitions occurring at 48 K and 35 K, in spite of the fact that a large amount of Fe^{3+} ions remains paramagnetic down to lowest temperature. Analysis of neutron diffraction data suggested that it possesses a long-range commensurate spin density wave (SDW)-like magnetic ordering of Fe^{3+} ions at T_{N1} ~ 48 K, where spins are aligned along *b* axis with a propagation vector of $\vec{k}$ = (0, 0, 1/3) (Figure 7.1(a)) [2]. Upon further cooling, another magnetic phase transition occurs around T_{N2} ~ 36 K, below which an incommensurate noncollinear cycloidal antiferromagnetic ordering of Fe^{3+} ions appears with a propagation vector of $\vec{k}$ = (0, 0, 0.35), where the cycloids of Fe^{3+} spins lie in the *bc* plane (Figure 7.1(b)) [2]. As discussed in Chapter 1, among the spiral magnetic structures, only cycloidal and transverse conical spin arrangements can induce electric polarization through the inverse Dzyaloshinskii-Moriya interaction or spin current mechanism [3-5].

In this work, we have carried out detailed magnetic and electric measurements in order to investigate the multiferroic properties caused by the cycloidal magnetic structure. Indeed we have found a dielectric anomaly around the cycloidal ordering temperature (T_{N2} ~ 35 K), below which the electric polarization emerges. The dielectric anomaly and electric polarization are strongly influenced by the external magnetic fields. These results suggest that $BaYFeO_4$ is a magnetoelectric multiferroic or type-II multiferroic. Further, in addition to the two known magnetic phase transitions (T_{N1} ~ 48 K and T_{N2} ~ 36 K), we have found another anomaly in magnetization around T^* ~ 17 K. Using dc magnetic memory effect and magnetization relaxation measurements, we have shown that this anomaly is associated with the appearance of a re-entrant spin glass state, which suggests that the spin glass state and cycloidal magnetic ordered state coexist at low temperature.

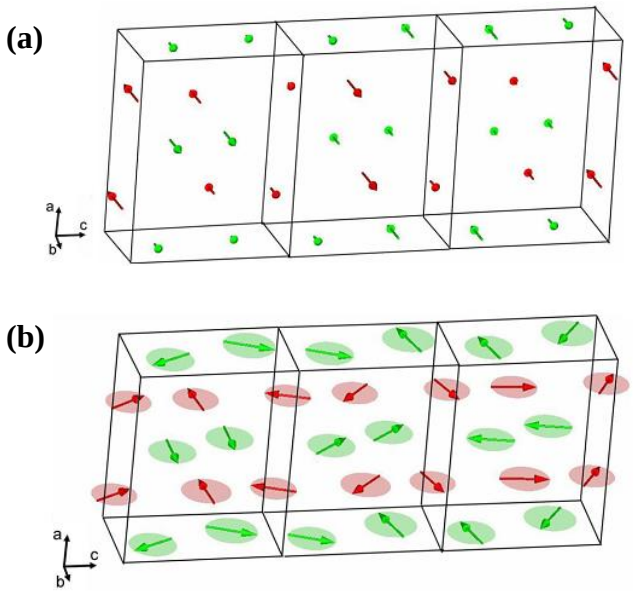

Figure 7.1 (a) Spin density wave (SDW)-like magnetic structure of Fe^{3+} spins in $BaYFeO_4$ below T_{N1} ~ 48 K, (b) Cycloidal magnetic structure of Fe^{3+} spins in $BaYFeO_4$ below T_{N2} ~ 35 K. These figures are adapted with permission from Ref. [2], © (2014) by the American Chemical Society.

7.2 Experimental section

Polycrystalline sample of $BaYFeO_4$ was prepared by a sol-gel reaction method. First, Y_2O_3 was dissolved in distilled water heated at 100 °C with adding nitric acid drop by drop. After dissolving completely, the temperature was reduced to 80 °C and $Fe(NO_3)_3$, $9H_2O$ and $Ba(NO_3)_2$ were added according to cation stoichiometry and dissolved. Then, citric acid was added to the solution and the solution was stirred continuously and kept at 80 °C for 12 hour. The obtained gel was heated at 200 °C for 12 hour in air. Then the dried powder was heated at 650 °C for 8 hour in oxygen atmosphere. After that, the powder sample was ground and heated in air at 1000 °C and 1200 °C for 12 and 24 hour, respectively. Then pellets were made and sintered at 1250 °C for 24 hour in air. The rare earth oxide Y_2O_3 was heated at 900 °C for 12 hour in air before use.

Physical properties were investigated by different measurements, such as dc and ac magnetization, dielectric and pyroelectric current (discussed in Chapter 2). We have followed a heating rate of 12 K/min in pyroelectric current measurements.

7.3 Results and discussion

7.3.1 Structure

Room temperature X-ray diffraction pattern of $BaYFeO_4$ is shown Figure 7.2. Rietveld refinement was performed with the orthorhombic space group *Pnma*. The structure parameters obtained from the Rietveld refinement are given in Table 7.1 [6]. The crystal structure is displayed in Figure 7.3. It can be seen in Figure 7.3(a) that Fe^{3+} ions are distributed in two different 4*c* sites. In one site, Fe^{3+} ions form square pyramids with five O^{2-} ions, while the Fe^{3+} ions in the other site form octahedra with six O^{2-} ions. The octahedra and squire pyramids are interconnected with each other by a corner sharing and four of these polyhedra form a ring. As shown in Figure 7.3(b), these rings are periodically arranged along *b* axis using corner sharing between the polyhedra and form the three dimensional structure. In Figure 7.3(c), one such ring is shown, where the Fe - O bond lengths are mentioned. The obtained values of bond lengths are consistent with the earlier study [1]. Ba^{2+} ions occupy two different sites surrounded by eleven and twelve O^{2-} ions, while Y^{3+} ions are distributed in two different site coordinated by seven O^{2-} ions. In the X-ray diffraction data (Figure 7.2), a minor impurity phase of Y_2O_3 is found, as indicated by the 2nd row of vertical bars. Since Y_2O_3 is nonmagnetic, it will not affect any properties of $BaYFeO_4$ investigated in this work.

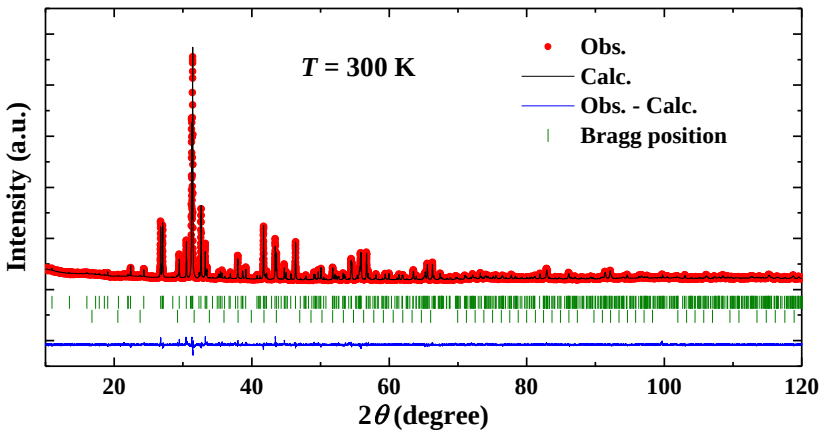

Figure 7.2 Results of Rietveld refinement of X-ray diffraction data of $BaYFeO_4$ collected at room temperature. The 1st row of vertical bars represents the Bragg positions of $BaYFeO_4$, while the 2nd row of vertical bars indicates the Bragg positions of a minor (~ 3%) impurity phase of Y_2O_3.

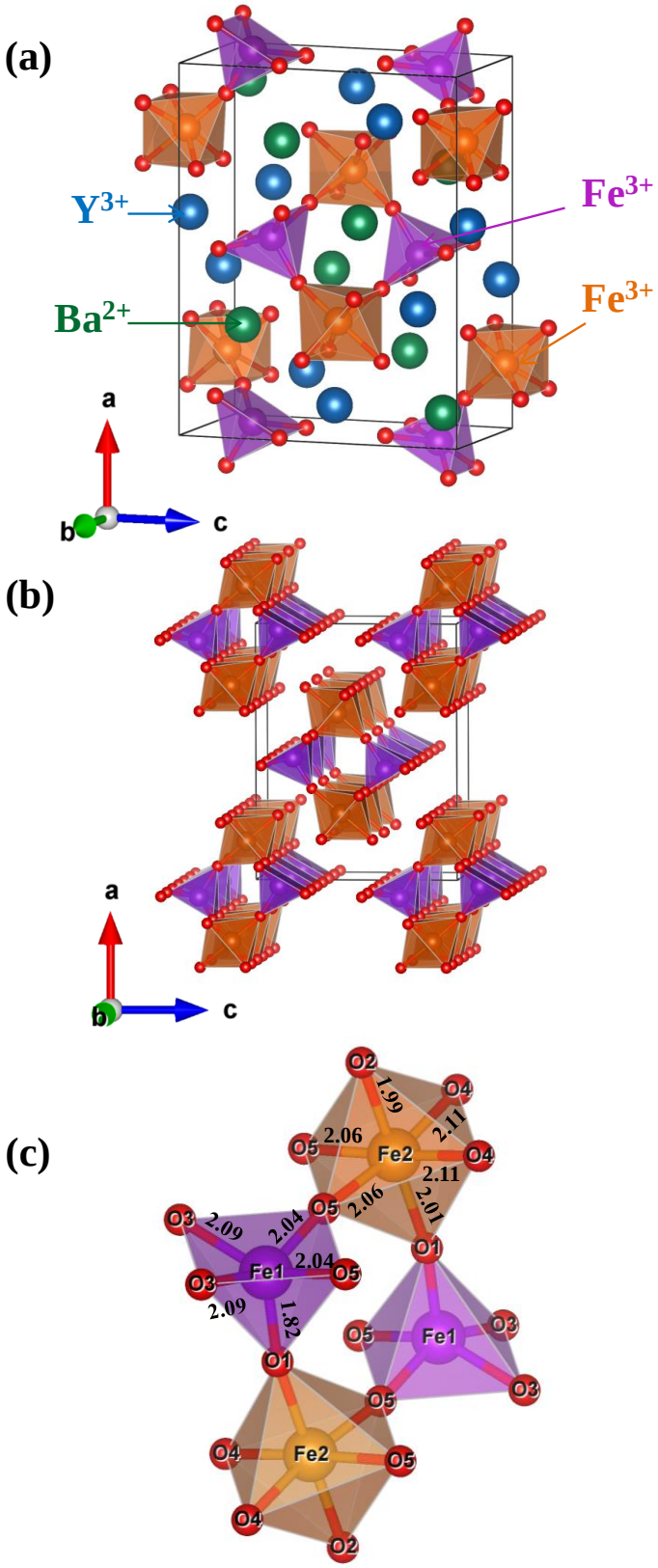

Figure 7.3 (a) Crystal structure of $BayFeO_4$ (b) The periodic arrangement of four-membered ring formed by the octahedra and square pyramids of Fe^{3+} ions along *b* axis. Ba^{2+} and Y^{3+} ions are not shown in this diagram. (c) The bond distances (Å) in the square pyramid and octahedra of Fe^{3+} ions in a ring.

Tables 7.1 Crystallographic parameters of $BaYFeO_4$ obtained from Rietveld refinement of X-ray diffraction data collected at room temperature

Atom	Wyckoff position	*x*	*y*	*z*	B_{iso} (Å^2)	Occ.
Ba1	4*c*	0.2116(1)	0.25	0.6750(2)	0.65(3)	0.5
Ba2	4*c*	0.4153(1)	0.25	0.3958(1)	0.65(3)	0.5
Y1	4*c*	0.4129(2)	0.25	0.0160(2)	0.66(4)	0.5
Y2	4*c*	0.1428(2)	0.25	0.3117(2)	0.66(4)	0.5
Fe1	4c	0.4714(3)	0.25	0.7187(4)	0.50(7)	0.5
Fe2	4*c*	0.1912(3)	0.25	0.0239(4)	0.50(7)	0.5
O1	4*c*	0.5847(13)	0.25	0.6170(13)	1.19(11)	0.5
O2	4*c*	0.2966(11)	0.25	0.1636(14)	1.19(11)	0.5
O3	8*d*	0.0116(7)	0.4920(19)	0.3624(9)	1.19(11)	1
O4	8*d*	0.2215(8)	0.4865(18)	0.4317(11)	1.19(11)	1
O5	8*d*	0.1116(9)	0.0106(20)	0.1343(9)	1.19(11)	1

Space group: *Pnma*; a = 13.14508(14) Å, b = 5.69557(6) Å, c = 10.24904(10) Å, $\alpha = \beta = \gamma = 90°$, V = 767.332(14) Å^3; χ^2 = 2.04

Fe - O bond lengths (Å) in the square pyramid and octahedra of $BaYFeO_4$ at room temperature

Cation	O1	O2	O3	O4	O5
Fe1	1.82(2)		2.09(1)		2.04(1)
			2.09(1)		2.04(1)
Fe2	2.01(2)	1.99(2)		2.11(1)	2.06(1)
				2.11(1)	2.06(1)

7.3.2 Magnetic properties

Temperature dependent magnetization M (T) data measured with field-cooled (FC) and zero-field-cooled (ZFC) conditions under a magnetic field of 1 kOe are shown in Figure 7.4(a). As reported earlier, the anomalies are observed around 48 K and 35 K in M (T) data [1,2]. The anomaly around 48 K is due to the appearance of long-range spin density wave (SDW)-like antiferromagnetic ordering of Fe^{3+} moments, while the anomaly around 35 K is due to the cycloidal magnetic ordering of Fe^{3+} moments (Figure 7.1) [2]. In addition to these anomalies, an anomaly around T^* ~ 17 K is observe in both ZFC and FC magnetization. This anomaly is also seen in the M (T) data in earlier studies [1].

However, the origin of this anomaly was not addressed. Below 17 K, FC magnetization increases while ZFC magnetization decreases sharply. This bifurcation between FC and ZFC magnetization indicates that the anomaly around T^* ~ 17 K could be associated with a spin glass transition [7]. The nature of the M (T) data above T_{N1} ~ 48 K is not like a paramagnetic state. It decreases with increasing temperature up to ~ 100 K and then it increases up to 390 K. This behavior could be due to the presence of short-range magnetic interactions in the paramagnetic state [2].

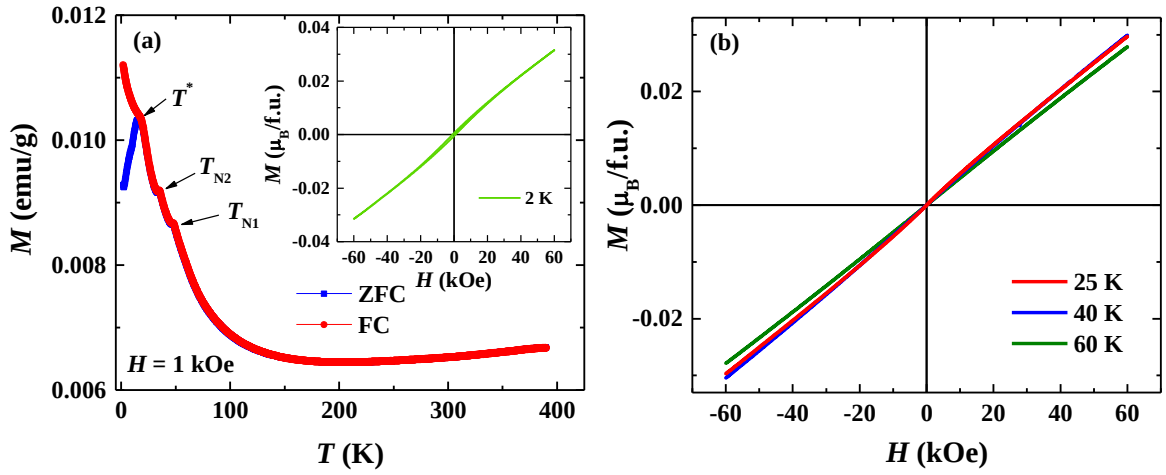

Figure 7.4 (a) Temperature dependent field-cooled (FC) and zero-field-cooled (ZFC) magnetization measured under a magnetic field of 1 kOe. (b) Magnetic field dependent magnetization measured at different temperatures. The inset of (a) shows the magnetic field dependent magnetization at 2 K.

Magnetic field dependent magnetization M (H) data at different temperatures are shown in Figure 7.4(b). M (H) data measured at 25 K and 40 K indicate the antiferromagnetic behavior, while it is consistent with the paramagnetic nature at 60 K. On the other hand, M (H) data measured at 2 K exhibits a tiny hysteresis loop as shown in the inset of Figure 7.4(a). This type tiny hysteresis loop is a typical characteristic of a spin glass state [7].

In order to verify the spin glass state below T^* ~ 17 K, memory effect experiments were carried out. In this experiment, the sample was cooled to a particular temperature T_W under zero magnetic field and then the sample temperature was halted for two hours at T_W. After that, the sample was cooled to 2 K, and the magnetization was measured during

warming in the presence of a magnetic field of 1 kOe. The results of memory effect experiments performed with different halting temperatures are shown in Figure 7.5(a). The conventional ZFC magnetization data is also shown in the same figure for comparison. Clear dips are observed in the magnetization data when the halted temperature T_W is below T^*. Such dip is absent in the data where $T_W > T^*$ and in conventional ZFC magnetization data. The presence of such dips in the magnetization data in memory effect experiments suggests that the anomaly around $T^* \sim 17$ K in M (T) is associated with a spin glass transition [8-10]. Since this spin glass state appears below the long-range antiferromagnetic ordering temperature, this state is a re-entrant spin glass state. In addition to this memory effect experiments, ac susceptibility (χ') measurements were carried out (Figure 7.5(b)). Although a broad peak is found around T^* in χ' (T) data for different frequencies, the shift of the peak with increasing frequency is not very clear.

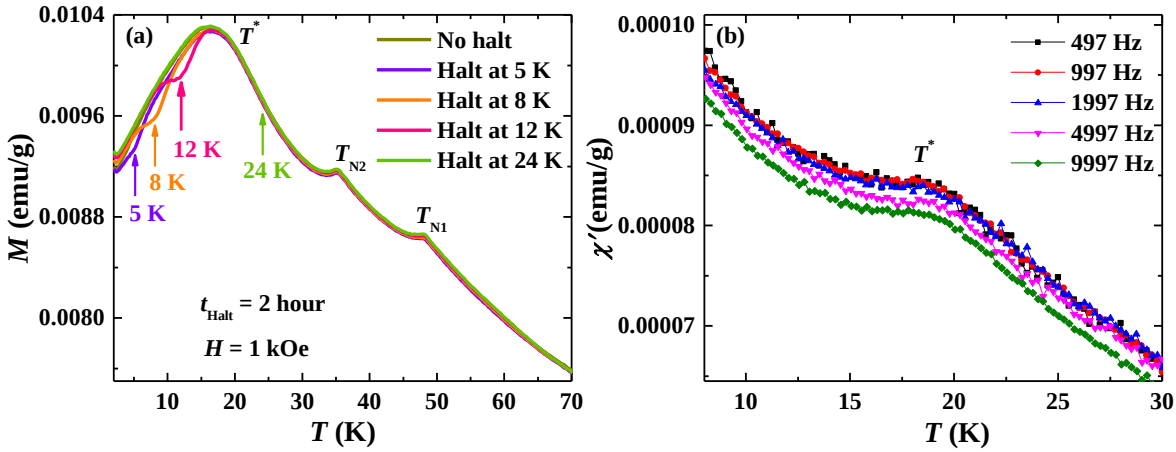

Figure 7.5 (a) Results of memory effect experiments with various halting temperatures, (b) Temperature dependent ac susceptibility at various frequencies.

To explore further the spin glass state, we have performed magnetization relaxation experiments, where the sample was cooled to a particular temperature under field-cooled (FC) condition with a magnetic field of 1 kOe and then the magnetization data were recorded with time after setting magnetic field to zero. The normalized magnetization data, $m(t) = M_t/M_{t=0}$, are shown in Figure 7.6(a). As expected for a spin

glass state, the magnetization relaxes with time. These data are further treated with a stretched exponential equation, which is given by [11,12],

$$m(t) = m_0 - m_g e^{-\left(\frac{t}{\tau}\right)^{\beta}}$$

where m_0 and m_g are associated with the initial remanent magnetization and the glassy component of magnetization, respectively. τ and β are the relaxation time constant and stretch exponential coefficient. The value of β should be between 0 and 1 for a spin glass system. The relaxation parameters obtained from the fits are given in Table 7.2. The values of β is consistent with the spin glass state. The relaxation time τ continuously increases with decreasing temperature. This indicates that spin clusters may exist in the spin glass state.

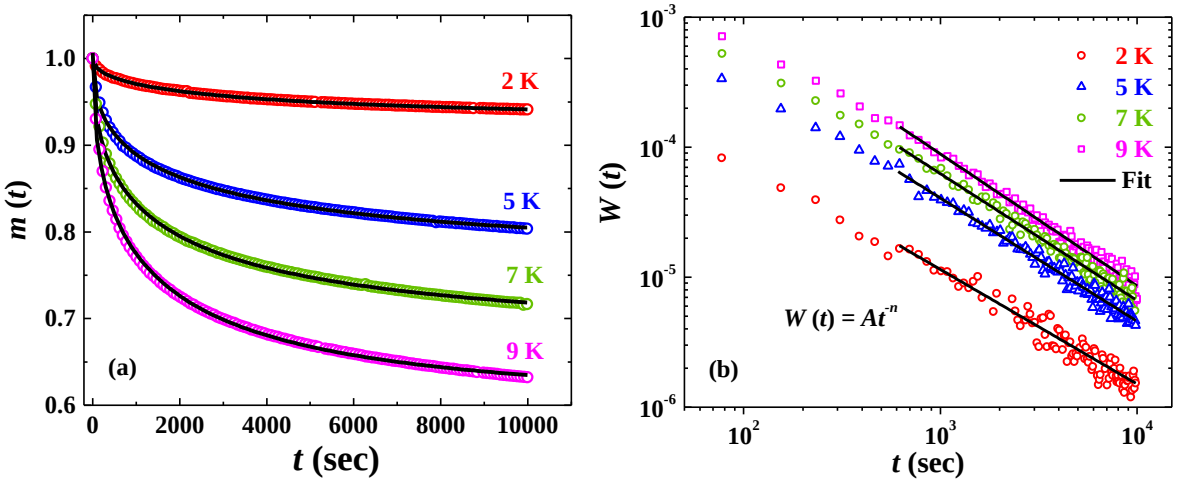

Figure 7.6 (a) Magnetization relaxation data m (t) (= $M_t/M_{t=0}$) recorded at different temperatures after a field-cooled process under a magnetic field of 1 kOe. The solid lines represent fits to a stretch exponential equation. (b) W (t) *vs.* time data at different temperatures, where $W(t) = -\frac{d}{dt}[\ln m(t)]$. The solid lines represent fits to a power law ($\sim At^{-n}$).

For further confirmation of the spin-clusters, we have used a model as proposed by Ulrich [13]. This model suggests that, for any spin glass state, the parameter W (t), which is defined by, $W(t) = -\frac{d}{dt}[\ln m(t)]$, should decay with time as,

$$W(t) \sim At^{-n}$$

The value of n should remain constant throughout the temperature below T^*, if it is a simple atomic spin glass state. The calculated $W(t)$ data is plotted in Figure 7.6(b) and it is fitted with the above equation. The values of n obtained from the fits are given in Table 7.2. It can be seen that the value of n does not remain constant, it increases with increasing temperature. This result indicates that the spin glass state is not an atomic spin glass; spin-clusters are also present in the spin glass state.

Table 7.2 Magnetic relaxation parameters obtained from the fits in Figure 7.6(a, b)

T (K)	β	τ (sec)	n
2	0.498(5)	3792(104)	0.881(16)
5	0.455(6)	2402(76)	0.947(12)
7	0.460(6)	1776(42)	0.975(9)
9	0.476(6)	1390(27)	1.015(8)

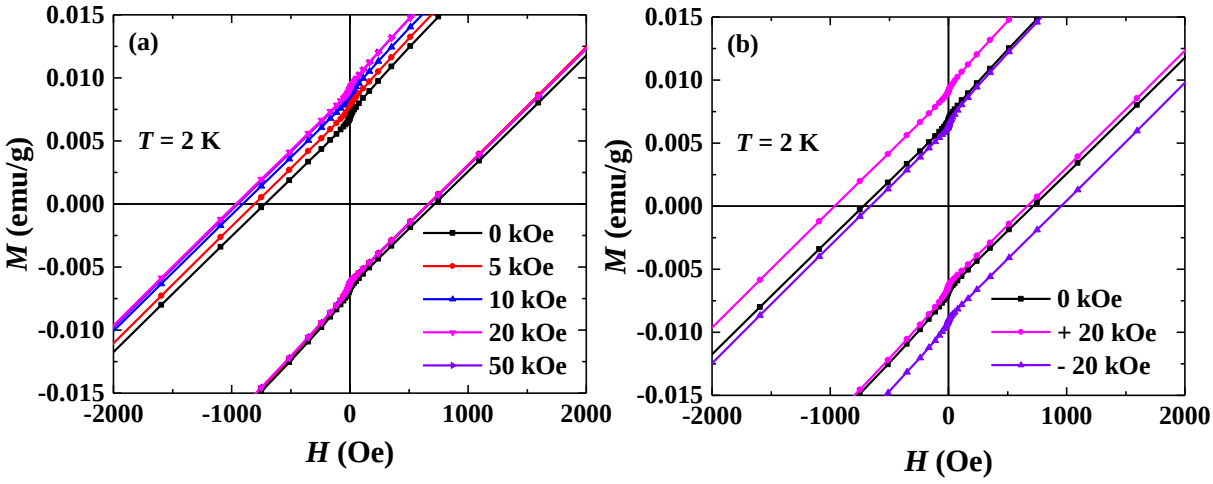

Figure 7.7 (a) Magnetization *vs.* magnetic field data at 2 K measured after cooling the sample under various positive magnetic fields (b) The reversible shift of the magnetization *vs.* magnetic field data due to the cooling under opposite magnetic fields.

The above results indicate that both spin glass and long-range cycloidal ordered state coexist at low temperature. To explore further this coexistence of two magnetic states, we have investigated exchange bias effect at 2 K. Magnetic field dependent magnetization data M (H) were recorded after cooling the sample to 2 K under different magnetic fields. As shown in Figure 7.7(a), the M (H) loops, measured after cooling the

sample under positive magnetic fields, are shifted along the negative *H* axis. The shift of the *M* (*H*) loops can be reversed by applying opposite cooling field (Figure 7.7(b)). These results suggest the presence of exchange bias effect at low temperature. The exchange bias effect is an evidence of the coexistence of spin-cluster glass state and long-range antiferromagnetic ordered state. The spin glass state could be due to the complex crystal structure where a large amount of Fe^{3+} moments do not take part in long-range ordering, but these can freeze at low temperature. Therefore, the spin glass state and long-range ordered state occur independently, and thus they can coexist at low temperature.

7.3.3 Magnetoelectric multiferroic properties

Temperature dependent dielectric constant ε_r (*T*) data measured with 100 kHz under magnetic fields of 0 and 80 kOe are shown in Figure 7.8(a). A clear anomaly is observed around T^* ~ 35 K in ε_r (*T*) under zero magnetic field, where the cycloidal magnetic ordering appears. Further, the dielectric anomaly is disappeared under a magnetic field of 80 kOe. The existence of dielectric anomaly at the magnetic ordering temperature and its suppression under magnetic field suggests the presence of a strong magnetodielectric effect.

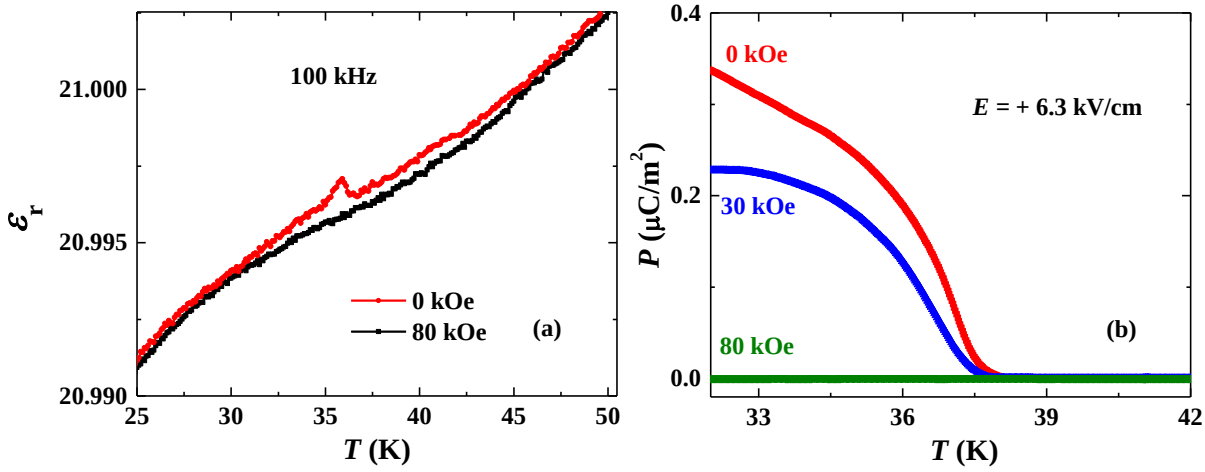

Figure 7.8 (a) Temperature variation of dielectric constant at 100 kHz measured under magnetic fields of 0 and 80 kOe. (b) Temperature evolution of electric polarization obtained from pyroelectric current measurements under an electric field of + 6.3 kV/cm and different magnetic fields.

Pyroelectric current measurements were carried out in order to find out whether the cycloidal magnetic ordering induces electric polarization. A sharp asymmetric peak is found around T^* ~ 35 K in pyroelectric current data. Electric polarization P (T) is calculated by integrating pyroelectric current data with measurement duration and is shown in Figure 7.8(b). The spontaneous electric polarization appears around the cycloidal magnetic ordering temperature under zero magnetic field. The onset of the emergence of spontaneous electric polarization P (T) is slightly shifted to higher temperature, which is due to the high heating rate (12 K/min) followed in measuring pyroelectric current. The high heating rate is necessary in this case because the electric polarization is very small; otherwise the electric polarization would not be detected by pyroelectric current measurement. Magnetic field strongly influences the electric polarization as shown in Figure 7.8(b). The electric polarization decreases with increasing magnetic field and finally it is completely suppressed under a magnetic field of 80 kOe. Thus, the presence of dielectric anomaly and the appearance of electric polarization around the cycloidal magnetic ordering temperature, which are strongly suppressed by the external magnetic fields, suggest that the compound $BaYFeO_4$ is a magnetoelectric multiferroic or type-II multiferroic. It is obvious that the inverse DM interaction is responsible for the cycloidal magnetic ordering induced electric polarization in the present compound. The electric polarization due to the inverse DM interaction is given by [3,4,14],

$$\Delta P = P^{sp}\vec{e}_{ij} \times \left(\vec{S}_i \times \vec{S}_j\right)$$

where $\vec{S}_i$ and $\vec{S}_j$ are the two neighboring spins, $\vec{e}_{ij}$ is a unit vector connecting the spins and P^{sp} is a constant factor. As shown in Figure 7.1(b), the cycloids formed by the Fe^{3+} moments lie in *bc* plane and the unit vector $\vec{e}_{ij}$ is along *c* direction. Thus, the electric polarization according to this model has to be along *b* direction. Studies on single crystal are necessary in order to confirm this electric polarization direction and also the switching of electric polarization, although the electric polarization in this polycrystalline sample can be switched by reversing electric field (not shown).

7.4 Conclusion

In conclusion, we have investigated the magnetic and magnetoelectric multiferroic properties of a complex oxide $BayFeO_4$. It exhibits multiple magnetic phase transitions. With decreasing temperature, it exhibits a spin density wave (SDW)-like magnetic ordering of Fe^{3+} moments at T_{N1} ~ 48 K and then the spin arrangement changes to a cycloidal structure below T_{N2} ~ 35 K. Upon further cooling, the compound enters into a re-entrant spin glass state at T^* ~ 17 K, below which both long-range cycloidal ordering and spin glass state coexist. Interestingly, electric polarization is found to appear below the cycloidal magnetic ordering (T_{N2} ~ 35 K), where a dielectric anomaly is also found and these are strongly affected by applied magnetic fields, suggesting that $BaYFeO_4$ is a magnetoelectric multiferroic or type-II multiferroic material.

References

[1] F. Wrobel, M. C. Kemei, and S. Derakhshan, *Inorganic chemistry* **52,** 2671 (2013).

[2] C. M. Thompson, J. E. Greedan, V. O. Garlea, R. Flacau, M. Tan, P.-H. T. Nguyen, F. Wrobel, and S. Derakhshan, *Inorganic chemistry* **53,** 1122 (2014).

[3] H. Katsura, N. Nagaosa, and A. V. Balatsky, *Phys. Rev. Lett.* **95,** 057205 (2005).

[4] M. Mostovoy, *Phys. Rev. Lett.* **96,** 067601 (2006).

[5] Y. Tokura, S. Seki, and N. Nagaosa, *Rep. Prog. Phys.* **77,** 076501 (2014).

[6] H. Rietveld, *J. Appl. Crystallogr.* **2,** 65 (1969).

[7] J. A. Mydosh, *Spin glasses* (Taylor and Francis, 1993).

[8] K. Jonason, E. Vincent, J. Hammann, J. P. Bouchaud, and P. Nordblad, *Phys. Rev. Lett.* **81,** 3243 (1998).

[9] R. Mathieu, M. Hudl, and P. Nordblad, *EPL (Europhysics Letters)* **90,** 67003 (2010).

[10] D. Choudhury, P. Mandal, R. Mathieu, A. Hazarika, S. Rajan, A. Sundaresan, U. Waghmare, R. Knut, O. Karis, and P. Nordblad, *Phys. Rev. Lett.* **108,** 127201 (2012).

[11] A. Bhattacharyya, S. Giri, and S. Majumdar, *Phys. Rev. B* **83,** 134427 (2011).

[12] R. S. Freitas, L. Ghivelder, F. Damay, F. Dias, and L. F. Cohen, *Phys. Rev. B* **64,** 144404 (2001).

[13] M. Ulrich, J. García-Otero, J. Rivas, and A. Bunde, *Phys. Rev. B* **67,** 024416 (2003).

[14] T. Kimura, *Annu. Rev. Condens. Matter Phys.* **3,** 93 (2012).

Summary of the thesis

Exploring new magnetoelectric multiferroics and understanding the mechanism of origin of electric polarization is important to achieve room-temperature magnetoelectric multiferroic so that these materials can be used in future devices. In this thesis, we have started with the aim to explore new magnetoelectric multiferroics and investigated four different systems. Firstly, we have worked on a bismuth based oxide $BiMnFe_2O_6$ that has two potential mechanisms, i.e., the presence of lone pair active Bi^{3+} ions and the spiral magnetic order of Fe^{3+}/Mn^{3+} spins, which can induce ferroelectricity. We have shown that this compound is not multiferroic. We have extended this work by investigating the Sm-substituted $Bi_{1-x}Sm_xMnFe_2O_6$ compounds, but still we could not induce ferroelectricity. However, we have found some rich magnetic properties and magnetodielectric effects. The important result presented in this thesis is the discovery of linear magnetoelectric effect in the *A*-site magnetic spinels, Co_3O_4 and $CoAl_2O_4$. We have demonstrated that the linear magnetoelectric effect arises due to the single-ion contributions of the magnetic ions (Co^{2+}) located at a local noncentrosymmetric site. We have further explored the magnetic ground state of the latter compound using the magnetoelectric study, which has been a controversial issue. Another interesting outcome of this thesis investigation is the finding a new series of magnetoelectric multiferroics, $RFeWO_6$ (R = Dy, Eu, Tb and Y), which belong to ordered aeschynite-type polar (space group: $Pna2_1$) magnets family. These oxides possess an unusual noncollinear magnetic ordering of Fe^{3+} spins below $T_N^{Fe} \sim 15$ - 18 K. Our results suggest that the electric polarization (P) at the paramagnetic state is of the form of (0, 0, p_z) while in the magnetic ordered sate it has a form of (p_x, 0, p_z), where the component p_x arises solely due to the magnetic ordering. Hence, these polar magnets are not only significant in view of new magnetoelectric multiferroics, but also it may help in designing further new multiferroics in this polar magnets family with high transition temperature. $DyCrWO_6$, another isostructural compound of these multiferroics family, has been investigated, but the multiferroicity is not observed. However, temperature induced magnetization reversal and large magnetocaloric effect are observed at low temperatures. Finally, we have explored the multiferroic and magnetic properties of another complex oxide, $BaYFeO_4$, which exhibits multiple magnetic ordering.